Anderson, Liam James (2013) ***Investigations into plasma deposited linalyl acetate thin films for applications in organic electronics.*** **PhD Thesis, James Cook University.**

Anderson, Liam James (2013) ***Investigations into plasma deposited linalyl acetate thin films for applications in organic electronics*****. PhD thesis, James Cook University.**

Investigations into Plasma Deposited Linalyl Acetate Thin Films for Applications in Organic Electronics

Thesis submitted by

Liam James Anderson

in May 2013

for the degree of Doctor of Philosophy

in the School of Engineering and Physical Sciences

James Cook University

Supervisors: A/Prof. Mohan Jacob, A/Prof. Ronald White

DECLARATION

I declare that this thesis is my own work and has not been submitted in any form for another degree or diploma at any university or institute of tertiary education. Information derived from the published and unpublished work of others has been acknowledged in the text, and a list of references is given.

Liam Anderson

May, 2013

STATEMENT OF ACCESS TO THIS THESIS

I, the undersigned, the author of this work, understand that James Cook University will make this work available for use within the University Library, and via the Australian Digital Thesis Network, for use elsewhere.

I understand that as an unpublished work, a thesis has significant protection under the Copyright Act. I do not wish to place any restriction on access to this thesis. However, any use of its content must be acknowledged and could potentially be restricted by future patents.

____

Liam Anderson

May, 2013

STATEMENT ON THE CONTRIBUTIONS FROM OTHERS

This thesis included the following contributions of others:

Funding: Support was provided from an Australian Postgraduate Award throughout the duration of this thesis. Additional support was provided from the James Cook University School of Engineering and Physical Sciences through an extension scholarship and Graduate Research Scheme funding. Contributions to living expenses in Naples, Italy, for a period of three months were made by the University of Naples.

Editorial assistance: Assistance was provided by A/Prof. Mohan Jacob and A/Prof. Ronald White of James Cook University. Assistance was provided for text in Chapters 4 and 6 by co-authors of the published papers on which these chapters were based; Dr. Chris Easton of CSIRO, and Prof. Antonio Cassinese, Dr. Mario Barra and Dr. Flavia di Girolamo of the University of Naples.

Experimental assistance and data analysis: XPS measurements and extraction of data from these were performed by Dr. Chris Easton of CSIRO. Deposition of the organic semiconductor PDI-8CN$_2$ was performed by collaborators (Prof. Antonio Cassinese, Dr. Mario Barra and Dr. Flavia di Girolamo) at the University of Naples. AFM measurements and associated analysis of PDI-8CN$_2$ samples were conducted by collaborators at the University of Naples. Deposition of the organic semiconductor pentacene and IV measurements of the associated devices was performed by collaborators (Prof. Mitsumasa Iwamoto and Dr. Dai Taguchi) at the Tokyo Institute of Technology.

Contributions to co-authored publications: Although I have co-authored papers, I have received only partial assistance in terms of editing and access to facilities not available at James Cook University; this is substantiated by my first authorship on all papers relevant to this thesis. Three publications resulting from this work included contributions from others. In the publications *Optical properties of thermally evaporated PDI-8CN2 thin films* and *Effect of a plasma polymerised linalyl acetate dielectric on the optical and morphological properties on an n-type* *organic semiconductor*, editorial and experimental assistance was provided as noted above. Sections of these papers and Chapter 6 relevant to AFM imaging of PDI-8CN$_2$ include written contributions from collaborators at the University of Naples. In the publication *Compatibility of plasma deposited linalyl acetate thin films with organic electronic device fabrication techniques*, editorial and experimental assistance was provided as noted above. Sections of this paper and Chapter 4 relevant to XPS measurements include written contributions from Dr. Chris Easton of CSIRO.

Except for the cases noted above, I performed all experimental, analytical and editorial work.

ACKNOWLEDGEMENTS

First, I'd to thank my supervisors, Mohan Jacob and Ron White. Without your assistance, encouragement and patience this wouldn't have been possible.

Thanks to the JCU Engineering and Physical Sciences academic and support staff for all of your assistance with things small and large over the years, and the academic opportunities given to me.

Antonio Cassinese, Mario Barra and Flavia di Girolamo - thanks for giving me the opportunity to work with you, and all your help during my time with your research group. Your continued support of my work is greatly appreciated.

Thanks to everyone I’ve collaborated with; Dr. Chris Easton from CSIRO, Prof. Mitsumasa Iwamoto from Tokyo Institute of Technology, Prof. Antonio Cassinese, Dr. Mario Barra and Dr. Flavia di Girolamo from the University of Naples, Dr. Xiaojing Zhou from University of Newcastle and the COPE group from University of Queensland.

I'm grateful for the financial support provided to me throughout this PhD through the APA and EPS scholarships, GRS funding and University of Naples.

Thanks to my brothers, Shawn and Kris, and parents, for always supporting me.

Finally, thanks to all my friends. There are too many of you to name, but I appreciate everything.

ABSTRACT

Organic electronic device research continues to take place on predominately Si substrates utilising oxide dielectric barriers, which are unable to take advantage of the flexibility and optical transparency of organic semiconducting materials. These organic semiconductors are typically deposited by thermal evaporation or solution processing methods, and substrates must be compatible with exposure to temperatures on the order of 150 °C and insoluble in a variety of organic solvents, in addition to possessing desirable electrical, mechanical, optical and processing (e.g. low cost, large volume) properties. In this work plasma deposited linalyl acetate thin films were considered as a potential candidate for application in organic electronic devices.

Linalyl acetate is a component of the essential oil *Lavandula angustifolia*, which can be obtained non-synthetically. Both the monomer and deposition method are environmentally friendly, low cost and do not result in harmful waste or pollution. Thin films deposited from this monomer were fabricated using plasma enhanced chemical vapour deposition and their properties studied as a function of energy delivered to the reaction chamber.

Films were found to have minimal absorbance at optical wavelengths and were completely transparent. The refractive index of the material was found to be 1.55 – 1.58 at 589 nm and the optical band gap derived from the absorbance profile was 2.95 eV – 3.02 eV. The variation in these parameters was linked directly to variation in the energy used during the deposition. Independent of this energy, the surfaces of the plasma deposited thin films were smooth, free of defects and had an average roughness of 0.20 nm. The hardness of the films was between 0.30 GPa and 0.45 GPa, again correlated with the power density used. The underlying cause of this variation was shown to be related to an increase in carbon content as higher power densities were used.

Electrically, the films were highly insulating, possessing conductivities of less than 10^{-10} Ω^{-1} m^{-1} in all cases and a dielectric breakdown strength of 1.8 MV cm^{-1}. The dielectric function was measured from dc to RF frequencies. The relative permittivity at low frequencies (less than

10 Hz) was found to be 11, while the high frequency dielectric constant was found to be 3 – 3.5 at 100 kHz and 2.4 at optical frequencies. Dielectric loss spectra revealed complex underlying relaxation features present in plasma deposited thin films.

To confirm their applicability to organic electronics, the process compatibility of the thin films was studied. It was found that thermal degradation began at greater than 195 °C, the films were insoluble in a variety of organic solvents including the commonly used dichlorobenzene and chloroform, and possessed a surface free energy of ~45 mJ m^{-2}. Further, the interaction between the linalyl acetate surface and the n-type organic semiconductor PDI-8CN_2 was investigated and the material shown to influence the growth of the organic semiconductor in a manner similar to common surface treatments of SiO_2. An organic field effect transistor was fabricated, which included a linalyl acetate layer between the SiO_2 and pentacene organic semiconductor. Relative to a similar device without the linalyl acetate layer, improved performance characteristics were observed. In particular, the mobility was increased by two orders of magnitude, the on/off ratio improved, and the threshold voltage reduced.

CONTENTS

LIST OF ABBREVIATIONS

ac	Alternating Current
AFC	Alkaline Fuel Cell
AFM	Atomic Force Microscopy
AG	After Glow
ATR	Attenuated Total Reflectance
CA	Contact Angle
CC	Cole-Cole
dc	Direct Current
DC	Davidson-Cole
DLC	Diamond-Like Carbon
DOS	Density of States
FTIR	Fourier Transform Infrared
HN	Hevriliak-Negami
HOMO	Highest Occupied Molecular Orbital
IR	Infrared
IS	Impedance Spectroscopy
ITO	Indium Tin Oxide
IV	Current Voltage

JCU	James Cook University
JV	Current Density Voltage
KK	Kramers-Kronig
LHS	Left Hand Side
LUMO	Lowest Unoccupied Molecular Orbital
MEM	Micro Electro-Mechanical
MIM	Metal-Insulator-Metal
MIS	Metal-Insulator-Semiconductor
MOSFET	Metal Oxide Semiconductor Field Effect Transistor
MSE	Mean Square Error
MW	Microwave
OES	Optical Emission Spectroscopy
OFET	Organic Field Effect Transistor
OLED	Organic Light Emitting Diode
OPV	Organic Photovoltaic
OSC	Organic Semiconductor / Organic Semiconducting
OTFT	Organic Thin Film Transistor
PCB	Printed Circuit Board
PDLA	Plasma Deposited Linalyl Acetate

PECVD	Plasma Enhanced Chemical Vapour Deposition
PEMFC	Proton Exchange Membrane Fuel Cell
PF	Poole-Frenkel
PSD	Power Spectrum Density
PV	Photovoltaic
RC	Resistor/Capacitor
RF	Radio Frequency
RGA	Residual Gas Analysis
RHS	Right Hand Side
RMS	Root Mean Square
RS	Richardson-Schottky
RSGP	Rapid Step Growth Polymerisation
S/D	Source/Drain
SAM	Self-Assembled Monolayer
SCLC	Space-Charge Limited Conduction
SEM	Scanning Electron Microscopy
SPDR	Split-Post Dielectric Resonator
SPM	Scanning Probe Microscopy
STW	Surface Traverse Wave

TFL	Traps Filled Limit
TSCLC	Trapped-Space-Charge Limited Conduction
UV	Ultra Violet
UV-Vis	Ultra-Violet Visible
VASE	Variable Angle Spectroscopic Ellipsometry/Ellipsometer
VCG	van Oss, Chaudhury and Good
WCA	Water Contact Angle
XPS	X-ray Photoelectron Spectroscopy

LIST OF CHEMICAL ABBREVIATIONS

a-C:H	Amorphous Hydrocarbon / Diamond-Like Carbon
a-Si	Amorphous Silicon
DIM	Diiodomethane
EG	Ethylene Glycol
F/C	Fluorocarbon
HMDS	Hexamethyldisilazane
HMDSO	Hexamethyldisiloxane
OTS	Octadecyltrichlorosilane
P3HT	Poly(3-hexylthiophene)
PCBM	Phenyl-C_{61}-butyric acid methyl ester
PDI-8CN_2	N,N'-bis(n-octyl)-1,6-dicyanoperylene-3,4:9,10-bis(dicarboximide)
PMMA	Poly(Methyl Methacrylate)
TEOS	Tetraethoxysilane
TMS	Tetramethylsilane
TIPS	6,13-bis(triisopropylsilylethynyl)

LIST OF FIGURES

LIST OF TABLES

LIST OF SYMBOLS

Term	Definition	Units
α	Absorption coefficient	Dimensionless
	Extinction coefficient amplitude	Dimensionless
	Stretching factor of HN distribution	Dimensionless
β	Exponent factor	Dimensionless
β_{RS}	RS field-lowering coefficient	eV $m^{1/2}$ $V^{-1/2}$
β_{PF}	PF field-lowering coefficient	eV $m^{1/2}$ $V^{-1/2}$
β_{exp}	Experimental field lowering coefficient	eV $m^{1/2}$ $V^{-1/2}$
γ	Extinction coefficient band edge	nm
	Skewness factor of HN distribution	Dimensionless
γ^{+}	Electron donor component of surface free energy	mJ m^{-2}
γ^{-}	Electron acceptor component of surface free energy	mJ m^{-2}
γ_S	Surface free energy of a solid	mJ m^{-2}
γ_S^{AB}	Acid-base component of surface free energy	mJ m^{-2}
γ_S^{LW}	Lifshitz-van der Waals component of surface free energy	mJ m^{-2}
γ_S^{P}	Polar component of surface free energy	mJ m^{-2}
γ_S^{D}	Dispersive component of surface free energy	mJ m^{-2}
γ_L	Surface free energy of a liquid	mJ m^{-2}

γ_{SL}	Interfacial tension between solid s and liquid L	mJ m^{-2}
δ	Phase angle of $\varepsilon_c(\omega)$	°
$\boldsymbol{\varepsilon}$	Vector of discrete complex permittivity observations	Dimensionless
ε_n	n^{th} element of $\boldsymbol{\varepsilon}$	Dimensionless
$\varepsilon_{\delta n}$	Experimental noise in measured IS data point ε_n	Dimensionless
$\varepsilon_c(\omega)$	Complex dielectric function (of frequency)	Dimensionless
$\varepsilon_c(E)$	Complex dielectric function (of energy)	Dimensionless
ε_∞	High frequency dielectric constant, $\varepsilon_c(\omega)$ as $\omega \rightarrow \infty$	Dimensionless
ε_S	Low frequency dielectric constant, $\varepsilon_c(\omega)$ as $\omega \rightarrow 0$	Dimensionless
ε_r	Real part of $\varepsilon_c(\omega)$	Dimensionless
ε_i	Imaginary part of $\varepsilon_c(\omega)$	Dimensionless
ε_0	Permittivity of free space	F m^{-1}
ε_1	Real part of $\varepsilon_c(E)$	Dimensionless
ε_2	Imaginary part of $\varepsilon_c(E)$	Dimensionless
θ	Complex impedance phase angle	°
	Tilt of molecular chain axis relative to substrate	°
θ_S	Contact angle	°
κ	Dielectric constant	Dimensionless

λ	Wavelength	nm
	Regularisation parameter	Dimensionless
μ	Carrier mobility	$cm^2 V^{-1} s^{-1}$
ν	Wave velocity	$m s^{-1}$
	Kinetic chain length	Varies
ξ	Yasuda factor	J/kg
	Kramers-Kronig transform dummy variable	Dimensionless
	Correlation Length	nm
ρ	Electrical resistivity	Ω m
	Light reflectance ratio	Dimensionless
ρ_{es}	Electric field in resonant cavity	$V m^{-1}$
σ	Electrical conductivity	$\Omega^{-1} m^{-1}$
σ_{ac}	ac electrical conductivity	$\Omega^{-1} m^{-1}$
σ_{dc}	dc electrical conductivity	$\Omega^{-1} m^{-1}$
σ_{sat}	Saturation Value	Dimensionless
τ	Relaxation time	s
$\boldsymbol{\tau}$	Vector of discrete relaxation times	s
τ_n	n^{th} element of $\boldsymbol{\tau}$	s

τ_D	Characteristic relaxation time of a Debye relaxation	s
τ_{HN}	Characteristic relaxation time of a HN distributed $\varepsilon_i(\omega)$	s
υ	Kinetic chain length in polymerisation reaction	Dimensionless
ψ	Optimisation objective function	Dimensionless
ω	Angular frequency	rad s^{-1}
$\boldsymbol{\omega}$	Vector of discrete measured angular frequencies	rad s^{-1}
ω_n	n^{th} element of $\boldsymbol{\omega}$	rad s^{-1}
A	Amplitude of Gaussian oscillator	Dimensionless
	Absorbance	A. U.
	Cross sectional area	m^2
	Kernel matrix	Dimensionless
A_K	k^{th} row of kernel matrix A	Dimensionless
A_{nm}	n, m^{th} element of kernel matrix A	Dimensionless
$A(h_c)$	Tip area function, as a function of contact depth	Dimensionless
B_r	Broadening of Gaussian oscillator	eV
B_i	i^{th} Sellmeier coefficient (intensity of absorption peak)	Dimensionless
Δ	Phase angle of measured VASE signal	°
ΔG_{SLS}	Solubility of solid S in liquid L	mJ m^{-2}

$\Delta_{\ln(\tau)}$	Constant logarithmic spacing	ln(s)
E	Energy	eV
E_a	Activation energy	eV
	Centre energy of Gaussian oscillator	eV
E_g	Optical band gap	eV
Z	Complex impedance	Ω
|Z|	Magnitude of complex impedance	Ω
H	Hardness	GPa
I	Current	A
I_{on}	Channel current in transistor with applied gate-source bias	A
I_{off}	Channel current in transistor with no applied gate source bias	A
I_0	Intensity of incident light	W m^{-2}
I_t	Intensity of transmitted light	W m^{-2}
M	Molecular mass of monomer	kg
	Number of real valued fit parameters in VASE analysis	Dimensionless
N	Length of a vector/data set	Dimensionless
N_v	Density of states at the HOMO energy	Dimensionless
N_t	Density of traps	cm^{-3}

P	Pressure of plasma reactor	mTorr/micron
	Exponent of Tauc equation	Dimensionless
	Applied load during nano-indentation	N
P_{max}	Maximum load during nano-indentation	N
T	Temperature	°C or K
Ψ	Magnitude of measured VASE signal	Dimensionless
c	Speed of light in vacuum	$m\ s^{-1}$
d	Thickness	m
d_{act}	Length of plasma discharge	m
d_{gas}	Distance between monomer inlet and substrate in plasma reactor	m
f	Frequency	Hz
f_f	Resonant frequency of SPDR	Hz
$\mathbf{g}$	Vector of discrete relaxation time weights	Dimensionless
$\mathbf{g_{min}}$	Optimised distribution $\mathbf{g}$	Dimensionless
$\mathbf{g_{minK}}$	Optimised $\mathbf{g_{min}}$, calculated from $\boldsymbol{\varepsilon}$ with element k removed	Dimensionless
g(τ)	Distribution of relaxation times	Dimensionless
h	Displacement of AFM tip during nano-indentation	nm
	Planck's constant	eV s

h_f	Maximum displacement of AFM tip during nano-indentation	nm
	Thickness of film in SPDR sample	nm
h_c	Depth of nano-indentation	nm
k	Extinction coefficient	Dimensionless
	Spring constant of AFM cantilever	N m^{-1}
k_B	Boltzmann's constant	eV K^{-1}
m	Gradient of a linear function	Varies
n	Real part of refractive index	Dimensionless
n_o	Carrier density	cm^{-3}
q	Electron charge	C
r_p	Magnitude of p-polarised reflected light, as measured by VASE	Dimensionless
r_s	Magnitude of s-polarised reflected light, as measured by VASE	Dimensionless
t	Thickness	nm
x	Displacement of AFM cantilever	nm
C	Cauchy layer coefficient	Dimensionless
C_i	i^{th} Sellmeier coefficient (position of absorption peak)	nm
D	Dielectric loss	Dimensionless

F	Force	N
	Monomer flow rate	$cm^3 s^{-1}$
F_b	Applied electric field when dielectric breakdown occurs	$MV cm^{-1}$
G	Reactor geometry factor	Dimensionless
G_K	Weights of dielectric relaxation distribution	Dimensionless
J	Current density	$A m^{-2}$
J_0	Low-field current density	$A m^{-2}$
J_Ω	Ohmic current density	$A m^{-2}$
J_{SCLC}	Space-charge limited current-density	$A m^{-2}$
L	Channel length of a transistor	m
L	Regularisation matrix	Dimensionless
Q	Q-factor	Dimensionless
Q_0	Unloaded Q-factor	Dimensionless
Q_{DR}	Loss due to metallic portion of resonant structure	Dimensionless
Q_C	Loss due to dielectric part of resonant structure	Dimensionless
R_a	Average surface roughness	nm
R_m	Rate of deposition of plasma deposited thin film	nm
R_{RMS}	RMS surface roughness	nm

S	Scaling factor	Dimensionless
	Contact stiffness	N m^{-1}
V	Volume of plasma reactor	m^3
$V_0(\lambda)$	Cross-validation function	Dimensionless
V_{dis}	Volume occupied by plasma discharge	m^3
V_{DS}	Bias applied across transistor drain-source terminals	V
V_{GS}	Bias applied across transistor gate-source terminals	V
V_{gas}	Volume occupied by monomer	m^3
V_{th}	Transistor threshold voltage	V
W	Power applied to PECVD reaction	W
	Channel width of a transistor	m

LIST OF PUBLICATIONS

L.J. Anderson, M.V. Jacob, Effect of RF power on the optical and morphological properties of RF plasma polymerised linalyl acetate thin films, Applied Surface Science 256 (2010) 3293-3298

M. Barra, F. V. Di Girolamo, F. Chiarella, M. Salluzzo, Z. Chen, A. Facchetti, L. Anderson and A. Cassinese, Transport property and charge trap comparison for n-channel perylene diimide transistors with different air stability, Journal of Physical Chemistry C 114 (2010) 20387-20393

L. J. Anderson, M. V. Jacob, M. Barra, F. V. Girolamo and A. Cassinese, Optical properties of thermally evaporated PDI-8CN2 thin films, Physics Procedia 14 (2011) 29-33

L. J. Anderson, M. V. Jacob, Microwave characterisation of a novel, environmentally friendly, plasma polymerised organic material, Physics Procedia 14 (2011) 87-90

L. J. Anderson, M. V. Jacob, M. Barra, F. V. Girolamo and A. Cassinese, Effect of a plasma polymerised linalyl acetate dielectric on the optical and morphological properties on an n-type organic semiconductor, Applied Physics A 105 (2011) 95-102

L. J. Anderson, M. V. Jacob, Electrical characterisations of plasma polymerised linalyl acetate, Materials Science and Engineering B 177 (2012) 311-315

L. J. Anderson, M. V. Jacob, Temperature dependent electrical impedance spectroscopy measurements of plasma enhanced chemical vapour deposited linalyl acetate thin films, Thin Solid Films 534 (2013) 452-458

L. J. Anderson, C. D, Easton, M. V. Jacob, Compatibility of plasma deposited linalyl acetate thin films with organic electronic device fabrication techniques, Journal of Materials Science 48 (2013) 4851-4859

Chapter 1: Introduction

1.1 Rationale

Organic electronics is a rapidly developing technology, gaining attention in the 2000s, as development of organic semiconductors (OSC) reached the point where materials became capable of producing commercially feasible devices. Despite this, the current electronics market remains largely dominated by Si technology due to the substantial fabrication infrastructure available and the generally superior performance of devices over their organic electronic counterparts. However, Si technology has fundamental limitations with respect to its mechanical fragility, flexibility and cost of manufacture, whereas organic electronic devices have the potential to be fabricated on transparent, mechanically flexible substrates in large volumes (e.g. reel to reel processing) at very low cost.

Despite these advantages, organic electronic materials and devices remain, from a performance perspective, unable to compete with Si technology in many applications. Additionally, high performance organic materials remain high in cost and are damaging to the environment. Low cost materials, compatible with current organic electronic fabrication techniques and which improve device performance are in strong demand.

From 2007 – 2009, A/Prof. Jacob and Dr. Easton developed a new class of materials, derived from the Australian essential oil monomer *Lavandula angustifolia* using the radiofrequency (RF) plasma enhanced chemical vapour deposition (PECVD) technique. PECVD was used as it allows polymerisation of materials which cannot act as monomers in traditional polymer synthesis techniques. This work resulted in films with controllable thickness in the nanoscale range, derived from environmentally friendly sources which were optically transparent and had an array of potential applications, including electronics and biotechnology. Materials derived from essential oil precursors, which are a complex mixture of many components, suffer from poorly defined chemistry. Chemically, *Lavandula angustifolia* is composed of multiple chemicals, the dominant of which is 3,7-dimethylocta-1,6-dien-3-yl acetate (linalyl acetate), typically constituting 25% - 45% of the essential oil.

To obtain chemically well defined materials, linalyl acetate monomer was used with the PECVD technique to fabricate thin films which are derived from environmentally friendly techniques and products, and are mechanically flexible. Of particular interest was the electrical characterisation of the material, such that its suitability for organic electronic applications could be assessed.

1.2 Research Objectives

This project aimed to fabricate low cost, transparent thin films from environmentally friendly resources with precisely defined electronic properties, suitable for use in organic electronic devices. This was achieved by considering the following goals, each of which contributed to addressing the aim:

- To fabricate thin films derived from linalyl acetate monomer using PECVD and characterise the material's fundamental (optical, bulk chemical and morphological) properties.
- To determine the material's electrical properties. This included investigations into the mechanisms of charge transport through the material, the conductivity and resistivity of the material, the dielectric and loss properties of the material and the microwave (MW) properties of the material.
- To identify and investigate specific areas in organic electronics to which the thin films could be applied and determine the viability of the material in these applications.
- To investigate the relationship between the investigated properties and fabrication conditions, such that thin films optimised for specific applications can be developed.

Achieving the above objectives led to several contributions in the fields of material science and organic electronics. Plasma deposited linalyl acetate (PDLA) thin films constituted a new material, the characterisation of which contributed directly to the field. Indirect contribution was made through the development of analytical techniques which were required to characterise this unique class of materials. Development of this material has the potential to lead to transparent and flexible electronic devices, made from low cost and environmentally friendly processes and materials. In addition, use of this material is likely to lead to organic electronic devices with improved properties and functionality.

1.3 Document Organisation

This thesis consists of seven chapters, the body of which address directly the research objectives identified above. Chapter 1 outlines the motivation for this work and the context surrounding it.

Chapter 2 presents a review of literature related to the research objectives, with a particular focus on the PEVCD process, properties of films developed from this technology, and current trends in organic electronics, providing a detailed problem background.

Chapter 3 presents materials and methods, and details experimental procedures utilised throughout subsequent chapters.

Chapter 4 presents the developed plasma deposited thin films' fundamental properties. The optical properties in the Ultra Violet-Visible (UV-Vis) region were investigated through spectroscopic methods and are presented, as well as the surface morphological and tribological properties, investigated through Atomic Force Microscopy (AFM) and nano-indentation measurements. The chemical properties of the material were investigated by Fourier Transform Infrared (FTIR) spectroscopy and X-ray Photoelectron Spectroscopy (XPS). The theoretical basis for the measurement and analysis of these properties is presented as well their link to deposition conditions. Work in this chapter is largely reported in the journal article *L. J. Anderson, M. V. Jacob, Effect of RF power on the optical and morphological properties of plasma polymerised linalyl acetate thin films, Appl. Surf. Sci. 256 (2010) 3293-3298.*

Chapter 5 details the electrical properties of the thin films, beginning with characterisations at direct current (dc) frequencies which determined the conductivity of the films, their charge transport mechanism and dielectric strength using current-voltage (IV) measurements. The frequency dependent dielectric properties at multiple temperatures are presented, obtained through dielectric impedance spectroscopy, and a detailed overview of the analytical techniques given. Finally, the microwave dielectric properties at 10 GHz and 20 GHz are outlined. Work in this chapter is reported in the journal articles *L. J. Anderson, M. V. Jacob, Electrical characterisations of plasma polymerised linalyl acetate, Mater. Sci. Eng. B 177 (2012) 311-315, L. J. Anderson, M. V. Jacob, Temperature dependent electrical impedance spectroscopy measurements of plasma enhanced chemical vapour deposited linalyl acetate thin films, Thin Solid Films 534 (2013) 452-458* and *L. J. Anderson, M. V. Jacob, Microwave characterisation of a novel, environmentally friendly, plasma polymerized organic thin film, Phys. Proc.14 (2011) 87-90* and presented at the 9th International Conference on Nano-Molecular Electronics.

Chapter 6 investigates the compatibility of linalyl acetate thin films with current OSC deposition techniques through the investigation of the material's solubility and wettability, thermal degradation, and influence over the growth of thermally grown OSC layers. An Organic Field Effect Transistor (OFET) was fabricated using a PDLA buffer layer above a SiO_2 dielectric on a Si substrate and the device operating characteristics studied. Work in this chapter is reported in the journal articles *L. J. Anderson, C. D. Easton, M. V. Jacob, Compatibility of plasma deposited linalyl acetate thin films with organic electronic device fabrication techniques, J. Mater. Sci. 48 (2013) 4851-4859, L. J. Anderson, M. V. Jacob, M. Barra, F. V. Di Girolamo, A. Cassinese, Effect of a plasma polymerised linalyl acetate dielectric layer on the optical and morphological properties of PDI-8CN*$_2$ *thin films, Appl. Phys. A 105 (2011) 95-102* and *L. J. Anderson, M. V. Jacob, M. Barra, F. V. Girolamo, A. Cassinese, Optical properties of thermally evaporated PDI-8CN*$_2$ *thin films, Phys. Proc. 14 (2011) 29-33,* and presented as a poster at the 9th International Conference on Nano-Molecular Electronics.

Chapter 7 presents concluding remarks and recommendations for directions of possible future work in the area. Key results and contributions of the work to the fields of material and organic electronics are summarised in this chapter.

Chapter 2: Literature Review

2.1 Introduction

In this chapter an overview of literature relevant to the proposed work is presented. As the scope of this thesis was limited to the investigation of a new material derived from linalyl acetate and fabricated using PECVD for use in organic electronic applications, the literature review focused on two topics: plasma deposition and organic electronics. Plasma deposition of thin films was examined, beginning with the current understanding of the growth mechanisms involved. The relationship between the deposition parameters and properties of the resulting thin films was investigated and applications of PECVD thin films are presented. Subsequently, the background of organic electronic devices is given. This includes an overview of OFET devices and structures, current methods for fabrication of the devices, their performance characteristics and avenues for their improvement.

2.2 PEVCD

PECVD (plasma deposition or often referred to as plasma polymerisation) was the method used to fabricate insulating polymer-like thin films throughout the work of this thesis. This method has a long history, dating as early as 1874 [1]. It was not until the 1960s that plasma deposits gained significant interest and the field of plasma deposition received attention [2]. The method results in films which are pinhole free [3, 4], smooth [5, 6] and which adhere well to a variety of substrates, including flexible plastics [7, 8]. Furthermore, the ability to create coatings from a variety of materials which cannot be polymerised using traditional methods is a feature unique to plasma deposition [9]. Current understanding of the processes and mechanisms involved in PECVD, their relationship with internal system characteristics and external experimental variables and how these relate to the characteristics of the deposited thin films are discussed.

2.2.1 The Internal Properties of PECVD

Modelling the internal mechanisms involved in plasma deposition is complex, due to the difficulty of reconciling observed film properties with internal reaction parameters. This difficulty is twofold; first, the properties of resultant thin films vary drastically depending on the reactor type, process variables and feed gas. The most poignant demonstration of this is that the same process can remove material from a substrate, or deposit material onto a substrate, i.e. the process can both etch materials *and* form a plasma product on exposed surfaces, depending on reaction parameters [10]. Secondly, until recently, the ability to accurately measure properties of the plasma discharge had been significantly limited; measurement of the reactive species involved and density, temperature and source of electrons was difficult, if not impossible. These factors made the task of developing a description of the plasma deposition process difficult.

The key factor in any plasma is the dynamics of electrons, typically created through the ionisation of feed gases and their dissociated products [11]. Before any recombination reactions can take place, the presence of reactive species in the system is critical. When exposing the feed gas to the plasma field, it is the interactions of the feed gas molecules with charged plasma species which lead to the creation of the precursors necessary for the reactions to occur. The exact nature of these reactions is a topic of much study and debate [10-14], however, most proposed reaction pathways require many of the same building blocks; it is the way in which these interact in specific circumstances which remains unclear.

These building blocks are considered to be electrons, ionic species, radical species, monomer fragments and UV photons [15, 16]. The source of these species is driven by the interactions with the feed gas (monomer material to be deposited) and the plasma glow, where energetic electrons and ions in the plasma collide with the monomer units to dissociate monomer bonds, fragmenting it to ionic and radical species. Some proposed mechanisms of film growth require the ionisation of the monomer unit, while many others rely only on the presence of radical species produced from the fragmented monomer. Yasuda argues that ionisation of the monomer is unlikely, due to the energy required to dissociate many, if not all, bonds presence in most organic monomers being much lower than the tens of eV required to ionise the monomer [15]. Friedrich provided the dissociation energies of some common aliphatic (i.e. non conjugated) compound bonds [17], all of which are in the order of less than 5 eV. Hence it is most likely that the dissociation of monomer units occurs first, followed by the ionisation of the resulting fragments [15]. The end result is a combination of plasma species, including electrons, UV photons, ions and species resulting from plasma-monomer interactions, including monomer fragments, as ionic and radical species, as well as intact monomer species. It is thought that reactions take place on the surface of substrates within the reactor as well as in the gas phase. Due to bombardment of surfaces with charged, active species, polymer products radiated from the surface and formed in the gas phase also contribute to the reactions which form the final thin film material [16].

2.2.2 Reaction Pathway of Plasma Deposition of Thin Films

It is helpful first to discuss the properties of films resulting from plasma deposition, as it is necessary that any proposed mechanisms can address why these features are present, and how they come to be. The resulting material exists in the form of a thin film deposit on any surface exposed to the plasma glow, ranging from less than 10 nm to several μm in thickness. The deposits are well adhered to the surface, and tend to be insoluble in a variety of solvents, providing evidence that the films consist of a highly crosslinked structure [18, 19]. Additionally, after exposure to ambient conditions, incorporation of O_2 into the surface of the material has been observed, indicative of the presence of radical species in the bulk structure of the thin film [20, 21]. Thus the proposed reaction pathway must be capable of explaining: the formation of thin films, their adhesion properties, their crosslinked nature and why radicals species are incorporated into the bulk structure of the material.

Generally, proposed mechanisms use three stages to explain the thin film formation [16]:

1. Creation of active species in the gas phase.
2. Interaction and recombination of active species in the gas phase and at surfaces in the plasma.
3. Surface reactions with charged, bombarding particles.

Stage 1 has been discussed in Section 2.2.1; stages 2 and 3 are now outlined.

After the formation of the active species, there are monomer units, monomer fragments, ions, radicals, electrons and photons present in the gas phase. The growth mechanism is considered to be a radical dominated mechanism, i.e. recombination of radicals is the main contributor to the increase of molecular weight of the material [16]. This can happen in both the gas phase or at the substrate surface by the recombination of adsorbed species. There is evidence that formation of a polymer in the gas phase occurs at higher pressures and results in ‘powder-like’ deposits [17], and hence recombination reactions with adsorbed species at the substrate surface are preferred. Recombination in the gas phase may produce intermediate compounds which can contribute to the formation of the thin film [17]. Another important consideration is the bombardment of adsorbed particles and reaction products at the surface of a substrate by the charged active species in the gas phase. This is caused by the development of a self bias across materials exposed to the plasma, which results in the attraction of charged particles to the surface.

The result of this bombardment is twofold; ion and photon bombardment causes ablation, or sputtering of the deposited film back into the gas phase, which is also associated with the formation of radical products in the bulk of the material [10, 15]. Bombardment of the bulk film by active species is also partially responsible for the crosslinking and insolubility observed in many plasma deposited films, for the high concentration of radicals embedded in the film, and some of the ageing reactions.

Explanations of plasma deposition mechanisms and reaction pathways include the contributions of several factors, including initial kinetic reactions to form reactive species, interaction of reactive species via radical growth reactions in the gas phase and at the surface, and bombardment of surfaces by active species, resulting in ablation of deposited species back into the gas phase. This is outlined in Figure 2.1 [16]:

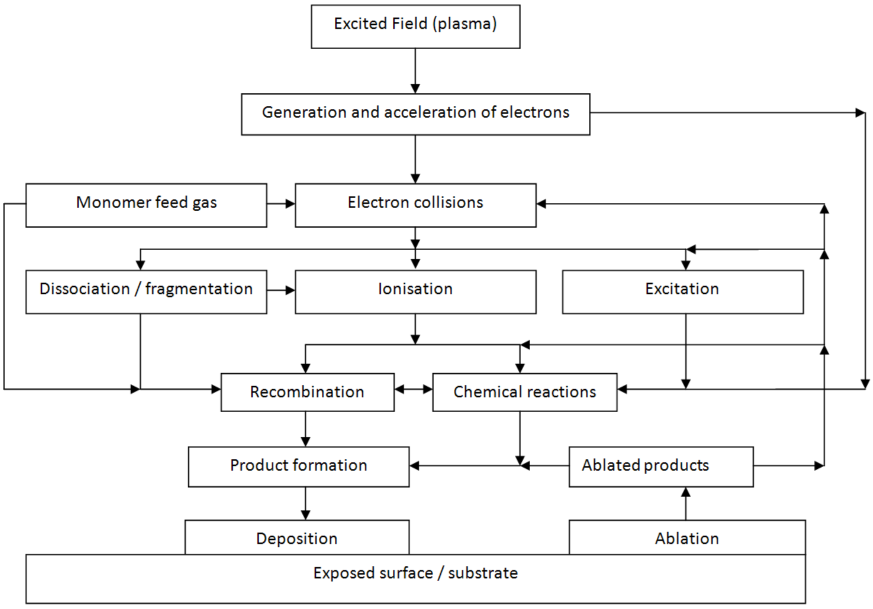

Figure 2.1: Plasma deposition process

The complex processes at play in the recombination and chemical reaction steps can be explained by the Rapid Step Growth Polymerisation (RSGP) mechanism, proposed by Yasuda [15]. In this scheme, polymerisation occurs via the formation of reactive species, in this case radicals, via the excitation of a monomer with a plasma. The scheme consists of two cycles, or stages of reaction, as well as a third stage which represents the interactions between these cycles. Cycles I and II describe similar reactions, i.e. the addition of reactive species to monomer units, however cycle I describes a process dominated by species with a single reactive site. These reactions are described by:

$$M + plasma \rightarrow M_{fragN}^{\bullet} \tag{2.1}$$

where M represents monomer units, $M_{fragN}\bullet$ represents the N^{th} generated fragmented monomer radical product, and (2.1) describes the formation of active species via monomer-plasma interactions. Following this reaction, radical products may interact with monomer units (2.2), or other radical products (2.3):

$$M_{frag1}^{\bullet} + M \rightarrow M_{frag1}^{\bullet} - M \tag{2.2}$$

$$M_{frag1}^{\bullet} + M_{frag2}^{\bullet} \rightarrow M_{frag1} - M_{frag2} \tag{2.3}$$

The product resulting from (2.2) can be thought to be a small unit of polymer product, $P_N\bullet$, which will contribute to film growth, until recombination with another radical product, terminating chain growth:

$$P_N^{\bullet} + P_N^{\bullet} \rightarrow P_N - P_N$$

$$\text{or} \tag{2.4}$$

$$P_N^{\bullet} + M_{frag3}^{\bullet} \rightarrow P_N - M_{frag3}$$

Reaction (2.4) describes radical chain growth polymerisation. Reactions of intact monomer units M with reactive species as described in (2.2) and (2.4), while possible, are not likely to dominate given the high likelihood that the monomer units have dissociated into reactive products upon exposure to the exciting plasma. The product of (2.2) can also be considered a radical monomer fragment, at the beginning of cycle I. Additionally, the product from (2.3), as part of cycle I of the RSGP mechanism, describes a stable product which can no longer contribute to product growth. Hence the RSGP scheme describes a reactivation of products $P_N - P_N$ via plasma excitation such that reactions in this scheme can contribute to the overall film growth.

Cycle II describes reactions of diradical species, $\bullet M_{fragN}\bullet$, which can continue to contribute to film growth without subsequent reactivation of reaction products. The two reactions which describe cycle II are:

$$^{\bullet}M_{frag4}^{\bullet} + M \rightarrow {}^{\bullet}M_{frag4} - M^{\bullet} \tag{2.5}$$

$$ {}^{\bullet}M_{frag5}^{\bullet} + {}^{\bullet}M_{frag6}^{\bullet} \rightarrow {}^{\bullet}M_{frag5} - M_{frag6}^{\bullet} \tag{2.6} $$

The products of both (2.5) and (2.6) are each diradical species, which can contribute to continued film growth or become biradical species at the beginning of cycle II. As before, reaction (2.5) is unlikely to occur in a plasma deposition reaction, given the strong likelihood that monomer units will dissociate into radical fragments. Cycle II can continue to contribute to growth of the thin film so long as diradicals or monomer units/fragments with double or triple bonds continue to exist.

The final reaction pathway is the interaction between cycle I and II products, i.e.:

$$ M_{frag7}^{\bullet} + {}^{\bullet}M_{frag8}^{\bullet} \rightarrow M_{frag7} - M_{frag8}^{\bullet} \tag{2.7} $$

This reaction can be thought to produce a radical monomer fragment, $M_{frag9}\bullet$, which becomes an input to cycle I. The entire mechanism can be outlined as follows [16]:

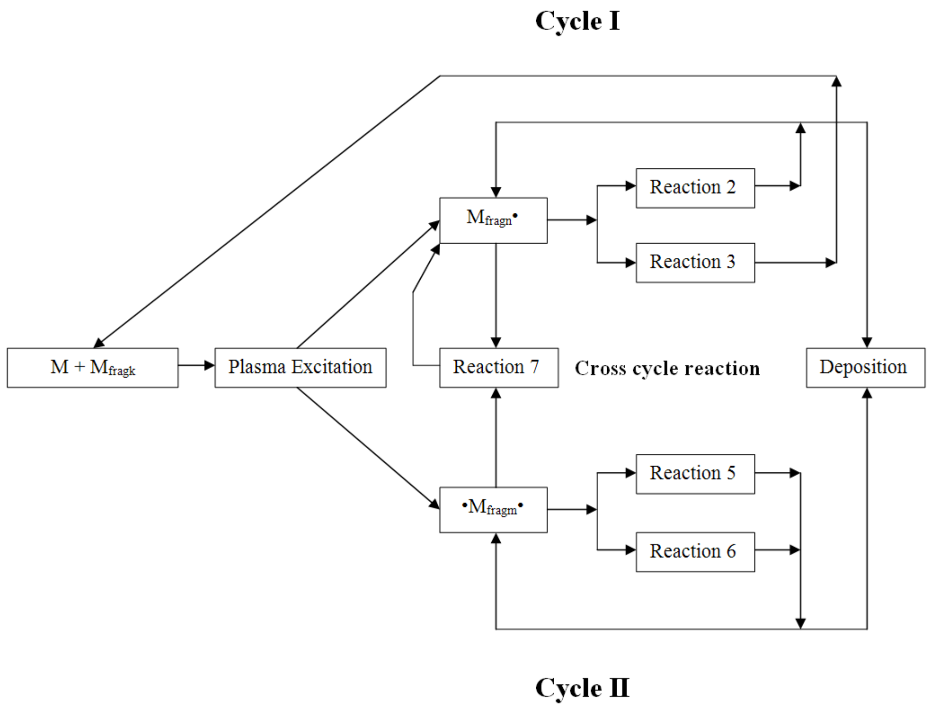

Figure 2.2: RSGP mechanism

The kinetic chain length, υ, is a measure of the number of monomer units that are added to the polymer chain by one initiating reaction before termination of the chain occurs, and increases with monomer concentration and decreases with reactive species concentration. As the concentration of monomer units is quite low in a plasma system, given the tendency for the monomer to dissociate into radical fragments, the concentration of reactive species is very high and very short kinetic chain lengths occur [17]. Were this not the case (i.e. (2.2) and (2.5) dominated), the above scheme would describe free radical chain growth polymerisation. However, as υ is short, the reactions begin and terminate quickly and deposition occurs in a series of small steps, resulting in a film of very short, branched, randomly terminated and crosslinked polymer chains.

The RSGP mechanism describes reactions between reactive species in a generalised sense; above the reactive species were considered to be radical monomer fragments, however nothing prevents these reactive species from being ionic, for example. As well as this the location of the reactions are not specified, only the reactions between reactive species. Thus RSGP can apply to gas phase, plasma sheath and surface reactions.

2.2.3 Relationship between Deposition Parameters and Film Properties

2.2.3.1 Control Parameters

Creation of reactive species in the gas phase is determined by the electron energy in the gas phase [11, 13, 15]. This energy leads to dissociation of the organic molecules, rather than ionisation, as the dissociation energy of the chemical bonds is generally much lower than the ionisation energy [15], resulting in a much higher concentration of free radicals in the gas phase than ions [21]. From a manufacture and control perspective, it would be ideal to control directly the electron energy distribution to provide the desired properties in the resulting thin films; however, measurement of this distribution is exceedingly difficult [22] and hence such a process is currently infeasible. It is known that several *external* control parameters will influence the behaviour of the reaction. These parameters are: the geometry of the reactor [23], the monomer [16, 20, 21], the flow rate of the monomer through the system [5, 24], the power delivered to the system [7, 20, 25] and the system pressure [16, 26, 27]. All of these factors have been shown to significantly influence the properties of resulting films [16].

Use of different geometry reactors while maintaining other parameters of the deposition constant resulted in different behaviour of amorphous hydrocarbon (a-C:H) thin films deposited from tetramethylsilane (TMS) and hexamethyldisiloxane (HMDSO) monomers [23]. Hegemann *et al* further investigated the significance of reactor geometry on the behaviour of films deposited from methane and HMDSO, and ascribed the different behaviours to the change in volume which the plasma occupied [16].

The strong dependence of film properties on the monomer was demonstrated through the investigation of films fabricated using isomeric monomers by Denis *et al* [21]. In this particular study, no compositional differences were present between the monomers; only the molecular structure was varied. For this apparently small difference in monomer, below a power threshold, differences in the chemical composition of the films were observed as a result of monomer structure, ascribed to differences in bond dissociation energies in the different isomers. Differences in monomer composition then have even more significant influence over the properties of resulting films, as shown by both Hegemann [16] and Mangindaan [20].

A decrease in monomer flow rate results in a larger residence time and hence an increase in the fragmentation of the monomer [16, 24, 28]. In a similar manner, power delivered to the reaction relates to the energy delivered to monomer molecules, resulting in increased monomer fragmentation [7] and change in film properties. The final external control parameter, pressure, influences the deposition indirectly by influencing the plasma volume and the distribution of reactive species in this volume [16, 27]. All of these parameters interact in complex and unpredictable ways. In an attempt relate the deposition conditions and film properties through a single parameter, the composite parameter, W/FM was developed, where W is the power absorbed by the plasma in W, F is the flow rate of the monomer in mol s^{-1} and M is the molecular mass of the monomer in kg mol^{-1}. As the parameter M is constant for a given monomer, the composite parameter is often reduced to W/F.

This parameter describes the energy delivered to each monomer unit in the reaction [23], and is considered to be proportional to the concentration of activated species in the plasma [5]. It is related to the degree of fragmentation of the monomer [8]. This has been experimentally investigated by monitoring the composition of the plasma discharge as a function of W/FM by several research groups [7, 19, 21, 29]. In a thiophene discharge subject to variation in the parameter W/FM, it was found that only the intensity of the emission lines in the Optical Emission Spectroscopy (OES) spectrograph changed [29], indicative of the formation of more reaction products, likely as a result of an increase in the number of monomer molecules becoming fragmented. The plasma was shown to contain N_2^-, CH, H and O reaction products, and no emission corresponding to sulphur was detected, though it was expected from the structure of the monomer. More recently, Denis *et al* have investigated the gas phase chemistry of several amine precursors using Residual Gas Analysis (RGA) mass spectroscopy in both continuous wave and pulsed wave plasmas under fixed flow rate, varying power conditions [19, 21]. In all cases, the increase in value of W/FM correlated to a) a reduction in intact monomer functionality, principally the $-NH_2$ component and b) an increase in fragmentation of monomers, evidenced by a decrease in the normalised intensity of the precursor signal in the spectra. Additionally, it was shown that a critical power can be reached, beyond which the differences in monomer structure have less influence over plasma properties, due to their complete fragmentation. Below this threshold however, differences in the plasma chemistry were related to differences in the bonding energies of the monomers, and hence it was shown that changing W/FM can allow for selectivity in the degree to which the monomers are fragmented. In the case of the hydrocarbon monomer styrene, reaction products CH, H_2 and H_α were observed in the plasma discharge through OES [7]. The relative concentrations of these products was found to increase up to a power level of 100 W in fixed flow / fixed monomer conditions and beyond this power, H_2 and CH were found to decrease. The decrease in relative concentrations above 100 W was attributed to further dissociation of the H_2 and CH species.

The studies demonstrate the relationship between the reaction products in the plasma, controlled by W/FM, and the chemical composition of the resulting thin films and hence relate W/FM to film properties. Kiesow and Heilmann showed that the increased monomer fragmentation induced by higher power density resulted in a decrease in dc conductivity due to loss of the thiophene monomers conjugated structure [29]. Similar behaviours were observed by Denis *et al*, in this case evidenced by the concentration of primary amine functionality in the deposited thin films decreasing significantly and the degree of crosslinking increasing with increases in power density [19, 21]. FTIR and XPS measurements of thin films plasma deposited from styrene showed a similar relationship between the plasma and film chemistry, and composite parameter [7]. While these examples explicitly relate the composite parameter, plasma chemistry and film properties, numerous other studies exist which also demonstrate the varying degree of monomer fragmentation and its influence on film properties as the composite parameter is varied [3, 5, 23, 26, 30].

Due to the evidence showing the link between W/FM film properties, attempts have been made to relate the growth kinetics of plasma deposited thin films and the composite parameter, often referred to as ‘macroscopic kinetics’ [5, 13, 16, 22, 23, 28, 31, 32]. The theory relies on the basis that the plasma deposition process is governed by the energy provided per unit monomer in the plasma region, and relates the growth rate of the thin films to the controlling parameter W/F through the relation:

$$\frac{R_m}{F} = G \exp\left(\frac{-E_a}{W/F} \right) \tag{2.8}$$

where G is a reactor dependent geometry factor, R_m is the rate of film growth and E_a is the (apparent) activation energy [16]. Such a relationship is desirable as it relates the controlling parameters W and F to an immediately measurable internal parameter, the deposition rate, which can be monitored *in situ* and allow more direct process control without necessitating knowledge of less tangible parameters such as electron energy distribution functions, or precise gas phase chemical compositions. The relationship is not expected to hold over the entire possible domain of W/F in $[0, \infty)$ due to the effects of processes not described in (2.8), such as ablation, ionisation temperature effects, oligomer dominated reactions and other non-linear effects which become prevalent at extremes of the range of energy input [16]. Essentially, in the region where a single chemical reaction pathway exists, (2.8) should hold and hence relates growth rate directly to the number of products available for reaction and the energy delivered to them. Energy ranges which result in a significant change in reaction pathway will hence deviate from the relationship provided [33]. In this region, then, E_a is the slope of the linear fitting of $(W/F)^{-1}$ to $\ln(R_m/F)$ and describes a minimum energy threshold which must be overcome for dissociation of the monomer units to occur [28] and is a monomer dependent property. Hegemann showed that this parameter correlates to the minimum energy required to create film forming products by determining the apparent activation energy and bond order for a group of monomers and showing their approximate equivalency [16]. While Hegemann *et al*, as well as others [5, 23] have successfully used the macroscopic approach to describe the behaviour of growth rates as a function of energy input to the deposition, there are some shortcomings associated with the model; most notably that while geometry and pressure influence the behaviour of the deposition, they are not explicitly embedded in (2.8) [13, 28, 32, 34]. This is addressed in part by the geometry factor, G and by modification of (2.8) to include a scaling factor, S:

$$S = \left.\frac{W}{F}\right|_{dep} = \frac{W}{F}\frac{d_{act}V_{gas}}{d_{gas}V_{dis}} \qquad (2.9)$$

where d_{act} is the length of the plasma discharge, d_{gas} is the distance between the monomer inlet and substrate location, V_{gas} is the volume occupied by the monomer and V_{dis} is the volume occupied by the plasma discharge [16]. Pressure and geometry are implicitly included in the scaling factor as they influence the shape of the plasma region and hence influence d_{act} and V_{dis}

in the final equation. There are still some issues with the use of S however, in particular for non-parallel plate reactors, or conditions where precise determination of the plasma volume is difficult [28].

Based on this approach and the determined activation energy parameter, different regions of growth kinetics can be identified within a system. The distinction made is between monomer sufficient (energy deficient) and monomer deficient (energy sufficient) deposition regimes [3, 5, 23, 24]. In the monomer deficient regime, the monomer flow rate is typically low and the power level is large, resulting in a high energy per molecule and complete dissociation of molecular bonds [3]. Hence increasing the power level does not result in an increased deposition rate, as maximum fragmentation has been reached; rather the deposition rate will decrease due to the increased effects of sputtering and ablation [5]. The deposition rate can be increased by increasing the flow rate of the monomer, providing more molecules to which the applied energy can be distributed. As the monomer flow rate is increased (or alternatively the applied energy is decreased), the monomer sufficient regime is entered. In this scenario, there are a large number of monomer molecules in the gas phase, and the applied energy is not sufficient to completely fragment them. Thus, increasing the monomer flow rate results in a decrease in deposition rate, as the degree of monomer fragmentation decreases. Increasing the power density will however result in an increase of monomer fragmentation and an increase of deposition rate. These different regions are often associated with different film properties. Tran *et al* found that in the monomer deficient region, the resulting films became very rough, due to the effects of ablation and gas phase formation of clusters which deposited onto the substrate, rather than film growth occurring at the substrate [5]. Other groups have shown that harder, more highly crosslinked films are obtained from monomer deficient depositions, compared to soft oligomeric films obtained in the monomer sufficient regime [23]. The distinction between these regimes has been correlated with the activation energy [23].

These studies show that film properties are strongly dependent on deposition conditions, and relate growth rate to power density and monomer flow rate. They do not however predict specific film properties such as chemistry, conductivity, transparency, permittivity or surface energy. As such, extensive studies are generally performed for a particular combination of monomer and system. Although specific predictions cannot be made, some common behaviours are present in the literature which can be useful to provide an expectation of a thin film material's properties and their dependence on deposition conditions.

Generally it is found that monomers become more fragmented as W/F increases, due to the increase in energy per unit monomer. This is evidenced in the plasma chemistry, as outlined above, where increasing W/F resulted in the appearance of additionally chemical functionalities in amine discharges, for example [19, 21]. The result of increased monomer fragmentation from the perspective of film properties is seen as a loss of chemical functionality in the thin film as compared to the monomer as the W/F parameter increases [3, 19, 25] and an increase in crosslinking density of the films [19, 30]. This has led to investigations of decreasing the effective power delivered to the deposition process through use of pulsed plasma systems in an attempt to increase the degree of monomer retention, especially in cases where the monomer has desirable properties such as biocompatibility characteristics [19, 20, 26] or presence of conjugated/aromatic structures which may increase the conductivity of thin films [25, 29, 35]. Pulsed plasma conditions lower the effective power delivered to the deposition chamber and additionally change the manner in which the deposition proceeds. During the plasma on cycle, monomer fragmentation and film growth proceed via mechanisms outlined in Section 2.2.2, however, during the off cycle the reaction products created interact with monomer units and chemical chain propagation occurs [36]. Resulting films therefore contain a greater concentration of monomer functionality and more regular structure than films deposited under continuous wave conditions [36-38].

The degree of monomer fragmentation and crosslinking directly influences film properties beyond simply the chemical properties and are also controlled by W/F. Many studies examine the relationship between W/F and morphological, optical, surface and electrical properties. For fabrication of very hard a-C:H thin films, high composite parameter conditions are often cited as necessary [8, 23, 39, 40], establishing a relationship between W/F and film hardness, likely due to the underlying increase in relative carbon concentration, crosslinking and film density [41, 42]. Film morphology and specifically surface roughness is regularly examined as a function of applied power density at fixed flow rate. In many cases, surface roughness is found to increase with increasing RF power [3, 5, 42], though where given, the Root Mean Square (RMS) roughness of plasma deposited thin films generally remains less than 1 nm, regardless of the composite parameter value. In cases of very high W/F values, well into the monomer deficient region, this roughness may increase significantly, such as the case for plasma deposited cyanopyridine thin films, where an increase in roughness from 0.43 nm to 3.63 nm was observed when the parameter W varied between 3 W and 60 W [3]. This large variation was attributed to gas phase reactions dominating, resulting in particle formation in the gas which was then deposited onto the surface. Increasing roughness also corresponds to significant changes in surface topography [3, 5].

Changes in monomer retention and crosslinking result in changes in optical properties. For example, the refractive index is often found to increase with W/F in plasma deposited thin films, due to an increase in their density [41]. As well, changes in absorption and transmittance spectra can be observed due to differences in chemical functionality of the films deposited at different W/F [3, 25, 35]. In general, the optical properties of thin films deposited using PECVD are strongly dependent on the W/F parameter [43-45], through a combination of the dependence of the optical properties on film morphology, structure and chemical functionality, and the influence of W/F and monomer fragmentation over these properties.

Governed in part by changes in surface chemistry, surface properties have also been shown to depend on the power density, such as the case of a thiophene deposition which showed significant dependence of contact angle (CA) and hence surface energy on the deposition parameter [46]. A similar dependence was observed for a-C:H films in both laboratory and industrial scale reactors [23], as well as for ethylcyclohexane deposits. In all cases, the water CA increased, indicating an increase of the hydrophobicity of the films and decrease of the surface energy. It is difficult to attribute this behaviour to one specific cause however, as surface energy and contact angles depend on several factors, such as surface topography, chemistry and crosslinking degree [47]. Related to the surface energy is the material solubility; the increase in crosslinking of the plasma deposited layers typically results in films which are less soluble in many common solvents [7, 22, 47]. It is noted that some researchers found a small fraction of the thin film is soluble [17], shown by [18], seen as a reduction of the C(=O)OX functional group in XPS measurements after rinsing in water. However, no change in any other functionality was observed, and the majority of evidence suggests that the bulk material is insoluble as shown in [18] and others [7, 48]. It is possible to decrease the degree of fragmentation and crosslinking sufficiently to result in films which are soluble, generally through use of very low W/F conditions or pulsed plasma systems [10, 22, 48].

Crosslink density, monomer fragmentation and resulting bulk chemical properties of thin films influence the electrical properties, and hence W/F has also been shown to modify the conductivity, breakdown capacity and permittivity of plasma deposited thin films [25, 29, 35, 46]. Research groups are often interested in the deposition of conducting or low resistivity thin films through PECVD and hence choose a monomer with an aromatic or conjugated structure such as pyrrole, thiophene or aniline [25, 29, 46, 49] with a goal of using low power conditions to maintain the monomer functionality. In thiophene films, conductivity was shown to decrease significantly (two orders of magnitude) as power density was increased, correlated with an increase in monomer fragmentation and reaction products observed in OES measurements during the deposition [29]. In a different approach, Jiang *et al* studied the effects of deposition pressure and benzene monomer feed location on the dielectric properties of the resulting thin films [50]. While these variables do not explicitly relate to W/F, XPS and FTIR analysis provided an indication of the degree of monomer fragmentation, which is related to the energy input to the deposition, and hence the link was implicit.

In their deposits, the researchers found that low pressure conditions with the monomer feed location downstream from the active plasma zone resulted in the largest retention of monomer structure, shown by an increase in aromatic functionality in FTIR and XPS data. Films with the least amount of monomer retention were fabricated under high power conditions when the monomer was fed directly into the plasma region. It was found that the films with the highest degree of monomer retention also had the highest dielectric constant and lowest loss, while films with the least degree of monomer retention had the lowest dielectric constant and highest loss. The research group relate the difference in dielectric properties to the mobility of structural features in the film; as films become more densely packed and crosslinked, with less monomer structure, they have less molecular mobility. It was shown that films with the highest degree of crosslinking (inferred by the strength of –CH and $–CH_2$ functionalities in FTIR data) had the highest dielectric strength, while the most aromatic film with the least amount of crosslinking had the lowest dielectric strength. Hence overall, the study demonstrated that a higher degree of monomer retention resulted in higher permittivity and lower loss, albeit at the cost of dielectric strength, while more crosslinked films deposited from more highly fragmented monomers (and therefore under higher input energy density conditions) provided high dielectric strength, low permittivity characteristics.

While these studies relate the degree of monomer retention and crosslinking to electrical properties, there are instances where monomer retention and chemical functionality remain relatively constant and crosslinking is the main factor governing film properties. Bae *et al* showed that the chemical structure of methyl- and ethyl- cyclohexane deposits at increasing input energies was relatively consistent, however significant differences in leakage current densities and dielectric constants were observed between samples [35]. The relationship between these parameters and W/F is similar to that described in other studies, where leakage current density and relative permittivity decrease as the energy density increases. Electrical conductivity in particular can be varied across several orders of magnitude through variation of W/F, and films' dielectric constants and loss can also be controlled to a degree. Most films fabricated using PECVD are low permittivity and have a dielectric constant of approximately 2.5 - 4 at low frequency, room temperature conditions [35, 46, 49, 51, 52], a conductivity of approximately $10^{-12} – 10^{-9}\ \Omega^{-1}\ m^{-1}$ [29, 46, 49, 51] and dielectric strength exceeding 1 MV cm^{-1} [35, 46, 50, 52].

2.2.4 Applications of PECVD Thin Films

2.2.4.1 Electronics and Sensing Applications

Subsequent to their initial discovery in the late 1800s, the first application of plasma deposited thin films was reported by Goodman in 1960 [2], and described the deposition of a film from a styrene monomer as a dielectric barrier in a battery [53]. Following this work, in 1963 Bradley reported on the electrical properties of plasma deposited thin films fabricated from a wide variety of monomers and identified their potential applications as dielectric and semiconducting layers in electronics [54]. Since these initial reports, modern electronic technology has advanced significantly, and in its current state it is reported that approximately two thirds of the fabrication steps in current semiconducting devices require plasma processing [53]. Due to its inherent compatibility with modern electronic device fabrication, there is a great deal of interest in potential electrical applications of plasma deposited thin films. A large degree of this interest is focussed on fluorocarbon (F/C) monomers, due to their existing integration in semiconductor plasma processing as an etching agent, and the ability of F/C monomers to shift between etching and deposition regimes in the same plasma process through adjustment of control parameters [5]. The few reported applications of plasma deposited thin films directly relevant to organic electronic devices are discussion in Section 2.3 of this chapter.

For application in conventional electronics, materials with low permittivities are required so that the detrimental effects of RC parasitics can be reduced as device geometries become smaller [6]. Additionally, a high level of thermal stability is required, as deposited layers will be exposed to multiple heating and cooling cycles throughout processing. Deposition of thermally stable, low permittivity F/C films has been demonstrated in several articles [6, 55, 56]. In a C_6F_6 plasma, films have been deposited on substrates at temperatures of up to 400 °C and the dielectric constant found to be 2 – 2.5 depending on substrate temperature and annealing conditions [6]. Uhlig *et al* deposited F/C films from C_4F_8 fluorocarbons mixed with CH_4 vapour and obtained films with a dielectric constant of 2 which were thermally stable up to 425 °C, shrinking by less than 1% after annealing at these temperatures. These studies demonstrate the compatibility of F/C thin films with electronic processing, and this was further demonstrated in more robust fabrication studies involving multiple processing steps including masking, etching, copper deposition and copper polishing [55], as well as deposition of F/C films into high aspect ratio trenches [57]. Optimisation of particular properties such as permittivity or thermal stability can lead to degradation in other performance characteristics, such as resistivity and associated leakage current densities [55, 56]. As such, investigations into further optimisation of the films and processes are required.

Looking more broadly at current research in polymer thin films and electronic applications, low dielectric constant, high dielectric breakdown, low leakage current intermetallic layers are required. A lower limit on the dielectric breakdown property of 1 MV cm^{-1} has been suggested [58] and many plasma deposited layers have demonstrated electrical breakdown above this limit. In investigations into the relationship between chemical structure and electrical properties, Jiang *et al* fabricated thin films from a benzene monomer with breakdown fields as high as 6.1 MV cm^{-1} [50]. In capacitive applications, pyrrole thin films with a dielectric constant of ~4 were found to have breakdown voltages exceeding 1.5 MV cm^{-1} [52]. Sufficient breakdown alone is not useful in insulating applications if the film conductivity and resulting leakage current density are too high. As established in Section 2.2.3, films deposited at higher energy deposition conditions typically have higher resistivities. Films of cyclohexane [59], polyaniline [49], tetraethylorthosilicate [60] and diphenyl [51] have all been demonstrated to have conductivities on the order of $10^{-11} – 10^{-12}\ \Omega^{-1}\ m^{-1}$ and are hence suitable for applications as insulating layers in electronics. Permittivity is an important property of the films and influences their specific application potential; in interelectrode dielectric layers, low permittivities are required in order to reduce RC parasitics by decreasing the effective capacitance for the same geometry, while in capacitive applications, higher dielectric constants are required in order to reduce the size of devices. Polyaniline thin films reported by Mathai *et al* had a dielectric constant of ~1.18 and they estimated a reduction in RC delay of 70% when compared to SiO_2 dielectric layers [49]. In comparison, diphenyl thin films which demonstrate low conductivity were measured to have a dielectric constant of 4, the same as SiO_2 and hence may not provide any exploitable advantage in interlayer dielectric applications [51].

As well as meeting required electrical properties, for applications it is important that candidate materials are compatible with a range of processing conditions, placing requirements on their adhesion, thermal and chemical stability, and mechanical properties [55]. Throughout these processing steps, the electrical properties should remain relatively unchanged. Towards the goal of processing compatibility, plasma deposited layers of glycidyl methacrylate were investigated and shown to improve the adhesion of subsequently deposited copper layers under certain processing parameters [61]. However, films deposited from a combination of toluene and tetraethoxysilane (TEOS) were shown to undergo significant changes in dielectric constant, surface energy, and volume when exposed to heating cycles, depending on the ratio of the precursors and structure of the films [62]. Research is required in determining optimised deposition conditions for plasma deposited films such that all requirements can be met. HMDSO films have generated interest due to their desirable mechanical properties and detailed existing studies of film properties. Low dielectric constant, high breakdown, low conductivity and thermally stable films of HMDSO were deposited in the presence of methane [63]. The films were shown to lose 10% of their thickness in optimised deposition conditions upon annealing at 400 °C, though optimisation of resistivity or breakdown voltage resulted in an increase of dielectric constant or reduction in thermal stability. This again highlights the need to perform application specific optimisation of film properties. In another application, ultrathin (~5 nm) HMDSO plasma deposited films were used as a protective coatings for soft polymers in scanning microscopy read/write storage applications [64].

It has been observed during electrical characterisations of plasma deposited thin films that their conductivities and other properties may be subject to variation when in the presence of different chemicals in the surrounding environment [65-67]. This property can be exploited for the development of transducers which use plasma deposited layers as the sensing layer. In 1996 a gas sensing and classification network was developed using plasma deposited layers from various monomers to fabricate sensors which demonstrated sensitivities to different chemicals [66]. The outputs from these sensors were then used as the input to a filter bank to perform classification of the detected gas, for applications in smoke detectors so that fire type could be classified. Another early demonstration of the applicability of plasma deposited thin films to sensing was the deposition of HMDSO films onto quartz resonators [67]. The films selectively adsorbed inhalant anaesthetics, changing the resonant frequency of the oscillators and allowing detection of vapours from atmosphere. In general, many plasma deposited thin film based sensors operate in this manner; thin films are deposited on a resonant structure, and changes in frequency measured as the films selectively adsorb various gases. Use of different monomers and variation of deposition parameters allows for sensing of different gases. Films deposited from HMDSO showed shifts in resonant frequencies of between 25 Hz and 250 Hz when exposed to hexane, chloroform, acetone, water and 2-propanol vapours [68] and were demonstrated to be suitable for sensing of polar vapours. Detection of methanol was shown using plasma deposited styrene and poly(methyl methacrylate) (PMMA) layers, and the long term ageing properties of the sensors thought to be improved in the plasma deposited layers as compared to their conventional polymer counterparts [69]. Deliberate modification of the plasma deposited surfaces can also be undertaken, in order to increase sensitivity to a particular gas, for example by increasing the porosity of the films to increase sensitivity to water vapour, as in the case of TEOS films deposited on quartz oscillators [70]. These films additionally showed sensitivity to dodecane and hexane vapours.

In regards to moisture detection, allylamine films were deposited on a surface transverse wave (STW) device and resulted in an increase of sensitivity to humidity of 24 times that of uncoated devices [65]. Variations in other film properties in the presence of vapours can also be exploited. The optical absorption spectrum of a porphyrin-containing plasma deposited polydimethylsiloxane film was shown to undergo a hypsochromic shift upon exposure to triethylamine [71]. However, the shift in colour was small (undetectable to the eye) and the material hence requires further development before it could be employed as a visual indicator. Resistivity of plasma deposited 2-propanol films was shown to decrease, resulting in a measurable increase in leakage current upon exposure of the device to acetone, demonstrating yet another possible avenue for sensor development [72]. Another interesting application of the selective adsorption of plasma deposited thin films is their use in Micro Electro-Mechanical (MEM) devices, particularly in bio-MEMs devices. Two such examples are the detection of glucose [73] and modification of micro-fluidic velocity [74]. In the case of the detection of glucose, plasma deposited layers of acetonitrile were used to provide primary amine surface functionality in the sensing device, resulting in a glucose concentration dependent current, suitable for biomedical applications. Biocompatible monomers of acrylic acid were used in a microfluidic MEMs device, and the modification of surface properties of the device resulted in an 8-fold increase in fluid velocity [74], providing the beginning stages of investigations into microfluidic velocity control in biomedical applications.

2.2.4.2 Membranes, Protective Coatings and Biomedical Applications

The same properties which make plasma deposited films useful as a sensing layers, namely their selective adsorption of a particular chemical, also allows for their use as membranes. Depending on the film characteristics, certain chemicals will adsorb into and pass through the membrane, while other chemicals will be blocked, allowing for applications in fuel cells and filtration. In a general application of the principle, F/C films have been deposited on silica membranes, and the permeation rates for He, N_2 and CO_2 investigated [4]. It was shown that the membranes could be fabricated to selectively allow permeation of the gasses and hence separate them. In Proton Exchange Membrane Fuel Cells (PEMFCs), membranes are required which maintain separation of reactants, such as methanol, and still permit conduction of protons [75]. Hence membranes which reduce diffusion of methanol are sought after. Plasma deposited layers have been exploited to enhance the methanol rejection of existing membranes while still maintaining desirable proton conduction properties. F/C films deposited on Nafion (a commercially available ion conductive membrane) resulted in a 10-fold reduction in methanol permeability, however proton conductivity was also reduced [76]. Proton transport could be improved, albeit at the cost of methanol rejection.

Films codeposited with chlorosulfonic acid demonstrated the highest ion conductivities; in this investigation, studies were performed by Jiang *et al* on films deposited from a mixture of styrene and trifluoromethane sulfonic acid onto Nafion membranes [75, 77]. In these works it was possible to obtain deposition conditions resulting in films which improved both proton conductivity and methanol rejection of the membranes. The deposition system used was a modification of the general plasma deposition chamber; in these cases the chamber had been separated into two regions, a plasma active region and a reaction region, often referred to as an afterglow (AG) reactor. This type of reactor allows even greater retention of monomer functionality by separating the reaction products from the high energy region where reactive species are generated, so that reactions can proceed without re-fragmentation/dissociation during a plasma on-cycle [77]. Maintaining sulfonic groups in deposited thin film allows for enhanced water uptake and proton conductivity [75, 77]. Membranes have also been fabricated for use in Alkaline Fuel Cells (AFCs), for example by plasma treatment of the gas diffusion electrode with 4-vinylpyridine monomer [78].

In filtration applications, plasma deposited thin films have been used to modify reverse osmosis membranes in order to enhance salt rejection. Commercial membranes modified with allylamine-based thin films were shown to increase salt rejection to greater than 90%, while maintaining water flux rates [79] and showed greater resistance to chlorine induced degradation. Further work on allylamine modification of microporous polyimide membranes showed the possibility of high flux, high rejection membranes under optimised deposition conditions with respect to power, pressure and monomer flow rate [80]. Further demonstration of filtration applications is provided by Gulec *et al*, where cellulose acetate membranes were modified with ethylenediamine thin films [81]. The modified membranes were used to separate mono- and disaccharides for use in food industry.

As another application afforded by their chemical selectivity, plasma deposited thin films have been investigated for use as chemically protective coatings, for example to prevent corrosion of metals or to protect materials in devices as an encapsulating layer. One such application is in the protection of restored metallic archaeological objects. Coatings which protect the metallic layers from corrosion and do not influence the visual appearance of the object are required for such applications. Films deposited from methane and propane were shown to be suitable for this purpose, and protected samples of iron, stainless steel and copper from corrosion in ambient conditions for the duration of a 289 day study [82]. The films were also shown to protect the samples in high humidity (>90%) environments over a period of 11 days, and were easily removable by plasma treatment in H_2. HMDSO films were shown to enhance the corrosion resistance of iron samples when a ratio of 80:20 of HMDSO to O_2 was employed during the deposition [83], and high deposition rates (and hence large scale efficiency) were achieved in these conditions. Particularly in electronic applications, protection of copper is of interest. To this end, cyclohexane and styrene films were shown to effectively protect copper substrates from corrosion [7, 59]. In both cases, the plasma film coated substrates were exposed to NaCl, though different properties were investigated. Bae *et al* examined the corrosion resistance of the copper substrates using impedance spectroscopy (IS) measurements and found that an ethylcyclohexane deposit provided protection efficiencies in excess of 90% [59]. In the case of styrene deposits, after immersion of coated substrates in NaCl solution for 60 hours, Choudhury *et al* showed that no visual evidence of corrosion of the copper was present for an optimised thin film, though no precise measurements were presented beyond photographs of the samples [7]. In the automotive industry, protection of galvanised steel is of importance, and plasma layers are of interest due to pre-existing plasma steps in the process [84]. Therefore, integration of a TMS film deposition into automotive parts treatment was investigated and found to provide an improvement in corrosion resistance in particular deposition conditions [84], and at worse comparable performance to barriers fabricated at higher cost.

The above applications all relate to protection of layers from corrosion, by separating substrates from damaging chemicals. It is also possible to apply the thin films as optical and mechanical protective layers. In a particularly novel use of plasma thin films, PMMA thin films were deposited on historical paper samples and exposed to UV irradiation [85]. After treatment, samples were found to have nearly no degradation, and no visual indication of damage, as required in heritage applications. Generally, siloxane coatings have been shown to be hard, and hence have found applications as mechanically protective overlays. One such example is in the encapsulation of photoluminescent structures, where as well as providing mechanical protection, HMDSO films were shown to improve the brightness by more than 20 times compared to conventional encapsulating materials. As mentioned above, HMDSO layers were also used to provide mechanical protection to soft polymers used in possible data storage applications [64].

Finally, due to the ability to provide specific surface functionalities, particularly in the case of low energy deposition conditions, plasma deposited thin films have been subject to a great deal of research for potential biomedical applications. The ability to tailor surface chemistry allows for the deposition of films which demonstrate cell-adhesive or cell-repellent properties and hence films can be made to be antifouling and to promote biocompatibility [53]. Acrylic acid coatings, for example, were shown to limit the growth of leukaemia cells, attributed to the presence of hydroxyl and carbonyl functional groups [86]. Brétagnol *et al* showed that surfaces can be optimised to promote cell adhesion and growth, or to reduce cell adhesion, by selection of deposition parameters of diethylene glycol dimethyl ether thin films, particularly the power parameter [87], likely corresponding to loss of anti-fouling functional groups at the film surface.

Antifouling surfaces are of particular interest in hygiene sensitive applications, such as food preparation and storage industries. Two plasma deposits (2-hydroxethylmethacrylate and polyethyleneglycolmethacrylate) were investigated by Mutlu *et al* to study the adsorption and growth of bovine serum albumin proteins on stainless steel surface [88]. Both samples were shown to greatly reduce the number of adsorbed proteins and the rate of adsorption when compared to untreated surfaces, and hence could be used to ensure antifouling conditions in food preparation environments with further development.

In regards to biocompatibility, surfaces with primary amine functionality are often desired due to their promotion of cell growth [89, 90]. Amine containing monomers were used to create thin films with primary amine surface functionalities, and it was found that growth of L-929 cells was promoted, especially when higher concentrations of primary surface amines were present, evidenced through XPS measurements [20]. As with microelectronic applications, as well as the necessary primary requirements, the materials investigated must be compatible with processing techniques specific to the particular industry under study. In the biomedical industry, sterilisation procedures require the films to be exposed to high heat, autoclaving and UV irradiation. Recently, research into the compatibility of biocompatible thin films with sterilisation procedures has been investigated [91]. This is of particular concern in the biomedical industry, as the growth conditions necessary to realise films with desirable biological properties (generally low energy conditions to promote retention of monomer functionality) often result in detrimental effects on other properties such as thermal and chemical stability. One study into several biocompatible monomers investigated the effects of different sterilisation procedures on the surface properties and cell attachment of the resulting thin films. It was found that in some cases, the sterilisation procedures have significantly detrimental effects on the biocompatibility of the films [91]. As the primary characteristics of the films develop further, more work on ensuring compatibility with all areas of processing will undoubtedly be required.

2.3 Organic Electronics

2.3.1 OSC Materials

2.3.1.1 Background and Properties

OSCs are carbon-based materials which exhibit semiconducting properties (e.g. field and temperature activated conductivity) and covers a large range of molecules. These molecules share the common feature of conjugation, and are often aromatic. OSC materials may be polymeric in nature (i.e. they consist of regularly repeating molecular units), such as poly(3-hexylthiophene) (P3HT) or poly(acetylene) [92], or oligomeric (i.e. they consist of small molecules), such as the thiophenes and cyclic acenes. Much like their inorganic counterparts, OSC materials can be separated into hole (p-type) [93] or electron (n-type) [94] conducting materials, though it should be noted that unlike in inorganic semiconductors where majority carrier type is an explicit property induced by doping, division of organic molecules into p- or n-type is somewhat arbitrary, and predominately a functional classification based on device behaviour [95].

Of the available OSC materials, several particular examples exist of materials which have been the subject of high interest. Pentacene, a linear acene, is by far the most investigated OSC in the literature [95-98]. Due to its insolubility, pentacene thin films were originally fabricated and investigated by means of thermal evaporation [96], however, in recent years soluble precursors, such as 6,13-bis(triisopropylsilylethynyl)pentacene (TIPS-pentacene) have become available which yield high quality pentacene thin films upon deposition from solution in a variety of organic solvents [98]. In addition to pentacene, thiophene oligimers and their various derivatives are another commonly studied OSC [99, 100], and as with pentacene, thin films derived from both evaporated and solution processed thiophenes result in high quality OSC films. P3HT, phenyl-C_{61}-butyric acid methyl ester (PCBM) and fullerenes (C_{60}, C_{70}) have also been the subject of much investigation and scientific interest [101-104]. In the case of these materials, their initially above average performances led to further work in their optimisation, resulting in further improved performance. Pentacene in particular has become a benchmark for OSC materials [95]. With the exception of the fullerenes, all of the above materials exhibit p-type characteristics. This is due to the fact that throughout the earlier periods of organic electronics research, fabrication of n-type materials with adequate mobilities and environmentally stable properties was a difficult challenge, only recently overcome [95, 105].

As mentioned, all OSCs display the common feature of conjugation in their molecular structure [95]. This is a result of the manner in which charge is transported through single molecule, and through the solid-state. Unlike inorganic semiconductors in which valance and conduction bands are formed across a crystal lattice, OSCs transport charge across molecular orbitals. As such, conjugated structure results in delocalised orbitals which span the molecule, preferably with a large amount of π-electrons, such that the orbitals are energetically accessible for charge injection [105]. In addition to favourable local charge transport, charge must be mobile across many molecules in the solid-state such that bulk charge transfer processes can occur, requiring molecular arrangement which results in maximal overlap of orbitals [99]. When favourable molecular packing arrangements occur, more efficient charge transport can result and hence the resulting films possess higher charge mobility [105-107]. The ability to transport charge is then both a molecular and bulk property of OSC materials; materials which have favourable molecular electronic properties may still result in poor device performance if desirable (e.g. crystalline or polycrystalline) molecular packing arrangements cannot be obtained.

Mobility (μ) is a material constant which relates carrier velocity to the applied electric field, accounts for how well charge transfers through a structure [108] and is typically the parameter of fundamental interest in an OSC. Research efforts are heavily focussed on improving mobility, and currently, values on the order of 10 $cm^2\ V^{-1}\ s^{-1}$ in a single crystal of rubrene are the largest reported for OSCs [95, 109]. As implied above, μ is a bulk parameter, and hence heavily influenced by molecular packing [106] and overall film morphology [98, 100, 110]. As a result, single crystals of OSC material, which represent optimal molecular packing, typically provide the highest achievable mobility for a particular OSC [107, 109, 110], as well as providing a theoretical maximum value [99] for that material. While useful for investigating upper limits on mobility, devices fabricated from single crystal OSCs are often considered impractical, due to the long processing times required to obtain crystals of high quality [111] and loss of mechanical flexibility. Second to high mobility, stability of material properties in ambient environments is considered as a fundamental requirement for the commercial viability of organic electronic devices [93]. Despite this, many reports available in literature still fabricate and measure devices in vacuum or inert atmospheres, such as in [98, 102, 105, 106]. In recent years, more effort towards improving the ambient characteristics of OSC materials has been expended, evidenced by the large number of reports based exclusively on operation of devices in ambient environments [93, 106, 112, 113].

The reason for poor performance of devices in air is due to degradation induced by doping, where molecules react with atmospheric O_2 and H_2O resulting in fundamental chemical changes which degrade electrical performance, and typically occur when a material’s ionisation potential (p-type) is too low or electron affinity (n-type) is too high [105, 114]. As electron affinity and ionisation potential are typically considered to be molecular properties, air stability is usually improved via direct adjustments to the semiconducting molecule, typically through substitution and functionalisation [93, 95, 106, 115]. Ambient stability can also be indirectly improved at the device level by reducing the exposure of the semiconducting layer to the environment by changing the device architecture, inducing changes in the electron affinity by changing the molecular packing [116], or by eliminating trapping sites, whose presence may allow air doping to occur [114].

2.3.1.2 Fabrication of OSC Thin Films

Early reports of organic semiconducting behaviour and devices typically focussed on films fabricated through thermal deposition of semiconducting material in vacuum, due to the insolubility of the materials under investigation [93, 96, 106, 110]. In recent years this deposition method continues to be used, despite trends towards solution processed devices, as thermally deposited layers generally have slightly higher mobilities than those deposited by solution, as for example in pentacenes [117]. To further improve molecular ordering in the resulting films and device mobility, substrates are often heated during the deposition process to temperatures between 100 °C and 200 °C [110, 118-121]. One of the lauded advantages of organic electronics is the potential for large area fabrication at low cost, through exploitation of solution processing methods such as ink-jet and roll to roll printing [94, 98, 100, 122]. Thus, the direction of organic electronics research has tended towards the fabrication of semiconductors and devices from solution rather than from methods requiring vacuum, due to the increased complexity and cost [102, 112, 118, 123, 124]. Multiple methods of obtaining a film from solution are possible, but common to all is the dissolution of OSC power in an organic solvent [125]. Thin films of semiconductor are formed on surfaces by deposition of the solution onto a substrate through spin coating [124], drop casting [126], ink-jet printing [94], transfer printing [100] or spray coating [122], and allowing solvent to evaporate, leaving the semiconducting solid on the surface. As organic solvents such as chloroform [113], dichlorobenzene [123], toluene [101] and xylene [127] are commonly used to dissolve the semiconductor, care must be taken to ensure that previously deposited layers or plastic substrates are not adversely affected or partially dissolved during deposition of the OSC solution [128, 129]. Additionally, a particular OSC will typically have better properties when deposited from a particular solvent (e.g. better crystallinity may result if a higher-boiling solvent is used), and hence difficulties can be encountered in fabricating optimised structures due to limitations in solvent choice [102, 129]. Deposition from solution may eliminate vacuum steps (assuming ambiently stable semiconducting materials) however heating steps may still be required. Thermal annealing is regularly utilised to evaporate extra solvent and to improve the molecular ordering of the thin films, and temperatures of up to 300 °C may be used [94], though temperatures of less than 150 °C are more common [113, 127]. From a fabrication perspective, all materials in a device should be capable of withstanding exposure to a variety of organic solvents and temperatures up to 200 °C without any degradation in their properties or electrical performance.

2.3.1.3 Organic Electronic Devices

In modern inorganic semiconducting technologies, semiconducting materials have been implemented in several applications, acting as conducting and semiconducting layers in junction devices (diodes, light emitting diodes and bipolar junction transistors) and field effect devices, principally the metal oxide semiconductor field effect transistor (MOSFET). Modern photovoltaic (PV) devices are fabricated using inorganic semiconductors. Hence, for widespread adoption, OSCs must be capable of filling all of these roles. Without doubt, the device most ubiquitous with modern electronics is the transistor, and hence development of organic thin film transistors (OTFTs) or organic devices equivalent in operation to the MOSFET (OFETs) is by far the most prominent field of organic electronics research [98, 99, 106, 110, 124, 125, 130]. Display technology is a large field of commercial interest as well, and hence materials with favourable emission characteristics and Organic Light Emitting Diode (OLED) devices are the subject of much investigation [131-134] due to the potential for low-cost and flexible displays. As trends tend more towards environmental awareness and renewable technology, organic PV (OPV) devices are becoming another well represented area of organic electronics research aimed towards developing commercially viable technologies [135-140]. Due to the fundamental importance of transistor devices [141], the strong influence of all layers over the device performance and the potential for many avenues towards further optimisation and development, OFET devices were the main subject of review.

2.3.1.4 OFETs

The OFET device consists of four layers in its standard form; the substrate, the gate electrode, the gate dielectric, the semiconducting channel and the source (S) and drain (D) electrodes [142]. Depending on the research group and application, several configurations of these basic components are possible, depending on the location of the gate and S/D electrodes relative to the semiconducting channel, and are illustrated in Figure 2.3 [95].

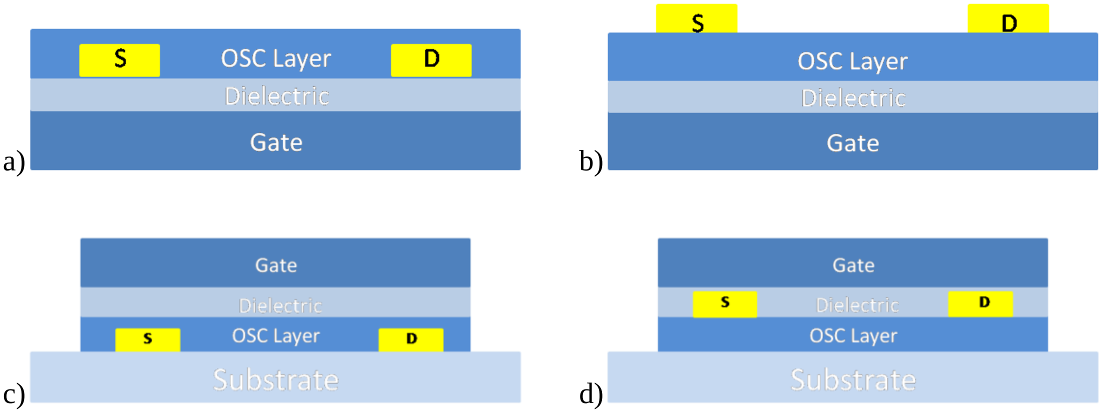

Figure 2.3: OFET configurations – (a) Bottom gate, bottom contact (b) Bottom gate, top contact (c) Top gate, bottom contact and (d) Top gate, top contact

These configurations are the bottom gate, bottom contact configuration, where both the gate and S/D electrodes are below the semiconducting channel; the bottom gate, top contact configuration where the gate is beneath the OSC channel and the S/D electrodes are deposited onto it; and the top gate, bottom contact configuration, where the S/D electrodes are deposited onto the substrate first, followed by the semiconducting channel and gate electrode. In all cases the configuration generally implies the order of fabrication of the component parts, and a gate dielectric layer is always present between the gate electrode and OSC channel. Additionally, due to overall improved device performance, top contact devices are largely preferred [101]. The devices behave in much the same way as an enhancement mode MOSFET; application of a voltage across the gate source terminals results in accumulation of charge at the interface [95]. When no gate-source bias is applied the conductivity of the channel is very small, and minimal current flows (the off current, I_{off}). When the gate-source terminals are sufficiently biased (the threshold voltage, V_{th}, is surpassed), accumulated charge at the interface allows for conduction through the channel upon application of a drain source voltage (the on current, I_{on}) [142].

Despite a large amount of enthusiasm for organic electronics being derived from the potential for flexible electronics, much of the current research on OFET devices is performed on Si substrates with a layer of SiO_2 [94, 98, 119, 141]. In these devices, the highly doped Si substrate acts as a gate electrode while the oxide layer acts as the gate dielectric. These are always bottom gate devices and may be top or bottom contact, with the OSC layer deposited directly onto the SiO_2 surface. In order to align with the Highest Occupied Molecular Orbital (HOMO) / Lowest Unoccupied Molecular Orbital (LUMO) bands of the OSC layer, such that efficient charge injection through an Ohmic barrier can occur [107], Au electrodes are used almost exclusively for the role of S/D electrodes in OFET devices in literature [115, 117, 125]. Hence the most common means of fabricating OFET devices is the deposition of an OSC as described above onto Si/SiO_2 substrates; if Au electrodes were not pre-fabricated on the substrates already for bottom contact devices, Au is then deposited above the semiconducting channel to complete the device.

In the case that Si substrates have not been used, the most common alternative for device fabrication is a glass substrate coated in Indium Tin Oxide (ITO) to form the gate electrode, which is then coated with a polymeric dielectric [96, 103, 117]. The final device structure typically investigated uses flexible substrates with thermally evaporated metallic electrodes and solution processed dielectrics and semiconductors. These devices are becoming more prevalent in recent years as fundamental issues with the semiconducting layers are overcome and more importance is placed on the development of commercially viable, flexible devices [124, 141, 143-146].

The criteria for ‘commercial viability’ is often defined in terms of adequate device performance, however, performance criteria have not been precisely defined for OFET devices. Device performance can generally be characterised by three criteria: the device mobility, the device on/off ratio (defined as I_{on}/I_{off}) and the device threshold voltage. In literature, some combination of these properties is generally reported or compared across multiple devices as evidence of device ‘performance’ [100, 119, 124, 129]. Currently, carrier mobilities are typically on the order of 1 $cm^2 V^{-1} s^{-1}$ for both p-type [147, 148] and n-type devices [149, 150], comparable with that of amorphous Si (a-Si) and nearing the order of magnitude necessary for commercial applications [117]. Device on/off ratios, which should be as high as possible in order to increase efficiency of logic devices (low on/off ratios generally imply a high leakage current), are typically reported on the order of 10^4 – 10^5 [117, 123, 141]. The final parameter, V_{th} typically varies a large amount in literature reports, though values are gradually shifting towards 0 V for p- and n- channel devices [102, 128, 151]. Ideally, designers should have full control over this parameter across a wide range of voltages to allow development of efficient and low-cost microelectronic circuitry, and many avenues towards this goal are under investigation [152-154].

Improvement of these performance characteristics is the subject of large focus. Some properties of device performance are inherent to the particular OSC, for example, air stability and limits of carrier mobility. At the device level however, all layers influence the overall behaviour and hence represent opportunities for performance optimisations. For example molecular arrangement of the semiconducting thin film largely influences bulk mobility and is partially determined by the surface on which the organic layer is grown [96, 109]. As devices move more towards flexible substrates which cannot utilise SiO_2 dielectric layers, new dielectrics and modifications to their surfaces are a highly explored avenue towards improving device characteristics, typically with the goal of passivating hydroxyl groups at the dielectric surface, which lead to trapping sites in the OSC and degradation in device performance [116, 124, 155]. As well as improvements in mobility and threshold voltage, modification of gate dielectrics or use of alternative materials can lead to improved on/off ratios, due to a reduction of the gate-source leakage component in I_{off} [129] and improved I_{on} values when higher dielectric constant materials allow higher capacitance per unit area and improved charge accumulation at the interface [109]. PECVD thin films of PMMA and terpinen-4-ol have been used in this way and shown to improve device operating characteristics in two of the only reported uses of plasma deposited thin films in organic electronics [156, 157]. Other avenues for improvement in operation characteristics are focussed on improving the interface between the S/D electrodes and the semiconducting channel. While the work function of Au electrodes is typically well matched to many OSC materials, the interface remains imperfect and high contact resistances adversely affect efficiency of charge injection across the interface. Application of self assembled monolayers (SAMs) to metallic S/D contacts has been investigated and shown to improve device operating characteristics [158-161], typically through reduction in contact resistance.

Given that sufficiently-high mobility n- and p-type OSC materials which are stable in air with moderate threshold voltages are now available, reports on complementary logic devices have begun to appear. Typically, these reports focus on simple complementary inverters, requiring only one n- and one p-type device [102, 141, 149], though some reports on more complicated structures such as nand and nor gates [125] and ring oscillators [103, 125, 141] are also available. There are not yet any reports in literature of complex, complementary organic integrated circuits, and as such the technology is still some time away from commercial viability. As OSC material properties continue to improve, it is expected that more application oriented research will be to take place.

2.4 Conclusions

Plasma deposited thin films were found to possess a wide variety of tuneable chemical, topographical and electrical properties. These properties were found to be dependent on the deposition chamber in use, the monomer, system pressure, monomer flow rate and deposition power. The fragmentation of the monomer induced during the reaction was shown to be the factor of primary importance in controlling the resulting thin film properties, and the degree of fragmentation related to the controlling parameter W/FM. Resulting deposits were shown to have applications in electronics and sensing, membranes, protective coatings and biomedicine.

Organic electronics was overviewed with a specific focus on OFET devices. It was found that the device operation is highly dependent on the organic semiconducting layer, which can be deposited from thermal evaporation or solution methods. Molecular ordering of the organic semiconductor was the factor predominately responsible for device mobility, and modifications to device structure such as surface treatments of dielectric and metallic layers were shown to improve the device operating characteristics.

Chapter 3: Materials and Methodology

3.1 Introduction

The properties of plasma deposited thin films such as the electrical, optical, morphological and chemical properties are strongly dependent on the conditions used during fabrication. Specifically, the composite parameter W/FM is sufficient to control the properties of the thin films, through indirect control of the degree of monomer fragmentation and reaction products in the plasma. Other indirect parameters such as the monomer and the geometry of the reactor also have a strong influence over resulting film properties. In this chapter, the methods used to meet the research objectives are outlined, with consideration given to findings from literature presented in Chapter 2.

3.2 Methodology

The four research objectives identified in Chapter 1 are outlined in Figure 3.1.

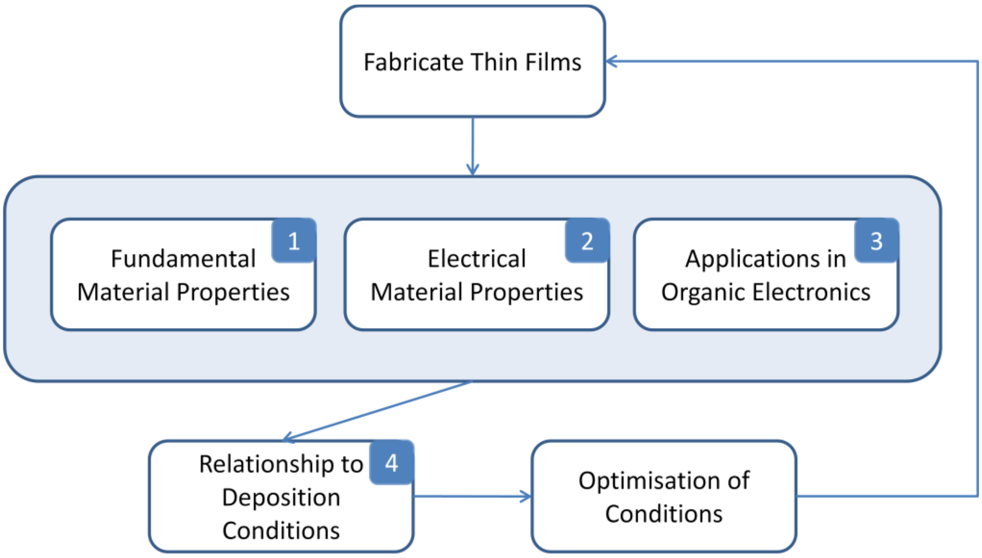

Figure 3.1: Overview of research objectives

In order to meet each of these objectives, each was first reduced to simpler components. Then, methods of characterisation for each component were outlined and the resulting material properties detailed.

3.2.1 Fundamental Material Properties

From the literature review, it was found that a set of properties is commonly investigated in thin film materials, due to their fundamental importance to applications, improved understanding of other material properties and influence of these characteristics over interactions with other materials and processes. These are the topographical, chemical and optical properties and were a subject of investigation in this thesis, as outlined in Figure 3.2. Topographical properties provide qualitative and quantitative information about the appearance of a surface and parameters such as surface roughness and hardness. These features can significantly influence the interaction of the surface with other layers, such as OSCs in device fabrication. A typical means of investigation of surface topography and hardness is AFM, and was used in this thesis.

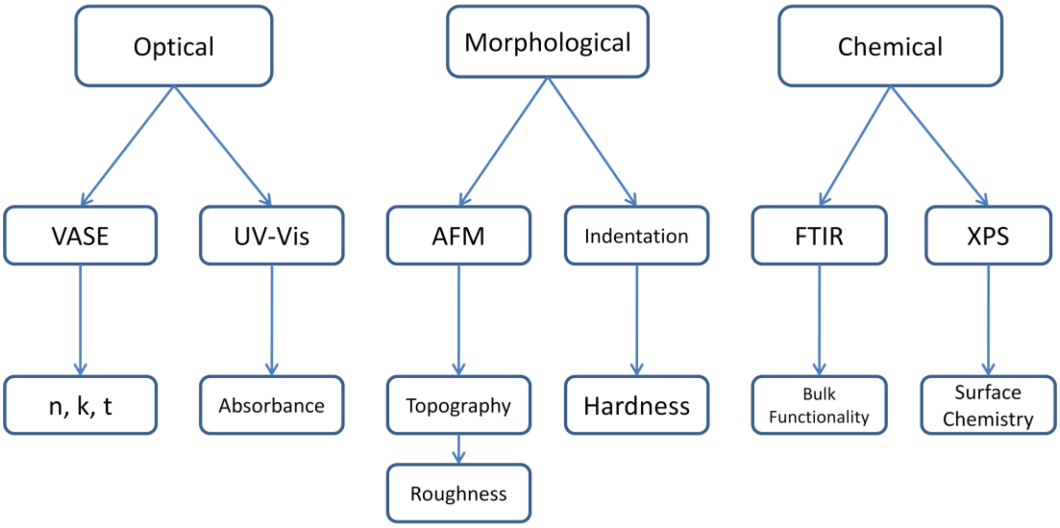

Figure 3.2: Outline of fundamental characterisations performed

Chemical properties are divided into surface bulk chemical properties. Bulk chemical properties are the elemental composition and molecular functionality and may provide detail as to chemical structure, while surface chemistry describes the elemental composition at the surface and surface chemical functionality. The surface chemistry functionality may differ from the bulk functionality due to the potential for surface reactions with atmospheric products subsequent to deposition, for example incorporation of O_2 into plasma deposited films as radicals interact with the environment. Multiple methods of obtaining this information are available, however the most prevalent in literature are FTIR spectroscopy to obtain the bulk chemical functionality and XPS to measure the surface chemistry. A material's optical properties describe the manner in which it interacts with light, through the complex refractive index as a function of wavelength. The absorbance profile can be obtained through direct measurement by using UV-Vis spectroscopy, and the complex refractive index, which contains the refractive index and extinction coefficient, can be derived through analysis Variable Angle Spectroscopic Ellipsometry (VASE) measurements. In order to determine the fundamental material properties, VASE, AFM, FTIR and XPS were performed, to obtain the parameters as outlined in Figure 3.2. Determination of the properties outlined constituted achievement of the first research objective, relating to the fabrication of thin films from linalyl acetate monomer and characterisation of their fundamental properties.

3.2.2 Electrical Properties

Electrical characterisation of a material requires determination of two fundamental properties: its electrical resistivity and its complex dielectric function. These properties are necessary to perform design of application specific, optimised electrical devices. A complete description is complicated by the fact that materials may behave differently as a function of the frequency of the applied signal; devices operating at dc will almost invariably behave differently to when an RF signal is applied, and therefore characterisation should be carried out across as wide a frequency range as feasible to obtain useful information for making application and design decisions. Additionally, it is important to know the electrical operating limits of the thin films and thus the onset of dielectric breakdown should be investigated to provide a complete electrical specification of the material.

From a physical perspective, understanding the material's charge transport properties may assist in optimisations in future work. The electrical properties were divided into three frequency regimes; the dc, ac, and MW frequency regions, each associated with a different measurement technique as shown in Figure 3.3.

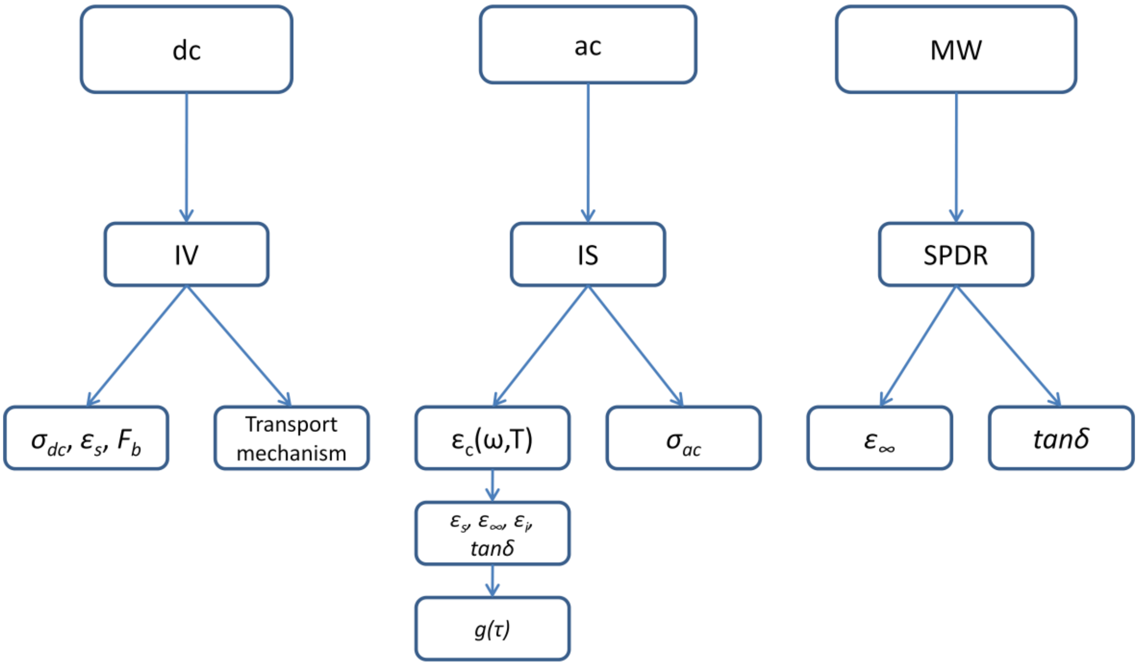

Figure 3.3: Outline of electrical characterisations performed

Here, ac is defined as any applied signal with a frequency of greater than 0 Hz and less than 1 MHz, frequencies between 1 MHz and 1 GHz are considered RF (though not explicitly considered here) and frequencies above 1 GHz are considered MW. In the dc region, JV curves were used to determine the material resistivity, dielectric strength, low frequency dielectric constant and charge transport mechanism. IS measurements were used in the ac region to determine the dielectric function of the material as well as its ac resistivity characteristics. Finally, in the MW regime a physical resonator structure was required to obtain accurate measurements of the dielectric properties and the split post dielectric resonator (SPDR) method was used to measure the dielectric constant and loss tangent of PDLA thin films.

3.2.3 Applications in Organic Electronics

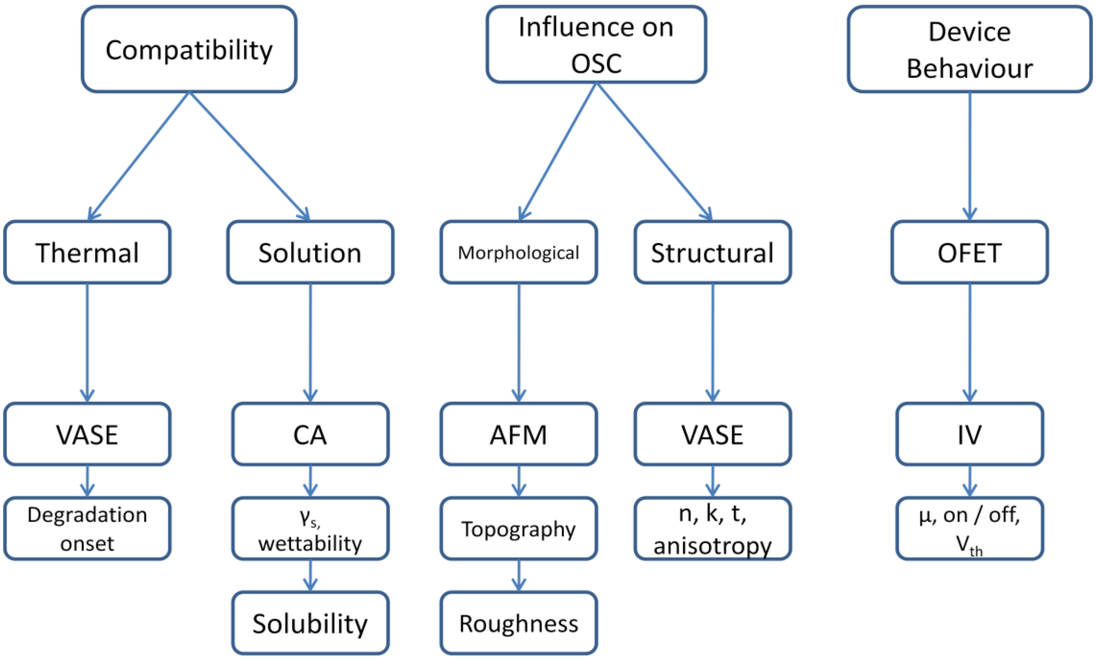

Figure 3.4: Outline of investigations into applications of PDLA thin films in organic electronics

Review of literature showed that OSC layers are the most critical element of most organic electronic devices. It was found that performance of OSC layers is highly influenced by the ordering of the molecular structures in the OSC thin film, which is profoundly influenced by other materials in the device and the processing conditions used during fabrication. Electrical characterisations performed also influenced the direction of studies into potential applications. Combining the needs of future development of organic electronic devices and results from electrical characterisations of linalyl acetate thin films, potential applications in organic electronics were identified and investigated through the scheme outlined in Figure 3.4. First, processing conditions commonly used in deposition of OSC layers were identified from the literature review as thermal evaporation methods and solution processing methods. In order to ensure compatibility with fabrication techniques, the effects of heating and solvent exposure on the PDLA layers were investigated. These studies were performed using VASE to observe the optical profiles and thickness as a function of temperature, and CA analyses to determine the interactions of PDLA thin films with various solvents. The influence of PDLA over the growth of OSCs was then investigated through a combination of VASE and AFM measurements in order to determine whether any changes in structural or morphological features were induced through the change in substrate surface. Finally, behaviour of OFET devices incorporating PDLA layers was investigated through JV analysis to examine the influence of the dielectric layer over the key operating parameters of mobility, on/off ratio and threshold voltage.

3.2.4 Optimisation of Thin Film Properties

The final research objective of this thesis was to determine the relationship between the fabrication conditions and thin film properties so that films with characteristics optimised for specific applications could be fabricated. The literature review showed that for plasma deposited thin films, the key parameter which determines the film properties is the composite parameter W/FM, which describes the energy provided to the reaction per unit monomer. It was seen that two distinct deposition regimes are commonly observed; the energy sufficient and energy deficient regimes. For a particular monomer, the molecular weight is fixed, and the ratio W/F is the controlling factor. In the case that the monomer flow rate is fixed, the power delivered to the deposition is the sole parameter which controls the degree of monomer fragmentation, reaction products, deposition kinetics and film properties. Therefore, in the studies outlined above, the parameter W was typically varied between 10 W and 75 W while the monomer, flow rate, pressure, and reactor properties remained fixed. 10 W was chosen as the lower limit, as problems with obtaining deposits occurred below this value, while 75 W was chosen as the upper limit of investigations due to higher powers beginning to interfere with the reliable operation of the pressure sensor. Additionally, at higher deposition powers, the plasma glow region began to extend into the inlet and outlet tubing causing further reliability issues. By investigating the variation in film properties with the control parameter, the relationship between deposition conditions and film characteristics was found, allowing deposition of optimised films for applications identified in the second and third research objectives.

3.3 Thin Film Fabrication Methods

Specific methods of device characterisation and analysis are presented in their relevant chapters, however, several processes were repeated for studies in multiple chapters, and are presented in this section. In particular, a detailed outline of the method used to fabricate plasma deposited thin films is provided, as well as the methods used to deposit metallic and OSC thin films in the fabrication of devices.

3.3.1 PECVD

Plasma deposition of organic thin films was performed in a custom build, glass chamber on a variety of substrates using a variety of power densities. To ensure reproducibility of results, samples were fabricated under identical fabrication conditions in all instances, and the only parameter that changed was the power delivered to the reaction chamber.

Different substrates were used depending on the specific study to be performed, however glass microscope slides were the most common substrate, utilised in the majority of experiments. All substrates underwent a cleaning process prior to deposition to ensure a surface free of contamination. This process was the same for all substrates with the exception of Si wafers, and is outlined below.

First, the substrates were placed in a sonicator of warm water and Extran for five minutes to remove the majority of macro- and microscale contaminates. Following this, substrates were sequentially rinsed in acetone and isoproponal to further clean the surface and dried in air. All substrates were stored in a closed container, in otherwise ambient conditions. For studies requiring Si substrates (such as electrical characterisation of OFET devices), a different procedure was used. Si/SiO_2 wafers with a photoresist, pre-diced to 10 mm^2 sections were purchased from Fondazione Bruno Kessler. In order to remove the photoresist and cleanse the oxide surface of organic residues, substrates were placed in a sonic bath of acetone for five minutes, followed by another five minute sonic bath in isoproponal and finally dried in N_2.

Si/SiO$_2$ substrates were always used in a deposition immediately following cleaning, and no storage was necessary.

Deposition was performed a custom built, glass RF reaction chamber, 0.75 m in length with an inner diameter of 0.055 m (approximate volume of 0.0018 m^3). The chamber includes two removable end caps, so that substrates can be placed inside the chamber and to allow thorough and routine cleaning of the system. One of these end caps includes two inlets, one of which is used to introduce inert gas (generally Ar) to the system, and the other to monitor system pressure. An outlet to a vacuum pump is present on the second end cap to evacuate the system to useful pressures. Two inlets are built into the length of the tube which act as monomer inlets. The design of the reactor is such that the pressure at the beginning of the reaction, the deposition time and monomer flow rate can be controlled. The system pressure is monitored via a Javac vacuum gauge, while monomer flow rate is kept constant via a vacuum stopcock on the monomer inlet. RF power is delivered to the system via an ENI RF generator at 13.56 MHz through a matching network and capacitively coupled copper electrodes.

The power of the RF signal could be controlled on the supply and was varied between 10 W and 75 W. Above 75 W the strength of the field began to interfere with nearby sensitive electronics (such as the vacuum gauge) and overheat the matching network. Due to these considerations the highest power used in any study was generally 75 W to ensure accurate pressure readings and correct operation of the matching network. The copper electrodes were placed 0.12 m from the monomer inlet and 0.095 m apart, with the active electrode closest to the monomer inlet. The electrode configuration used was based on the uniformity of the RF discharge it produced, and the corresponding uniformity of resulting thin films for the particular reaction chamber utilised throughout this work.

For deposition of PDLA thin films, 5 mL of monomer (in all cases, linalyl acetate purchased from Australian Botanical Products Pty. Ltd., Australia) was used without further purification.

The monomer flow rate was kept constant via a vacuum stopcock, and estimated using the following relation:

$$F = 16172 \frac{V}{T} \frac{dp}{dt} \tag{3.1}$$

where F is the flow rate (cm^3 min^{-1}), T the temperature (295 K), V the volume of the chamber (1.8 L), p the pressure (mbar) and t time (s). The rate of change of pressure with respect to time for the monomer was evaluated in two steps: first, the system was evacuated to a stable starting pressure, all inlets/outlets to the system closed and the pressure of the system measured every 10 seconds for 120 seconds to establish a baseline leakage rate for the system. This process was repeated with the monomer inlet open after the base pressure had been reached. The value dp/dt was determined by subtracting the leakage pressure change from the pressure change when the monomer inlet was open, plotting this value against time and taking a linear regression. The gradient was then equal to dp/dt and corresponded to an increase in pressure of approximately 2.66 x 10^{-3} mbar every 10 seconds. Substitution into (3.1) gives the estimated monomer flow rate to be 2 cm^3 min^{-1} for this system.

To produce films with consistent and repeatable properties the follow steps were taken:

1. Before a group of depositions, the reaction chamber and substrates were cleaned. This ensured that the substrate surfaces and internal walls of the reactor were free of contaminants which could become part of the film structure during the deposition procedure. The reactor was routinely cleaned as thin films form on all surfaces exposed to both the RF field and monomer.
2. The reaction chamber was connected to the vacuum pump, pressure gauge and gas (Ar) inlet and evacuated to a low pressure, evaporating residual alcohols left in the chamber from the cleaning procedure. The electrodes and power source were connected to the chamber as previously outlined.
3. At low pressure (~100 micron) RF glow at a power of 25 W was initiated and the apparatus left for approximately 60 minutes. Due to etching effects without the

presence of a monomer, this RF field served to further clean the interior surface of the reaction chamber and further remove contaminants remaining from the cleaning process. After 60 minutes the discharge was stopped and the system exposed to atmosphere.

4. The system was again evacuated, this time to 200 micron, 5 mL of monomer placed into the flask and the monomer inlet opened. This caused the monomer to degas, and matched the pressure of the monomer inlet to that of the tube during deposition, such that sudden increases in pressure did not occur when the monomer inlet was opened. No substrate was in the reactor at this time so that its surface was not exposed to contamination in the form of monomer vapour.
5. The chamber was exposed to atmosphere and a substrate placed between the two electrodes, the left edge of the substrate aligned with the inside edge of the left (ground) electrode. The tube was partially evacuated and Ar passed through the system for 60 seconds to ensure an O_2 free surface.
6. When the chamber reached a pressure of 100 micron, RF glow was initiated, causing a sharp rise in pressure. Once the pressure had reached 150 micron, the monomer inlet was opened, beginning the deposition.
7. Depending on several factors, the deposition was allowed to continue for a predetermined amount of time. As discussed in the literature review, the deposition time is the variable which most fundamentally determines the final film thickness, with increased deposition time resulting in thicker samples. RF power of the discharge also influences the film thickness, and in the monomer sufficient regime, higher powers result in thicker films. This behaviour was confirmed for the monomer and deposition used throughout this thesis (shown in detail in Chapter 4).
8. When the deposition was complete, the monomer inlet was closed and the RF glow extinguished. The sample was left under vacuum for a minute, then removed and stored in a closed box in otherwise ambient conditions.

3.3.2 Thermal Evaporation of Metals

Several studies throughout this work, particularly those investigating the behaviour of electronic devices, required the deposition of metallic layers to provide a conducting surface. Metals were deposited using thermal evaporation which took place in a Hivac thermal evaporation unit. A shutter is placed directly between the substrate holder and evaporation source, so that the deposition does not begin immediately after the metal begins to evaporate. In this way impurities were removed first, prior to metal depositing on the sample.

All substrates were cleaned prior to being placed inside the deposition chamber. A small length (0.1 m) of high purity metallic wire (Ag, Au or Al depending on the particular device being fabricated) was placed within the alumina-tungsten boat and the system evacuated to a pressure of 0.2 mbar. At this pressure, the plasma source was initiated to further clean the substrates for one minute. When the pressure reached a base pressure of ~10^{-5} mbar, a high current was passed through the alumina-tungsten boat as a means of heating it until the metal changed phase. After 30 seconds, the shutter was removed from between the boat and substrates, and the deposition begun. The deposition was continued until the entire length of wire in the boat had evaporated, then the shutter closed while any remaining residue was burned off the boat so that it was clean for the next deposition.

To define electrode structure a shadow mask was used, where a physical layer was placed over the portion of the substrate which does not define the electrode. For MIM structures on standard glass substrates (25 mm x 75 mm), samples were fabricated such that there were two devices on each substrate. The top electrode was 5 mm x 10 mm and defined by the shadow mask. Following deposition, samples were stored under vacuum until the next fabrication step was performed, in order to prevent oxidisation and degradation of the deposited metallic layers.

While not explicitly part of thermal evaporation, deposition of metallic electrodes often required a final step before useable devices were formed. Due to the thinness of the metallic layers, in order to interface with any other electronic or measurement device, it was necessary that copper wires were attached to the thin film electrodes on the device. This was achieved using Ag paste to bond the wire to the surface of the electrode.

Given the sensitivity of electrical measurements, it was important that the deposited electrodes be of sufficient quality not to influence the data. For MIM structures where the resistivity of a thin film dielectric was to be measured, contacts which had a linear (i.e. Ohmic) JV dependence minimal resistivity when compared to that of the sample under test were used. To ensure this, a device consisting only of electrodes was fabricated and its JV characteristics measured. In this way, the resistance of the entire testing apparatus including leads, connectors, electrodes and oxide layers was determined. It was seen that the response was Ohmic, with a resistance of only 3 Ω. Considering that plasma deposited thin films are generally insulating, with an expected resistance in the order of MΩ, this test confirmed that the deposited metal layers were of more than sufficient quality for the devices made and that the effects of the electrodes and testing apparatus were negligible during electrical measurements of the plasma deposited thin films.

3.3.3 Deposition of OSCs

Thermal evaporation of OSC materials is a similar process to the thermal evaporation of metals, however given the sensitivity of resulting films, their quality and operating characteristics to processing conditions, a different system with more control of significant deposition parameters was used. Of particular importance are the chamber and substrate temperature, temperature of the OSC powder and the rate of deposition of the OSC film onto the substrate. The system consists of a main chamber where the evaporation occurs, two Knudson cells, a quartz microbalance to monitor the approximate thickness of the deposited layers *in situ*, temperature controllers, and a load-lock system to introduce the samples to the main chamber without breaking high vacuum conditions.

The Knudson cell, quartz microbalance, temperature controllers and vacuum systems are each in place as part of control for process variables. Each Knudson cell is temperature controlled, so that the temperature, and thus rate of deposition can be adjusted. By monitoring the thickness of a layer deposited on the quartz microbalance with time, the rate of deposition can be observed. Combined with the temperature controlled Knudson cells, this provides a means of maintaining a constant rate of deposition of the OSC layer. The final temperature controller is used to heat the entire system, including the substrate, to a uniform temperature. This heating takes place prior to deposition to ensure uniform temperature throughout the entire chamber.

To deposit OSC layers, substrates were cleaned samples loaded into the system and left in vacuum until a satisfactory pressure (~10^{-7} mbarr) and temperature (~100 °C) were met. The evaporation was begun by slowly heating the Knudson cell until a film was detected on the Quartz microbalance and this temperature maintained. The rate of deposition was observed and the temperature of the Knudson cell adjusted throughout to maintain a constant rate (~1 nm min^{-1} for PDI-8CN$_2$ and 0.5 Å s^{-1} for pentacene) until the desired film thickness was reached (calculated as the deposition rate x length of deposition).

Following the deposition, samples were kept in a desiccator and shielded from light by Al foil. All optically transparent sections of the evaporation system were also similarly covered to prevent exposure to light throughout processing.

3.4 Conclusions

In this chapter, a methodology to meet the four identified research objectives has been detailed. This methodology provides an outline for the measurements performed, the results they provided, and the way in which they satisfied the project goals. In addition, this methodology addressed the issue of consistency in deposition, measurement and analysis and details the steps taken to ensure accurate and reproducible fabrication of samples. Materials and methods used to fabricate thin films of linalyl acetate, metals and OSCs were also provided in this chapter.

Chapter 4: Fundamental Characterisations

4.1 Introduction

The fundamental properties of a material can be defined as its optical, physical and chemical properties. Optical properties can be precisely quantified in terms of the complex refractive index, $\tilde{n}(\lambda) = n - jk$, where the real part n describes the refractive index, and the imaginary part k, the extinction coefficient, describes the degree to which the material will absorb light. As this property is a function of wavelength, λ, information regarding material colour and transparency are also embedded in the extinction coefficient profile.

Physical properties of a material include its surface topography and mechanical properties. These must be investigated on the nano-scale for thin films, and the key measurement technique utilised was AFM. AFM is not a direct, optical measurement technique, though it provides surface profile information. From AFM the surface uniformity, roughness and presence of defects was determined. Using the same apparatus, nano-indentation was performed to determine the hardness of the material.

The chemical properties of a material describe its elemental and molecular building blocks. The presence of particular elements and functional groups can be determined, as well as the bonding environments in which they occur. This data provides important information regarding the chemical reactivity of the material. It also provides deeper understanding as to the chemical, physical and kinetic pathways through which the fabrication of the material has occurred. The chemical properties of a material will in some degree influence many of its other properties and hence a detailed understanding of these is important. The principle means of measuring the chemical properties in this work were FTIR and XPS.

In this chapter, results of measurements performed to evaluate PDLA thin film’s fundamental properties are presented. Results of these studies helped to guide further experiments and provided a foundation for application specific investigations.

4.2 Optical Properties

4.2.1 VASE Measurements

4.2.1.1 Theory and Methods

VASE is a technique which allows the determination of a sample's optical properties as a function of wavelength as well as its thickness. The measured parameter is the complex reflectance ratio, ρ, described by a magnitude (Ψ) and phase (Δ) component. The general equation of ellipsometry is given by [162]:

$$\rho = \frac{r_p}{r_s} = \tan(\psi) e^{j\Delta} \qquad (4.1)$$

where r_p and r_s denote the amplitude of p- and s- polarised reflected light normalised to their initial values. As VASE measures a ratio rather than an absolute value it is a robust and accurate method of measurement [163].

It is evident from (4.1) that the properties of interest, namely the complex refractive index, and thickness t, are not a direct result of a VASE measurement. These properties are the result of a modelling and regression process applied to the data rather than directly measurable parameters [162]. The modelling process requires a description of each optically unique layer of the sample under study and several refinements before final values are reached. Due to the fact that parameters are determined as the result of regression analysis, care must be taken to ensure a unique solution consisting of uncorrelated fitting parameters [162-164]. Optical properties and thickness are just two parameters that can be determined; depending on the complexity of the sample and modelling procedure, several more properties such as interfacial and surface roughness, anisotropic properties and intermixing ratios can be determined when applicable [165-167].

The regression is carried out by minimising the mean squared error (MSE) parameter, defined by [164]:

$$MSE = \sqrt{\frac{1}{2N - M} \sum_{i=1}^{N} \left[\left(\frac{\psi_i^{\mathrm{mod}} - \psi_i^{\mathrm{exp}}}{\sigma_{\psi,i}^{\mathrm{exp}}} \right)^2 + \left(\frac{\Delta_i^{\mathrm{mod}} - \Delta_i^{\mathrm{exp}}}{\sigma_{\Delta,i}^{\mathrm{exp}}} \right)^2 \right]} \qquad (4.2)$$

where N is the number of measured Ψ, Δ pairs and M is the number of real valued fit parameters. The Levenberg-Marquardt algorithm is used to perform the optimisation and is described elsewhere [164]. This algorithm occasionally settles on local rather than global minima of the objective function surface and fitting from several, widely separated initial guesses should be attempted to ensure that the global minimum has been found [162]. All analysis of ellipsometry data was performed in the WVASE32 software, which was packaged with the J.A. Woollam Co., Inc. VASE used for data acquisition. This software package implemented the optimisation algorithm, however, checks for uniqueness of fits and a true global minimum were performed on results from all data analyses.

An archetypal example of the fitting process for a typical sample deposited on a glass substrate is presented below. Unless otherwise noted, this procedure has been used for the analysis of all ellipsometry data presented in this thesis, and is relevant to all experiments and analysis presented as it was how sample thickness was determined in all cases.

4.2.1.2 Analysis of a Typical Sample Deposited on a Glass Microscopy Slide

Figure 4.1 shows the typical measured values of ellipsometry across the measured spectrum of 200 nm – 1000 nm and angles of 55° - 65° to ensure measurement about the Brewster angle, which reduces sensitivity of the data to noise and systematic errors [164].

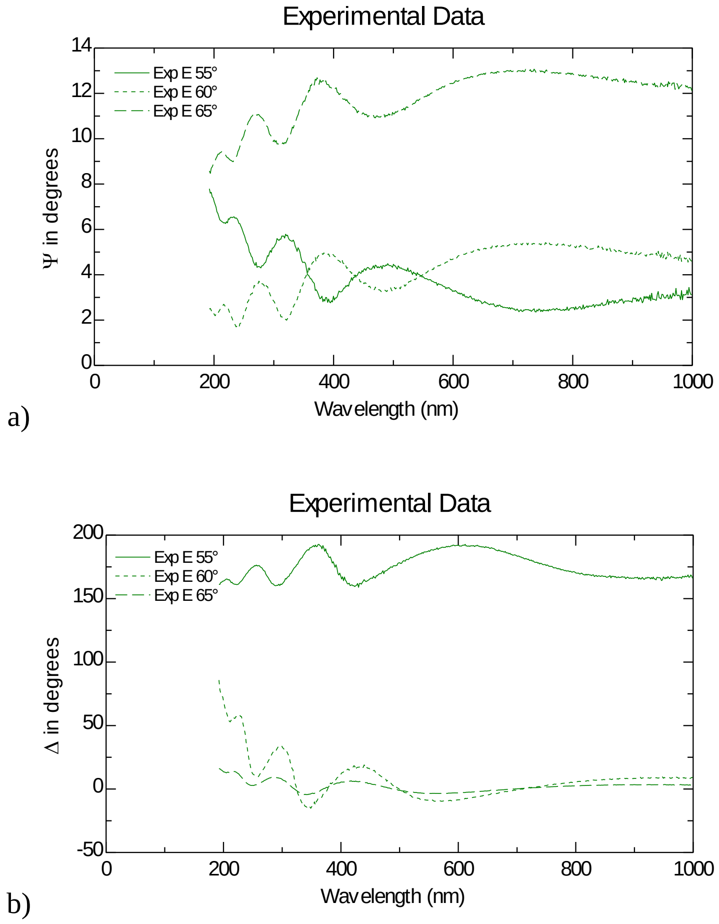

Figure 4.1: Experimental (a) Ψ and (b) Δ data

The analysis of the system begins with a layer by layer optical description of the sample. Generally, this consists of a layer for the substrate on which the sample is deposited and then subsequent layers to model the optical properties of the thin film of interest. In the case of this example, an optically transparent glass microscopy slide was used as the substrate, and a layer added to the model which describes the optical properties of this slide. This process ensures that the optical properties obtained for the film do not include contributions from the substrate.

It can be seen in Figure 4.2 that a model including only a substrate is insufficient to adequately describe the experimentally obtained data. Even at this early stage of analysis, were an inappropriate model selected for the substrate there would be much more drastic differences between the modelled data and experimental data.

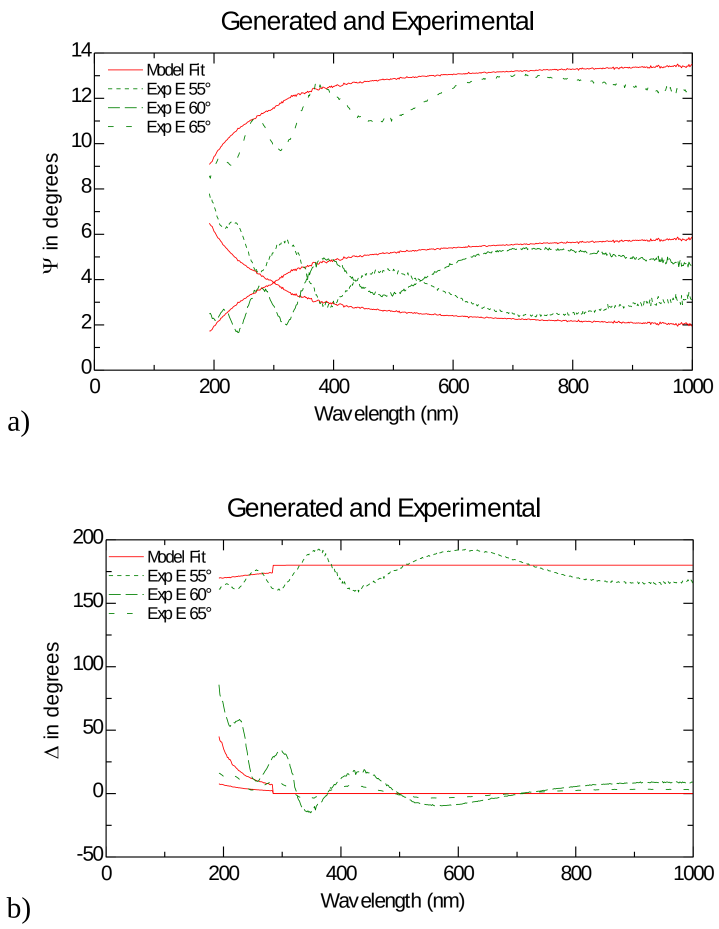

Figure 4.2: Experimental and modelled (a) Ψ and (b) Δ data after inclusion of a substrate layer

An optical model of the thin film must be determined. PDLA thin films are optically transparent and non-absorbing in the visible spectral range and hence their extinction coefficient tends to zero as wavelengths become longer. Such behaviour is well modelled by a Cauchy layer, described mathematically as [164]:

$$\tilde{n}(\lambda) = A + \frac{B}{\lambda^2} + \frac{C}{\lambda^4} + j\alpha \exp\left(\beta\left(12400\left[\frac{1}{\lambda} - \frac{1}{\gamma}\right]\right)\right) \qquad (4.3)$$

where A, B and C are parameters which describe the refractive index of the layer and α, β and γ are the extinction coefficient amplitude, exponent factor and band edge respectively, which describe the extinction coefficient of the layer, modelled as an exponential absorption tail. When modelling Cauchy layers, advantage can be taken of the fact that the extinction coefficient is zero at high wavelengths and the parameters A, B and C are sufficient to describe the optical behaviour of the film in this region. Estimates for A, B and C, as well as the thickness of the sample, are obtained by considering only the refractive index at high wavelengths to simplify the model and fitting procedure.

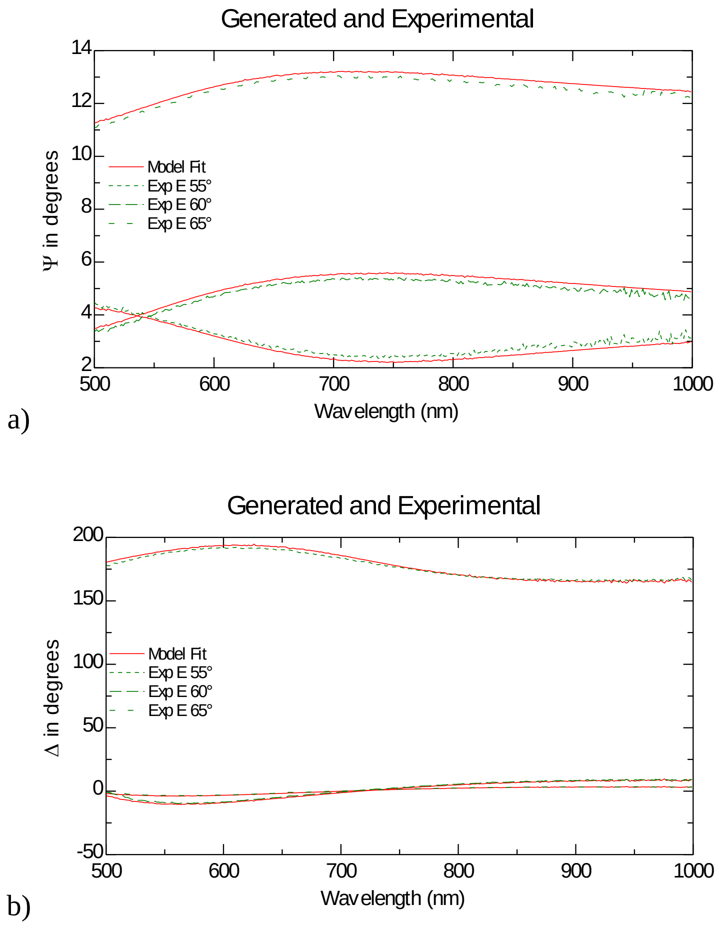

Figure 4.3: Result of fitting Cauchy layer refractive index parameters and film thickness to experimental (a) Ψ and (b) Δ data at high wavelengths

Figure 4.3 shows the modelled system from fitting these parameters to experimental data at high wavelengths, resulting in A = 1.5179, B = 0.0089486, C = 0, t = 282.6720 nm and an MSE of 2.776. As C is the coefficient of a λ^{-4} term, if the band edge γ occurs at higher wavelengths as was the case here, it is typical for the model to show minimal sensitivity to the parameter and be left out of fitting entirely [162, 164].

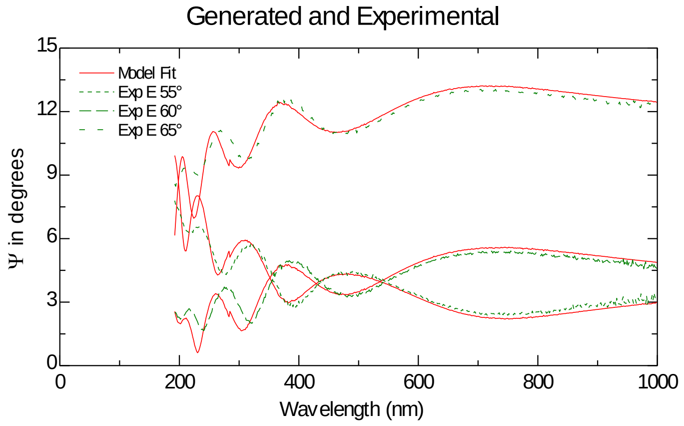

a)

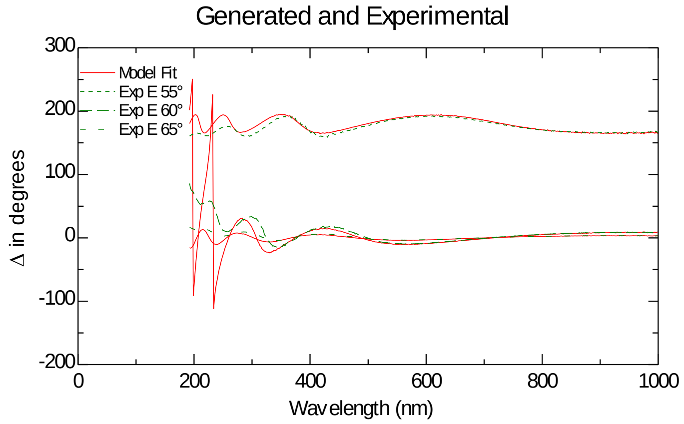

b)

Figure 4.4: Modelled (a) Ψ and (b) Δ data across entire spectrum

Figure 4.4 shows the result of this model extended to the entire measured spectrum. While the model adequately describes experimental data above approximately 400 nm, below this point the model loses accuracy. This is due to the fact that the model extinction coefficient is still zero across the entire spectrum, while in reality absorption in the UV region takes place.

As the refractive index parameters have been estimated, the model is now improved across all wavelengths by fitting the extinction coefficient parameters α, β and γ at low wavelengths while leaving A, B and C fixed at their initial estimates.

This is shown in Figure 4.5, where α = 0.010958, β = 0.74555 and γ = 400 nm, resulting in an MSE of 5.843. The model has substantially improved in the lower wavelength regions, though at very low wavelengths the Cauchy model does not provide an entirely adequate description of the sample's optical behaviour. Further improvements to the model are made by replacing the Cauchy description of the thin film with a General Oscillator description.

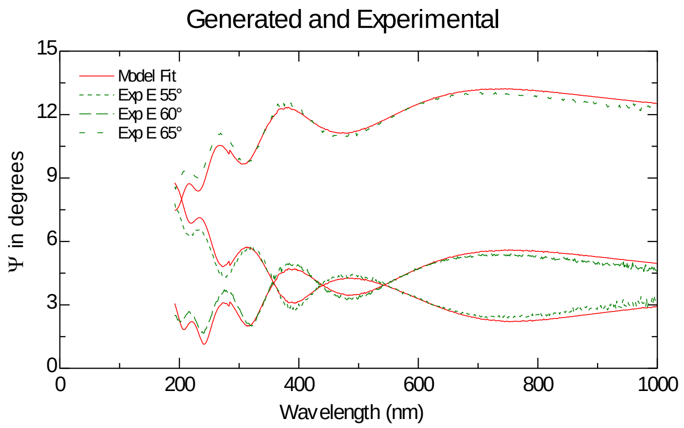

a)

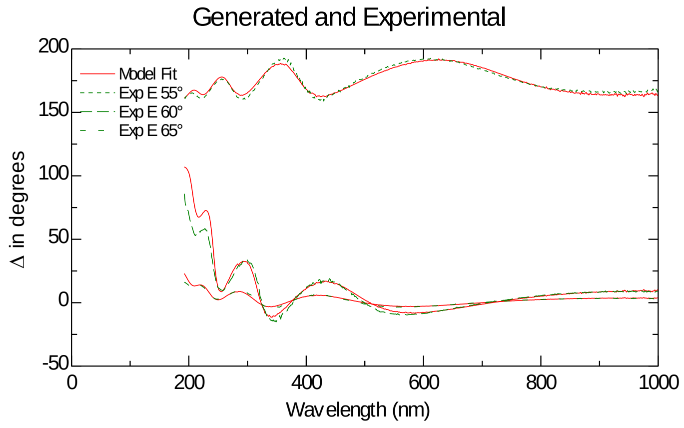

b)

Figure 4.5: Experimental model to (a) Ψ and (b) Δ data after fitting for extinction coefficient parameters α, β and γ

4.2.1.2.1 General Oscillator Models

The general oscillator model replaces the Cauchy description of the optical constants of the layer of interest with generalised parameters which model the absorption features of the material. The refractive index is then obtained by exploiting the Kramers-Kronig (KK) consistency of the dielectric function. Several oscillators may be used, the summation of which provides the final set of modelled parameters. It is a common technique to model a Cauchy layer first to provide an initial estimate for the optical properties of the layer, which is then replaced with a general oscillator model to allow more precise modelling of the layer's absorption behaviour and does not depend on assumptions such as an exponential band edge or complete transparency [162].

Depending on the characteristic shape of the material's dispersion behaviour, different oscillator models are required. The shape of the absorption depends on the physical source of the absorption in the material, and hence correct choice in oscillator can provide information on physical characteristics of the film, such as its electronic band gap, E_{gap}. Different types of materials such as insulators, semiconductors, doped semiconductors and conductors have different characteristic absorption shapes, so correct choice of the oscillator used to describe this shape is important to properly model the experimental data and determine the optical properties of the thin film.

In amorphous materials, absorption bands are often Gaussian in shape, due to a random distribution of atomic and molecular bond lengths and angles about a central mean value [168]. As a result, absorption in the material occurs at normally distributed resonant frequencies and the width of the absorption features is Gaussian in nature. If little is known about the physical and chemical characteristics of the material and simplifying assumptions cannot immediately be made, summed Gaussian oscillators are useful to capture the features present and inform further fitting efforts [162, 168]. As established in Chapter 2, plasma deposited thin films are generally amorphous in nature, and hence the assumption of absorption bands with a Gaussian shape is a reasonable starting point.

The Gaussian oscillator describes the real (ε_1) and imaginary (ε_2) components of the complex dielectric function, $\varepsilon_c(E)$, where E is the photon energy (related to wavelength, λ, and frequency, f) as [164]:

$$\varepsilon_2(E) = A \cdot \left(\exp\left[-\left(\frac{E - E_a}{\sigma} \right)^2 \right] - \exp\left[-\left(\frac{E + E_a}{\sigma} \right)^2 \right] \right) \tag{4.4}$$

$$\varepsilon_1 = \frac{2}{\pi} P \int_0^{\infty} \frac{\xi \varepsilon_2(\xi)}{\xi^2 - E^2} d\xi \tag{4.5}$$

$$\sigma = \frac{B_r}{2\sqrt{\ln(2)}} \tag{4.6}$$

where A is the amplitude, E_a the centre energy and B_r the broadening of the absorption peak, which become the fit parameters of the model, rather than the optical constants themselves. (4.5) provides the relationship between $\varepsilon_2(E)$ and $\varepsilon_1(E)$ via the KK transform.

In the case of PDLA thin films, the previously modelled Cauchy layer optical properties are used as the starting point for modelling the material's optical properties with a single Gaussian oscillator. The oscillator’s parameters are selected as optimisation variables and a fit performed. This procedure determines a starting set of parameters for the Gaussian oscillator. Although n is derived from the KK transform of k, parameters are available to better fit the optical profile to experimental data. These parameters are the offset value and complex poles, which are used to describe features in the absorption beyond the measured spectral range which affect the result of the transform [164]. These may be necessary as the KK transform requires integration of $\varepsilon_2(E)$ between 0 and ∞, while only a limited spectral bandwidth is measured [164]. If these parameters are ignored, the quality of the fit may be poor and hence they should be accounted for.

After fitting the oscillator parameters to the initial guess provided from the Cauchy layer, the thickness is chosen as a fit parameter, and the thickness and oscillators variables optimised to provide the best fit to the experimental data.

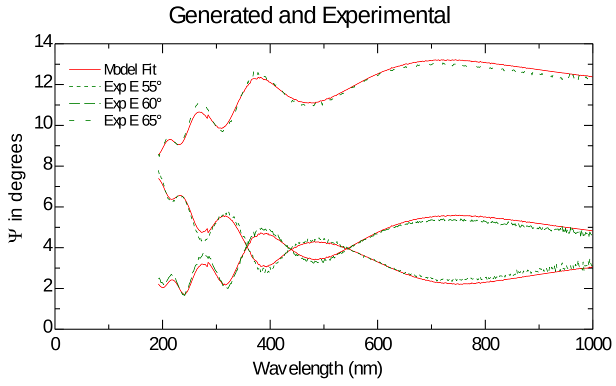

a)

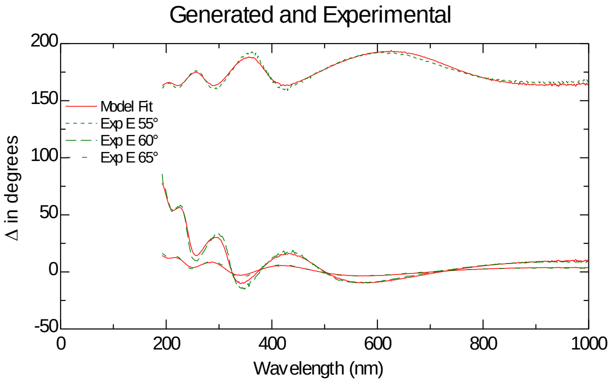

b)

Figure 4.6: Experimental and modelled (a) Ψ and (b) Δ data after fitting with general oscillator parameters

Figure 4.6 shows the result of the fitting of the Gaussian oscillator parameters and thickness of the layer to experimental data, where an MSE of 3.49 was obtained. The thickness of the layer was determined to be 283.37 nm and the optical profile of the sample is shown in Figure 4.7.

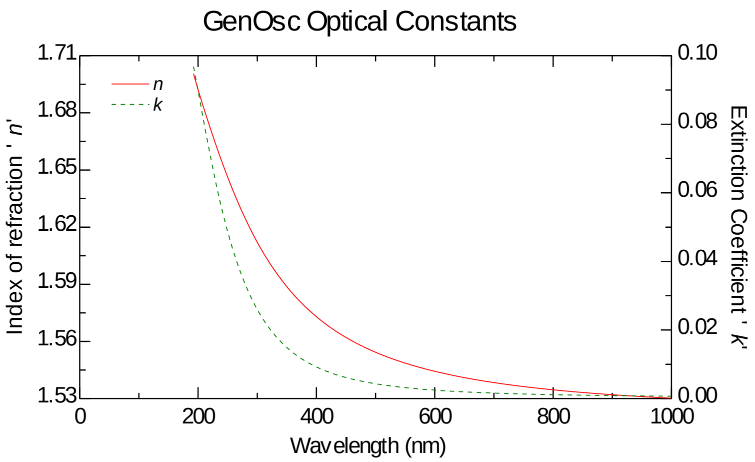

Figure 4.7: Optical properties of general oscillator model

4.2.1.2.2 Uniqueness, Correlation and Sensitivity

It is important to ensure the model obtained is unique, i.e. the fitting result is only obtainable by one single set of values for the fit parameters. If the same model can be reproduced by changing the value of one variable, and then 'balancing' the effect of this change by modifying another, these variables are said to be correlated and the fit cannot be called unique. This is particularly important for variables with intended physical significance, such as thickness; if the thickness value is correlated with some other variable, it could essentially be any value desired, as the effect of this change would be accounted for elsewhere. When the model is unique and a minimised MSE achieved, the values obtained from the fitting procedure are highly accurate.

To ensure uniqueness, the correlation matrix is studied. This matrix presents a measure, between -1 and 1, of correlation between variables obtained from the covariance matrix. An element approaching these limits is indicative of correlation between two variables used in the fitting procedure. Table 4.1 shows the correlation matrix for fit to experimental data shown in Figure 4.6.

Table 4.1: Correlation matrix of fit parameters

	PolePos	**PoleMag**	**Offset**	**Thickness**	**A**	**E_a**	**B**
PolePos	1	0.95	-0.88	-0.81	0.26	0.29	0.26
PoleMag	0.95	1	-0.99	-0.81	-0.05	0.00	0.03
Offset	-0.88	-0.99	1	0.79	0.17	0.10	0.04
Thickness	-0.81	-0.81	0.79	1	-0.17	-0.20	-0.26
A	0.26	-0.05	0.17	-0.17	1	0.96	0.83
E_n	0.29	0.00	0.10	-0.20	0.96	1	0.95
B_r	0.26	0.03	0.04	-0.26	0.83	0.95	1

The parameters used to modify ε_1 (pole position and magnitude and offset) to account for the limited spectral range of the KK transform were highly correlated with one another, and with the thickness. This indicates that in this case, not all parameters were necessary for the fitting and the KK transform from the oscillator parameters are sufficient to accurately describe the refractive index without much further modification. They were therefore removed as fit parameters. Secondly, there were some correlations between the properties of the oscillator, A, E_a and B_r. This is because the shape of absorption profile can be obtained by many combinations of these parameters. Despite this, correlation between these variables is not problematic, as the optical profile itself is the feature of physical importance. So long as this uniquely influences the final fit, and the same shape is consistently obtained for various starting parameters of A, E_n and B_r, these correlations are not of great concern.

After removing the modifying fit parameters and performing a minimisation, the following correlation matrix was obtained.

Table 4.2: Final correlation matrix

	Thickness	**A**	**E_a**	**B_r**
Thickness	1	0.16	0.00	-0.19
A	0.16	1	-0.32	-0.73
E_n	0.00	-0.32	1	0.82
B_r	-0.19	-0.73	0.82	1

By removing the modifying parameters pole magnitude and position, and offset, the correlations between other variables were also reduced. The thickness value changed to 283.39 nm (a difference of less than 0.02 nm), was uncorrelated with all other fit parameters and was therefore unique, and the final value obtained from the fit. Additionally, the correlation between the oscillator properties reduced to less than 0.9 and, coupled with the above reasoning, was not of concern. The optical profile did not change from Figure 4.7 and all properties of physical interest of the thin film were uniquely determined.

4.2.1.3 Relationship between Thickness, Optical Properties and Deposition Conditions

The thickness of plasma deposited thin films is a function of several parameters, including the monomer used, deposition time, system geometry and pressure [27, 169, 170]. The work of this thesis was carried out on a completely new monomer, one of the most significant parameters in determining the rate of deposition, which in turn has significant influence over the other properties of the material [34]. The thickness of the film was studied as a function of deposition time using an RF power level of 75 W and the same system pressures, with a fixed reactor geometry for each deposition. Deposition times of 5, 15, 60 and 80 minutes were used and regression analysis performed to determine the rate of deposition. From methods outlined in Chapter 3, the monomer flow rate was known to be ~2 cm^3 min^{-1}, and the deposition was begun at a system pressure of 150 mTorr.

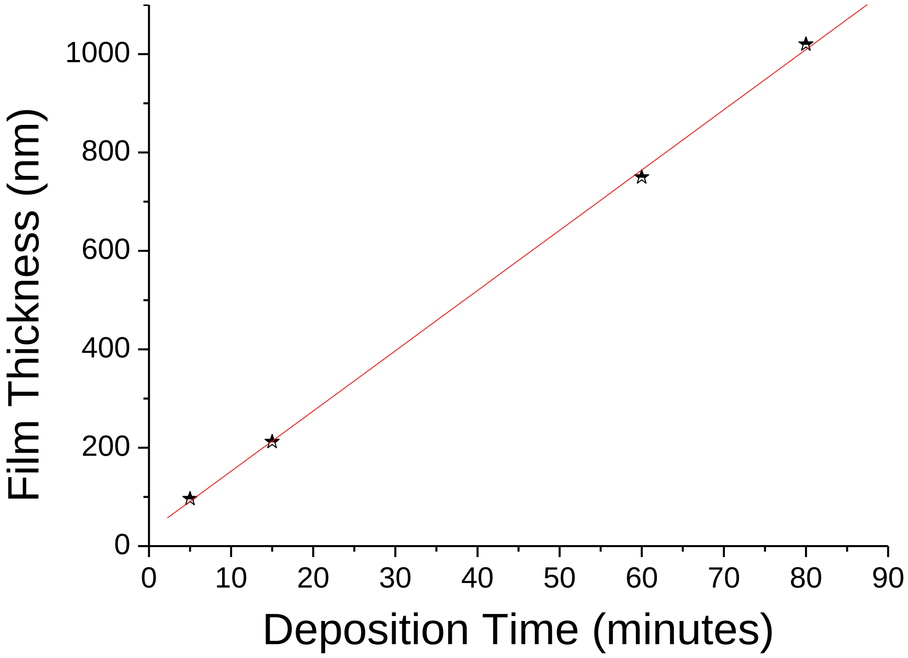

Figure 4.8: Film thickness as a function of power density

Figure 4.8 shows that the samples' thickness increased linearly as a function of deposition time, at a rate of approximately 10 nm min^{-1}. This linearity is expected and is in good agreement with the behaviour of other plasma deposited thin films [16, 170]. The value of 10 nm min^{-1} provides a starting approximation to aid in deciding the required deposition time for films with specific thicknesses in other studies and applications.

The optical properties for films deposited at 75 W for increasing deposition times are shown in Figure 4.9. The refractive index and extinction coefficient are shown on the left and right axes respectively. Of primary importance is the fact that the optical parameters did not show any dependence on film thickness when deposited under otherwise identical conditions. This shows that the time spent in the reaction chamber did not significantly influence the structure of the material, by inducing further crosslinking or changes in density. Additionally, as the absorption features shown by k remained constant with variations in film thickness, it was inferred that no significant changes in the molecular structure of the film occurred, as these would have directly influence the absorption features of the material, either through a shift in peak location, magnitude, the emergence of new peaks or some combination of these [171].

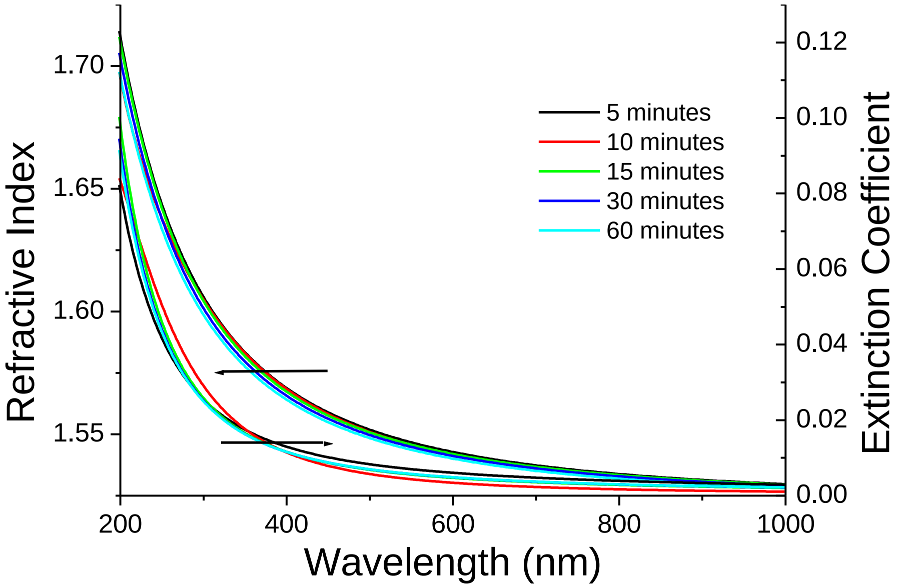

Figure 4.9: Optical properties for films of different deposition times

The shape of the absorption curve was characterised by a single peak at low wavelengths, with a shallow, exponential roll off as wavelength increases. After approximately 600 nm the extinction coefficient decayed to less than 0.01, quantitatively confirming observation that the material is transparent in this region.

The refractive index behaved as expected for transparent media and the material's dispersion was well described by the Sellmeier equation [172]:

$$n^2(\lambda) = 1 + \sum_{i=1}^{N} \frac{Bi\lambda^2}{\lambda^2 - C_i} \tag{4.7}$$

where B_i and C_i are the ith Sellmeier coefficients. The result of fitting B_i and C_i for each sample is shown in Table 4.3. While fitting for N = 3 was performed, coefficients B_2 and B_3 were zero and only one term was required to model the material's dispersion.

Table 4.3: Sellmeier coefficients for films of different thicknesses

Time	**t (nm)**	**B_1**	**C_1 (nm^2)**	**$C_1^{1/2}$ (nm)**	**ε_∞**
5 min	124	1.33	12980	113.92	2.33
10 min	161	1.33	12343	111.09	2.33
15 min	248	1.33	12899	113.57	2.33
30 min	465	1.33	12577	112.14	2.33
60 min	745	1.33	12254	110.69	2.33

The values of B_i and C_i represent an absorption resonance of strength B_i at a wavelength of $\lambda^2 = C_i$. For films of all thicknesses, the only absorption resonance occurred at the same wavelength, approximately 112 nm, with the same strength of absorption, approximately 1.33. From B_i, the relative dielectric constant of the thin film can be estimated as [173]:

$$\varepsilon_{\infty} = 1 + \sum_{i=1}^{N} B_i \tag{4.8}$$

and is shown in the final column of Table 4.3. The value of ε_{∞} for all films was approximately 2.33, and represents the dielectric constant at high frequencies, or the asymptotic value which the real part of dielectric function will tend to as wavelength tends towards infinity. The rate of deposition was again found to be approximately 10 nm min^{-1}.

Deposition time is one external parameter that can be manipulated to affect the final film thickness, though the *rate* of deposition should remain constant. The deposition rate is affected by other parameters, and of particular interest was how film thickness was affected by variations in RF power, as this was the principle control parameter. The manner in which RF power affects deposition rates is unique to particular systems and monomers [16, 170]. The relationship between the effect of RF power and the growth rate of PDLA thin films in the reactor described in Chapter 3 was established.

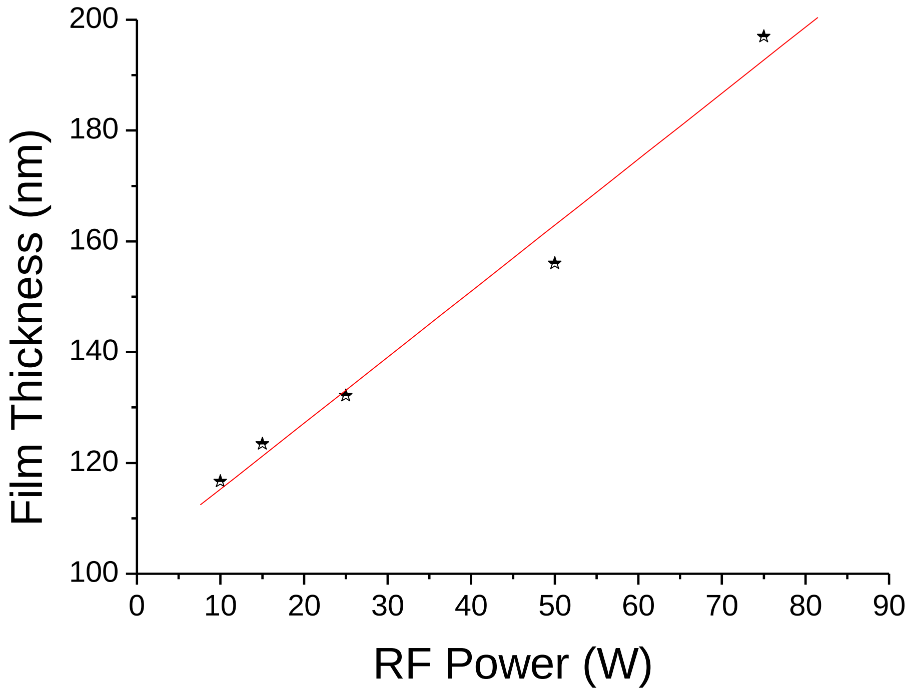

Figure 4.10: Variation of film thickness with RF power

Figure 4.10 shows the thickness determined from VASE measurements for depositions of 20 minutes where RF powers of 10 W, 15 W, 25 W, 50 W and 75 W were used. A linear dependence of thickness with increasing RF power was observed. This shows deposition occurred in the monomer sufficient reaction region, and that high RF powers introduced more reaction products than they did ablation of deposited films [10, 16]. In the case of linalyl acetate, no non-linear regions were encountered in the range of input powers and deposition times investigated. This established that as RF power was increased, the rate of deposition would increase and films would be thicker for the same deposition times. The change in reaction products, rate of growth and increased bombardment of the surface also likely influenced the properties of the film and was investigated in subsequent studies.

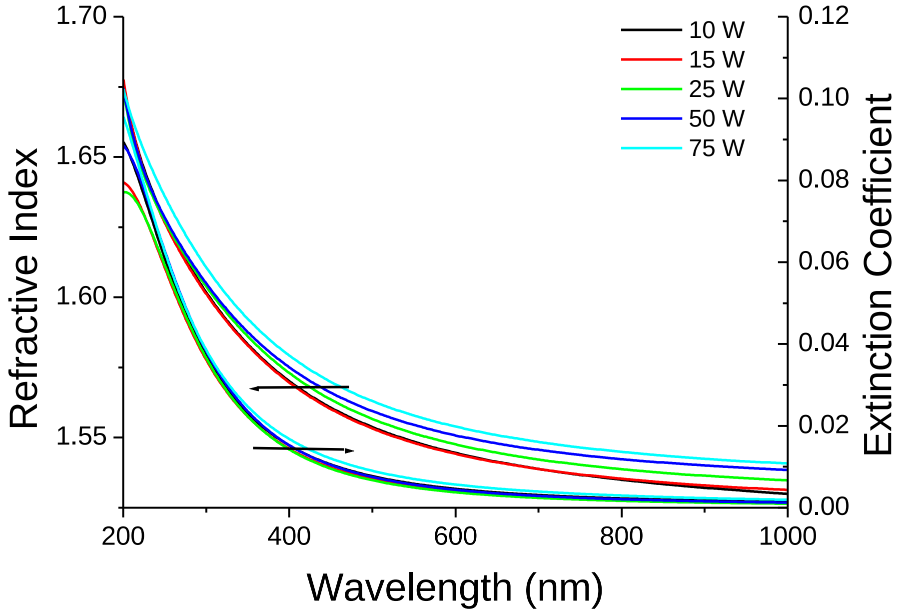

Figure 4.11: Optical properties of films deposited with different input energies

Figure 4.11 shows the variation of the refractive index and extinction coefficient when films were deposited with different input energies for the same deposition time. Qualitatively the absorption behaviour for all films was approximately the same, with peak features in the same location for all films at sub-200 nm wavelengths and the magnitude of the extinction coefficient being approximately the same for all films. Examining the dispersion behaviour of the films, those deposited with higher input energies had slightly higher refractive indices, particularly evident at higher wavelengths.

Table 4.4 shows the Sellmeier coefficient for the films presented in Figure 4.11. The value of B_1 and hence ε_∞ was found to increase slightly with increases in the input energy used during the deposition, indicative of some structural differences in the films when fabricated under different conditions. The most likely explanation is an increase in the density of the films when fabricated under higher energy conditions on substrates with increased temperatures. The increased bombardment of the substrate by charged species likely induced a higher degree of crosslinking which contributed to the higher value of refractive index [174]. The differences between films fabricated at 10 W and 15 W were minimal, both qualitatively and quantitatively. It is believed that the difference of 5 W in energy at these low powers was not significant enough to induce any change in film structure or modify the deposition process. For this reason, in further studies, films deposited at 15 W were not investigated.

Table 4.4: Sellmeier coefficients for films deposited with different input energies

Power (W)	**t (nm)**	**B_1**	**C_1 (nm^2)**	**$C_1^{1/2}$ (nm)**	**ε_∞**
10	116	1.34	11076	105.24	2.34
15	123	1.34	11068	105.20	2.34
25	132	1.36	10655	103.22	2.36
50	156	1.37	10419	102.07	2.37
75	196	1.38	10513	102.53	2.38

The dispersive and absorbance behaviour of the films is similar to that of plasma deposited HMDSO, lavender oil, and terpinen-4-ol thin films, all of which show similar dependencies of dispersion and absorbance on wavelength and power density [175-177]. The variation in the refractive index with changes in power density was less for PDLA thin films than for plasma deposited terpinen-4-ol thin films and of a similar range to plasma deposited *Lavandula* *angustifolia*. This is likely due to the composition of the starting monomers used; *Lavandula angustifolia* has linalyl acetate as one of its principle constituents (25% - 40%) and hence the relationships between plasma deposited thin films of linalyl acetate and *Lavandula angustifolia* and deposition conditions share some similarities. Terpinen-4-ol however is a component of tea tree oil, and not present in *Lavandula angustifolia* and hence its properties are influenced by deposition conditions in different ways. In the case of thin films derived from both *Lavandula angustifolia* and linalyl acetate, while a degree of control of the refractive index via input power is present, it is deemed too insignificant (less than 1% variation at 589 nm) to be effective in most applications.

4.2.2 UV-Vis Spectroscopy

4.2.2.1 Theory and Methods

UV-Vis spectroscopy is a direct measurement of a sample's absorbance, as the logarithm of the ratio of incident light intensity to transmitted light intensity, i.e. [178]:

$$A(\lambda) = \ln\left(\frac{I_t(\lambda)}{I_0(\lambda)}\right) \tag{4.9}$$

where A is absorbance, I_0 the intensity of the incident light and I_t the intensity of the transmitted light, measured at the detector. The absorbance is proportional to the absorption coefficient, α, scaled by the path length the light must travel through the sample, i.e. the thickness [179]. From the absorbance profile, $A(\lambda)$, the optical band gap of the material can be determined. In an organic material, the optical band gap represents the energy required to excite a carrier from the HOMO to the LUMO.

For amorphous materials, the principle absorption edge is described by three sections; the low, mid and high energy regions [180]. The low energy region is considered intrinsic to the material, and is related to the level of disorder and crosslinking present in the material. In the mid energy region the absorption coefficient increases exponentially with photon energy, hν. In the high energy region, the absorption coefficient is described by the relation [179, 181, 182]:

$$\alpha h\nu = B\left(h\nu - E_{gap}\right)^{P} \tag{4.10}$$

where B is a constant independent of energy and P describes the nature of the electronic transition responsible for absorption. For amorphous semiconductors, P takes the value 2, corresponding to indirect allowed electron transitions. P may also take values of 0.5, 1.5 and 3, indicating direct allowed, direct forbidden and indirect forbidden transition respectively [183]. Determining which value of P should be used is performed by plotting $(\alpha h\nu)^{1/P}$ versus photon energy for each possible value of P, commonly known as Tauc plots. The value of P that gives the most linear Tauc plot determines the type of transition present [183].

To perform this analysis, absorbance measurements of the glass substrate and ambient background were taken, and subtracted from the absorbance profile of the sample to obtain the film absorbance. Custom software was written in MATLAB which takes as its input the measured film absorbance data from UV-Vis spectroscopy and the thickness determined from VASE analysis, and converts these to Tauc plots using each possible P. The linearity of the band edge is then assessed by performing a linear regression in the high energy region, and the plot which yields the highest R^2 value is considered the most linear. The value of P corresponding to this plot is then used to determine the type of transition present. From (4.10), extrapolation of this linear region to the photon energy axis gives the value of the optical band gap.

4.2.2.2 Absorbance and Band Gap as a Function of Power Density

The absorbance and optical band gap of PDLA thin films was examined, and the relationship between these properties and the input power density investigated. These measurements were performed on samples deposited with input energies of 10 W, 15 W, 25 W, 50 W and 75 W for consistency with data presented in Section 4.2.1. Depositions of 60 minutes in length were performed to minimise errors in the measurement [176].

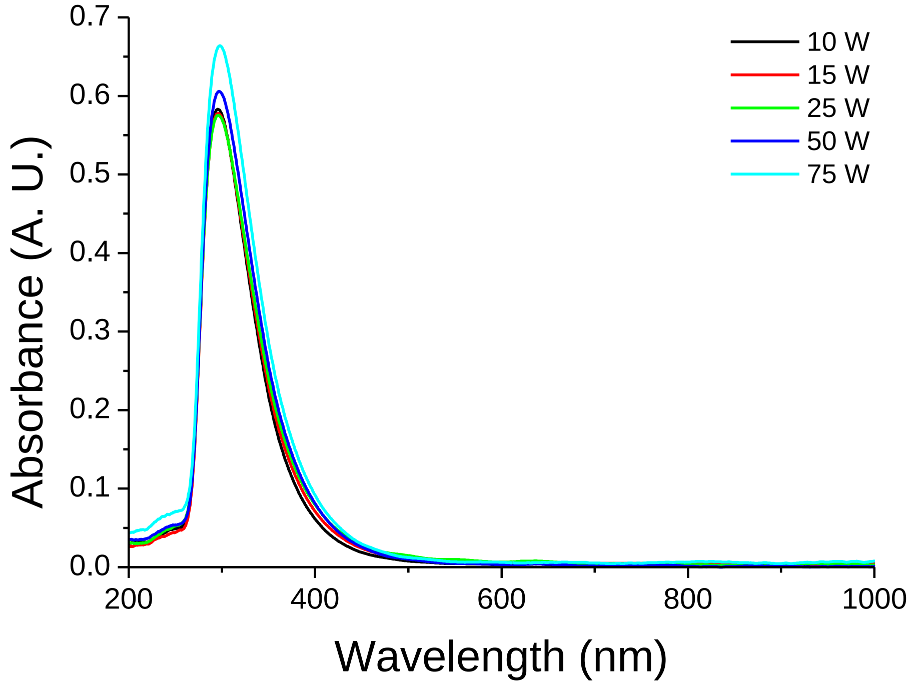

Figure 4.12: Absorbance profiles for thin films deposited with different input energies

Figure 4.12 shows the measured absorbance spectrum of the samples. A single absorption peak was present at approximately 300 nm for all samples, independent of deposition power. There was a slight difference in the magnitude of this peak, easily explained by the relationship between absorbance and absorption coefficient. The measured absorbance, as presented in Figure 4.12, is a function of the absorption coefficient and the path length of the light. Hence inherent in the measured absorbance data is a dependence on the thickness of the sample. As shown in Section 4.2.1.3, samples deposited at higher input energies for identical deposition times resulted in thicker samples and this difference explains the tendency of the absorbance magnitude to increase with power density.

Aside from this difference in the magnitude of the absorbance peak, no shift in peak location or broadening was observed with variations in input energy, in good agreement with the behaviour observed in the extinction coefficient determined from VASE analysis. This behaviour is also similar to other plasma deposited thin films, such as those deposited from thiophene, pyrrole, *lavandula Angustifolia* and terpinen-4-ol [175, 176, 184]. In all cases, the absorbance spectra for the films remained unaffected by variations in the input energy used during the deposition.

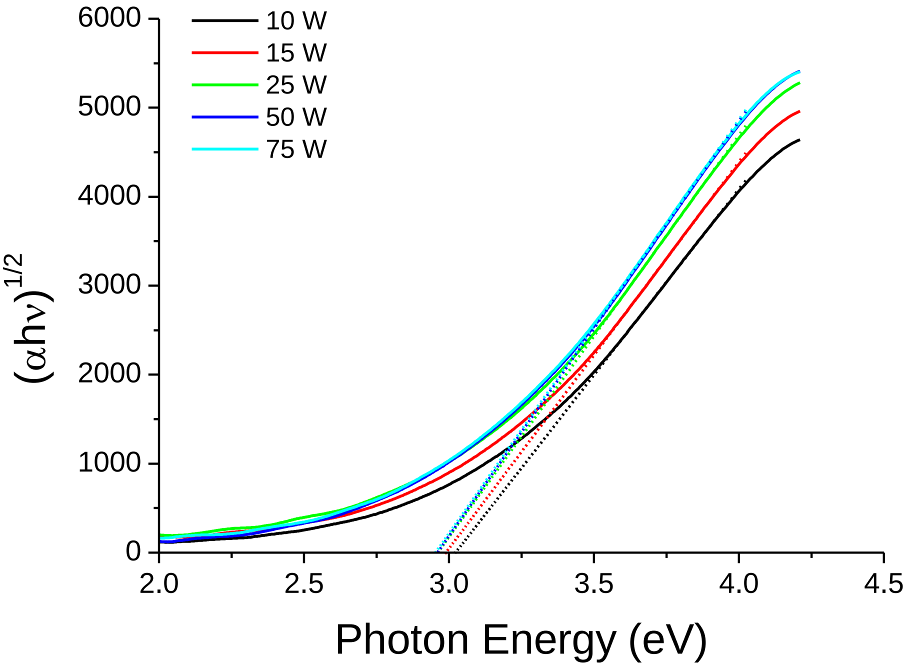

Figure 4.13: Tauc plot and extrapolation of linear region to the photon energy axis

From absorbance measurements, Tauc plots were generated for all measured data. Using P = 2 gave the most linear absorption edge, compared to P = 0.5, P = 1.5 and P = 3, indicative of indirect allowed transitions. The result of the regression, and extrapolation of the linear portion of the Tauc plot to the photon energy axis, is shown in Figure 4.13. The optical band gap of the films was approximately the same for all input power densities used, varying from 3.02 eV at 10 W to 2.95 eV at 75 W. While a relationship may exist between optical band gap and power density, considering possible errors in the measurement and fitting procedures, the range of variation is too insubstantial to be of use; no change in the fundamental electronic nature of the material (i.e. a change from insulating to semiconducting or semiconducting to conducting) could be induced by the varying the input power conditions across the feasible 65 W range available.

Considering the optical band gap to be ~3 eV, PDLA thin films were classified as either insulating or semiconducting. Given the anticipated highly amorphous and disordered structure of the thin films due to the manner in which they have been deposited, low carrier mobilities and conductivities were expected and hence the films were considered for applications as insulators. Appropriate doping may be capable of producing films which are semiconducting, given the band gap value. More in depth characterisations of the electronic properties and potential applications of the thin films are provided in Chapter 5 of this thesis. Optical band gaps and absorbance profiles (i.e. the optical transparency) were consistently reproducible across a range of deposition conditions, including when input power and film thickness were varied and a wide range of applications are therefore possible.

4.3 AFM Studies

4.3.1 Theory and Methods

AFM is a scanning probe microscopy (SPM) which is frequently used to image the surface of thin film materials [185-188]. As with all SPM measurements, the technique is based on performing a line by line scan across the plane of a samples surface, and measuring the force interactions between the scanning probe and the sample surface, resulting in a discretised map of these interactions, F(x,y) [189]. In the case of AFM, a Si or Si_3N_4 cantilever with a sharp tip at its end is generally used as the scanning element [189]. The radius of curvature of the tip is typically on the order of 10^1 nm. When very close to the sample's surface, the cantilever undergoes deflection due to force interactions between its tip and the samples surface, described by Hooke's law:

$$F = -kx \tag{4.11}$$

where F is the force of the interaction, k the spring constant of the cantilever and x the displacement of the cantilever from its equilibrium position. The displacement of the cantilever is measured using a laser reflected from its surface onto a split photodiode detector array and k is known.

Figure 4.14 shows the forces acting on the tip (vertical scale) as a cantilever is brought closer to a sample (horizontal scale). Three distinct regimes of tip-sample interactions are observed [191].

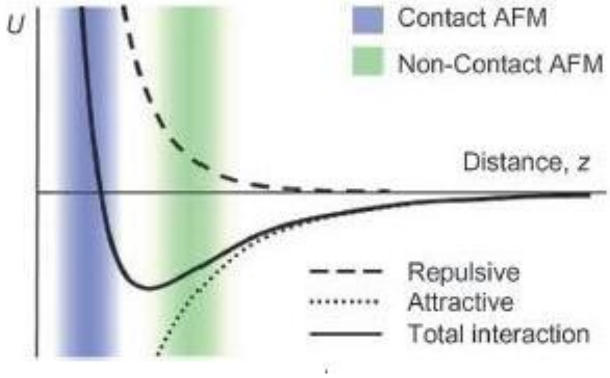

Figure 4.14: Tip-sample force interactions as a function of vertical distance [190]

In the first region, at the far right of the displacement axis, there is no interaction between the tip and sample as the distance is too great for the small forces involved to sufficiently interact. As the tip moves closer to the sample, force interactions between the tip and sample begin to pull the tip towards the sample and it is in the attractive regime. This regime is characterised by the very close proximity of the tip and surface, however the two are *not* in contact with one another. When the tip comes close to the surface, the forces act to push the cantilever away, and it is said to be in the repulsive regime. Measurements can be performed in either the repulsive or attractive regimes depending on the method used.

In the simplest measurements, the tip is in the repulsive regime. As the scan proceeds, the deflection of the tip as it passes over features of the surface is measured and the map F(x,y) is formed. This is known as variable deflection mode. As the tip is in constant contact with the sample, this is a form of contact mode scanning. In constant force mode, the tip is adjusted to maintain a constant deflection of the cantilever and hence constant height above the surface, known as constant force mode. In this mode, the adjustments necessary to maintain the constant deflection are recorded and form the map F(x,y).

Both constant force and variable deflection scans are forms of static, contact mode scanning, where the tip is in contact with the surface of the sample at all times. Care must be taken to ensure the cantilever is of sufficiently low stiffness to prevent damage to the surface being scanned (i.e. the spring constant of the cantilever should be less than the spring constant of the inter-atomic bonds of the material), particularly in the case of soft materials. Low stiffness cantilevers also alleviate some issues due to noise and drift associated with static measurements. However, in the case of very soft samples, or samples which are easily damaged by the scale of force interactions utilised, methods where the tip is not in contact, or only makes intermittent contact with the surface are required.

Modes in which the microscopy tip are not in contact with the sample surface are non-contact modes, and are dynamic modes, in contrast to the previously described contact modes, which are static modes. This distinction between static and dynamic modes arises from the movement of the cantilever; in static modes, no movement or vibration of the cantilever is induced and the measured/controlled parameters are directly related to Hooke's law. In dynamic modes, the cantilever is made to vibrate at or very near to its resonant frequency and fixed in close proximity to the sample surface in the attractive regime. By changing the tip height to maintain a constant frequency and amplitude of oscillation, the force map can be generated.

The final mode is a combination of the contact and non-contact modes, and is called tapping or semi-contact mode. This mode is most similar to non-contact modes, in that it is a dynamic mode where the cantilever is made to oscillate near its resonant frequency in the attractive regime. However, in semi-contact mode the magnitude of these oscillations is sufficient for the tip to intermittently come into contact with the surface and enter the repulsive regime, tapping the surface before rising with the cycle of its oscillation. This allows the measurement to benefit from the less destructive aspects of non-contact modes by avoiding dragging the tip across the surface, such that very sensitive or soft materials can be investigated in a non destructive way. In addition, the drawbacks of pure non-contact modes, such as the difficulty in finding close enough tip-sample distances while avoiding sticking, are alleviated.

In order to ascertain the hardness of a thin film, nano-indentation can be performed, where an AFM cantilever (or more specialised nano-indentation tip) is brought into contact with the sample using a known force and the displacement of the tip is measured. As with VASE measurements, the hardness of the thin film is not directly measured, rather it is a parameter derived from analyses of the experimental data. In the case of nano-indentation, the measured data is the force-displacement curve of the nano-indenter. The typical shape of such a curve is shown in Figure 4.15.

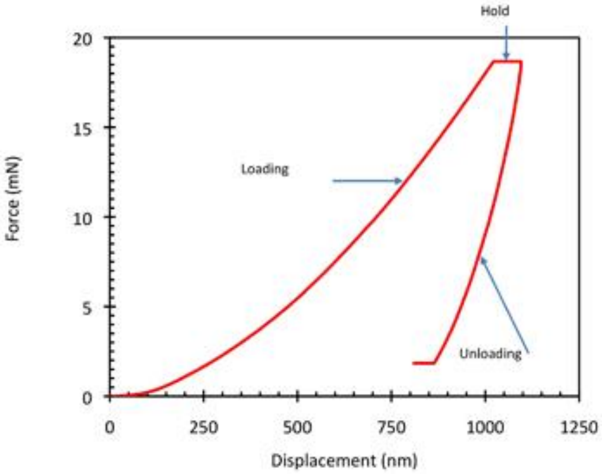

Figure 4.15: Typical force-displacement curve for nano-indentation [192]

The force-displacement curve consists of three distinct sections; the loading section, as the tip is brought into contact with and pushes into the sample; the maximally loaded section, where a constant force is maintained for a brief period of time, and the unloading section where the tip is removed from the sample. The maximally loaded section may not always be used, however for soft samples it is included to allow for viscoelastic relaxation effects [193], which if ignored may influence the shape of the unloading curve. From the unloading section of the force-displacement curve, the load, P, is estimated as a power law function [193]:

$$P = A\left(h - h_f\right)^m \tag{4.12}$$

where h is the displacement and h_f is the maximum displacement. From the derivative dP/dh evaluated at the maximum displacement, i.e. the rate of change of load with respect to distance at the instantaneous point at which the tip is first removed from the sample, the contact stiffness, S, can be calculated. Knowing S allows the contact depth, h_c to be calculated from [193]:

$$h_c = h_f - 0.75\frac{P_{\max}}{S} \tag{4.13}$$

where P_{max} is the maximum load applied to the sample. Knowing the surface area of the indentation and the maximum applied load allows the calculation of the hardness H. For a Berkovitch tip the surface area of an indentation can be approximated by a polynomial as a function of the contact depth [193]:

$$A(h_c) = C_0 h_c^2 + C_1 h_c^1 + C_2 h_c^{1/2} + C_3 h_c^{1/4} + \ldots + C_8 h_c^{1/128} \tag{4.14}$$

For each tip used, the coefficients C_i must be determined to give the calibrated tip area function. After h_c is determined from (4.13) its value can be substituted into (4.14), which allows determination of the hardness [41, 193]:

$$H = \frac{P_{\max}}{A(h_c)} \tag{4.15}$$

The fitting of (4.12) to the experimental force-displacement curves, determination of h_c, $A(h_c)$ and H were all performed automatically along with control of the nano-indentor via the TriboScope®3.5 software package. Indentation force was controlled such that indentation depth remained less than 10% of the total film thickness to avoid the influence of substrate hardness.

4.3.2 Topography of PDLA Thin Films

To investigate the surface of the PDLA thin films, tapping mode AFM was used to produce topographical images. These images provide information on the material's surface properties, and some information on the bulk characteristics. For example, presence of defects such as lumping or pinholes through the material can be identified via AFM by the presence of sudden, sharp peaks and valleys. Furthermore, the average surface roughness, R_a, can be determined from AFM topography. This value is important for any application involving subsequent deposition of layers above the plasma deposited thin films; surface roughness can greatly influence the morphology of metallic, semiconducting and bio-films and their bulk properties [194-196]. In organic electronic devices the surface of the dielectric can play a dominating role in determining the overall device properties and hence characterisation of the material's surface is an important step in determining its appropriateness for various applications [195-197]. These properties were again investigated as a function of the deposition conditions utilised, and the variation in film properties induced by change of the input energy to the deposition the key parameter of interest.

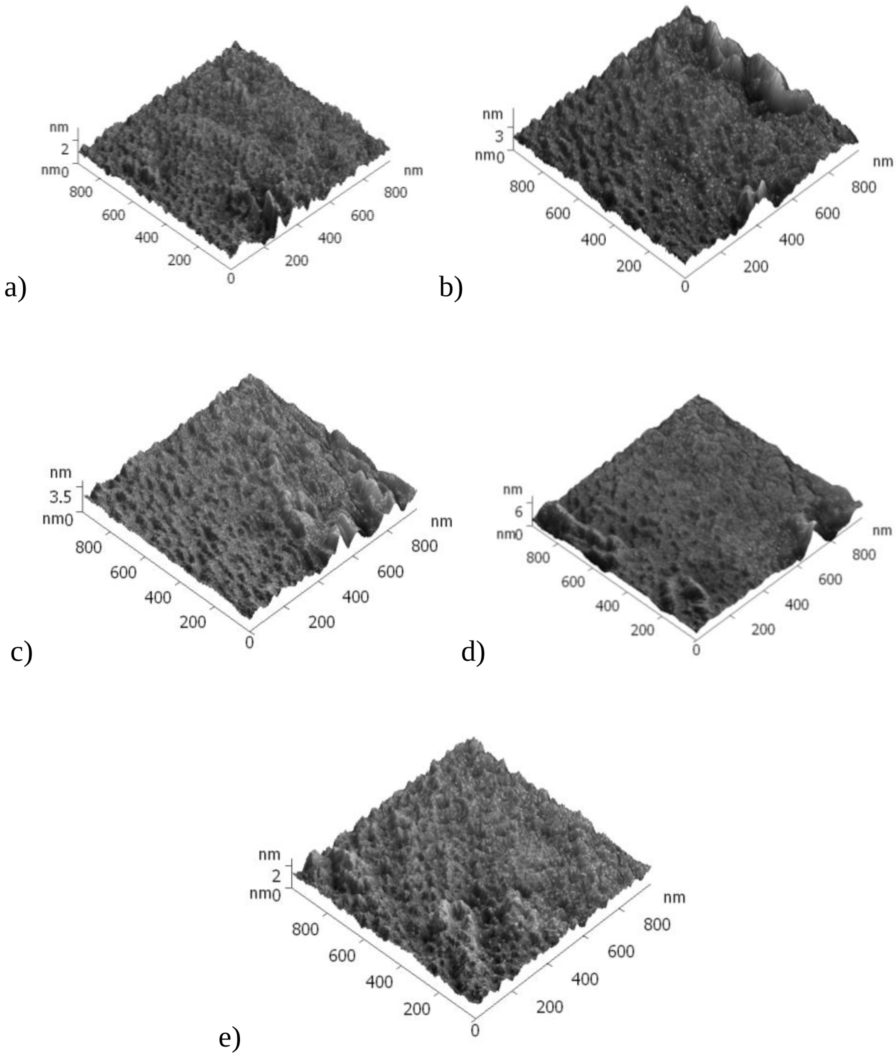

Figure 4.16: 1 μm x 1 μm AFM images of PDLA thin films at (a) 10 W (b) 15 W (c) 25 W (d) 50 W and (e) 75 W

Figure 4.16 shows the topographic images obtained from an NT-MDT NTEGRA Prima AFM, using tapping mode scans under ambient conditions. Tapping mode scans were used to ensure the surface of the material was undamaged by the scanning process given its expected softness, based on literature reported properties of other plasma deposited thin films [198, 199]. There was no significant difference in the appearance of films deposited at varying RF power levels; all films consisted of small peaks and valleys of approximately 1-2 nm in height and the films were completely amorphous at their surface. Given the isotropic nature of plasma deposited thin films and their surface properties, there is no reasonable basis on which to assume any level of (poly)-crystallinity within the samples. From their appearance, no particular deposition condition resulted in more amorphous films than any other. The thin films were therefore not modified in any significant way by exposure to the increasingly powerful energy levels within the reactor.

To further aid in comparison of the thin films, and to better quantify their properties, the surface roughness of the samples across the 1 μm^2 measured area was determined. For all samples the average roughness, R_a was determined to be approximately 0.20 nm, again demonstrating that the samples' morphological properties were not significantly affected by power density. The roughness measured for the samples was low, comparable to that of thermally grown SiO_2 [196]. The smooth surfaces obtained by PDLA are therefore appropriate as interfacial or substrate layers, to be coated with other materials, as their roughness should have a minimal effect on the growth properties of additional layers. It has been shown that for pentacene OFETs, the properties of the device are not affected by the surface roughness of the dielectric layer when it is below 0.5 nm RMS [195, 196]. PDLA layers may therefore be investigated as dielectric layers in bottom-gate OFETs for example, should desirable electrical properties also be found. The influence of other surface properties and electrical properties should also be investigated, however no significant influence on the operation of devices should be induced as a result of the morphological properties of PDLA thin films.

4.3.3 Hardness of PDLA Thin Films

The hardness of the material was evaluated using nano-indentation, and investigated at power levels of 10 W, 15 W, 25 W, 50 W and 75 W. The results of this are shown in Figure 4.17. Film hardness increased with RF power in a linear relationship ($R^2 = 0.98965$), increasing by approximately 0.002 GPa W^{-1}, varying from a minimum of 0.30 GPa at 10 W to a maximum of 0.45 GPa at 75 W. The likely explanation for this behaviour is related to the increase in fragmentation of monomer units during the deposition process, as well as the increase in crosslinking of these samples [200, 201], both of which result in a film which consists of a larger number of short, densely packed units. While the variation is small, the slight increase in refractive index with power density does support the presence of an increase in film density. The range of variation in the hardness was much more significant than in optical properties however; H varied by approximately 30% across the range of input powers investigated, indicative of significant bulk structural variations between films. It is also useful that the mechanical properties were significantly influenced while the optical and surface properties were maintained essentially constant.

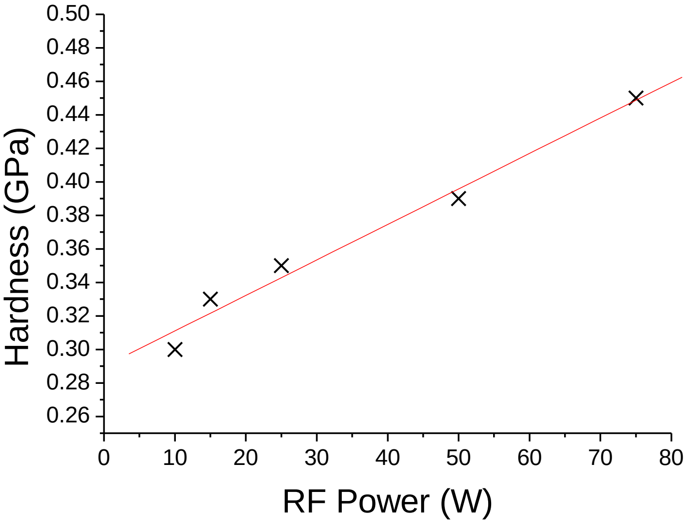

Figure 4.17: Hardness of PDLA thin films as a function of power density

The value of hardness is comparable to that of other plasma deposited hydrocarbon thin films, such as poly-acetylene which has a reported hardness of 0.4 GPa [202]. Diamond like thin films (α-H:C) deposited via plasma methods have been obtained with hardnesses of up approximately 16 GPa [203], though at the cost of other functionality. Given their comparability to other similar thin films, PDLA thin films offer an alternative to these with desirable surface and mechanical properties.

Table 4.5: Summary of properties determined in AFM studies

Power (W)	Roughness (nm)	Hardness (GPa)
10 W	0.21	0.30
15 W	0.21	0.33
25 W	0.20	0.35
50 W	0.20	0.39
75 W	0.19	0.45

4.4 Chemical Composition Studies

4.4.1 FTIR Spectroscopy

4.4.1.1 Theory and Methods

FTIR spectroscopy is a transmission measurement, similar to UV-Vis spectroscopy, in that it provides a measurement of a sample's absorption of light at particular wavelengths, in this case in the IR spectrum. However, unlike UV-Vis spectroscopy as described in Section 4.2.2, FTIR spectroscopy collects spectral data at all measured wavelengths simultaneously (referred to as the Fellgett advantage) [204, 205]. In an FTIR spectrometer, a broadband light source is used to produce the test beam, which is then passed through an interferometer.

The source wave, containing all wavelengths under investigation, is split by the beam splitter and approximately 50% is transmitted to a primary mirror and 50% reflected to a second mirror. Upon reflection, these signals return to the beam splitter, and 50% of each is returned to the source and 50% of each goes to the output. Assuming the two waves that go to the output are in phase, they will constructively interfere and produce an output with a maximum. This arises when mirrors one and two are equidistant from the beam splitter, and is referred to as the Zero Path Distance (ZPD). In the interferometer, the position of mirror two is varied, and hence a difference in the optical path travelled by the beams arises. This difference in Optical Path Distance (OPD) results in only certain wavelengths of the beams constructively interfering. As the distance of the translating mirror is varied, different interference patterns result and hence the magnitude of the output beam varies in a decaying, periodic manner. This output is referred to as the interferogram, and contains embedded in it information regarding *all* wavelengths of light in the incident beam. Mathematically, the Fourier Transform of the interferogram magnitude with respect to the distance of the mobile mirror results in the output spectrum.

By placing a sample in the path of the output beam and measuring the interferogram, the wavelengths at which the sample absorbs light are determined. This absorption occurs due to the excitation of molecular structures in the sample, and hence the resulting absorption spectrum provides qualitative and quantitative information regarding the material's bulk chemistry. The magnitude of the absorption is dependent on both the molecular structure of the material and its thickness; it is essentially determined by the 'amount' of a feature which is present to absorb the light and will hence be dependent on not only the particular feature but also the volume through which it is present. For this reason, quantitative analysis of FTIR data is not always possible.

FTIR was typically performed by suspending samples in or depositing them on an IR transparent medium, such as a KBr disc and performing a transmission measurement. Modern FTIR spectrometers commonly employ Attenuated Total Reflectance (ATR) systems and do not require the transmission of the source beam through the entire sample. In an ATR system, the source beam is passed into a material (typically diamond) with a high refractive index and undergoes total internal reflection. At the boundary between the crystal and the surrounding medium (in this case, the sample under investigation), an evanescent wave is produced, whose magnitude is determined by the absorption of light in the sample. In these studies an ATR-FTIR has been used. Due to the typically thickness of the thin films (less than 1 μm) and the typical penetration depth of the evanescent wave (~2 μm), substrate effects may be present in the data at wavelengths which the substrate absorbs if IR transparent substrates are not used [206].

4.4.1.2 ATR-FTIR as a Function of Power Density

Initially, an ATR-FTIR measurement was performed on a sample deposited at 75 W onto a KBr substrate to conduct primary analysis and determine whether important features were present in the low wavelength region. Figure 4.18 shows the ATR-FTIR spectrum of a PDLA thin film deposited at 75 W. The thin film consisted of predominately hydrocarbon structures, evidenced by several strong absorption peaks associated to stretch and bending modes of C-H functionalities. A detailed peak assignment is provided in Table 4.6. In addition to the C-H functionality, oxygyen in the form of hydroxyl groups is evidenced by the broad peak at 3484 cm^{-1} and a ketone functionality at 1708 cm^{-1}.

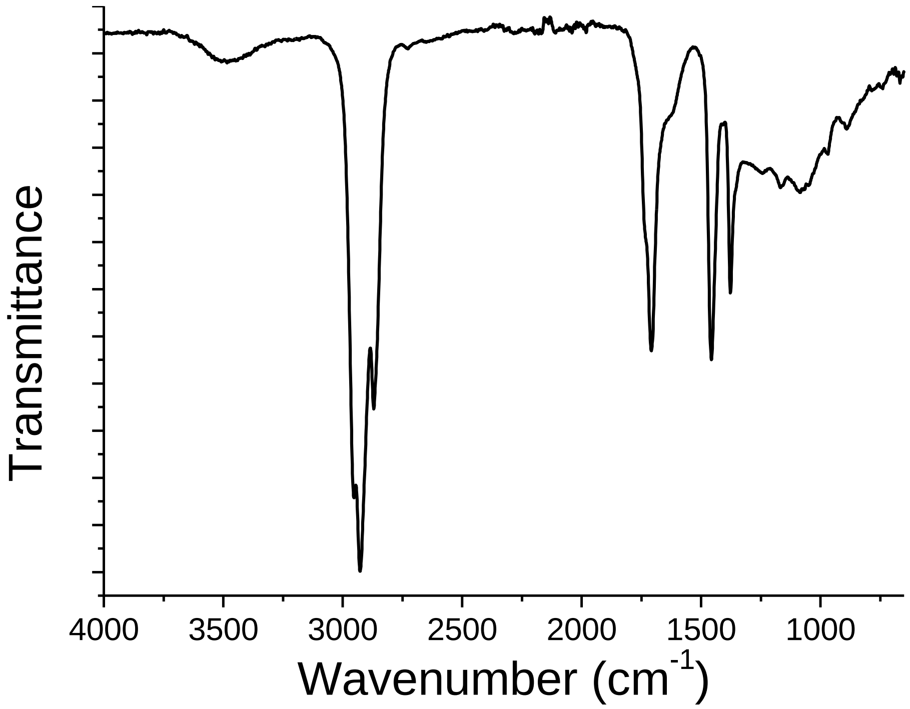

Figure 4.18: ATR-FTIR spectrum of PDLA thin film deposited at 75 W

This oxygen was in all likelihood due to the ester in the linalyl acetate monomer, and post-deposition reactions between atmospheric O_2 and surface radicals present from the deposition process.

Table 4.6: FTIR peak assignments for PDLA thin films

Wavenumber (cm^{-1})	**Intensity**	**Assignment**
3484	Medium (broad)	O-H stretch
2948	Very Strong	C-H a. stretch
2927	Very Strong	C-H a. stretch
2870	Very Strong	C-H s. stretch
1708	Strong	C=O stretch
1456	Strong	C-H a. bend
1376	Strong	C-H s. bend
1167	Weak	C-O stretch
1082	Small to non-existent	C-O stretch
967	Small to non-existent	C-H stretch
893	Small to non-existent	C-H stretch

Figure 4.18 and Table 4.6 show that no significant spectral information was contained below approximately 1300 cm^{-1}, and only very weakly absorbing features were present in this region. As glass begins to absorb approximately 1200 cm^{-1}, it was determined that experiments could be conducted on glass substrates. Samples were deposited at input energies of 10 W, 25 W, 50 W and 75 W on glass slides to investigate whether different power densities significantly influenced the chemical structure of the films.

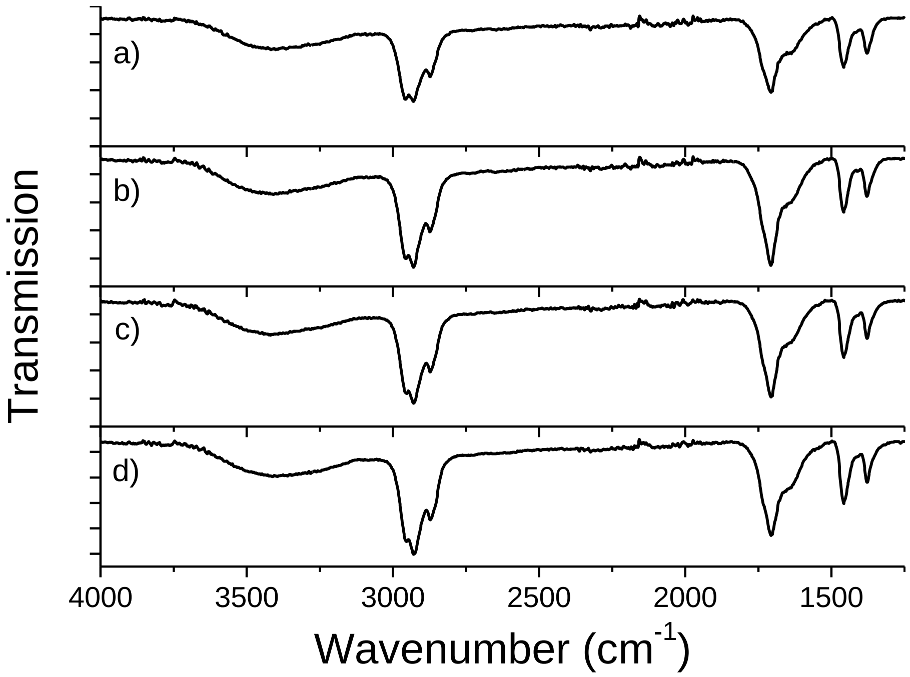

Figure 4.19: ATR-FTIR spectra of PDLA thin films deposited at (a) 10 W (b) 25 W (c) 50 W and (d) 75 W

Figure 4.19 shows that minimal differences were present between samples deposited at different power densities. Absorption peaks were present at the same locations in all spectra, with approximately the same relative intensity. Films displayed the same hydrocarbon nature, with the addition of some oxygen. This is an interesting result, given similar plasma deposited thin films typically show a strong dependence on power density and significant decrease in the presence of functional groups [175, 198]. Other works show that specific functional groups present in the monomer can be retained if sufficiently low-energy deposition conditions are employed [207, 208]. In the case of PDLA thin films the lowest energy condition used (10 W) was sufficient to result in fragmentation of the monomer similar to that induced by the highest energy condition (75 W), evidenced by the fact that none of the monomer functional units were retained in films deposited at 10 W. Differences in films (chemical and otherwise) were then likely due to the increase in UV and ion bombardment of the films during the deposition, and differences induced by increased substrate temperatures at higher energy conditions, rather than chemical differences.

From a device fabrication perspective, a chief concern is the presence of oxygen in the material, particularly if this oxygen is present at the surface of the thin film as suspected. This is because OSCs have been shown to be highly susceptible to H_2O at the dielectric/semiconductor interface, believed to be due to reactions between O_2 at the dielectric surface and atmospheric moisture [209]. The presence of H_2O leads to trapping of charge carriers at the interface, and a reduction in device mobility. These effects are significantly reduced by surface treatment of the dielectric layer [155, 210]. Comparing the spectrum of PDLA thin films to plasma deposited PMMA thin films, plasma deposited PMMA layers have a much higher concentration of oxygen, yet without surface modification were able to successfully act as a dielectric barrier in an OFET device [156]. PDLA thin films should therefore, from a chemical perspective, be similarly capable of such applications.

4.4.2 XPS

4.4.2.1 Theory and Methods

XPS measurements exploit the photoelectric effect by irradiating the surface of a material or sample under study with low energy X-rays. This irradiation results in electrons within the material becoming excited and dissociated from their bonding environment into the vacuum of an analysis chamber, where they are subsequently collected in a high resolution electron spectrometer. These emitted electrons will have an energy characteristic of their bonding environment, and the number of electrons detected at each energy level can therefore be related to the amount of an element present in the material. When present in a chemical bonding environment, shifts in the characteristic emission energy of an element occur, and hence XPS is used to determine the bonding environment in which a particular element is present. In organic compounds, where carbon is present in multiple functional groups, analysis of the peak associated with carbon 1s orbital is used to determine the functional groups present in the material. XPS measurements are confined to the first several nm of a material due to the fact that electrons excited from deeper within the material are more likely to undergo scattering events prior to reaching the electron detector. Additionally, due to their small 1s cross-section both hydrogen and helium are not detectable through XPS.

4.4.2.2 XPS as a Function of Power Density

Representative survey spectra for samples deposited at each power level are shown in Figure 4.20. The most dominant peaks were by far those associated with C 1s, O 1s and N 1s orbitals, and are labelled.

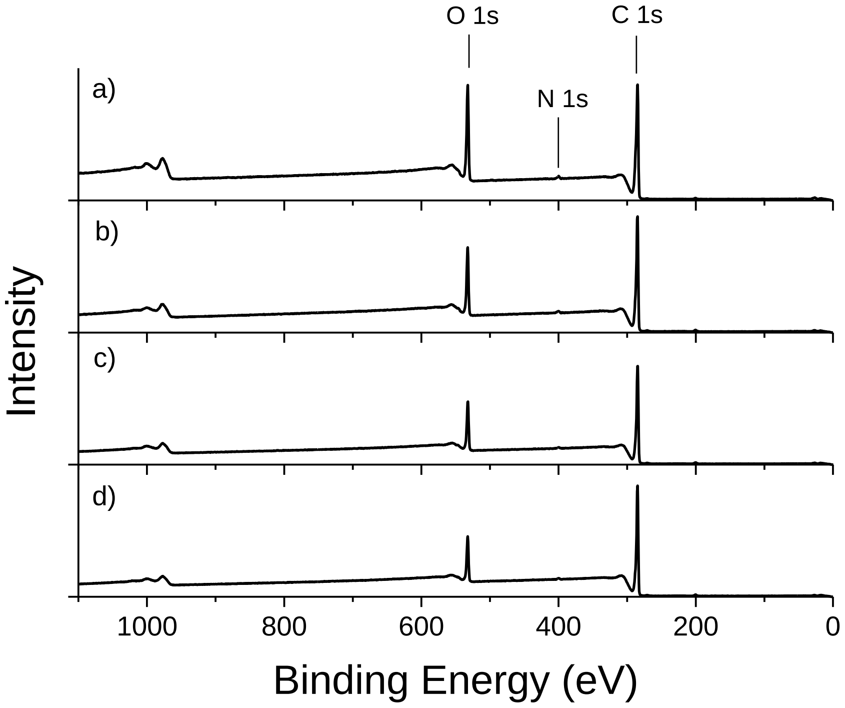

Figure 4.20: XPS survey spectra of samples deposited at (a) 10 W (b) 25 W (c) 50 W and (d) 75 W

From these spectra, the atomic percentage of elements present at the surface was determined, and is shown in Table 4.7. Contaminants Na, N, Ca, Cl, S and Si are included for completeness, however the main point of interest is the percentage of carbon and oxygen present. As the power density was increased, the atomic concentration of carbon increased from ~78% to ~86%, and that of oxygen decreased from ~21% to ~13%. This is attributed to the increase in monomer fragmentation as the power density is increased, in agreement with the behaviour of other plasma deposited thin films in literature.

Table 4.7: Atomic percentage of PDLA thin films fabricated at various power densities

	10 W	**25 W**	**50 W**	**75 W**
Na	0.03	0.00	0.00	0.00
O	20.95	16.90	15.19	13.14
N	1.02	0.85	0.57	0.67
Ca	0.02	0.00	0.00	0.00
C	77.73	81.82	83.79	85.78
Cl	0.21	0.42	0.43	0.40
S	0.02	0.02	0.03	0.01
Si	0.03	0.00	0.02	0.00

To determine the functional groups present at the surface of the material, high resolution spectra of the C 1s peak were taken, the results of which are shown in Figure 4.21.

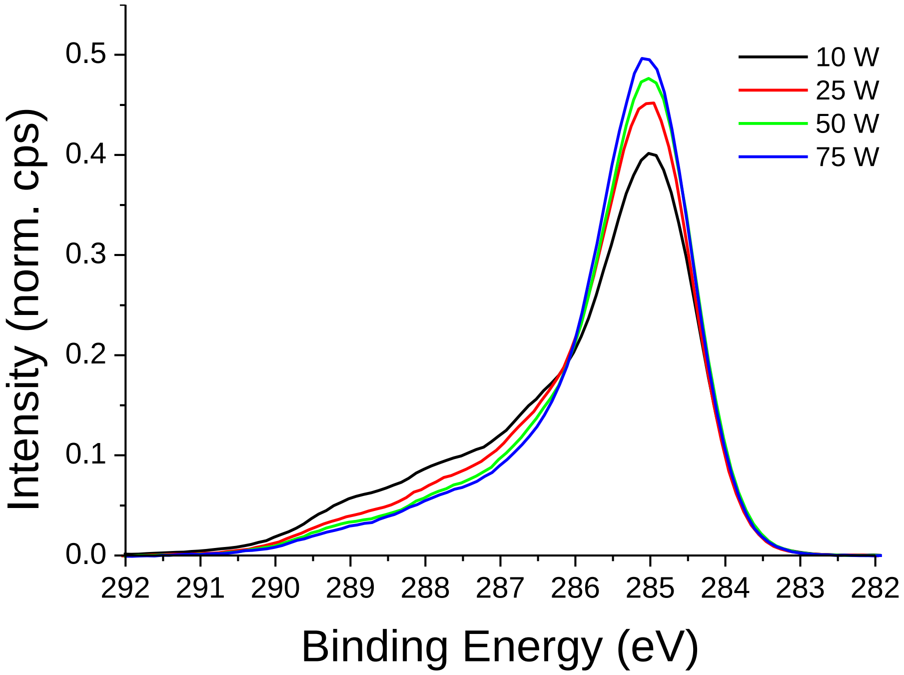

Figure 4.21: High resolution C 1s spectra

The C 1s peak consists of the superposition of multiple peaks, resulting from the multiple bonding environments in which carbon atoms participate in the organic thin films. The C 1s peak can be fitted to by several components in order to determine these bonding environments and further investigate the changes in the thin film properties as a function of power density.

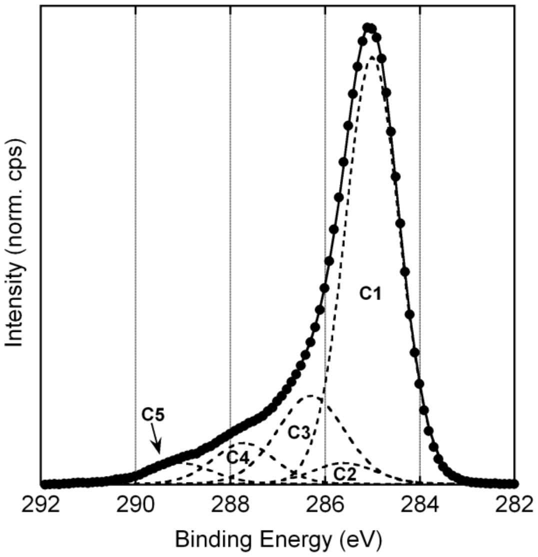

Figure 4.22: Component fitting to C 1s spectrum for sample deposited at 75 W

Figure 4.22 shows the result of fitting to the C 1s spectrum. As this figure is similar for samples deposited at all energies, only the fitting for a sample deposited at 75 W is shown. It was found that five components were present in the C 1s spectrum; C1 – CH_x; C2 – Secondary shift associated with O-C=O; C3 – C-O, C-N; C4 – (N)-C=O, O-C-O, and C5 – O-C=O (e.g. acid, ester). By far the peak associated with hydrocarbons (C1) was the most dominant, followed by C3, C4 and C5. While adventitious carbon may be present, its contribution to the measured C 1s spectrum should be minimal and hence the reported chemical functionality is attributed to the film chemistry. To compare differences between samples, the relative concentrations of each of these components relative to the total concentration of carbon were determined, and are presented in Table 4.8.

As power density was increased, the relative concentration of the hydrocarbon component increased from 0.603 to 0.690, while all other (oxygen containing) components decreased in magnitude. The C5 component is of interest due to the presence of the acetate ester in the monomer; the C5 groups at the surface of the material decreased as the power density was increased, which when coupled with the increase of hydrocarbon content is indicative of a further degree of fragmentation of the monomer units, consistent with deposition in the monomer sufficient deposition regime.

Table 4.8: Concentration of component relative to total concentration of carbon

	10 W	**25 W**	**50 W**	**75 W**
C1 + C2	0.61	0.65	0.68	0.69
C3	0.23	0.22	0.21	0.19
C4	0.08	0.07	0.07	0.07
C5	0.09	0.07	0.05	0.05

4.5 Conclusions

The optical, morphological, tribological and chemical properties of PDLA thin films were studied. These properties form a set of fundamental characteristics for the material, and provided qualitative and quantitative knowledge which guided further experimentation, potential applications and aided in the understanding of other investigations.

The optical properties were determined across the UV-Vis spectrum, from 200 nm – 1000 nm as a function of thickness and power density. The material was found to be optically transparent, i.e. its absorbance and extinction coefficient tend to zero beyond wavelengths of approximately 600 nm, with the band edge at approximately 400 nm, corresponding to an optical band gap of 3 eV. The optical band gap was determined via analysis of the absorbance profile and production of Tauc plots, which indicated indirect allowed transition phenomena. A single absorbance peak was observed at low wavelengths in the UV region in both the absorbance and extinction coefficient profiles. No significant variations in absorbance profiles were observed with changes in the power density used. The highly reproducible value of the band gap of 3 eV, combined with the material's optical transparency make the film a promising candidate for optically sensitive and more generalised electronic applications as a transparent insulating layer.

The dispersive behaviour of all films was well described by Sellmeier coefficients and a single set of parameters was sufficient to model the observed data. The Sellmeier coefficients indicated the presence of a single absorption feature in the UV region, the magnitude of which was found to be nearly constant for all films. Variations in power density did result in very minor (less than 1%) changes in the refractive indices of the thin films, which was also reflected in the Sellmeier coefficients having slightly stronger magnitudes of the absorption feature at higher power densities. These variations were considered so small as to be negligible in all but the most optically sensitive applications and within experimental error bounds.

The analysis of AFM measurements confirmed the films were smooth, uniform and defect free. No evidence of crystallinity was observed and the films were found to be completely amorphous, with average surface roughness values of ~0.2 nm across the 1 μm^2 area investigated. These properties were found to be maintained when the input energy to the deposition was varied between 10 W and 75 W; no observable or measurable changes were induced in the topographical properties of the films with significant variation in the input power used. This behaviour is useful, as it allows the tuning of other, power sensitive properties, while maintaining desirable surface properties such as a smoothness and uniformity. The low value of roughness indicates that the material could be used as an interface layer, without introducing changes in subsequent layers as a result of morphological influences.

In contrast to this, investigations of the tribological properties of the material via nano-indentation revealed a much more significant dependence of the hardness on the power density. Higher values of RF power were found to produce harder films. A variation of approximately 30% in hardness was observed in the range of power values examined. The material's hardness is therefore a tuneable parameter, which may be directly controlled via the deposition parameters to provide films with application optimised properties. For example, if the material is to form an external layer, it may be desirable that it is harder and more resistant to mechanical wear, and higher power densities could be used to produce harder films. If the material were to be used as an interfacial or sacrificial layer, it may be useful for it to be softer, and as the morphological properties are not modified, a lower power level could be used to produce softer films with desirable surface properties without affecting the above layers.

FTIR measurements showed the material to consist predominately of hydrocarbon functionalities, in addition to hydroxyl and ketone functional groups. Bulk chemical functionality was not significantly influenced by the input energy within the range of RF fabrication powers investigated in FTIR measurements, however XPS measurements showed an increase in the hydrocarbon content coupled with a decrease in oxygen content as power density was increased.

Table 4.9 provides a summary of the investigations and key results provided in this chapter. The optical properties of PDLA remain essentially constant with variation in power density, as does the optical band gap, morphological and chemical properties of the material. An important implication of this is that the rate of deposition, generally considered a direct function of power density, does not affect these properties. Optically and morphologically sensitive applications benefit greatly from this property, as large, uncontrollable changes in deposition parameters which may occur (particularly in plasma systems due to the non-uniformity of large scale fields) will not significantly affect the key performance requirements of the PDLA layers. It may also allow for optimisation of other, energy and growth rate dependent properties of the film, such as hardness, to be optimised for particular applications while maintaining the optical and topographical properties of the material. Harder films are likely desirable in all applications and higher power densities will likely be the most appropriate fabrication conditions for most uses of the thin films.

Given that the films are both optically transparent and smooth, they are appropriate for any layer within electronic or optical applications where optical transparency is required. The smoothness of the films means that subsequent layers can be deposited on them without the topography of the PDLA layer influencing their growth. The lack of pinholes is also highly desirable for electronic insulating applications where their presence may result in sporadic short circuits, high leakage currents and poor device performance. However, high thicknesses coupled with high dielectric constants result in interference from parasitic capacitances which are also undesirable. The ability to produce very thin films that are pinhole free (the results presented in Figure 4.16 were for films of 100 nm) is critical for electronic applications so that short circuits may be avoided and the effects of parasitic capacitance and interconnect interference reduced. Given the structure of the material and the general electrical behaviour of other plasma deposited thin films in the literature, it is expected that PDLA layers would be insulating, and from optical studies, an estimate of the high frequency dielectric constant of ~2.4 indicate the material is low permittivity. The material is therefore a candidate for insulting and dielectric barrier layers in electronic devices, however, more involved studies on the electronic properties of the material were necessary before this could be proved. Surface characteristics of the material also needed to be further quantified to ensure full compatibility with other organic electronic materials and processes currently in use. These studies were the focus of the investigations presented in Chapter 5 and Chapter 6.

Table 4.9: Summary of chapter results

Property investigated	Parameter	Remarks	Power dependence	Relationship
Optical	*n*	Dispersive, described by first order Sellmeier coefficient	Minimal	~1% increase in n as RF power was increased from 10 W to 75 W
	k	Optically transparent, single absorption feature in UV	None	-
	Absorbance	Optically transparent, single absorption feature in UV, optical band gap of ~3 eV	Minimal	~1% decrease in E_g with increase in RF power from 10 W to 75 W
Morphological	*Topology*	Smooth, uniform, pinhole and defect free	None	-
	R_a	~0.2 nm	None	-
Tribological	*Hardness*	~10^{-1} GPa	Strong	~30% increase in hardness from 0.30 GPa to 0.45 GPa as RF power was increased from 10 W to 75 W
Chemical	*Functional Groups*	Hydrocarbon with oxygen	Small	Increase in hydrocarbon and decrease in oxygen as power density increased

Chapter 5: Electrical Characterisations

5.1 Introduction

Before implementation in electronic devices and hardware, it was critical that an in depth understanding of PDLA's electrical properties be established. The most important of these properties are the dielectric constant and conductivity. The former provides a measure of the material's ability to store charge under an applied electric field and knowledge of this parameter guides the design of electrical devices such as capacitors, transistors and microelectronics. Conductivity provides a geometry independent relationship between an applied voltage and the resulting leakage current density, a critical design parameter. Furthermore, understanding the precise nature of these properties as a function of deposition conditions, applied field, frequency and temperature provides greater insight into the structural and chemical properties of the material of interest.

The electrical properties of PDLA thin films were investigated from dc to GHz frequencies. The principal motivation for this is that different frequency ranges probe different characteristics of the sample and provide more understanding of the material's properties, not just from the perspective of electromagnetic characterisations, but with regards to chemical, structural and physical properties as well. From a practical point of view, there are three frequency ranges of interest which are investigated in this chapter; the dc, ac and MW frequency ranges. In general, each frequency regime corresponds with a particular measurement and analysis technique. In the dc region, JV measurements were the principal technique utilised, while in the ac region, IS measurements were performed. At MW frequencies, resonant cavity techniques were used.

A material's conductivity is determined through analysis of its characteristic JV curves. As well as this, the mechanism of charge transport through the material can be understood, and from this the material's dielectric constant and/or carrier mobility found. By examining the point at which the material's conductivity sharply increases, the breakdown strength is measured. These properties are all necessary to understand the material’s usefulness as an insulating layer; the expected leakage current density through the material at an applied voltage and the limits of its operating range must be known so that proper design can be performed. The JV characteristics for devices formed from MIM structures where PDLA layers were used as the insulating layer are presented. Linalyl acetate layers were deposited using a range of thicknesses and power densities so that their influence on electrical properties could be determined. From analysis of the JV curves the mechanism of charge transport through the device was investigated and an estimate of the dielectric constant made.

Subsequent to the presentation and analysis of the dc properties, the results of IS measurements in the ac region are given. IS measures the impedance of a device across a range of frequencies, from which other parameters such as capacitance, loss and Q factor are derived. Combining these measurements with the device geometry, the complex dielectric function, $\varepsilon_c(\omega)$, of the insulating layer was derived. The real part of $\varepsilon_c(\omega)$ gives the relative permittivity or dielectric constant of the material, ε_r, and describes how a material stores charge under an applied electric field. This property determines the capacitive behaviour of the material and allows the classification of the material as low-, moderate- or high-κ. Low-κ materials (ε_r < ~3) are not optimum for charge storage and hence inappropriate for use in devices such as small-area capacitors. However, if their conductivity is sufficiently low, these materials are excellent candidates for insulators in electronic devices as their low dielectric constant results in comparatively lower capacitance, which in turn reduces parasitic capacitance, interlayer polarisation, and interference associated with these issues, allowing layers and wires to be fabricated closer together resulting in further miniaturization of devices [211, 212].

Permittivity is a frequency dependent property and it is important to know the range over which it can be expected to vary. Some materials may display high-κ characteristics in one frequency region and low-κ characteristics in another while others may maintain a relatively constant value of permittivity across the entire frequency spectrum. Knowledge of the complex permittivity over as wide of a frequency range as possible is therefore important in electronic applications of a material.

The imaginary part of $\varepsilon_c(\omega)$ gives information about a material's dielectric losses, ε_i. These losses may be induced by conduction losses in the material as well as relaxation losses and resonance effects [213-215]. From the perspective of electronics, the result is the divergence from ideal capacitive behaviour as a function of frequency; not all energy applied is stored as a result of loss and the phase angle of the capacitor is not exactly $-\pi/2$. The shape and location of peaks in $\varepsilon_i(\omega)$ provide information on the structural properties of materials. The location of peaks in $\varepsilon_i(\omega)$ due to dielectric relaxation is often temperature dependent, and to further understand the structural nature of the plasma deposited layers, IS measurements at several temperatures were performed and their results analysed.

At very high frequencies the dielectric function of the material remains of interest, however measurement of the device impedance becomes a practically difficult matter and techniques beyond IS must be used. Resonance cavity measurements are one such technique to determine the real and imaginary component of the dielectric function with a high level of accuracy in the microwave region (on the order of GHz) [216-218]. A disadvantage of this technique is that the frequency at which the dielectric measurement is performed is dependent on the physical construction of the resonant cavity and is hence a single, discrete value. While limited in terms of measurable frequencies, the technique remains powerful in its ability to determine ε_∞ and $\tan\delta$ with a high degree of accuracy at high frequencies, providing confirmation of other properties measured or extracted from lower frequency ranges.

In this chapter, the electrical properties of PDLA thin films are presented. The results of this chapter were then used as the basis of further investigations into the dependence of these properties on deposition conditions, applied field, frequency and temperature. These results provide a means of optimising the deposition conditions for application specific outcomes. Interpretation of this data also provided a deeper understanding of the material’s structure through analysis of temperature dependent dielectric relaxation features. Furthermore, the results presented were used to further examine potential applications to which the material is best suited.

5.2 JV Analysis

5.2.1 Theory and Methods

When investigating charge transport in an insulating thin film, three mechanisms are typically discussed in the literature. These are Richardson-Schottky (RS) transport, Poole-Frenkel (PF) transport and Space Charge Limited Conduction (SCLC) [219, 220]. RS and PF conduction are similar in their behaviour and description, due to their dependence on lowering of potential barriers, however they differ in the mechanism of charge transport [221]; RS is a barrier limited effect while PF describes a bulk limited effect [221]. In RS conduction, a potential barrier is formed at the metal-insulator interface due to the energy level misalignment of the metallic electrode and insulating thin film [222]. Application of a field results in the lowering of this potential barrier through the interaction of the applied field with the electrode image force [221]. PF conduction on the other hand is the lowering of the trap barrier in the bulk of an insulator [221, 223].

Functionally, both mechanisms result in an increase of current density after a potential barrier has been overcome, and are described by the equation [222]:

$$J = J_0 \exp\left(\frac{\beta V^{1/2}}{k_B T d^{1/2}} \right) \tag{5.1}$$

where J is the current density, J_0 the low-field current density, V the applied voltage, k_B is Boltzmann's constant in eV K^{-1}, T is temperature in K, and d the thickness of the sample. The parameter β is the field-lowering coefficient (with units of eV $m^{1/2}$ $V^{-1/2}$) and is dependent on whether RS or PF conduction is present [223]:

$$2\beta_{RS} = \beta_{PF} = \left(\frac{q^3}{\pi \varepsilon_0 \varepsilon_r} \right)^{\frac{1}{2}} \tag{5.2}$$

where β_{RS} is the RS field-lowering coefficient, β_{PF} is the PF field-lowering coefficient, q the charge of an electron, ε_0 the permittivity of free space and ε_r the dielectric constant of the material. The high frequency dielectric constant, ε_∞, is used as the electrons are only near the potential barriers for a short time [220]. As PF and RS mechanisms are well defined theoretically, measured JV curves can be readily examined qualitatively for agreement with (5.1) by plotting the natural logarithm of J against the square root of the applied field. In the case that this results in a linear plot, RS and PF can be differentiated by determining the value of the field-lowering coefficient, β [221]. From (5.1), the slope, *m*, of ln (J) vs $V^{1/2}$ will be equal to:

$$m = \frac{\beta_{\exp}}{k_B T d^{1/2}} \tag{5.3}$$

where $\beta_{\exp}$ is the experimentally derived field-lowering coefficient. If ε_∞ is known, theoretical values of β_{RS} and β_{PF} can be calculated and compared with $\beta_{\exp}$. The value of β which gives the best agreement with $\beta_{\exp}$ then determines whether RS or PF conduction is responsible for charge transport through the material [220-222].

The final mechanism which may typically govern charge transport through an insulator is SCLC. In SCLC, carriers are injected into the cathode at a rate greater than they can be transported through the insulating layer, resulting in an excess carrier density at the metal-insulator interface and formation of a space charge region [220, 224]. As the bulk properties of the insulator are the limiting factor in charge transport, the current density through the MIM device is given by the Mott-Gurney law [224]:

$$J = \frac{9}{8} \varepsilon_r \mu \frac{V^2}{d^3} \tag{5.4}$$

where μ is the carrier mobility, V the applied voltage and d the film thickness. As transport through the film is bulk limited, the current density is a function of the insulating material's mobility, dielectric constant, and thickness, and should exhibit a quadratic dependence on the applied voltage. The latter two properties result in two ways to check whether SCLC is present. If multiple devices of otherwise identical properties are fabricated, and the thickness of the insulating layer is varied, a thickness dependence conductivity should be observed [224, 225]. Secondly, plotting ln (J) as a function of ln (V) would result in a linear curve, with a gradient of 2. To determine whether SCLC is present in a device, analysis of log-log plots from devices fabricated with insulating layers of several thicknesses should be performed. If these conditions are satisfied for a known device geometry and ε_r is known from other measurements, the carrier mobility μ of the material can be determined by fitting of (5.4) to experimental data.

All JV measurements were performed using a Keithley 2636A source meter on MIM structures using PDLA layers as the insulating layer with Al electrodes. Measurements were taken between 0 V and 200 V and 200 data points used, with a step size of ~1 V. The voltage was applied as a staircase function, where each level was held for 50 ms / point. Due to fact that the MIM structures are capacitive, care was taken to ensure the true leakage current was measured, as application of a voltage step to the structure results in high initial charging current. To overcome this, several measurements at each voltage level were performed so that the current transient associated with each step change in voltage was recorded. The leakage current was taken as the final point of each transient to produce the IV data. The measured current was then divided by the area of the MIM structure to obtain the current density. The two-probe measurement technique was used in initial testing and the resistivity of the samples was found to be high (~GΩ) while the resistance of the experimental apparatus was found to be very small (~Ω). Separation of the contact and spreading resistances were hence unnecessary to obtain accurate measurements of the sample resistivity and four-probe techniques were not required.

5.2.2 Determination of the dc Electrical Properties

Measurements were performed on films deposited at energy levels of 10 W, 25 W, 50 W and 75 W to determine whether electrical properties were subject to variation due to changes in the control parameter. As well, the JV curves of films deposited at 75 W for several deposition times were examined, to determine the thickness dependence of the electrical properties.

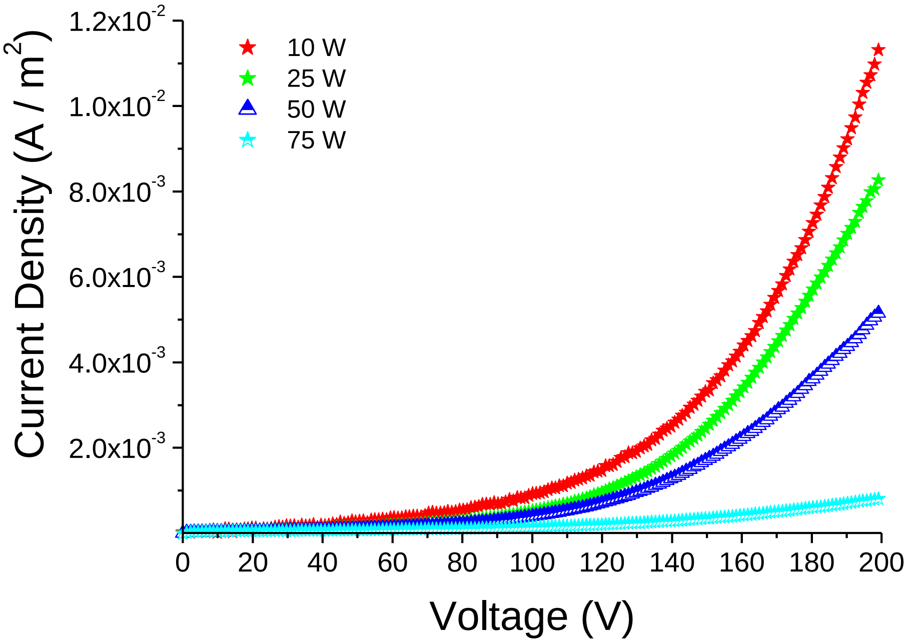

Figure 5.1: JV curves of PDLA thin films fabricated at various power densities

The JV curves for 10 W, 25 W, 50 W and 75 W samples deposited for 60 minutes to form the insulating layer in Al MIM devices are presented in Figure 5.1. The current density was field dependent and shows the beginning of a sharp increase with applied fields above approximately 80 V, though whether this dependence is quadratic or exponential is unclear. Over the range of applied field, the current density increased by approximately three orders of magnitude.

The dc conductivity, σ_{dc}, of the films was determined from the measured voltage, current and device geometry by:

$$\sigma_{dc} = \frac{Jd}{V} \tag{5.5}$$

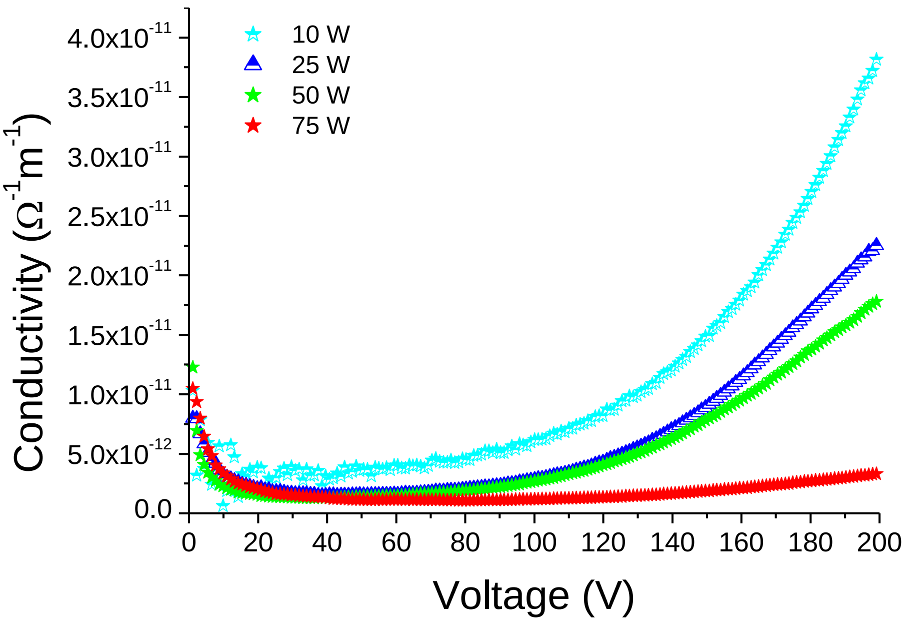

Figure 5.2: Conductivity of PDLA thin films fabricated at various power densities

where J is the current density, d the film thickness and V the applied voltage. Figure 5.2 shows that σ_{dc} was also field dependent, however given the overall magnitude of the values considered (~10^{-11} Ω^{-1} m^{-1}), the variation was small. The maximum value of σ_{dc} occurred at the highest applied voltage of 200 V for all films and was on the order of $10^{-12} – 10^{-11}$ Ω^{-1} m^{-1}. A strong correlation between samples deposited at higher power densities and lower values of σ_{dc} was observed; there was an order of magnitude decrease in conductivity between the 10 W and 75 W samples. There is a 200 nm difference in the thickness between these two samples as well, due to the difference in growth rates at higher power densities. As the conduction mechanism was not known, the variation in σ_{dc} could not be solely attributed to structural changes induced by the increased power density; if SCLC were present, from the form of (5.4), thickness dependent conductivity is an expected result.

The value of σ_{dc} was very low, even compared with other amorphous, plasma deposited insulators such as plasma deposited thiophenes, which are on the order of 10^{-4} – 10^{-8} Ω^{-1} m^{-1}, and plasma deposited polyanilines on the order of 10^{-6} – 10^{-8} Ω^{-1} m^{-1} [29, 226]. In the case of electronic devices utilising PDLA dielectric layers, leakage currents through the material would be comparatively lower than many other polymer interlayer alternatives for a given geometry.

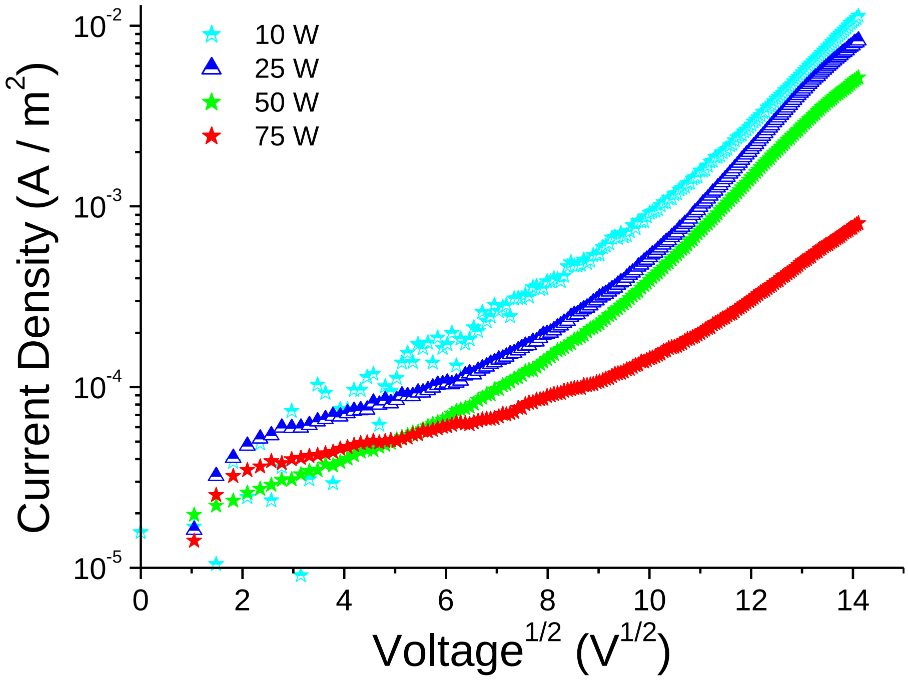

Figure 5.3: PF plot of experimental data

Figure 5.3 shows the same data as Figure 5.1, replotted on a semilog scale as a function of the square root of applied voltage. Due to the form of (5.1), a linear relationship between ln (J) and $V^{1/2}$ would imply the presence of either PF or RS transport. Figure 5.3 shows two distinct regions of linearity in the PF plot; a low field region below $V \approx 36$ V and a transition to a high field region above $V \approx 64$ V. This is indicative that multiple regimes of charge transport were present in the material. While linearity exists on the PF plot, based solely on Figure 5.3 it is difficult to state conclusively whether PF or RS mechanisms were dominating charge transport due to the presence of multiple regimes. A log-log plot of the experimental data was examined to determine whether SCLC better described the current-voltage relationship. Two regions of linearity were also present in the SCLC plot shown in Figure 5.4, at roughly the same voltage cut-offs as described for Figure 5.3.

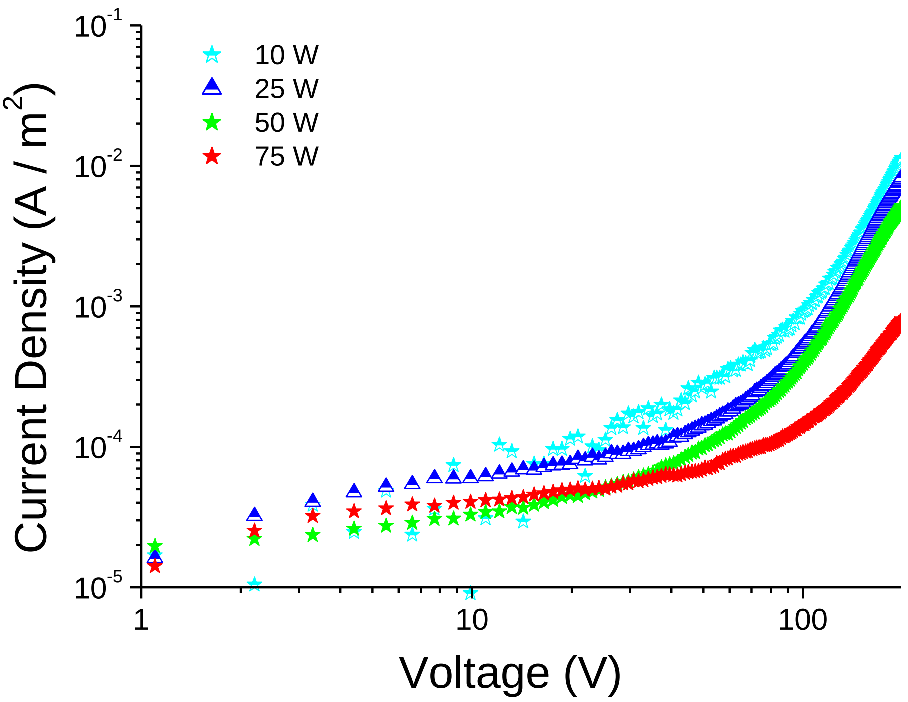

Figure 5.4: Log-log plot of experimental data

The low-field region in both plots is likely due to Ohmic conduction, i.e. [214]:

$$J_\Omega = \mu n_o q \frac{V}{d} \tag{5.6}$$

where J_Ω is the Ohmic current density, n_o the carrier concentration and q the electron charge. Ohmic conduction describes injection of carriers through the bulk of the material, limited only by the device geometry and number of carriers available for transport and the material mobility. In this region electrode and potential barrier effects have not yet begun to dominate charge transport through the device.

Simple qualitative analysis of both the PF and SCLC plots of the JV data was not sufficient to determine the nature of charge transport through the device; there was no clear and single region of linearity across the range of applied voltage and both plots show sections of linearity. Further analysis of both PF/RS and SCLC mechanisms was performed to assist in the characterisation of the material.

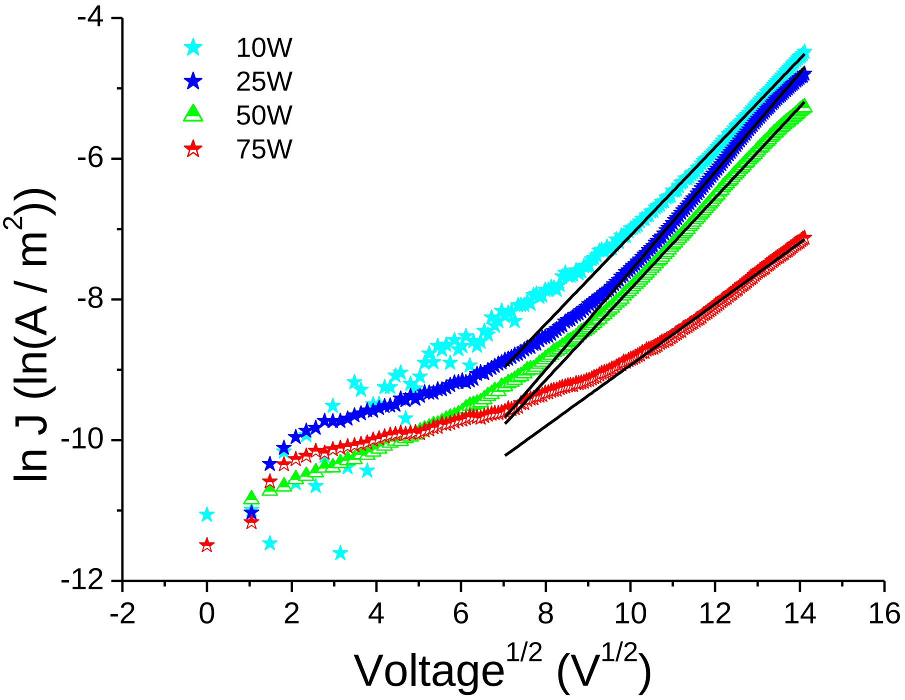

Figure 5.5: PF fit to high field region

Figure 5.5 shows the result of a linear fit to ln (J) vs $V^{1/2}$ applied in the region of $V^{1/2} > 10$ V. In this region a linear fit (in the form of (5.1)) described the JV characteristics well, with R^2 values typically greater than 0.99. From this fitting and (5.3), the β_{exp} values for the samples were determined and are summarised in Table 5.1. The theoretical value of β was derived from the value of ε_∞ found from VASE measurements, which may contribute to the discrepancy between the theoretical and experimental values observed. The values of β_{exp} for all samples are approximately equal at 1.3×10^{-5}, and only the 75 W sample was slightly lower, at 1×10^{-5}. These values were in best agreement with the theoretical β_{RS} of 2.45×10^{-5} rather than the β_{PF} value of 4.90×10^{-5}, indicative that from the context of a field activated mechanism, RS transport was prevalent.

An implication of the similar β_{exp} values for all samples is that, due to its relationship to ε_∞, the relative permittivity was similar for all samples, regardless of power density used. This was in agreement with the behaviour of the relative permittivity estimated from VASE measurements discussed in Chapter 4.

Table 5.1: Theoretical and experimental β values (eV $m^{1/2}$ $V^{-1/2}$) from JV measurements

Power	β_{RS}	β_{PF}	β_{exp}
10	2.45×10^{-5}	4.90×10^{-5}	1.317×10^{-5}
25			1.325×10^{-5}
50			1.374×10^{-5}
75			1.000×10^{-5}

If electrode limited transport were the only mechanism present there should not be a dependence of conductivity (and hence current density) on the thickness of the insulating layer in the device. To confirm that RS conduction dominated, samples were fabricated with insulating layers deposited using 75 W input energy and three different thicknesses, and the leakage current through these devices measured as a function of applied field.

Figure 5.6 shows a dependence of the measured current density on the thickness of the sample, for devices fabricated under otherwise identical deposition conditions. It would appear that carrier transport was a bulk limited process. However, the log-log plot of the measured data, as shown in Figure 5.4 is not linear across the entire range, and in the linear regions, the slope present is greater than 2. From (5.4), and the quadratic dependence of J on V, it is expected that this would be the case when SCLC is present. Despite this, the thickness dependence of conductivity could not be adequately explained by either RS or PF mechanisms and space charge effects must have been present to limit the overall current density through the devices.

Figure 5.6 also illustrates the breakdown behaviour of the material. The source meter used was set to limit the current to 100 μA; the transition from the continuous behaviour to the constant value of 20 A m^{-2} shows occurrence of electrical breakdown, where current through the insulator was limited only by the source meter.

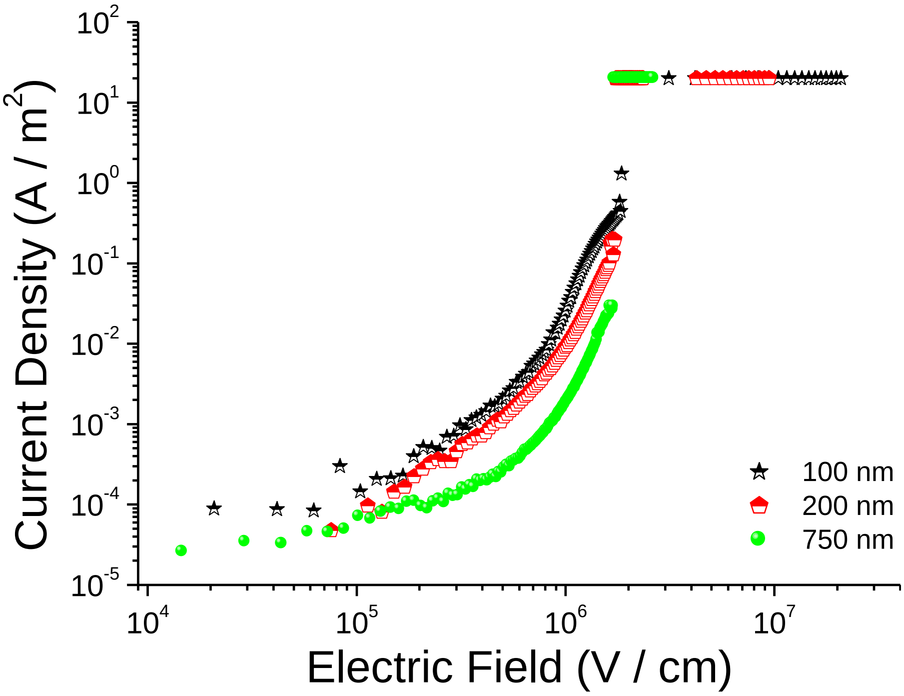

Figure 5.6: Current density versus applied field for different insulator thicknesses

For samples of all thicknesses, the field at which breakdown occurred, F_b was approximately 1.8 MV cm^{-1} and was independent of film thickness. The value of 1.8 MV cm^{-1} is comparable to plasma deposited polypyrrole, which has a reported value of 1.5 MV cm^{-1} [52], and similar to octafluorocylcobutane fabricated in the low pressure regime from a monomer injected into the system upstream from the plasma field which has a reported value of 2 ± 0.5 MV cm^{-1} [227]. The loss tangent of PDLA films is lower than both of these materials and its dielectric constant lies roughly between the two. The minimum field for low-κ dielectrics has been identified as 1 MV cm^{-1} [58], which was met by the PDLA thin films. The F_b of plasma deposited benzene thin films could be nearly doubled through adjustment of deposition parameters such as monomer inlet location, deposition rate and deposition pressure and it is likely that F_b of PDLA layers could be increased through further optimisation of deposition procedures for this particular variable [227].

An additional possibility is the presence of SCLC with trapping effects (TSCLC) due to imperfections in the insulator structure. Giving consideration to the expected highly fragmented, randomly terminated, radical rich structure of PECVD thin films, the manifestation of trapping effects in JV characteristics could be reasonably expected. TSCLC is characterised by three distinct regions of JV dependence as shown in Figure 5.7. The JV characteristic of devices dominated by TSCLC will fall within a triangle formed by three regimes of operation [214, 228]. These regimes are the Ohmic regime, as described by (5.6), which is active in the low field region and forms the lower edge of the triangle. In this region, conduction is limited by trapping effects. When the trapping sites have been filled, there is an inrush of carriers and a sharp rise in current with a small increase in applied field. This is known as the Traps Filled Limit (TFL) region, and forms the right edge of the triangle. This edge is vertical at the extreme limit, and is characterised by a region of the JV curve with a slope greater than 2 on a log-log plot. The TFL current density is given by [214, 228]:

$$J = \mu N_V \left(\frac{\varepsilon_r \varepsilon_0}{N_t} \right) \frac{V^{L+1}}{d^{2L+1}} \tag{5.7}$$

where N_V is the density of states (DOS) at the HOMO, N_t the density of traps and L a parameter related to the slope of the curve. After the sharp increase of current following the filling of trap sites, space charge begins to form and limit bulk conduction, and the JV curve approaches the limit of SCLC in the high field region. This is in the form of (5.4), and extrapolation of this behaviour into the low-field region forms the hypotenuse of the triangle. Figure 5.4 and Figure 5.6 show measurements which fall inside such a triangle in all cases. In Figure 5.4 sufficient field has not been reached to reach SCLC and hence no region of the curve has the expected slope of 2.

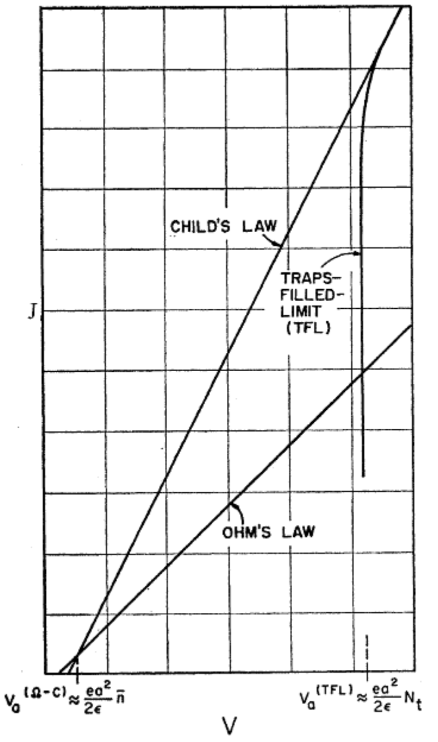

Figure 5.7: TSCLC regimes [228]

In Figure 5.6 it is seen that when significantly high fields were applied, dielectric breakdown occurred prior to the formation of a space charge and manifestation of SCLC effects. This is not uncommon for materials which display this behaviour [214]. By extrapolating the SCLC section of the curve to the low field region, and finding the intersection with the Ohmic region, the carrier concentration can be determined. Due to the large number of assumptions required to verify TSCLC conduction, and the fact that no true trap free SCLC region was identifiable in the JV data, it was impossible to definitively determine whether TSCLC was the mechanism responsible for charge transport. Due to this, no detailed analysis regarding TSCLC (e.g. extraction of mobility) was undertaken. RS conduction gave the best agreement with theoretical models and was assumed to be the dominant mechanism, though due to the observation of thickness dependent conductivity, it is believed that space-charge effects were also present.

5.3 AC Analysis

5.3.1 IS Measurements

5.3.1.1 Theory and Methods

The Hioki 3522 LCR meter used for measurements is capable of measuring multiple impedance parameters. In these investigations, the magnitude and phase of the impedance, loss factor (tan δ) and equivalent series and parallel capacitances were measured. The series and parallel capacitances gave identical values in these investigations and are denoted as the parameter C. From C and knowledge of the MIM structure's geometry, it was possible to determine the real part of the permittivity of the material as a function of the measured frequencies using the relationship:

$$\varepsilon_r(\omega) = \frac{dC}{\varepsilon_o A} \tag{5.8}$$

where d and A are the thickness and cross-sectional area of the MIM structure, C the measured capacitance and ε_o the permittivity of free space. Knowing $\varepsilon_r(\omega)$ and tan δ it was possible to determine the imaginary part of the permittivity as a function of frequency:

$$\frac{\omega\varepsilon_i(\omega) + \sigma(\omega)}{\omega\varepsilon_r(\omega)} = \tan\delta \tag{5.9}$$

where ω is the frequency in rad s^{-1} and σ(ω) is the conductivity of the sample. As can be seen in Figure 5.2, the dc conductivity of the samples was very low. The ac conductivity of the samples as a function of frequency was determined from the measured impedance and device geometry:

$$\sigma(\omega) = \frac{\Re e\{Y\}d}{A} = \frac{d\cos\theta \big/ |Z|}{A} \tag{5.10}$$

where Y is the device admittance and θ the phase angle of the device impedance.

5.3.1.2 Measurements under Ambient Conditions

IS measurements were performed on samples deposited at 10 W, 25 W, 50 W and 75 W for 30 minutes, forming the insulating layer in MIM structures. The ac conductivity determined from measurements and (5.10) is shown in Figure 5.8, where the low frequency conductivity of ~10^{-11} Ω^{-1} m^{-1} was in good agreement with the low field region of the dc conductivity shown in Figure 5.2. As frequency reached the upper limit of the measured range at 100 kHz, the ac conductivity remained small, at less than 10^{-6} Ω^{-1} m^{-1}.

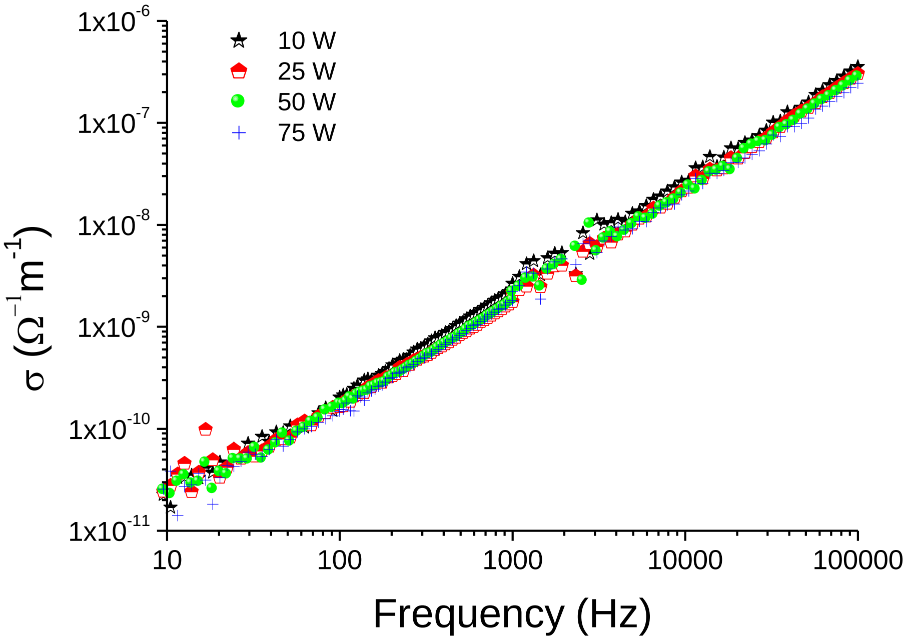

Figure 5.8: AC conductivity from ambient IS measurements

Rearrangement of (5.9) to isolate $\varepsilon_i(\omega)$ results in:

$$\varepsilon_i(\omega) = \frac{\omega\varepsilon_r(\omega)\tan\delta - \sigma(\omega)}{\omega} \tag{5.11}$$

The effect of low conductivities in (5.11) is entirely negligible, and hence it can be simplified to:

$$\varepsilon_i(\omega) = \varepsilon_r(\omega)\tan\delta \tag{5.12}$$

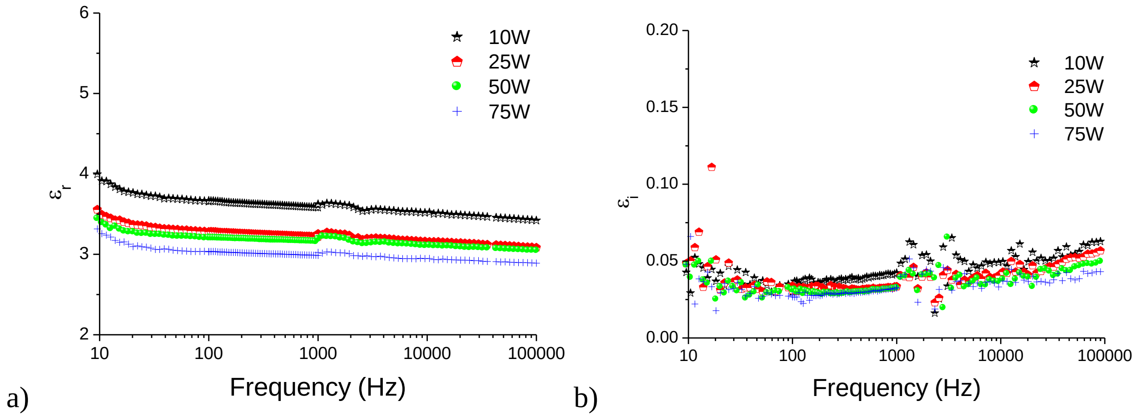

Figure 5.9: (a) Real and (b) Imaginary part of the complex permittivity of samples deposited at various RF powers

Figure 5.9 shows the complex permittivity of four samples taken under ambient conditions. Noise in the measurement in both the real and imaginary parts was due to the instrument automatically adjusting its measurement range and unfortunately could not be controlled. The measured loss tangent is related to the measured impedance phase angle, which in the region of high noise varied by less than 1°, and put the device at the limits of its phase resolution. Both of these factors contributed to high levels of noise, particularly in the loss tangent, which influenced the imaginary part of the permittivity shown in Figure 5.9.

All samples had approximately the same frequency dependence of the dielectric constant and there was a small variation in value depending on the fabrication power used. The behaviour correlates well with data from Section 5.2, where β_{exp}, proportional to the material’s dielectric constant, was found to be constant for samples fabricated with the different input RF powers. In the low frequency region, the higher dielectric constant has been previously reported for other plasma deposited thin films [51, 52]. This effect is attributed to interfacial phenomena at the metal/insulator interfaces such as the formation of depletion regions and interfacial polarisations, due to inefficiency of charge migration through the interface under applied electric field [52, 229, 230]. At higher frequencies however, interfacial phenomena become less dominant, and the measured capacitance approaches the bulk, or insulator capacitance [229]. In this region, the dielectric constant for all samples remained steadily decreasing. The dielectric constant is composed of contributions from electronic, ionic and orientational polarisations, i.e.:

$$\varepsilon_r = \varepsilon_{electronic} + \varepsilon_{ionic} + \varepsilon_{orientational} \tag{5.13}$$

Considering the refractive index at optical frequencies where only electronic phenomena contribute to the dielectric constant [227], we obtain:

$$\varepsilon_{electronic} = n^2 \tag{5.14}$$

From the optical data, the refractive index at an optical frequency of 700 nm is approximately 1.55, resulting in $\varepsilon_{electronic}$ of 2.4. Hence, electronic phenomena contribute to approximately 70 - 80% of the determined dielectric constant at frequencies greater than 10 Hz. The remaining contributions were therefore from ionic and orientational phenomena in the bulk of the plasma deposited thin film. These contributions were low due to the large amount of crosslinking induced by the plasma deposition process which resulted in a lack of molecular mobility, and the low ionic polarisation of molecular structures present in the bulk of the material [227]. It is also thought that increased molecular mobility available in samples deposited at lower input energies due to a decrease in crosslinking may explain the higher dielectric constant of these samples. The contribution of ε_{ionic} and $\varepsilon_{orientational}$ in PDLA thin films is slightly larger than those reported for other PECVD thin films [227].

Figure 5.9b presents $\varepsilon_i(\omega)$ across the measured frequency spectrum. All samples showed similar behaviour, reaching a minimum value at approximately 100 Hz before beginning to increase again. In the measured spectrum, no signs of α- or β-relaxation peaks were evident. Both the magnitude and characteristics of the loss values as a function of frequency are similar to other plasma deposited thin films [49, 51], though PDLA films generally had losses lower than these ($\tan \delta < 2 \times 10^{-2}$) across the measured frequency spectrum. Given the relatively low measurement temperature, it is likely that relaxation peaks existed outside the measured frequency range. The minimum in Figure 5.9b is indicative of relaxation peaks at higher or lower frequencies. To investigate this, impedance spectroscopy measurements were carried out at 323 K, 333 K, 343 K and 348 K on samples fabricated at 75 W. Only samples fabricated at one power level were investigated due to the similarity in the dielectric characteristics of samples deposited at different energies as presented in Figure 5.9.

5.3.1.3 Measurements as a Function of Temperature

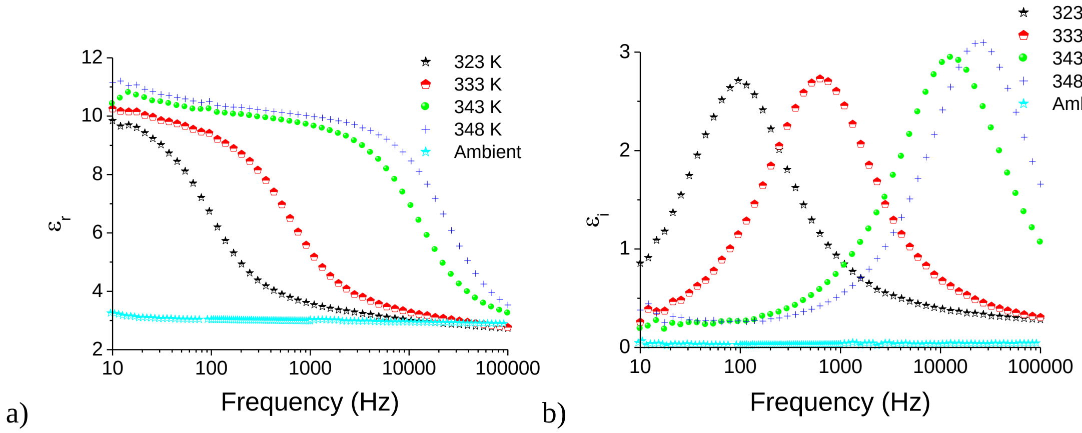

Figure 5.10: (a) Real and (b) Imaginary part of the complex permittivity of samples deposited at 75 W, measured at varying temperatures

The maximum temperature investigated was 348 K as the conducting epoxy used to attach the electrodes to the devices began to breakdown shortly thereafter. Figure 5.10a shows the real part of the measured permittivity at four different temperatures, as well as the measured data under ambient conditions (T = 298 K). The imaginary part of the measured dielectric function at these temperatures is presented in Figure 5.10b. In contrast to the ambient temperature measurements, clear evidence of distinct relaxation features was visible in the measured data at all temperatures, shifting from lower to higher frequencies as temperature increased. The peaks are wide, indicating contributions from multiple relaxation times.

Typically, a material which has a single relaxation peak such as that observed in Figure 5.10b, is described by a characteristic Debye relaxation, as single peaks tend to exhibit a single characteristic relaxation time [217]. The complex dielectric function produced from a single Debye relaxation is given by [231]:

$$\varepsilon_c(\omega) = \frac{\varepsilon_s - \varepsilon_\infty}{1 + j\omega\tau_D} + \varepsilon_\infty \qquad (5.15)$$

where ε_s and ε_∞ are the low and high frequency dielectric constants respectively, j is the imaginary unit and τ_D is the characteristic Debye relaxation time. The relationship in (5.15) describes a symmetric relaxation peak centred on τ_D, which decays quickly to 0 at low and high frequencies, as shown in Figure 5.11.

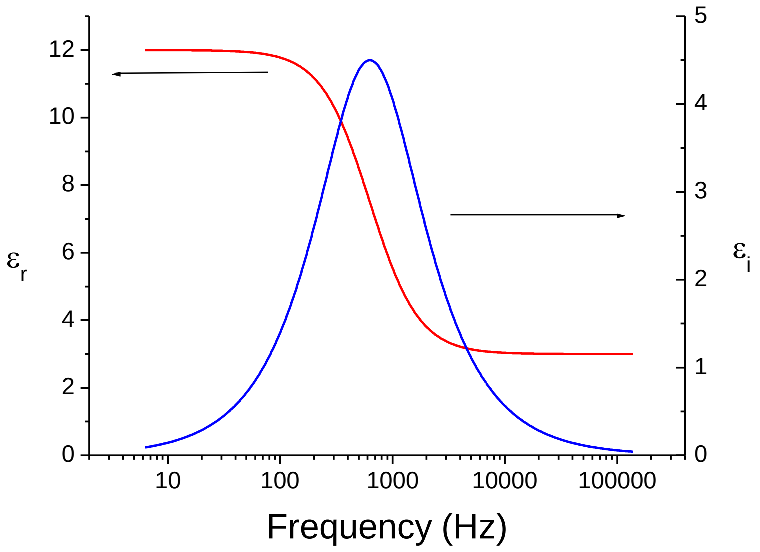

Figure 5.11: Complex dielectric function produced by a Debye relaxation

As the imaginary part decays to 0 at high and low frequencies, the real part reaches a constant value at low and high frequencies. These constants, which $\varepsilon_r(\omega)$ moves between, are defined by the parameters ε_s and ε_∞. The goal of analysis was to determine key parameters by fitting of theoretical models, such as (5.15), to the experimental data shown in Figure 5.10. It can be seen in Figure 5.10 that at low and high frequencies the loss had not decayed to zero and that the relative permittivity had not reached a constant value, but was slightly decreasing. Fitting of (5.15) to the experimental data resulted in a poor fit, as seen in Figure 5.12.

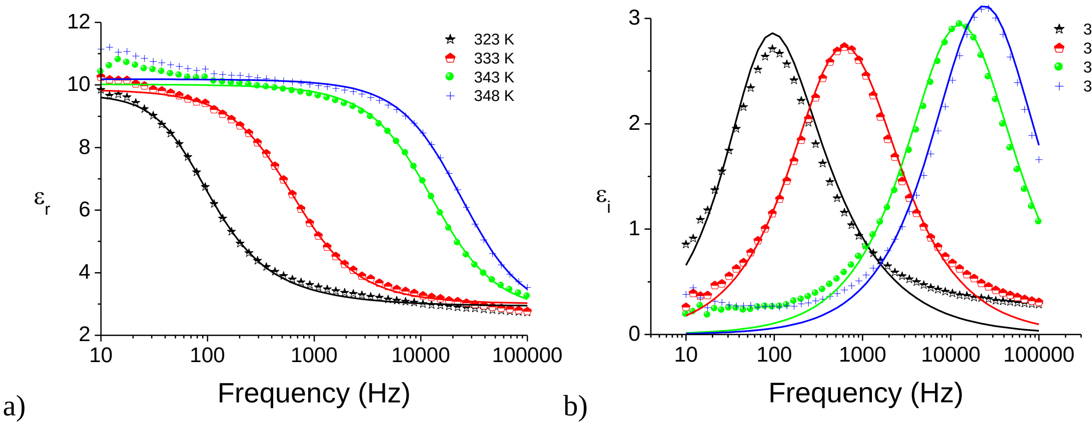

Figure 5.12: (a) Real and (b) Imaginary part of the complex permittivity (points) and fit using Debye relaxation model (lines)

As expected, the low and high frequency regions were described poorly by the Debye model, although the main peak was well described. This is indicative of a main, dominant relaxation feature, and it was expected several additional features distributed across lower and higher frequencies were needed to account for the losses in these regions. In a generalised case, the dielectric function of a material can be described by the weighted superposition of Debye relaxations [231]:

$$\frac{\varepsilon_c(\omega)-\varepsilon_\infty}{\varepsilon_s-\varepsilon_\infty}=\int_{-\infty}^{\infty}\frac{g(\tau)d\ln(\tau)}{1+j\omega\tau} \tag{5.16}$$

where g(τ) is a continuous function describing the distribution of relaxation times. Known distributions are often assumed for g(τ), such as the Hevriliak-Negami (HN), Cole-Cole (CC) and Davidson-Cole (DC) distributions [231]. In addition, the distribution could be composed of several of each of these, so long as the normalisation condition, defined by (5.17) is met [231]:

$$\int_{-\infty}^{\infty}g(\tau)d\tau=1 \tag{5.17}$$

The parameters defining the distributions can then be allowed to vary and the model fit to the experimental data. However, this method requires *a priori* knowledge or assumptions regarding the expected distribution of relaxation times if a fit of any quality or physical significance is to be obtained. If nothing about the distribution of relaxation times is known, as was the case in this work, it is arbitrary to assume a general form of g(τ). Instead, it would be better to determine the function g(τ) directly from the data itself, without presumption of any particular shape. Mathematically, determining g(τ) from (5.16) is a Fredholm integral equation of the first kind, which is an ill-posed problem [232]. Considering that $\varepsilon_c(\omega)$ is measured at a discrete set of frequencies, ω_n, where n = 1, 2, 3,..., N, (5.16) can be converted to a matrix equation:

$$\boldsymbol{\varepsilon} = A\mathbf{g} \tag{5.18}$$

where **ε** is a vector of N complex observations, ε_n, at each frequency ω_n, modified by constants ε_s and ε_∞ to reflect the left hand side (LHS) of (5.16), **g** is a vector of length M, where each element g_m is the value of the distribution function at some discrete relaxation time, τ_m, taken from the vector **τ** where m = 1, 2, 3, ..., M. The elements of **τ** are logarithmically spaced such that the difference between consecutive values is a constant, denoted by $\Delta_{\ln(\tau)}$. Finally, *A* is a kernel matrix which acts on **g** to produce the behaviour defined in (5.16), where each element is given by:

$$A_{nm} = \frac{\Delta_{\ln(\tau)}}{1 + j\omega_n \tau_m} \tag{5.19}$$

The goal is to determine the value of **g** from the kernel matrix *A* and the observations **ε**. However, two problems arise; first, **ε** will always contain some contribution from measurement noise, $\varepsilon_{\delta n}$, and deviate from the true value by some small amount [233]. Secondly, examining *A*, while the length of **ω** is determined from the number of experimentally measured points, the length of **τ** is completely arbitrary – there can be as many or as few relaxation times as desired. Thus (5.18) is an ill-defined system, and due to the nature of *A*, small deviations in **ε** (such as those from $\varepsilon_{\delta n}$) will cause large variations in **g** if least squares or matrix inversion methods are used to obtain a solution [232, 233].

Consider the case where a known HN distribution has been used to create a complex dielectric spectrum. Using this spectrum as the experimental data, **ε**, the generating distribution function g(τ) can be obtained from matrix inversion methods. No noise or error has been added to the observation vector. The generating distribution function and subsequent solution are shown in Figure 5.13.

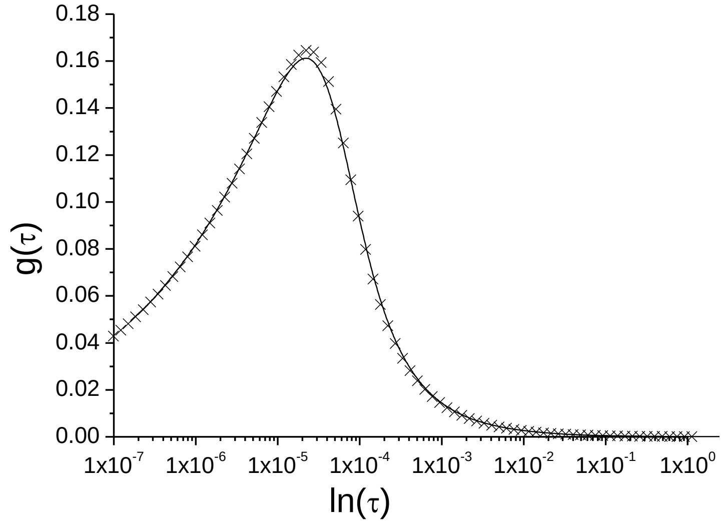

Figure 5.13: Generating distribution function (crosses) and solution (line) with no noise

The solution provides a good estimate to the function that generated it. However, if a small amount of randomly distributed noise is added to the generated complex dielectric function prior to solving for g(τ), the solution quickly deteriorates:

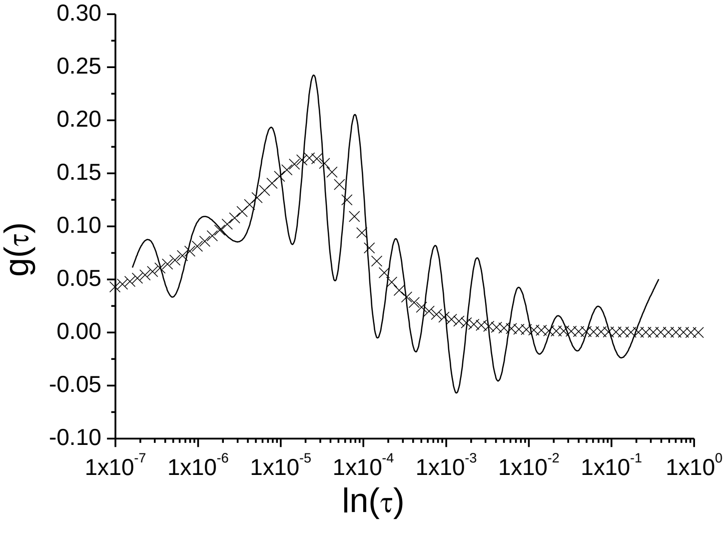

Figure 5.14: Generating distribution function (crosses) and solution (line) with noise added

The same solution method, while yielding a good fit to the experimental data, produces a meaningless result for the distribution of relaxation times, and thus is not appropriate to apply to experimentally obtained data. Even were the result not as obviously inaccurate as that in Figure 5.14, it would still be impossible to know whether the solution obtained was correct, and whether features present were a result of the actual behaviour of the sample or due to the influence of noise in the measurement.

In order to obtain an approximate solution for **g** which only deviates slightly from the true distribution when obtained from a noisy measurement, regularisation methods must be used. In the case of spectroscopy problems, Tikhonov regularisation methods have been applied [232-234]. Considering the solution to (5.18) as a minimisation problem:

$$\Psi = \left\| \boldsymbol{\varepsilon} - A\mathbf{g} \right\|^2 = \min \tag{5.20}$$

where ‖ . ‖ is the standard 2-norm of a vector. Tikhonov regularisation introduces an extra term to (5.20) related to the norm of **g**:

$$\Psi = \left\| \boldsymbol{\varepsilon} - A\mathbf{g} \right\|^2 + \lambda \left\| L\mathbf{g} \right\|^2 = \min \tag{5.21}$$

where λ is the regularisation parameter and L is the Tikhonov matrix. L is often the identity matrix, but may also be a second order difference operator such that a smoother solution is forced [232, 234, 235]. In this work the identity matrix was used for L. Introduction of the second term forces a solution which minimises the residuals as well as the solution norm. This forces a solution which fits the experimental data well, but remains well behaved. The balance between the priority of these factors is determined by the regularisation parameter, where small λ will result in the solution approaching that of (5.20) and becoming more influenced by noise in the measurement, while large λ will result in an overly smooth solution with a very small norm, essentially approaching zero. Correct choice of the regularisation parameter is therefore important – very high values for this parameter will result in solutions which may have had critical features inadvertently removed, while too small λ may introduce features which begin to diverge from the true behaviour of g(τ). (5.21) can be solved directly to find the optimum solution, $\mathbf{g_{min}}$ as [235]:

$$\mathbf{g_{min}} = \left(A^H A + \lambda L^H L\right)^{-1} A^H \boldsymbol{\varepsilon} \qquad (5.22)$$

where H is the Hermitian transpose. There are several methods used to choose the value of λ, the most common of which is the L-curve method [235-238]. (5.21) is solved using a range of values for the regularisation parameter via (5.22), and the residual norm and solution norm recorded. A log-log plot of $\|\boldsymbol{\varepsilon} - A\mathbf{g}\|^2$ vs $\|L\mathbf{g}\|^2$ is then produced. When λ is very small, the solution of (5.21) approaches that of (5.20), and the residual norm is very low, while the solution norm is very high. As λ increases, the residual norm stays relatively constant for a period of time, while the solution norm decreases. Eventually a point is reached where the solution norm is not decreasing, however the value of the residual begins to increase. Thus, as λ moves from small through large values, a curve with the shape of an L is traced, the corner of which represents the optimal balance between the minimised residual and solution norms.

As an alternative to the L-curve method, ordinary cross validation can be used to estimate λ [235]. In this method, at some λ, $\mathbf{g_{minK}}$ is determined from (5.22), where the k^th^ element of **ε** has been removed. This value is then estimated from $\mathbf{A_K}$ x $\mathbf{g_{minK}}$, where $\mathbf{A_K}$ is the k^th^ row of *A*. This is carried out for all k, and the cross validation function defined as [235]:

$$V_o(\lambda) = \frac{1}{N}\sum_{k=1}^{N}\left\|\varepsilon_K - \mathbf{A_K}\mathbf{g_{minK}}\right\|^2 \qquad (5.23)$$

This function is then evaluated across a range of λ, and the value corresponding to the minimum of $V_o(\lambda)$ taken as the regularisation parameter. In order to determine the most appropriate method for selection of λ, simulated dielectric spectra were produced from known distributions g(τ), with uniformly distributed random noise of known magnitude added. L-curve and ordinary cross validation methods were used to determine the value of λ, then used to solve (5.21) for $\mathbf{g_{min}}$.

A known distribution function consisting of the superposition of several HN distributions was used to generate a complex dielectric function, and uniform random noise added to form a simulated measurement spectrum. The solution for $\mathbf{g}_{\mathbf{min}}$ was then determined via regularisation methods, using both L-curve and cross validation to determine the value of the regularisation parameter. The solution $\mathbf{g}_{\mathbf{min}}$ and the generated distribution were then compared to each other.

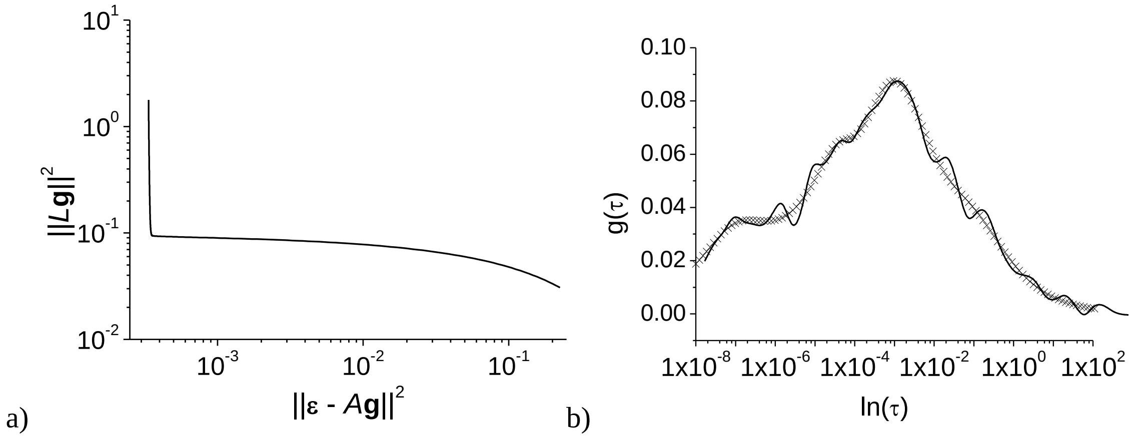

Figure 5.15: (a) Generated L-curve and (b) Resulting relaxation time distribution (line) compared to generating distribution (crosses)

Figure 5.15 shows the generated L-curve and solution for $g(\tau)$, $\mathbf{g}_{\mathbf{min}}$ when the L-curve method was used to determine λ. Despite a very clear and distinct point representing the optimal value of λ, Figure 5.15b demonstrates that in this case, the L-curve method resulted in a value of λ which was too low, and allowed a solution with many erroneous features, not present in the relaxation distribution used to generate the data.

Figure 5.16 shows the generated cross validation function and resulting solution utilising the value of λ determined from this method. Figure 5.16a shows a clear minimum in the function $V_o(\lambda)$, while Figure 5.16b shows very good agreement between the resulting solution, $\mathbf{g}_{\mathbf{min}}$ and the function originally used to generate the data. For several cases, this behaviour was repeated, where the L-curve method provided a value of λ which underestimated what was required to obtain the true solution, while the cross validation method produced consistent and accurate results. For this reason the cross validation method was chosen to determine the optimal value for regularisation parameter when applying the method to the actual experimental data, presented in Figure 5.10.

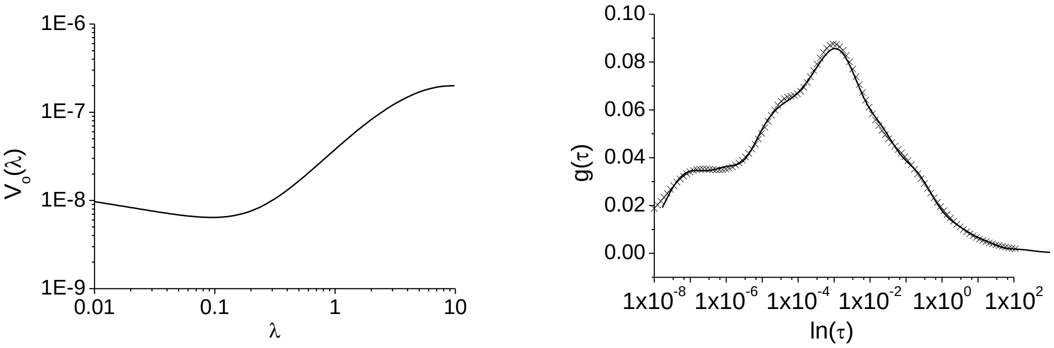

a) b)

Figure 5.16: (a) Generated $V_o(\lambda)$ and (b) Resulting relaxation time distribution (line) compared to generating distribution (crosses)

The relaxation time distribution function which was used to generate the testing data in this example is the worst-case scenario; there were several superimposed distribution functions, which had very close overlap. Such features are very difficult to distinguish from one another, however the cross validation method provided results which revealed the complex underlying distribution function and was suitable for application to the experimental data.

Prior to analysing the experimental data, one final step was added to the method to determine the optimal solution $\mathbf{g}_{\mathbf{min}}$ and the distribution of relaxation times of the material. The solution obtained from (5.22) does not necessarily satisfy the constraint implied in (5.17), i.e. the solution $\mathbf{g}_{\mathbf{min}}$ may not meet the normalisation criterion, and additionally, may include negative values which lack any physical meaning. To account for this, the overall method used is illustrated in Figure 5.17.

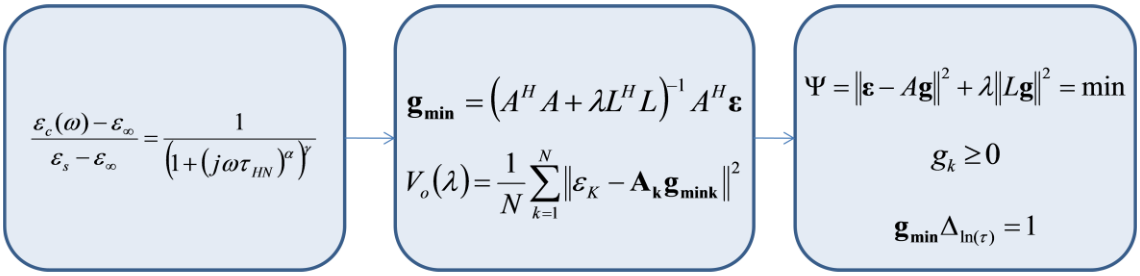

$$\frac{\varepsilon_c(\omega)-\varepsilon_\infty}{\varepsilon_s-\varepsilon_\infty}=\frac{1}{\left(1+(j\omega\tau_{HN})^{\alpha}\right)^{\gamma}}$$

$$\mathbf{g}_{\mathbf{min}}=\left(A^H A+\lambda L^H L\right)^{-1}A^H\boldsymbol{\varepsilon}$$

$$V_o(\lambda)=\frac{1}{N}\sum_{k=1}^{N}\left\|\varepsilon_K-\mathbf{A}_{\mathbf{k}}\mathbf{g}_{\mathbf{mink}}\right\|^2$$

$$\Psi=\|\boldsymbol{\varepsilon}-A\mathbf{g}\|^2+\lambda\|L\mathbf{g}\|^2=\min$$

$$g_k\geq 0$$

$$\mathbf{g}_{\mathbf{min}}\Delta_{\ln(\tau)}=1$$

Figure 5.17: Method to determine the distribution of relaxation times from experimental data

The method consisted of three stages:

1. The initial dielectric spectra is fitted assuming a HN distribution, to obtain an estimate for the parameters ε_s and ε_∞, which were required to generate the vector of observed spectra, **ε**, which was scaled by these parameters.
2. Using the measured data $\varepsilon_c(\omega)$ and the estimated parameters ε_s and ε_∞, **ε** was obtained and a solution to $\mathbf{g}_{\mathbf{min}}$ determined using (5.22) and the cross validation method.
3. Using the optimal value of λ and $\mathbf{g}_{\mathbf{min}}$ from stage 2) as a starting estimate, $\mathbf{g}_{\mathbf{min}}$ was again determined, this time from (5.21) using optimisation, subject to the constraints that the solution be normalised and positive.

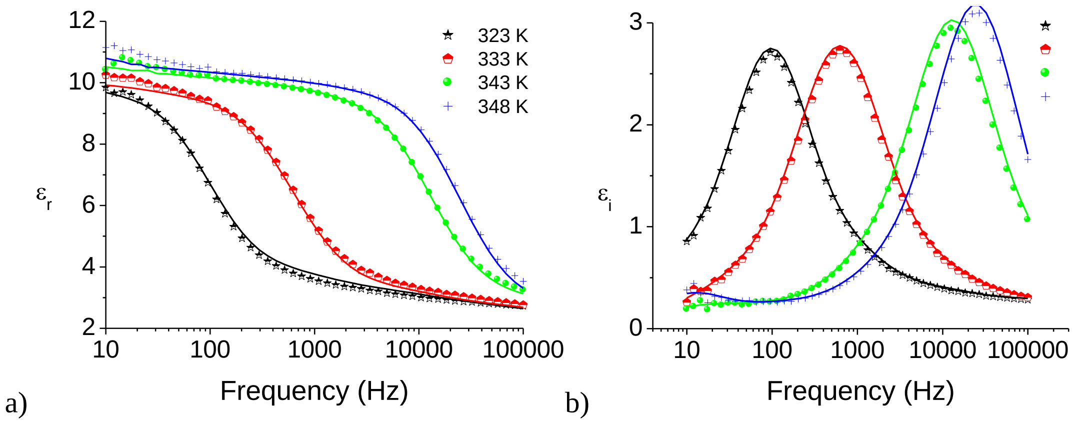

Figure 5.18: (a) Real and (b) Imaginary part of the complex permittivity (points) and fit using distribution of relaxation times (lines)

Figure 5.18 shows the real and imaginary components of the dielectric function generated from the determined distribution functions at the measured temperatures. Better agreement between experimental and modelled data was seen compared to when a single HN distribution was used as the underlying dielectric function as in Figure 5.12, particularly in the imaginary component of the data, where the issue of underestimating this data outside the range of the peak was no longer present. The most significant deviation of the model from the measured spectra occurred at low frequencies in the real part of the dielectric function. In this frequency range, the impedance of the device under test is became significant, reaching the limits of the measurement device. In addition, at lower frequencies the measurement error in the magnitude and phase of the LCR meter became larger. At these frequencies, due to the increased error in impedance due to the high impedance of the sample and higher measurement error, there was likely a larger amount of error in the measurement which produced this behaviour. Interfacial and polarisation effects, which were not modelled, may also have influenced the measured dielectric behaviour [49, 52].

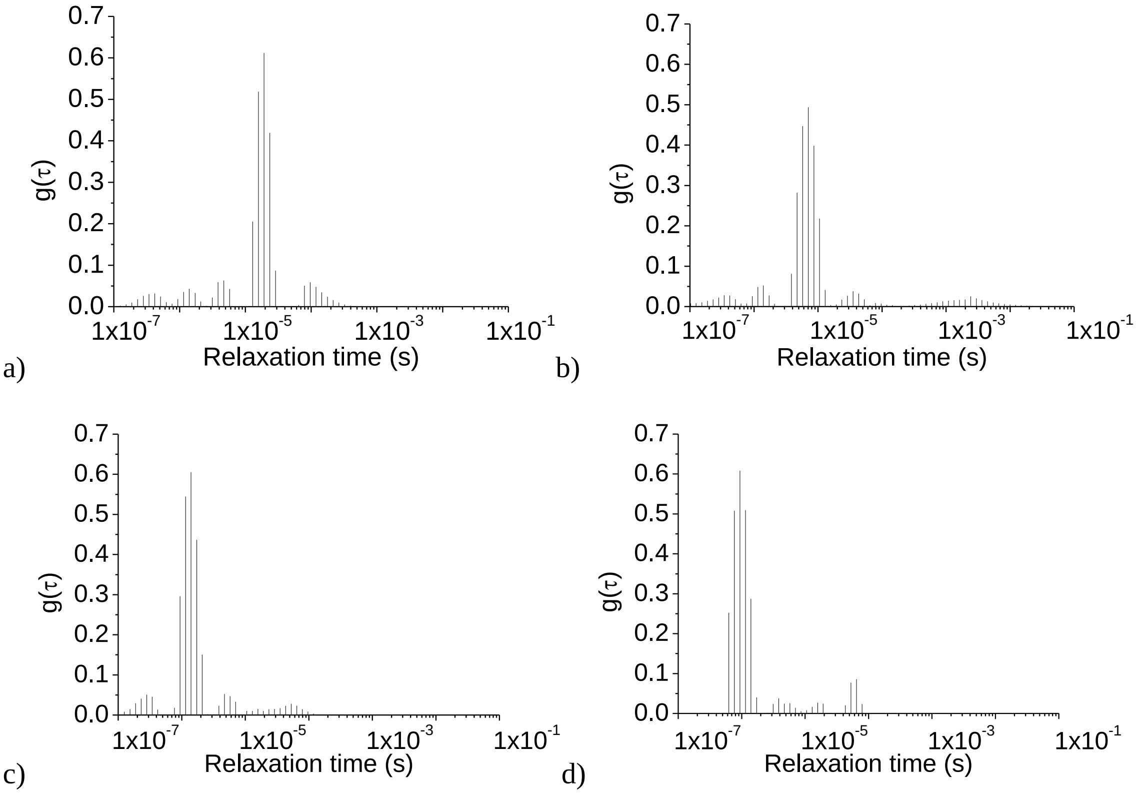

Figure 5.19: Distribution of relaxation times evaluated from dielectric spectra at (a) 323 K (b) 333 K (c) 343 K and (d) 348 K

The approximate discrete relaxation time distributions derived from measurements at each temperature are displayed in Figure 5.19 as histograms, showing the relative contribution of each relaxation time to the overall dielectric function. Each of the distributions showed similar important features. All distributions showed a dominate feature of higher magnitude than the others, which moved to smaller relaxation times as the temperature increased. This feature was generally left skewed, and corresponded to the peak measured in the imaginary permittivity data. Outside of this peak there were approximately four additional peaks which contributed to the overall dielectric function. These were all of similar magnitude and produced contributions which account for losses beyond the main peak in the imaginary permittivity data. The behaviour at relaxation times below the principle group characteristic to measurements at 323 K, 333 K and 343 K was not present in the sample measured at 348 K. This is due to the fact that at 348 K, a large portion of the relaxation peak was outside the measurable frequency range of the meter. In the absence of features to fit to, there was no reason for the model to produce any non-zero relaxation behaviour in this region. It is believed that if the full peak were able to be recorded, the extra peak in the relaxation time distribution would be present. A similar argument is made for the peaks at the slower relaxation times in the measurement taken at 323 K, where the low frequency portion of the loss peak was cut off due to frequency limitations.

The presence of these additional peaks in the relaxation time distribution reveals information not immediately evident from the dielectric spectroscopy measurements, which indicated the presence of a single relaxation process. In actuality, while one process dominates, the overall response was determined from the superposition of multiple additional processes. Correlating this behaviour to exact structural features is an extremely difficult task especially in the presence of multiple relaxation processes, and even in the case of so-called simple polymer networks, a subject of much debate [239-241]. The presence of these features does however further demonstrates the high fragmented, crosslinked nature of the plasma deposited films.

From the initial stages of fitting, the low frequency dielectric constant, ε_s was found to be ~11 in all cases, and the high frequency dielectric constant was found to be ~3. The high frequency value was in good agreement with those obtained in Chapter 4 and Section 5.2 of this chapter.

5.4 Microwave Measurements

5.4.1 Theory and Methods

The SPDR technique was used to determine the high frequency dielectric constant and high frequency loss tangent at frequencies of 10 GHz and 20 GHz. $TE_{10\delta}$ mode SPDRs with resonant frequencies of 10 GHz and 20 GHz were used to first measure the resonance frequency and Q-factor of the resonant cavity with a quartz substrate with no deposited film present. Subsequent to film deposition, the resonant frequency and Q-factor of the resonators were again measured. From the shifts in resonance frequency and Q-factor induced by samples, ε_r was numerically determined from (5.24) [216]:

$$\varepsilon_r = 1 + \frac{f_s - f_f}{h_f f_s K_\varepsilon(\varepsilon_r, h_f)} \tag{5.24}$$

where f_s is the resonant frequency of the SPDR with the substrate only, f_f is the resonant frequency of the SPDR with the substrate and deposited film, h_f is the thickness of the film and K_ε is a function of ε_r and h_f, the value of which is evaluated using the Rayleigh-Ritz technique [216]. Iterative procedures are then used to evaluate further values of K_ε and ε_r until convergence is reached. The loss tangent tan δ was then determined from (5.25) [216]:

$$\tan\delta = \left(Q_0^{-1} - Q_{DR}^{-1} - Q_c^{-1}\right) / \rho_{es} \tag{5.25}$$

by measuring the unloaded Q-factor of the resonator, Q_0, with and without the sample present, where Q_{DR}^{-1} is the loss due to the metallic part of the resonator, Q_c^{-1} is the loss due to the dielectric part of the resonator and ρ_{es} is the electric field filling the cavity. An Agilent Technologies E8364B network analyser and custom software was used to measure the resonant frequency and Q-factor for all microwave measurements and derive the permittivity and loss values from these.

5.4.2 SPDR Measurements

SPDR measurements were conducted on three films on quartz substrates, deposited for 60 minutes at 25 W such that their thickness was sufficient to minimise errors in the measurement and ensure a sufficient shift in the resonant frequency of the cavity [242].

Table 5.2 shows the determined values for the real part of the permittivity and the loss tangent at 10 GHz and 20 GHz for these samples. There was large deviation in the measurement between samples, attributed to the high sensitivity of the SPDR measurement technique to small variations in the material’s properties induced by changes in temperature and humidity for example, as well as small variations in the samples’ thicknesses and the inability to measure this property in the exact location that the measurement was taken. Examining the average values obtained in the last row of the table, the high frequency dielectric constant of the samples was approximately 2.4 at both frequencies, though there is an apparent decrease as frequency increases, which was expected. The determined value of 2.4 is in good agreement with estimates obtained from VASE and IS measurements.

Table 5.2: Dielectric properties of PDLA thin films determined from SPDR measurements at microwave frequencies

Sample	**ε_r (10 GHz)**	**ε_r (20 GHz)**	**tan δ (10 GHz)**	**tan δ (20 GHz)**
1	2.17	2.57	0.03	0.03
2	2.75	2.10	0.07	0.07
3	2.38	2.40	0.05	0.05
Average (μ ± σ)	2.44 ± 0.29	2.36 ± 0.24	0.051 ± 0.023	0.058 ± 0.023

5.5 Conclusions

In this chapter, the electrical properties from dc up to 20 GHz have been presented. These electrical properties provide information regarding the material’s conductivity and resistivity, as well as its permittivity, which in turn can be used to create devices with precisely defined electrical behaviour with respect to resistance and capacitance.

From the shape of the JV curves, several possible mechanisms for the conduction mechanism were found. A PF plot showed a clear relationship between ln (J) and $V^{1/2}$ and further analysis showed agreement between the experimental result and the predicted result from a RS mechanism. However, neither of these mechanisms predicts thickness dependent conductivity, which was observed in the material when measurements of different thickness samples were performed. To explain this behaviour, SCLC was explored. Pure SCLC was not observed to occur, however the shape of the experimental curves did correlate to a degree with that predicted by TSCLC. All samples reached their breakdown limit prior to behaviour expected from TSCLC being observed, and hence no analytical results could be obtained. Given the very good agreement between the experimental results and different aspects of both RS conduction and TSCLC, it is believed that a mixture of the two regimes determines the charge transport through the material, where both interface and bulk effects limit the conductivity. The breakdown field of the material, regardless of thickness, was found to be approximately 1.8 MV cm^{-1} and is sufficient for applications in organic electronic devices

IS measurements were performed on samples in ambient conditions, and repeated in a heated environment for samples deposited at 75 W, in both cases across a frequency range of 10 Hz – 100 kHz. Samples measured in ambient conditions had a relative permittivity of ~3 at high frequencies and low loss. No peaks or evidence of relaxation were notable in the dielectric spectra in the room temperature measurements, however subject to heating, peaks in the loss spectra became evident, shifting to higher frequencies as temperature increased. Significant steps were taken to obtain a theoretical model which exhibited the shape and nature of the measured dielectric spectra at each temperature. It was found that multiple peaks in the relaxation time distribution were present, with one principle peak correlating to the single loss peak in the dielectric spectra, and several secondary peaks at shorter and longer relaxation times to account for the non-zero low and high frequency losses observed in the experimental data. The presence of these multiple peaks suggests a highly complex structure consisting of several principle components. Orientational and ionic phenomena were shown to make a small contribution to the total dielectric constant at high frequencies and became more significant at lower frequencies, indicative of low mobility and fixed molecular structures in the material.

The permittivity and loss tangent were measured at two MW frequencies using the SPDR technique. A dielectric constant of ~2.4 was found from the average of three samples deposited at 25 W, and the loss tangent was found to be ~0.05 from the same set of samples, both of which were in good agreement with both the optical measurements performed in Chapter 4 and estimates of ε_∞ determined from IS measurements.

PDLA thin films were shown to be highly insulating with low relative permittivities, and the relationship between the material geometry and a device’s electrical behaviour precisely defined. These results show that the material is a promising candidate for use in electrical and electronic devices for several applications, where its high resistivity and breakdown field are desirable, while its low permittivity ensures that interference due to parasitic capacitances and cross talk are minimised. Further, insight into the structure of the material has been provided through structural features revealed in IS measurements subject to heating and examination of the electrical conduction mechanisms. The expected electrical characteristics of the material described in the previous chapter based on band gap measurements were confirmed, and the material is a strong candidate for applications in organic electronics where its low permittivity, high resistivity, flexibility and transparency can be exploited. Results from this chapter provided the foundation for the construction of such devices.

Table 5.3: Summary of chapter results

Property Investigated	**Parameter**	**Remarks**	**Power Dependence**	**Relationship**
DC Electrical	σ_{dc}	~10^{-11} Ω^{-1} m^{-1}	High	Order of magnitude increase when deposited at higher powers
	Conduction Mechanism	RS/TSCLC	None	-
	F_b	~1.8 MV cm^{-1}	-	-
AC Electrical/Structural	ε_r	$\varepsilon_s \approx 11$, $\varepsilon_\infty \approx 3$	Small	Decrease in permittivity as power increased
	ε_i	~0.05	None	-
	σ_{ac}	~1 x 10^{-7} Ω^{-1} m^{-1} at 100 kHz	None	-
	$g(\tau)$	One dominant peak, multiple secondary peaks	-	-
Microwave Electrical	ε_r	~2.4	-	-
	$\tan \delta$	~0.05	-	-

Chapter 6: Compatibility with Organic Electronic Device Fabrication Techniques

6.1 Introduction

A wide range of organic electronic devices can be made, such as OLEDs, OPVs and OFETs. Fabrication of these devices can require multiple deposition techniques, such as thermal evaporation, spin coating, drop-casting, ink-jet printing and transfer printing. In addition, complete devices also require the deposition of multiple sub-layers to form the conducting, semiconducting and insulating layers which define the device geometry and determine its overall behaviour.

Considering the OFET, the OSC layer, which is typically deposited on top of the dielectric layer, can be either thermally evaporated or solution processed. If thermal evaporation is used, the dielectric layer may be exposed to high temperatures for long periods of time, and if the OSC is solution processed, the dielectric will be coated in organic solvents such as chloroform, dichlorobenzene and toluene. The device may subsequently be heated to anneal the solution deposited layer and remove excess solvent [126, 243]. It is important that the deposited layers are not adversely affected by these processing methods so that the completed device behaves correctly. Due to the sensitive nature of OSCs, it is important that the use of new materials does not adversely affect the final properties of the OSC layer. A poor interface between the dielectric and OSC layer can lead to severe device degradation, or devices which fail to work [197].

Solution processing methods are becoming a more important means of OSC fabrication as organic electronic technology develops [124, 244, 245], in principle due to the low associated cost and high potential throughput if techniques such as inkjet and roll-to-roll printing can be perfected. In these processing methods, OSC powder is dissolved in an organic solvent and applied to surface of the device through a variety of methods, and depending on the architecture, may be directly on the dielectric layer. The interface between the OSC and the dielectric is of critical importance for the overall operation of the device [197], and hence it is important to predict what interactions may take place during the fabrication process.

In this chapter, the compatibility of PDLA thin films with typical organic electronic devices was investigated. Processing techniques required for the OFET were the principal focus given their prevalent role in electronics and detailed study in literature. The effects of thermal annealing and solution processing on dielectric layers were also investigated. The thermal characteristics of PDLA were studied by monitoring the thickness and optical properties of samples under heating through VASE measurements. To understand the interaction of the material with organic solvents, its surface properties were investigated using CA measurements. The effect of PDLA layers as a substrate for growth of OSCs was investigated by examining the effect of a PDLA dielectric surface on the growth of an organic semiconductor using AFM and VASE measurements. The IV measurements were performed on an OFET device utilising the p-type OSC pentacene, deposited by thermal evaporation onto a PDLA coated Si/SiO$_2$ substrate. This device included the PDLA/OSC interface and the morphology and electrical characteristics of the OSC layer were subject to the influence of the PDLA surface. This provided a demonstration of the application potential of PDLA layers in organic electronic devices.

Results of this chapter provide an understanding of the types of processing methods that PDLA thin films can be used in without degradation, as well as examples of its interactions with important OSCs. These can then be used to guide development of devices utilising PDLA thin films, particularly in regards to their geometry and fabrication so that the integrity of the device is maintained.

6.2 Thermal Degradation

6.2.1 Theory and Methods

Thermal degradation studies were performed on PDLA thin films using VASE measurements to monitor the thickness and optical profile of the samples when placed in a sealed stage and heated from 25 °C to 400 °C. Samples were deposited for a period of 40 minutes to ensure that they were thick enough that material remained through the full range of the measurement. Films were deposited on Si substrates in order to remove the affect of backside scattering due to the inability to place dispersive tape in the thermal system. Due to the structure of the stage used to heat the samples, VASE data could only be taken at an incidence angle of 70°. Taking VASE data in this manner allowed derivation of the material's thickness and optical properties as a function of temperature, allowing investigation into the thermal degradation of the material. The onset of this degradation provides an upper limit for the useable temperature range of the material, not just in applications but during fabrication as well.

6.2.2 Thickness and Optical Properties as a Function of Applied Temperature

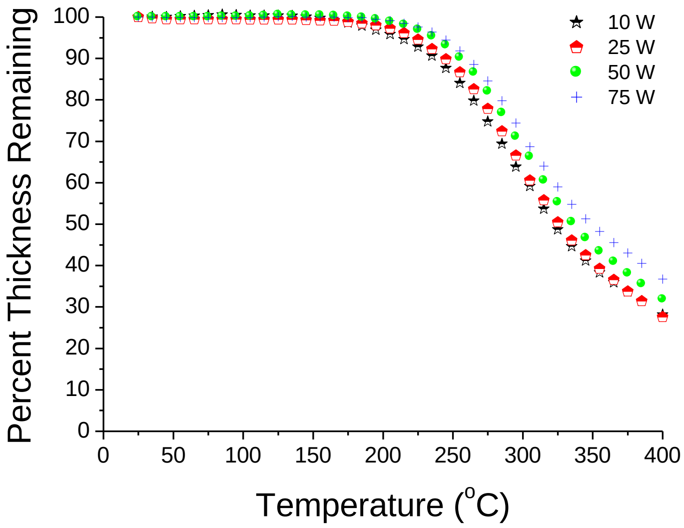

Figure 6.1: Percentage of original thickness remaining as a function of applied temperature

Samples were fabricated at deposition energies of 10 W, 25 W, 50 W and 75 W and measurements were performed from 25 °C – 400 °C in steps of 5 °C, incremented every 5 minutes to investigate the thermal degradation. Figure 6.1 shows the thickness of the samples as a function of the applied temperature. To compare the results from all films, their thicknesses have been normalised to the first measurement under ambient conditions (T = 25 °C). The onset of thermal degradation happened at approximately 200 °C for all films. Rapid degradation was present between 250 °C and 350 °C, though the exact mechanism cannot be well understood without supporting temperature dependent chemistry measurements. Films deposited at higher input energies of 50 W and 75 W began to degrade at slightly higher temperatures and at a slower rate than those deposited at lower input energies. By 400 °C, sample thicknesses had not completely decayed, though this was likely due to their substantial initial thickness. Samples deposited on glass with smaller initial thicknesses had less than 0.5% material remaining when 400 °C was reached, though this data has not been presented due to issues with obtaining reliable optical profiles from samples deposited on glass when measured in the heating stage. The degradation behaviour is much like other, similar plasma deposited thin films [246, 247].

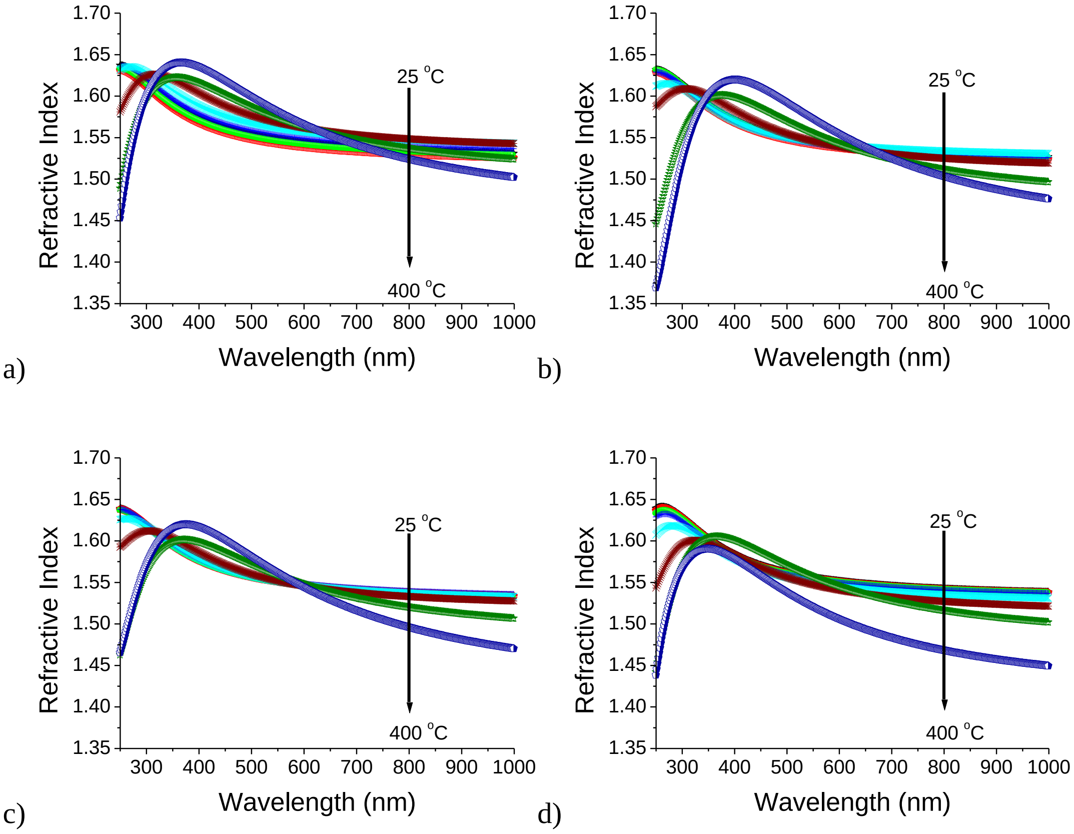

Figure 6.2: Refractive index at (a) 10 W (b) 25 W (c) 50 W and (d) 75 W

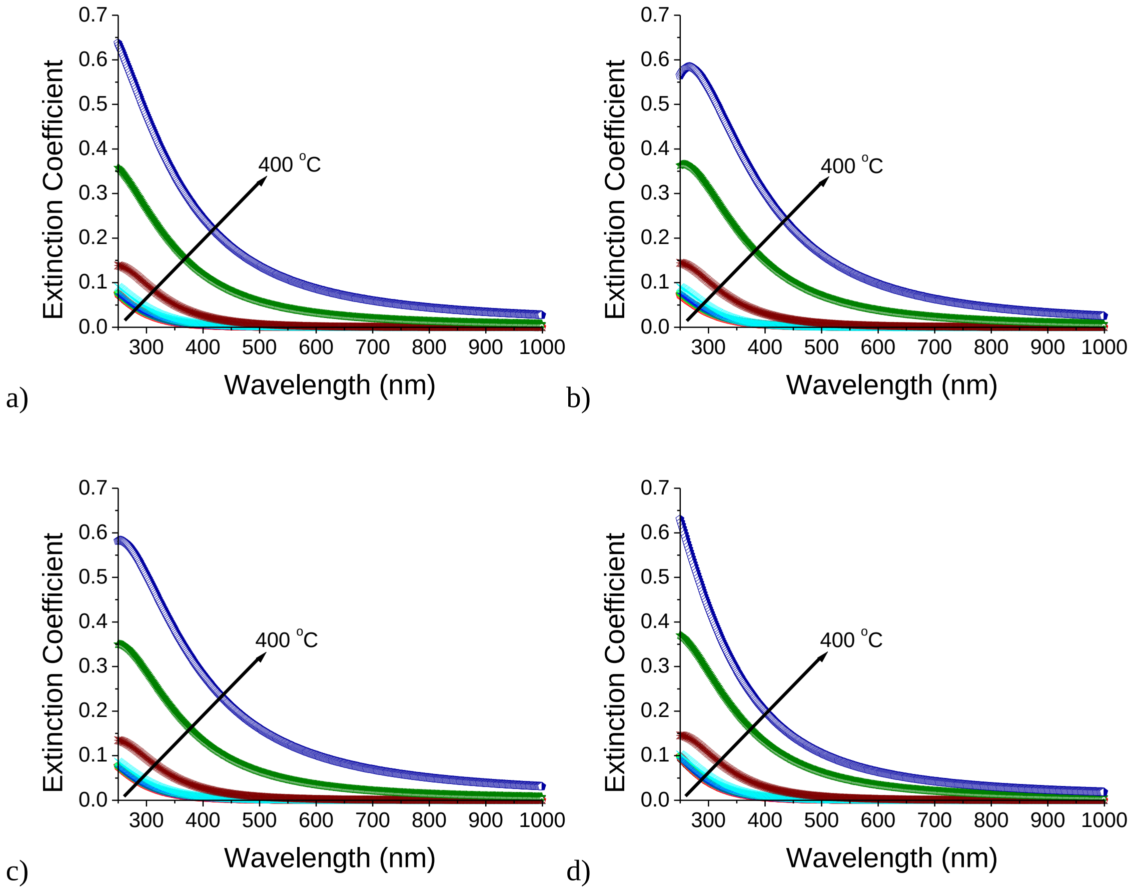

Figure 6.3: Extinction coefficient at (a) 10 W (b) 25 W (c) 50 W and (d) 75 W

Figure 6.2 and Figure 6.3 show the optical profiles of samples as they were heated. All samples displayed approximately the same optical behaviour as heating was applied, in regards to both the shape of the profiles and their changes as a function of temperature. The single peak present at 200 nm in the refractive index of samples measured under ambient conditions slowly moved to higher wavelengths as temperature was increased, ending at approximately 375 nm – 400 nm for all samples, and samples deposited at lower energies were on the higher end of that range. The magnitude of this peak also changed slightly (~3% variation) as the temperature increased, though no clear trend or correlation with temperature was evident.

No changes in the wavelength of the loss peak in the extinction coefficient data were present as temperature increased, however the overall magnitude of the extinction coefficient increased significantly, due to the changes in the material structure resulting in more absorption at these wavelengths. Some changes in colour were evident to the eye and are seen in the extinction coefficient data where the samples began to absorb at high wavelengths when the temperature went above 200 °C. To better understand how the optical properties changed as the temperature increased, the refractive index and extinction coefficient at 589 nm were plotted as a function of the sample temperature.

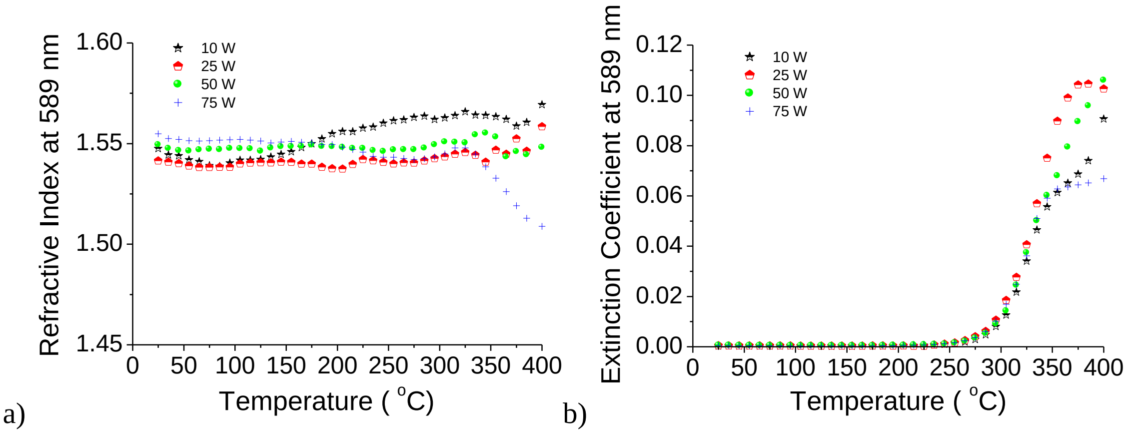

Figure 6.4: (a) Refractive index and (b) Extinction coefficient at 589 nm

Figure 6.4 shows that the optical properties of the material remained stable until above 200 °C, beyond the point at which physical degradation had begun, demonstrating the samples can be safely heated to 200 °C without detrimentally affecting their optical properties. The extinction coefficient did not begin to increase until above 250 °C, prior to this remaining at approximately 0, showing that the material remained transparent when these temperatures were applied. The refractive index remained relatively stable temperatures up to 300 °C were applied. 200 °C is a much higher temperature than typically used to anneal OSC films [248-251], and results therefore show that PDLA layers could be used in devices requiring thermal annealing or thermal evaporation of layers, without adverse effects with respect to the film's thickness and optical properties.

6.3 CA Measurements

6.3.1 Theory and Methods

The transient nature of the CA provides useful information regarding surface/liquid interactions and surface energy properties of a material. Using a combination of different liquids allows determination of several surface properties of the material, including its total surface energy, Lifshitz-van der Waals, electron donor and electron acceptor parameters. These parameters allow the prediction of the interaction between the surface and other liquids, without the need to test them directly. Therefore, once the CA measurements had been performed and the surface properties of the material known, they could be used to predict the interaction of PDLA thin films with organic solvents such as those typically used in the solution processing of OSC layers. Whether or not the solvent would dissolve the material could be determined, as well as the degree to which the material and liquid interact. This is of use when determining which solvent to use if OSC layers are to be directly solution processed onto dielectrics formed from PDLA thin films.

CA measurements were performed using water, ethylene glycol (EG) and diiodomethane (DIM) as probe liquids to simplify analysis, as discussed in Section 6.3.3. CA values were determined using the static sessile drop method (drop volume ≈ 6 μL), by recording the interface of surface/liquid at one second intervals for a period of 30 seconds, and using image processing software to fit the recorded drop shape with the Young-Laplace equation. Measurements were performed 10 times on each sample, and the angle from both the left and the right side of the drops for all measurements used to produce an average for each sample at each time point for analysis. Statistical outliers were removed from the dataset prior to determining the mean values for each sample and solvent combination.

6.3.2 Transient CA Analysis

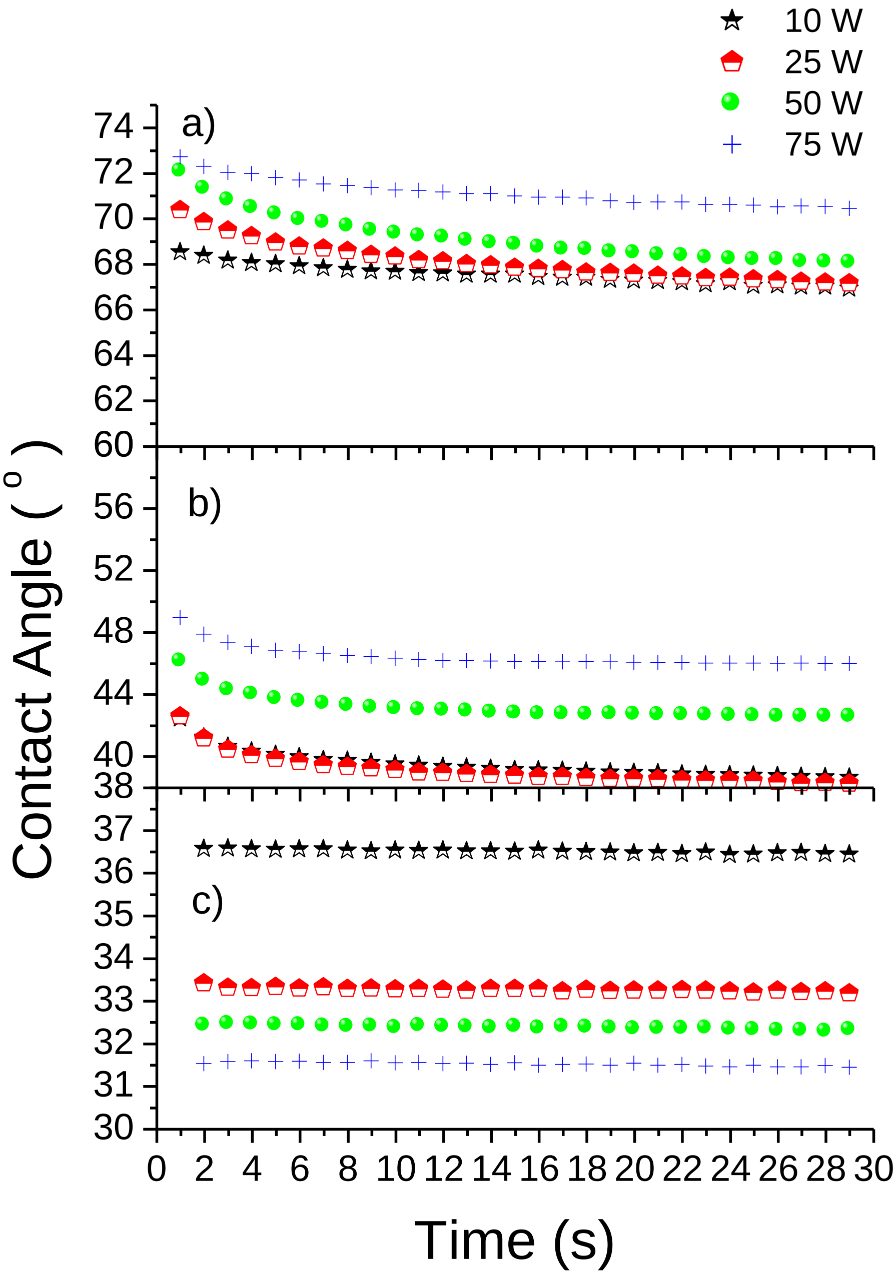

Figure 6.5: CA between (a) Water (b) EG (c) DIM and PDLA thin films

CA measurements were performed on samples deposited at 10 W, 25 W, 50 W and 75 W. Examining the transient behaviour of the CA for each solvent and energy level, samples in contact with water and EG solvents had a small negative gradient. This behaviour was likely due to interactions between the solid-liquid interface, and in the case of the high initial rate of change in measurements using EG, may be indicative of absorption of solvent into the film

[252, 253]. When in contact with EG, the 50 W and 75 W samples stabilised to have a smaller gradient compared to the lower energy samples, while all samples in contact with water had approximately the same gradient towards the end of the measurement. In addition, the CA increased (i.e. the samples became more hydrophobic) as the power density was increased in the case of water and EG measurements.

Measurements with DIM gave very stable CAs for all samples, remaining approximately constant for the entire measurement, having a gradient of approximately -0.003° sec^{-1}. These results show that the material was generally stable in contact with solvents.

6.3.3 Determination of Surface Parameters

From CA measurements there are multiple ways to determine the surface properties of a material. In the analysis of CA data in this thesis, three methods were employed to obtain estimates of the total surface energy and where available, its component parts. These values were then each used in further analysis to obtain a range of results that were compared to ensure the validity of the conclusions reached. In all calculations, the CA value at the end of the measurement time (the steady state angle) was used when the parameter θ_S was required, and these angles are summarised in Table 6.1.

Table 6.1: CAs (in °) used in determination of surface parameters

Deposition Energy	Water	Diiodomethane	Ethylene Glycol
10 W	66.95	36.44	38.68
25 W	67.18	33.19	38.27
50 W	68.10	32.33	42.63
75 W	70.46	31.45	46.02

6.3.3.1 The VCG Method

The first method used to determine the interfacial tension is derived from the model by van Oss, Chaudhury and Good (VCG) [254]. In this model, the total surface energy is determined from the contributions of two key components, an apolar contribution associated with Lifshitz-van der Waals interactions, γ^{LW}, and a contribution from polar Lewis acid-base interactions, γ^{AB}. The acid-base interactions can be further defined in terms of the electron acceptor, γ^{-}, and electron donor, γ^{+}, parameters through the relation [255]:

$$\gamma^{AB} = 2\sqrt{\gamma^{+}\gamma^{-}} \tag{6.1}$$

The total surface energy for a material, γ_s, is then given by [255]:

$$\gamma_S = \gamma_S^{\ LW} + \gamma_S^{\ AB} \tag{6.2}$$

Throughout this chapter, the subscript s denotes a *surface* parameter while the subscript L denotes a *liquid* parameter. In the cases that the specific liquid is known, the subscript denotes the liquid. In order to determine the parameters γ_S^{LW}, γ_S^{+}, γ_S^{-} and the resulting surface energy from measured CA data, the Young-Dupre equation was used [255]:

$$\frac{(1+\cos\theta_S)\gamma_L}{2} = \sqrt{\gamma_S^{\ LW}\gamma_L^{\ LW}} + \sqrt{\gamma_S^{\ +}\gamma_L^{\ -}} + \sqrt{\gamma_S^{\ -}\gamma_L^{\ +}} \tag{6.3}$$

In (6.3), γ_S^{LW}, γ_S^{+} and γ_S^{-} are all unknown parameters, θ_S is the measured CA, and γ_L, γ_L^{LW}, γ_L^{+} and γ_L^{-} are known parameters of the liquid used during the CA measurement. By using three different liquids with known properties and performing three measurements, (6.3) creates a set of simultaneous equations. Liquids are generally chosen such that one is high energy and apolar, where γ_L^{+} and γ_L^{-} equal 0, and the remaining liquids are polar [256]. In these experiments, DIM was used as the apolar liquid, and EG and water were used as the polar liquids. This allows (6.3) to reduce to an equation where the only unknown is γ_S^{LW}, which can be solved:

$$\gamma_S{}^{LW} = \frac{(1+\cos\theta_s)^2 \gamma_{DIM}{}^2}{4\gamma_{DIM}^{LW}} \tag{6.4}$$

For the case of DIM, since there is no polar contribution to the total surface energy, the apolar contribution and the total surface energy are equal. Hence (6.4) can be reduced to:

$$\gamma_S{}^{LW} = \frac{(1+\cos\theta_s)^2 \gamma_{DIM}}{4} \tag{6.5}$$

When water is used as the probe liquid, (6.3) can be arranged to:

$$\frac{(1+\cos\theta_S)\gamma_{WAT}}{2} - \sqrt{\gamma_S{}^{LW}\gamma_{WAT}{}^{LW}} = \sqrt{\gamma_S{}^{+}\gamma_{WAT}{}^{-}} + \sqrt{\gamma_S{}^{-}\gamma_{WAT}{}^{+}} \tag{6.6}$$

Similarly for EG:

$$\frac{(1+\cos\theta_S)\gamma_{EG}}{2} - \sqrt{\gamma_S{}^{LW}\gamma_{EG}{}^{LW}} = \sqrt{\gamma_S{}^{+}\gamma_{EG}{}^{-}} + \sqrt{\gamma_S{}^{-}\gamma_{EG}{}^{+}} \tag{6.7}$$

In the LHS of both (6.6) and (6.7), all parameters are known, since $\gamma_S{}^{LW}$ is determined from (6.4). (6.6) and (6.7) define two simultaneous equations in two unknowns, which can be written as the matrix equation:

$$\begin{bmatrix} \sqrt{\gamma_{WAT}{}^{-}} & \sqrt{\gamma_{WAT}{}^{+}} \\ \sqrt{\gamma_{EG}{}^{-}} & \sqrt{\gamma_{EG}{}^{+}} \end{bmatrix} \begin{bmatrix} \sqrt{\gamma_S{}^{+}} \\ \sqrt{\gamma_S{}^{-}} \end{bmatrix} = \begin{bmatrix} \frac{(1+\cos\theta_S)\gamma_{WAT}}{2} - \sqrt{\gamma_S{}^{LW}\gamma_{WAT}{}^{LW}} \\ \frac{(1+\cos\theta_S)\gamma_{EG}}{2} - \sqrt{\gamma_S{}^{LW}\gamma_{EG}{}^{LW}} \end{bmatrix} \tag{6.8}$$

and solved to determine $\gamma_S{}^+$ and $\gamma_S{}^-$, which are then substituted into (6.1) and (6.2) to determine the total surface energy γ_S. The VCG method thus provides γ_S, $\gamma_S{}^{LW}$, $\gamma_S{}^{AB}$, $\gamma_S{}^+$ and $\gamma_S{}^-$ for the material on which the CA measurements have been performed. Table 6.2 shows the total surface energy and associated components derived from a VCG analysis of the CA data. The total surface energy, γ_S was between 44 mJ m^{-2} – 45.5 mJ m^{-2} for all samples investigated.

Table 6.2: Surface parameters (mJ m^{-2}) derived from the VCG method

Deposition Energy	γ_S^{LW}	γ_S^{+}	γ_S^{-}	γ_S^{AB}	γ_S
10 W	41.40	0.20	13.20	3.30	44.60
25 W	42.90	0.20	12.70	2.80	45.60
50 W	43.20	0.050	13.20	1.30	44.50
75 W	43.60	0.00	12.00	0.30	43.90

This is similar to the value of ~44 mJ m^{-2} for PET obtained by Wu et al. [257] as well as 44.3 mJ m^{-2} for PEI and 42 mJ m^{-2} for PMMA and thus the total surface energy is similar to other common polymer surfaces used as dielectrics in OFET devices. In comparison to similar thin film materials, plasma deposited thin films derived from *Lavandula angustifolia* essential oil [252] and terpinen-4-ol [253] were found to have a total surface energy of 36 mJ m^{-2} – 40 mJ m^{-2} and 31 mJ m^{-2} – 37 mJ m^{-2} respectively, derived using the same combination of solvents as outlined above.

Data additionally shows that PDLA thin films were monopolar in nature, due to the comparatively large value of the donor component γ^- with respect to the acceptor component γ^+. This is common in polymer surfaces [254, 258] and in good agreement with the tendency of monopolar materials to have a strong electron donor component [254]. Such monopolar surfaces may be dissolved in polar solvents such as water. Based on the donor and acceptor components of the liquid, the upper limit on γ_S^- which results in the material *not* dissolving can be found. For water, this limit is 28 mJ m^{-2}, and results in Table 6.2 show that this upper limit was never exceeded and hence the material is not expected to dissolve in water. The donor component did not seem dependent on power density, though interestingly the acceptor component decreased by two orders of magnitude as deposition energy was increased from 10 W to 75 W. This correlates with the decrease in surface oxygen (polar functionality) observed in XPS measurements in Chapter 4.

The Lifshitz-van der Waals component of the total surface energy was found to be the dominant term, and increased with increasing power density, from 41.35 mJ m^{-2} to 43.61 mJ m^{-2}. A dominant γ_S^{LW} term is again consistent with literature values for a wide range of other polymer materials.

6.3.3.2 The Neumann Method

The Neumann method is derived from the combination of the Young equation, and the equation of state [259, 260], and relates a measured CA directly to the total surface energy of the solid, providing no additional information regarding surface interactions in the way that the VCG approach does. The Neumann equation is given by [259, 260]:

$$\frac{1+\cos\theta_S}{2} = \sqrt{\frac{\gamma_S}{\gamma_L}}\exp\left(-\beta(\gamma_L-\gamma_S)^2\right) \tag{6.9}$$

(6.9) defines a non-linear equation in γ_S. In order to determine the surface energy of the solid, (6.9) was rearranged to the following form:

$$0 = \gamma_S \exp\left(-2\beta(\gamma_L-\gamma_S)^2\right) - \gamma_L \frac{(1+\cos\theta_S)^2}{4} \tag{6.10}$$

The right hand side (RHS) of expression (6.10) was then evaluated for a range of values of γ_S and the intersection with the *x*-axis found to give the solution. The range of values for γ_S was chosen to form a domain around the solution obtained using the VCG method. The Neumann method provides a different estimate of the surface energy for every different liquid measured, shown in Table 6.3.

The surface energy derived from water and DIM both lie in a similar range to values derived using the VCG method, albeit slightly lower, between 41 mJ m^{-2} and 44 mJ m^{-2}. Values derived from EG measurements provided the lowest estimates of 35 mJ m^{-2} – 39 mJ m^{-2}. γ_S values obtained via the Neumann method also showed dependence on the power density, though this was likely due to the direct dependence on θ_S in (6.9). The Neumann method is noted in literature as having several shortcomings, particularly when applied to polar and non-hydrophobic systems [257]. Additionally, since every value of γ_S obtained is directly dependent on a single CA value, errors are in no way averaged out or reduced. These shortcomings noted, results from the Neumann method still provided reasonable estimates of the surface energy, in good agreement with those obtained via VCG methods and other polymer thin films in literature as discussed in Section 6.3.3.1.

Table 6.3: Surface parameters (mJ m^{-2}) determined from the Neumann method

Deposition Energy	Water	Diiodomethane	Ethylene Glycol
10 W	43.60	42.10	38.90
25 W	43.50	43.40	39.00
50 W	42.90	43.80	37.20
75 W	41.40	44.10	35.80

6.3.3.3 The Fowkes Method

The Fowkes Method is derived through the combination of Young's equation and the Berthelot hypothesis [260]. The Fowkes method can be used to determine γ_S for a solid by performing CA measurements with at least three liquids. Using the Fowkes approximation, the equation to calculate the surface energy is given as [256, 260]:

$$\left(\frac{1+\cos\theta_S}{2}\right)\left(\frac{\gamma_L}{\sqrt{\gamma_L{}^D}}\right) = \sqrt{\gamma_S{}^P}\sqrt{\frac{\gamma_L{}^P}{\gamma_L{}^D}} + \sqrt{\gamma_S{}^D} \qquad (6.11)$$

where γ_S^P is the polar component and γ_S^D is the dispersive component, and these are generally recognised to equal γ_S^{AB} and γ_S^{LW} respectively. If multiple CA measurements are performed with different liquids, a plot of the LHS of (6.11) as the dependent variable versus $(\gamma_L^P/\gamma_L^D)^{1/2}$ as the independent variable results in a linear plot whose slope is given by $(\gamma_S^P)^{1/2}$ and whose y-intercept is given by $(\gamma_S^D)^{1/2}$. By fitting a linear function to this plot, γ_S^D, γ_S^P, and hence γ_S can be determined.

Table 6.4: Surface energies and components (mJ m^{-2}) derived from Fowkes analysis

Deposition Energy	$\gamma_S^D = \gamma_S^{LW}$	$\gamma_S^P = \gamma_S^{AB}$	γ_S
10 W	38.10	8.20	46.30
25 W	39.40	7.70	47.10
50 W	39.10	7.20	46.30
75 W	39.30	6.00	45.40

Total surface energy values derived from the Fowkes method were in good agreement with those derived using the VCG and Neumann approaches, in the range of 45 mJ m^{-2} – 48 mJ m^{-2}, slightly higher than those estimated by the VCG approach. The Fowkes method is dependent on fitting a linear function to a plot which has as many data points as there are probe liquids used; in this case there were only three points to base the fitting on. As such, there was error associated with values obtained in this manner, as small errors in the CA measurement may have produced larger deviations in the fit parameters when small data sets were used. The estimate of γ_S^{AB} obtained from the Fowkes method was much higher when compared to the value obtained through the VCG method, though both show the same behaviour of decreasing in value as the power density increased. The Lifshitz-van der Waals component was again found to be the dominant component of the total surface energy, at ~39 mJ m^{-2} for all samples.

6.3.4 Surface Wetting Envelopes

If the dispersive and polar components of a material's surface energy are known, the wetting envelope of that material can be determined. The wetting envelope provides the expected CA between a surface and liquid with known dispersive and polar components. The wetting envelope defines the range of surface energy values of liquids that result in a particular CA, where each angle is presented as a single boundary of the curve. By placing a boundary on the curve at a CA of 0°, it can be determined whether a particular liquid will completely wet the surface, or have a measurable CA. This predictive tool is useful in choosing material and solvent combinations in solution processed organic electronics, where complete wetting of a surface area may be desirable, to ensure uniformity of deposited layers.

The wetting envelope is determined by rearranging [261]:

$$\gamma_L (1+\cos\theta_S) = 2\left(\sqrt{\gamma_S{}^D \gamma_L{}^D} + \sqrt{\gamma_S{}^P \gamma_L{}^P}\right) \tag{6.12}$$

where:

$$\gamma_L = \gamma_L{}^D + \gamma_L{}^P \tag{6.13}$$

Substitution of (6.13) into (6.12) and rearranging results in:

$$\frac{1+\cos\theta_S}{2} = \frac{\sqrt{\gamma_S{}^D \gamma_L{}^D} + \sqrt{\gamma_S{}^P \gamma_L{}^P}}{\gamma_L{}^P + \gamma_L{}^D} \tag{6.14}$$

where $(\gamma_S{}^D)^{1/2}$ and $(\gamma_S{}^P)^{1/2}$ are known constants determined from analysis of the CA measurements and $\gamma_L{}^D$ and $\gamma_L{}^P$ are variables. To form the wetting envelopes, the LHS of (2.9) is evaluated for the desired constant angles, θ_S, and these values used to contour the 3D plot produced by the RHS of (2.9). These contours provide the wetting envelope for each desired CA. As (2.9) depends explicitly on the knowledge of both the solid and the liquid's surface energy components, γ^D and γ^P, wetting envelopes can only be determined when both these parameters are known, and similarly can only be used to predict the behaviour of liquids with known energy components. For this reason, wetting envelopes could only be generated for surface energy values derived from the VCG and Fowkes methods, as the Neumann method provides no information beyond the total surface energy.

For samples deposited at each power density, wetting envelopes were produced using surface energy components derived from both VCG and Fowkes analysis methods, in order to compare the predicted and measured interactions for each method.

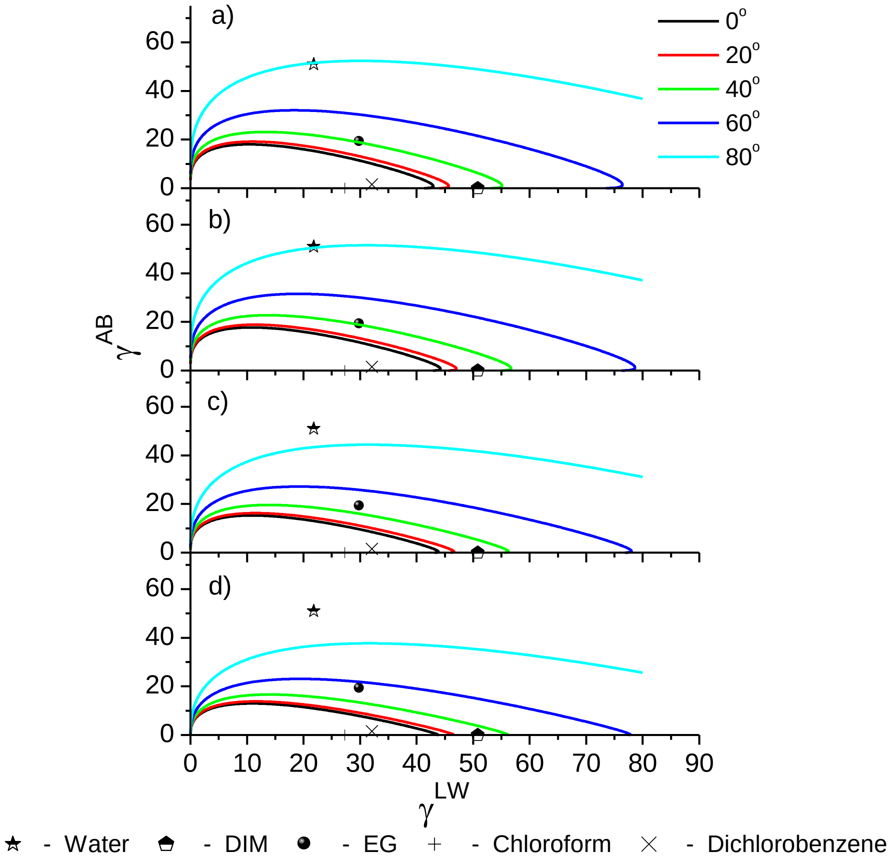

Figure 6.6: Wetting envelopes at 0°, 20°, 40°, 60° and 80° using surface energy components derived from the VCG method for samples deposited at (a) 10 W (b) 25 W (c) 50 W and (d) 75 W

Figure 6.6 and Figure 6.7 show the determined wetting envelopes for all samples, and have superimposed upon them the specific surface energy components for common solvents used in analysis and deposition of OSCs for which the polar and dispersive contributions are known. The superimposition of these upon the figures serves two purposes; first to aid as a check of the determined surface energy parameters for the PDLA thin films, and secondly to predict the behaviour of some solvents when placed on a surface coated in PDLA thin films.

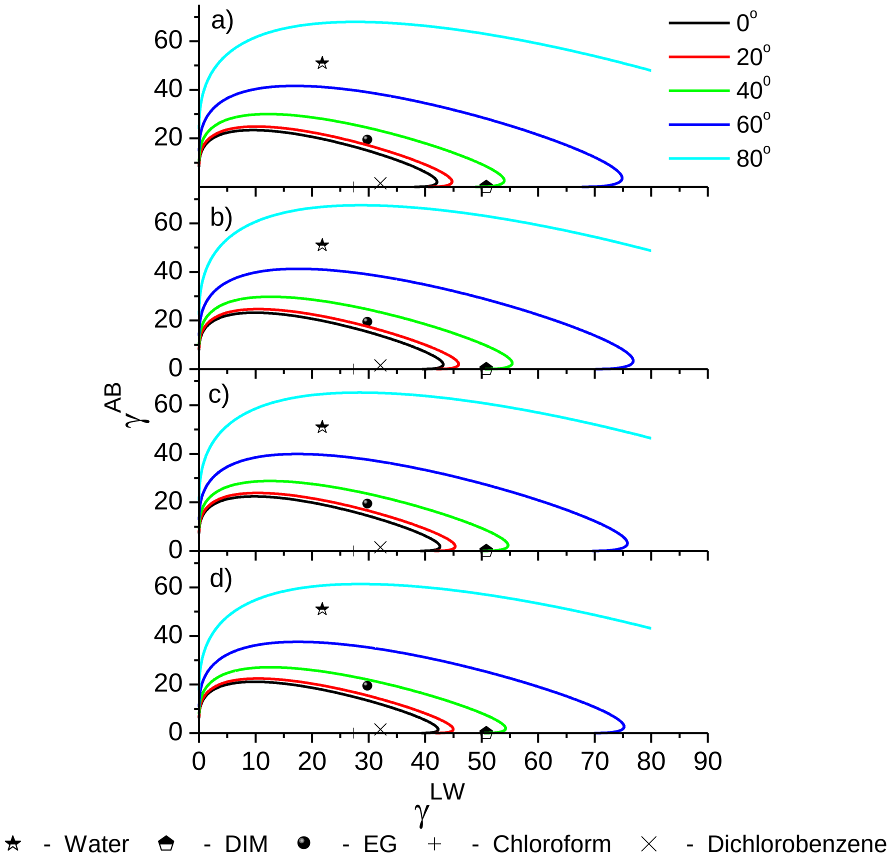

Figure 6.7: Wetting envelopes at 0°, 20°, 40°, 60° and 80° using surface energy components derived from the Fowkes method for samples deposited at (a) 10 W (b) 25 W (c) 50 W and (d) 75 W

Wetting envelopes from the VCG method incorrectly predicted the CAs made by the tested probe liquids, when compared to the measured values in Table 6.1. For example, the wetting envelopes indicate that the contact angle made with water should be 80° or larger, while the maximum measured angle when water was used as a probe liquid was 70°, a fact which is much better reflected in the curves obtained using surface energy values determined from the Fowkes analysis. The overall behaviour of the measured data was reflected better in wetting curves derived from the Fowkes method, though there was a slight tendency to underestimate the expected contact angles, while the VCG method in all cases overestimated the contact angle by a large degree. It is therefore believed that the surface energy estimates provided by the Fowkes analysis were a better representation of the true behaviour.

As a predictive tool, the expected behaviour of chloroform and dichlorobenzene was examined, as these solvents are commonly used in the deposition of OSC layers from solution [122, 123, 262, 263]. In both cases, it was found that the expected contact angle falls within the 0° boundary and hence these solvents would completely wet the surface. Depending on the desired application this may be beneficial, though in this case it means the contact angle with these liquids cannot be measured. If complete wetting of the surface by drop casting or other solution processing methods is desired, both of these solvents would be appropriate in conjunction with the PDLA dielectric surface.

6.3.5 The Interfacial Tension and Solubility

Once the surface energy of the thin films was obtained from the methods outlined above, it was possible to determine the way in which it would interact with solvents such as those employed in the deposition of solution processed OSCs to determine its suitability for these fabrication techniques. The interfacial tension between a solid and liquid given by Young’s equation was determined [256, 260, 261, 264]:

$$\gamma_{SL} = \gamma_S - \gamma_L \cos\theta_S \tag{6.15}$$

(6.15) was applicable for use with values of γ_S derived from all methods. When the VCG approach was used, an alternative equation could determine the interfacial tension, γ_{SL} [255]:

$$\gamma_{SL} = \left(\sqrt{\gamma_S{}^{LW}} - \sqrt{\gamma_L{}^{LW}}\right)^2 + 2\Lambda \tag{6.16}$$

where:

$$\Lambda = \sqrt{\gamma_S{}^+\gamma_S{}^-} + \sqrt{\gamma_L{}^+\gamma_L{}^-} - \sqrt{\gamma_S{}^+\gamma_L{}^-} - \sqrt{\gamma_S{}^-\gamma_L{}^+} \tag{6.17}$$

(6.16) is dependent on $\gamma_S{}^+$ and $\gamma_S{}^-$, which were determined only by the VCG approach.

Knowing the interfacial tension between the solid-liquid interface, the solubility of the solid in that liquid was found from [254]:

$$\Delta G_{SLS} = -2\gamma_{SL} \tag{6.18}$$

As (6.16) depends on parameters only available for liquids whose contact angle was measured, and specific values only obtained through the VCG method, solubility values were only available for the three liquids with which CA measurements were performed and are presented in Table 6.5.

Table 6.5: Interfacial tension (mJ m^{-2}) and solubility (mJ m^{-2}) in measuring liquids using the VCG approach

Deposition Energy	**Water**		**Diiodomethane**		**Ethylene Glycol**	
	γ_{SL}	ΔG_{SLS}	γ_{SL}	ΔG_{SLS}	γ_{SL}	ΔG_{SLS}
10 W	16.10	-32.20	3.80	-7.60	6.90	-13.80
25 W	17.40	-34.80	3.10	-6.20	7.70	-15.40
50 W	17.40	-34.80	1.60	-3.20	9.00	-18.00
75 W	19.60	-39.20	0.60	-1.20	10.30	-20.60

Interpretation of ΔG_{SLS} is based on the sign and magnitude of the value obtained; highly positive values indicate that the solid is solvophillic to the solvent, while highly negative values indicate that the solid is solvophobic to the solvent. ΔG_{SLS} approximately equal to 0 indicates that the solid is partially dissolved in the solvent [252].

The presence of no negative interfacial tensions for any of the liquids in Table 6.5 shows that material is insoluble in the three liquids used in testing. For measurements which used water or EG as a probe liquid, the solubility became larger in magnitude as the power density was increased, indicating that these samples were less soluble. However, measurements using DIM as the probe liquid resulted in interfacial tensions which, while positive, were small in magnitude and indicate that swelling or partial dissolution may have occurred. Figure 6.5 does not show in evidence of this occurring in the transient CA measurement, where a non-zero rate of change of CA with respect to time would be expected if solid-liquid interactions were occurring.

Table 6.6 presents a similar analysis when the surface energy derived from all methods was used, in conjunction with (6.15) and (6.18), and was extended to predict the interfacial tension between the plasma deposited thin films and solvents typically used in organic electronics: acetone, chloroform and dichlorobenzene. Acetone is commonly used in cleaning of surfaces prior to deposition, while chloroform and dichlorobenzene are both commonly used to dissolve OSCs prior to deposition. In the case of the VCG and Fowkes methods, one value for the parameter γ_S per sample was obtained; when using the Neumann method, an estimate of the surface energy was obtained from every liquid used to probe the surface. In Table 6.6, when predicting the interfacial tension between solvents not used to probe the material directly via the Neumann method, the surface energy used was that obtained from water. Using the surface energy obtained from EG or DIM would not result in a change of sign in the interfacial tension. In (6.15) the parameter θ_S was not obtainable for all solvents investigated due to spreading of the liquid, and hence an angle of 180° was assumed. This resulted in a worst-case estimate of the interfacial tension, as the term $\gamma_L \cos\theta_S$ is maximised when $\theta_S = k180°$, where $k \in \mathbb{N}_o$, and there would be no sign change in the interfacial tension were a smaller angle used.

The elements in Table 6.6 derived from surface energy values obtained from the VCG method compare well to those in Table 6.5, despite use of (6.15) rather than (6.16) to determine the interfacial tensions. Values for the interfacial tension for all solvents derived from each of the three methods for all power levels remain positive, and indicate that samples deposited at all investigated power densities should be insoluble for all solvents, including those used in solution processing of organic electronics. The interfacial tension and solubility for DIM samples was again close to zero, showing that all three methods predict partial dissolution of the solid when in contact with this liquid.

Table 6.6: Interfacial tension (mJ m^{-2}) and solubility (mJ m^{-2}) parameters between PDLA thin films and common solvents

Solvent	**Method**	**10 W**		**25 W**		**50 W**		**75 W**	
		γ_{SL}	ΔG_{SLS}	γ_{SL}	ΔG_{SLS}	γ_{SL}	ΔG_{SLS}	γ_{SL}	ΔG_{SLS}
Water	*VCG*	16.10	-32.20	17.40	-34.80	17.40	-34.80	19.60	-39.20
	Neumann	15.10	-30.20	15.20	-30.40	15.70	-31.40	17.10	-34.20
	Fowkes	17.80	-35.60	18.90	-37.80	19.10	-38.20	21.00	-42.00
DIM	*VCG*	3.80	-7.60	3.10	-6.20	1.60	-3.20	0.60	-1.20
	Neumann	1.30	-2.60	0.90	-1.80	0.80	-1.60	0.80	-1.80
	Fowkes	5.40	-10.80	4.60	-9.20	3.40	-6.70	2.00	-4.00
EG	*VCG*	7.20	-14.40	8.00	-16.00	9.20	-18.40	10.60	-21.20
	Neumann	1.40	-2.80	1.30	-2.60	1.90	-3.80	2.40	-4.80
	Fowkes	8.80	-17.60	9.50	-19.00	11.00	-22.00	12.00	-24.00
Acetone	*VCG*	20.60	-41.20	21.60	-43.20	20.50	-41.00	19.90	-39.80
	Neumann	19.60	-39.20	19.40	-38.80	18.90	-37.80	17.40	-34.80
	Fowkes	22.30	-44.60	23.10	-46.20	22.30	-44.60	21.40	-42.80
Chloroform	*VCG*	17.30	-34.60	18.30	-36.60	17.20	-34.40	16.60	-33.20
	Neumann	16.30	-32.60	16.10	-32.20	15.60	-31.20	14.10	-28.20
	Fowkes	19.00	-38.00	19.80	-39.60	19.00	-38.00	18.10	-36.20
Dichlorobenzene	*VCG*	11.00	-22.00	12.00	-24.00	10.90	-21.80	10.30	-20.60
	Neumann	10.00	-20.00	9.90	-19.80	9.30	-18.60	7.80	-15.60
	Fowkes	12.70	-25.40	13.50	-27.00	12.70	-25.40	11.80	-23.60

Interfacial tensions obtained through the Neumann method in all cases provided the lowest estimation of the interfacial tensions and free energy of interaction. This can be attributed to the poor performance of the Neumann method in polar systems [255, 257]. Results from Section 6.3.3.1 show PDLA thin films to be highly monopolar and the interactions studied are in polar systems. Neumann method may not be appropriate for these analyses. Values obtained from the VCG and Fowkes method were in much better agreement with each other. Of the three additional solvents examined, dichlorobenzene had the lowest interfacial tension, however the solubility parameter still indicated that the material would be non-soluble in this liquid. The interfacial tensions obtained for samples with a measurable contact data show a mild dependence on the power density, following the trends established by the variation in contact angles with power density for each probe liquid in Figure 6.5. The interfacial tension estimate between the solid and solvents used in organic electronics processing did not demonstrate any strong power density dependence, other than that present in γ_S. Despite this, it is anticipated that the interactions would have some power dependence due to the trends established by the CA measurements with other probe liquids. Overall however, the material appears to be insoluble in all solvents investigated.

6.4 Growth of Organic Layers

6.4.1 Theory and Methods

Films of PDI-8CN$_2$ were grown via thermal evaporation on substrates of Si with an SiO$_2$ oxide layer of 200 nm, which had a ~100 nm layer of PDLA present. Two such layers were grown at nominal thicknesses of 50 nm and 60 nm. These films were then studied with VASE and AFM in order to investigate the optical properties of the PDI-8CN$_2$ thin films and their morphology when grown on PDLA. Additionally, PDI-8CN$_2$ thin films were thermally grown on standard substrates of Si/SiO$_2$ used in the fabrication and testing of OFET devices, and the same characterisations performed. These measurements provided a basis of comparison for the film grown under standard conditions to which those grown on the new dielectric could be compared. In this way, the morphological and optical characteristics of the OSC were investigated to determine whether the dielectric layer induced significant differences in the semiconducting layer.

6.4.2 VASE Measurements of PDI-8CN$_2$

First, the modelling procedure and results for VASE measurements of PDI-8CN$_2$ grown on Si/SiO$_2$ substrates are presented. As the optical model for the PDI-8CN$_2$ is complicated, it was important that as much was known about the samples prior to attempting to model this layer so that correlations between fit parameters were avoided and a unique fit was ensured. The bare Si/SiO$_2$ substrate was first measured and optically modelled to obtain an accurate value for the thickness of the oxide layer. The Si and SiO$_2$ models present in the WVASE32 software were used, and a thickness of 197 nm obtained for the oxide layer, compared to the nominal value of 200 nm. A final measurement was then performed on each sample after the thermal evaporation of PDI-8CN$_2$ films. The PDI-8CN$_2$ film was modelled as a uniaxial anisotropic layer, coupled to two general oscillator layers to describe the ordinary and extraordinary optical constants (n_o, k_o, n_e and k_e). This was necessary as the PDI-8CN$_2$ layers are optically anisotropic; they have different optical properties along different axes, due to the preferential alignment of the organic molecules on the substrate.

The measurement and modelling procedure was possible due to this preferential alignment of the molecules, in the plane of the substrate, with the optical axis normal to the substrate surface. In this instance it is possible to perform a regression analysis and extract the ordinary and extraordinary optical constants from standard VASE measurements [265-267], as for uniaxial anisotropic (and truly isotropic) samples such as those with preferential alignment of molecules and an optical axis normal to the substrate surface (i.e. samples with in-plane isotropy), the off diagonal elementals of the Jones matrix are zero [268]. However, as VASE is less sensitive to the extraordinary optical properties, multi-sample analysis was performed to obtain better sensitivity to the anisotropy of the samples [269]. Multi-sample analysis also reduces the correlation between ordinary and extraordinary optical properties during the fitting procedure [165].

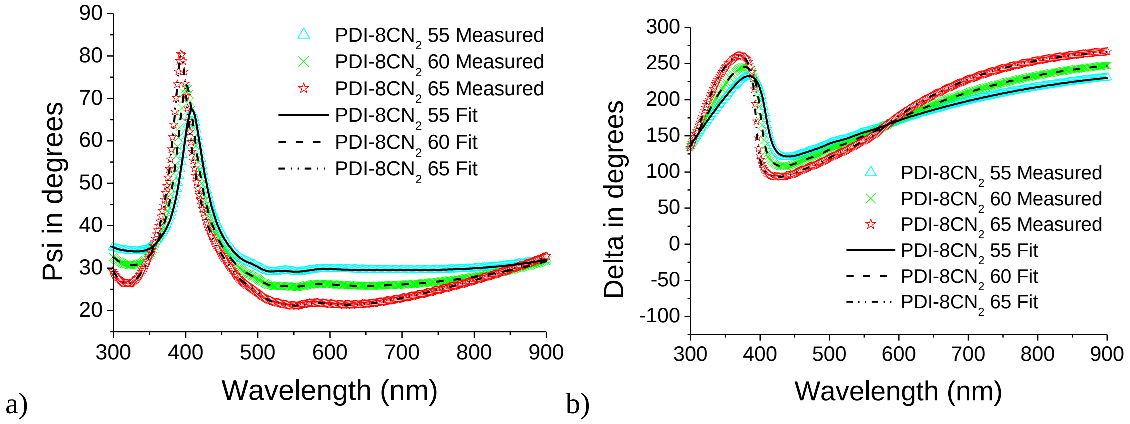

Figure 6.8: Measured (a) Ψ and (b) Δ data from VASE for a PDI-8CN$_2$ film grown on bare SiO$_2$

The raw data obtained from the VASE measurements on PDI-8CN$_2$ films grown on bare SiO$_2$ are shown in Figure 6.8. Initially the anisotropic layer was coupled to two Cauchy layers (one for the ordinary optical constants and the other for the extraordinary optical constants), to obtain a starting approximation for the film’s thickness and optical properties, and the Cauchy layers for both samples were coupled together. Performing the analysis in this manner significantly improved the quality and uniqueness of the fit, however, as the PDI-8CN$_2$ films were evidently different thicknesses, it must be assumed that the optical properties of the material are independent of thickness. Previous studies which include absorption spectra for several Perylene derivatives [266, 270] show that they are optically transparent, or near transparent at wavelengths greater than ~ 750 nm. It was therefore considered appropriate to assume a similar level of transparency at high wavelengths during the fitting procedure for PDI-8CN$_2$ in this study. To estimate the thickness and refractive index, a fit of Cauchy parameters and the thickness of the uniaxial layer was performed in the transparent spectrum of the sample, significantly reducing correlation between these variables during fitting.

Subsequently, the estimations of refractive index for the coupled Cauchy layers and the thickness of the anisotropic layer were used as a starting approximation for a point-by-point fit of the ordinary and extraordinary optical profiles. This fitting provided an initial estimate of the in- and out-of-plane optical profiles of the organic layers.

Each Cauchy layer was then converted to a general oscillator layer, and for PDI-8CN$_2$ films a combination of Lorentz, Tauc-Lorentz and Gaussian oscillators were used to fit to the absorption spectra determined in the point-by-point fitting procedure, which contained large amounts of noise and some erroneous features not present in the absorption spectra of PDI-8CN$_2$ in other studies. These oscillators were based on the shape of the estimates of the optical profiles obtained in the initial stage of fitting, where it can be seen that three distinct features were present in the extinction coefficient profile, in agreement with absorption measurements of the material. Parameters of the oscillators for both the ordinary and extraordinary layers and the thickness of the uniaxially anisotropic layer to which these were coupled were set as fit parameters and a final fit performed.

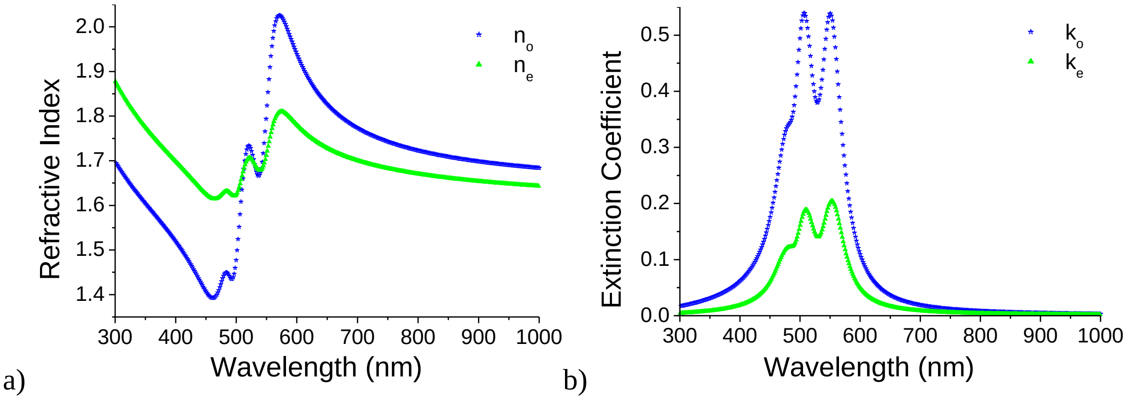

Figure 6.9: Ordinary and extraordinary (a) refractive indices and (b) Extinction coefficients of PDI-8CN$_2$ grown on bare SiO$_2$

The thickness value determined for the films as a result of the fitting process is 50.0832 nm, 68.4371 nm and 81.2232 nm, in good agreement with the nominal values of 50 nm, 65 nm and 80 nm. Extracted ordinary and extraordinary refractive indices and extinction coefficients are shown in Figure 6.9 a) and b), respectively. The optical profiles are similar to previous studies of Perylene derivatives [166, 271], where differences between the profiles presented in literature and those reported here are believed to be due to differences in the specific chemical and physical structure of the investigated Perylene compound.

In the case of both the refractive index and extinction coefficient, the magnitudes of the in-plane (ordinary components) profiles were much greater than those of the out-of-plane (extraordinary components) profiles. In the extinction profiles, the principle features were two peaks in absorption, one at 505 nm and 509 nm in the ordinary and extraordinary cases respectively, and another at 548 nm and 552 nm for the ordinary and extraordinary cases respectively. In addition to these features there was also a knee in the absorption spectra at 477 nm for both the in- and out-of-plane profiles. The position of these features matches well with those of the main peaks in the absorption spectra obtained by [270] for 50 nm thick PDI-8CN$_2$ films deposited on transparent glass substrates, further validating the fitting procedure used for optical data.

After obtaining the initial optical profile for PDI-8CN$_2$ films grown on standard substrates, VASE measurements were performed on substrates grown on PDLA thin films. The procedure used to model the OSC layers was the same as that outlined above, however, prior to the deposition and final VASE measurement of the PDI-8CN$_2$ layer, a VASE measurement of the Si/SiO$_2$/PDLA substrate was taken, and the PDLA thin film's thickness accurately determined.

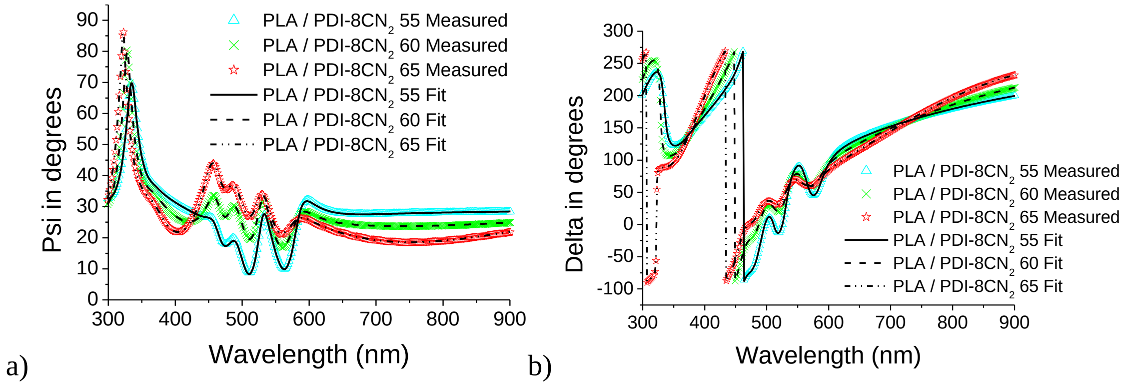

Figure 6.10: Measured (a) Ψ and (b) Δ data from VASE for a PDI-8CN$_2$ film grown on PDLA

The measured (dashed) and regressions (solid lines) to the Ψ and Δ data of PDI-8CN$_2$ grown on a Si/SiO$_2$/PDLA substrate are shown in Figure 6.10 a) and b). Once again, only the result for the 50 nm sample is displayed, due to the similarities in results. In the Ψ data the features evident in the reference PDI-8CN$_2$ film are still present, though a shift of the peak to shorter wavelengths by approximately 70 nm was observed. This shift can be attributed to the increased thickness of the overall structure due to the introduction of the PDLA layer, with its thickness (70 nm) corresponding exactly to the shift in the curves. New features were present in both the Ψ and Δ measurements, most notably oscillations between the wavelengths of 400 and 700 nm. The thicknesses determined from the analysis were 48.7523 nm and 58.0903 nm, once more in good agreement with the nominal values of 50 nm and 60 nm.

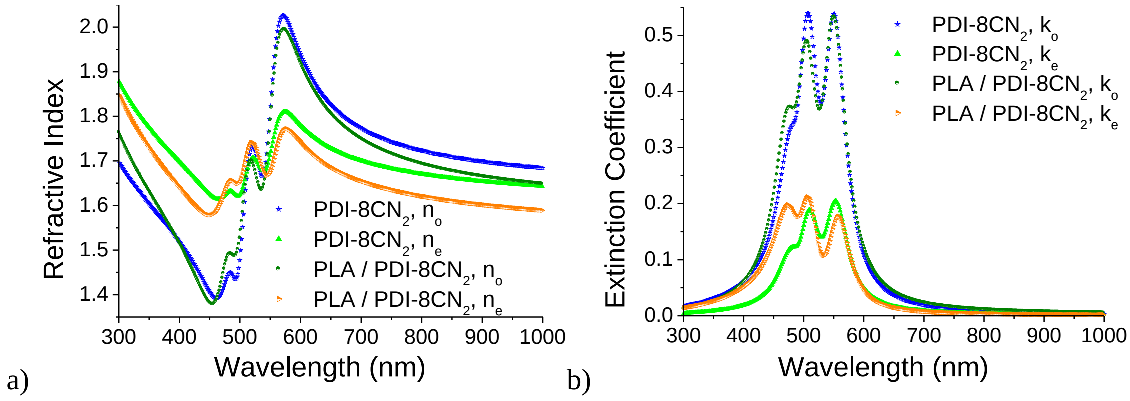

Figure 6.11: Comparison between ordinary and extraordinary (a) Refractive indices and (b) Extinction coefficients of PDI-8CN$_2$ films grown on SiO$_2$ and PDLA

Determined optical constants for a PDI-8CN$_2$ film grown on PDLA are shown in Figure 6.11 a) and b), as well as the optical constants for a PDI-8CN$_2$ film grown directly on SiO$_2$. The ordinary optical constants are similar between both films, with only small changes in magnitudes of features, while peak locations have not changed significantly. The knee present in the PDI-8CN$_2$ layer when grown on SiO$_2$ at 477 nm was present as a small peak at the same wavelength when grown on the PDLA dielectric. Extraordinary components displayed small differences between films. The general profile of the optical constants for the multilayer structure was similar to the original PDI-8CN$_2$ film, however differences in magnitude of the peaks and small shifts in location were present.

Differences in morphology evidenced themselves in the optical constants and in particular in the extraordinary components, observable by a change in peak magnitudes. Ordinary optical constants remained relatively consistent for all films. The magnitude of the extraordinary extinction coefficient profiles was significantly reduced when compared with the in-plane extinction coefficient, indicative of preferential alignment of the PDI-8CN$_2$ molecules on the surface of the dielectric. To quantify and compare the orientation of the molecules on the two dielectric surfaces, the order parameter Φ was used [265]:

$$\Phi = \frac{1}{2}\left\langle 3\cos^2\theta - 1 \right\rangle = \frac{k_o - k_e}{k_e - 2k_o} \tag{6.19}$$

where θ is the average angle between the optical axis and the chain axis of the molecules and Φ quantitatively describes the anisotropy of the film (Φ = 0 implies a completely isotropic film while Φ = -0.5 indicates a completely uniaxially anisotropic film). For each peak in the extinction coefficient profile for PDI-8CN$_2$ samples grown on both SiO$_2$ and PDLA dielectric surfaces, the value of Φ was calculated and from this θ was determined, shown in Table 6.7.

Table 6.7: Comparison of Φ and θ for PDI-8CN$_2$ layers grown on SiO$_2$ and PDLA dielectrics

Peak Location (nm)	**Φ (SiO$_2$)**	**Φ (PDLA)**	**θ (SiO$_2$)**	**θ (PDLA)**
~477	-0.39	-0.31	30.66°	27.04°
~505	-0.39	-0.36	30.66°	29.36°
~550	-0.37	-0.39	29.78°	30.66°

The value for θ determined from each of the three absorption peaks for samples grown on both dielectrics was approximately 30°. This demonstrates that although there were morphological changes induced by the presence of a PDLA film, there were no major structural changes in the PDI-8CN$_2$ thin films. The only value that did not agree as well with the rest of the data was the value of Φ (and corresponding θ) calculated from the 477 nm absorption peak. The discrepancy was not substantially large and was likely due to a small overestimation of the 477 nm extraordinary absorption peak during the fitting process. While the peak at 477 nm was undoubtedly a present feature, the difficulty in obtaining high sensitivity to extraordinary properties of a sample may explain this slight error.

6.4.3 AFM Measurements of PDI-8CN$_2$

AFM measurements were performed on PDI-8CN$_2$ layers grown on bare SiO$_2$ and PDLA layers in order to observe changes in the surface characteristics and morphology of the semiconducting layer induced by the different dielectric. These AFM measurements were performed on a different system than those in Chapter 4; in this instance an XE100 Park instrument operating in non-contact mode (amplitude modulation, silicon nitride cantilever from Nanosensor), located at the Università di Napoli, Federico II microscopy laboratory was used. All analysis was performed using software provided by Park Systems with the instrument.

Figure 6.12 shows that, in both cases, the PDI-8CN$_2$ films displayed crystalline islands which organised mainly in a ribbon-like grain structure. For films deposited on bare SiO$_2$ substrates, the crystallites were terraced and exhibited an oval shape with rounded corners, in agreement with previous reports [209]. On PDLA covered substrates the crystalline islands were more elongated in one direction and assumed a characteristic needle-like shape. While the terraced features were less visible, the overall size of the crystallites was increased and their edges preferentially faceted. The morphology of the films on PDLA covered SiO$_2$ substrates seemed to resemble very closely that of PDI-8CN$_2$ films deposited on octadecyltrichlorosilane (OTS) treated SiO$_2$ layers, as discussed by [270].

In order to obtain quantitative parameters able to better define the morphology of the PDI-8CN$_2$ films investigated in this work, R_{RMS} values were obtained through analysis software. The correlation length (ξ) and the saturation value (σ_{sat}) of R_{RMS} were extracted through the Gwyddion Scanning Probe Image Processor, by fitting the Power Spectrum Density (PSD) function:

$$PSD(f) = \frac{1}{L}\left|\int_0^L dx h(x) e^{i2\pi fx}\right|^2 \qquad (6.20)$$

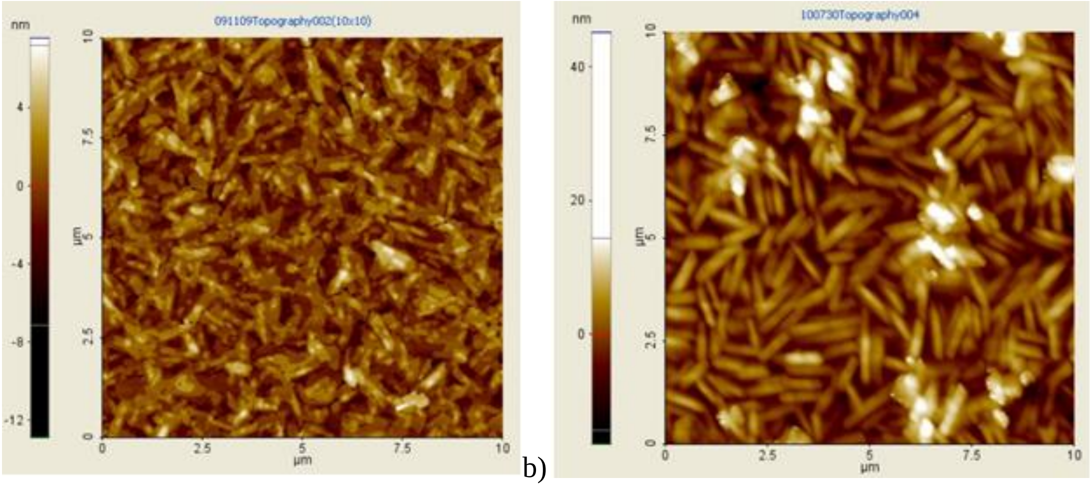

a) b)

Figure 6.12: 10 µm x 10 µm AFM images of PDI-8CN$_2$ grown on (a) Bare SiO$_2$ and (b) SiO$_2$ covered with a PDLA layer

where h(x) is the apparent topographical height with respect to the mean height, calculated on images of size L, x is the fast scan direction and f the spatial frequency. The PSD extracted for self-affine structures (i.e. those which preserve a similar morphology upon rescaling of the third dimension, z) exhibits a plateau at low frequency, followed by a power law decay. The inverse of the frequency corresponding to the intersection between the plateau and the decay region gives the correlation length, while the low frequency plateau is related to the saturated roughness.

Palasantas et al. [272] have demonstrated that ξ is directly correlated to the effective radius of the surface domains of the film under study, highlighting the characteristic features of the film growth mode. The results of this analysis, which more clearly identifies the differences in PDI-8CN$_2$ morphology on bare and PDLA covered SiO$_2$ substrates, are summarised in Table 6.8.

Table 6.8: Values of R_{RMS}, σ_{sat} and ξ for bare and PDLA covered substrates

Dielectric Surface	**R_{RMS} (nm)**	**σ_{sat} (nm)**	**ξ (nm)**
Bare SiO_2	1.7	1.78 ± 0.03	147.1 ± 0.7
PDLA covered SiO_2	5.6	4.68 ± 0.01	299.1 ± 1.9

It was confirmed that the samples grown on the PDLA surface exhibit simultaneously both a higher roughness (an increase of approximately 4 nm) and increased island dimension with an almost doubled ξ value. It is however very important to highlight that the agreement between R_{RMS} and σ_{sat} parameters validate the above described fitting procedure, based on self-affine fractal surface theory. It can be seen then that PDLA dielectrics have influenced the thermal growth of PDI-8CN_2, through the differences in the topography of the films. There were two likely sources of this influence of the dielectric over the morphological and optical properties of the PDI-8CN_2 film; the first is the change in topography of the dielectric and the second is the change in the surface properties of dielectric. As demonstrated by previous AFM investigations presented in Chapter 4, PDLA films exhibit very smooth surfaces with an average roughness of approximately 0.20 nm. According to various studies reported in literature, the influence of the dielectric topography on the growth of organic films is minimal when the roughness is less than 0.4 – 0.5 nm [195, 196]. Based on this reasoning, it would be expected that other factors directly related to PDLA should have an influence on the growth mode of PDI-8CN_2 films. For example, untreated SiO_2 has a contact angle with water of 35.72°, and a surface energy of ~60 mJ m^{-2} [210], i.e. SiO_2 is more hydrophilic and has a higher surface energy. Comparatively, OTS treated SiO_2 has a contact angle of ~79° and a surface free energy of ~28 mJ m^{-2}. As noted, the morphology of PDI-8CN_2 thin films grown on PDLA layers was similar to that when grown on OTS treated SiO_2; PDLA and OTS treated SiO_2 evidently have similar properties with respect to their surface energies. Differences in the morphology of the PDI-8CN_2 films grown on PDLA dielectrics were therefore attributed to the difference in the nature of the substrate surface, though the difference in surface chemistry likely also has an influence.

6.5 OFET Fabrication and Characterisation

6.5.1 Theory and Methods

A complete electronic device’s behaviour is governed not just by the properties of the individual layers, but is also influenced by the complex interactions between each of these with one another. In OFET devices, the interactions between the dielectric material and the OSC layer are particularly important. Steps towards quantifying the degree of this interaction were taken in Section 6.3.3, where the surface energy of PDLA layers was investigated. While useful, these characteristics do not ultimately determine the electrical behaviour of devices which include this interface. The fundamental and electrical properties of PDLA layers showed they would be a potential candidate for OFET device applications. To substantiate this, a Si wafer with an oxide layer of 500 nm was used as the substrate to fabricate the OFET device. This choice was made for compatibility with laboratory equipment and procedures, and allowed for the isolation of the interface effects over device performance. By ignoring this step it is difficult to attribute the cause of non-functional devices to any one source related to the dielectric layer. In the case where the SiO_2 layer is present, only the interface effects and influence of PDLA over the electrical properties of the OSC are under investigation and this is hence the most beneficial starting point. A pentacene layer with a nominal thickness of 100 nm was thermally evaporated on top of the PDLA layer at a rate of 0.5 Å s^{-1} monitored by a quartz microbalance, and the devices completed with 50 nm thick Au S/D electrodes with channel dimensions L/W equal to 50 μm and 3 mm respectively [273].

In an OFET the relationship between V_{GS}, V_{DS} and I_{DS} is typically given by two operating characteristics for the device, the transfer curve and the output curves. The transfer curve plots, for some constant V_{DS}, the output current I_{DS} as a function of the applied input voltage V_{GS}. The output curves plot the relationship between the output current I_{DS} and the output voltage V_{DS} at various values of constant applied input potential V_{GS}. These curves provide the electrical behaviour of a complete device, and are influenced by many parameters, such as the geometry of the device, the properties of the OSC and the resistivity and permittivity of the dielectric layer. The electrical properties of the complete device were hence studied through production of, and investigation into, the transfer and output curves (hence referred to as the IV curves) of the device. IV curves for the device were measured in air. In these experiments transfer curves were measured from -100 V to 100 V V_{GS} in the saturation regime ($|V_{DS}| = 100$ V) while output characteristics were measured between $0 \leq |V_{DS}| \leq 100$ V at six values of V_{GS} between $0 \leq |V_{GS}| \leq 100$ V.

6.5.2 IV Curves of a Pentacene OFET Device

In the saturation regime ($|V_{DS}|$ is large), the transfer curve of an OFET device closely follows the relation for a MOSFET device:

$$I_{DSAT} = \frac{WC_D}{2L}\mu(V_{GS} - V_{TH})^2 \tag{6.21}$$

where L and W are the channel length and width respectively, C_D is the capacitance per unit area of the gate dielectric, V_{GS} is the applied gate-source voltage and V_{TH} is the device threshold voltage. When the channel dimensions and dielectric capacitance are known, the carrier mobility and threshold voltage can be determined through analysis of the transfer curve by fitting a linear equation to $I_{DSAT}^{1/2}$ (V_{GS}). In the device with a composite dielectric structure, the equivalent dielectric capacitance was used in place of C_D, which accounts for the thickness and permittivity of both dielectric layers.. The gradient of the linearised transfer curve is given by:

$$\frac{d(I_{DSAT}^{1/2})}{dV_{GS}} = \sqrt{\frac{WC_D}{2L}\mu} \tag{6.22}$$

and allows the calculation of device mobility. Rearranging (6.22) results in:

$$\mu = \left(\frac{dI_{DSAT}^{1/2}}{dV_{GS}}\right)^2 \frac{2L}{C_D W} \tag{6.23}$$

The intercept of the linear fit with the V_{GS}-axis gives the threshold voltage. Analytically this value can be determined by relating the y-intercept parameter in the linear regression to the constant term in the expansion of (6.21):

$$c = -V_{TH}\sqrt{\frac{WC_D}{2L}\mu} \tag{6.24}$$

Rearranging (6.24) results in:

$$V_{TH} = \frac{-c}{\dfrac{dI_{DSAT}^{\ 1/2}}{dV_{GS}}} \tag{6.25}$$

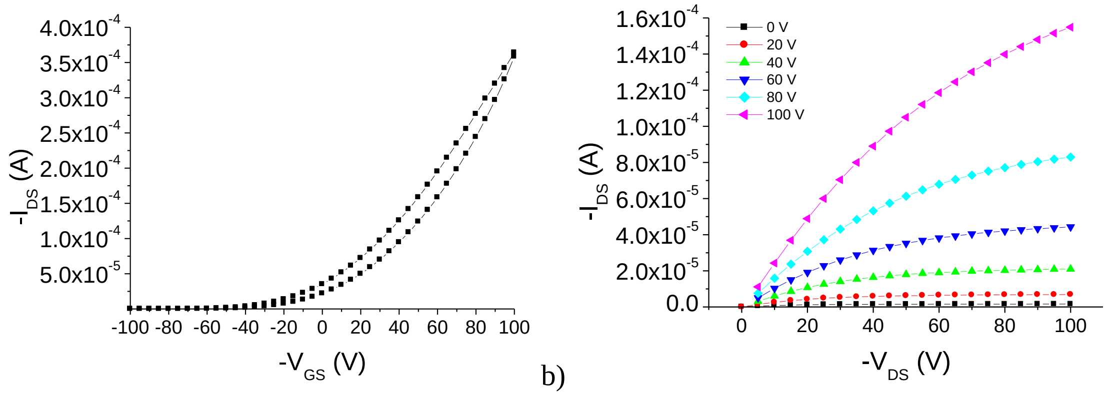

Figure 6.13: Pentacene OFET (a) Transfer and (b) Output curve

Figure 6.14 shows the result of fitting a linear curve to the modified saturation regime transfer curve for the pentacene OFET device including the PDLA layer shown in Figure 6.13. Due to the hysteresis present in the measured transfer curve, the top (forward going) current curve has been used in analysis. Using (6.24) and (6.25) and the results of this fit, the device mobility and threshold voltage were calculated to be 0.11 $cm^2\ V^{-1}s^{-1}$ and -44 V respectively. By examining the current at the most negative and most positive values of applied bias V_{DS}, the on/off ratio was determined to be 1.4173×10^5. These results were compared to those derived from a pentacene OFET fabricated under identical conditions with the same device geometry, directly onto SiO_2.

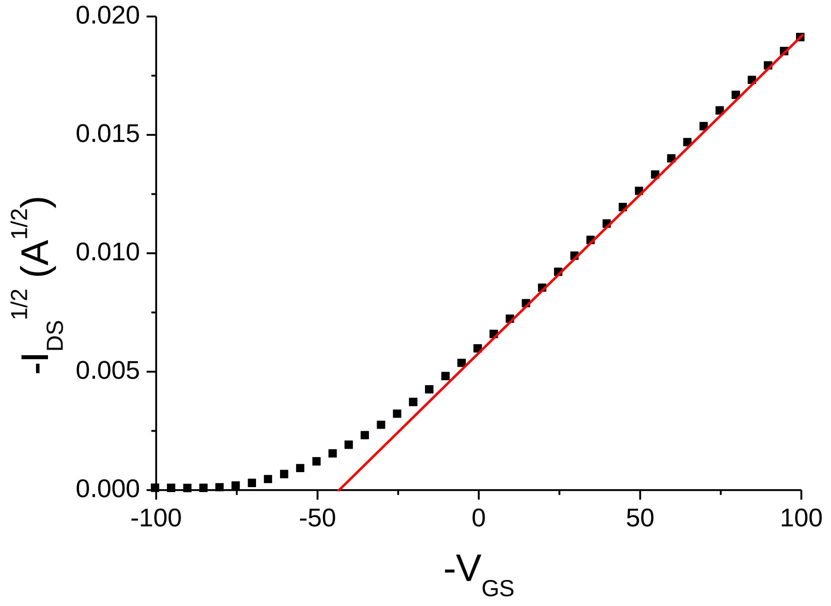

Figure 6.14: Linear fitting to $I_{DS}^{1/2}(V_{GS})$ (m = 1.3368 x 10^{-4}, c = 0.0059)

The device deposited on bare SiO_2 was found to have a mobility of 0.0033 cm^2 V^{-1} s^{-1}, a threshold voltage of -110 V and an on/off ratio of 361. Figure 6.15 shows that a large improvement in device characteristics is present when a PDLA dielectric layer is included in the device structure.

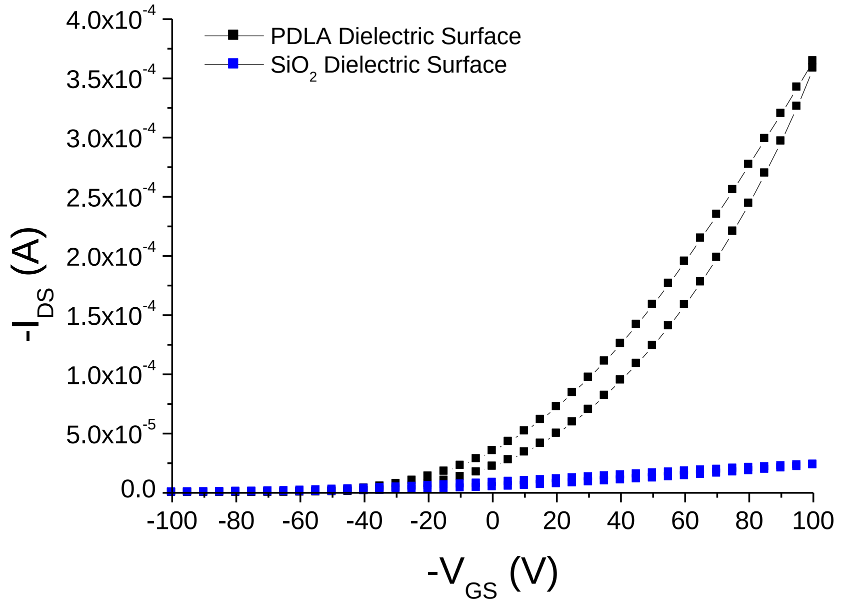

Figure 6.15: Comparison between transfer curves of pentacene OFET devices fabricated with and without a PDLA dielectric layer

Table 6.9: Operating characteristics of pentacene OFET devices fabricated with and without a PDLA dielectric layer

Parameter	**SiO_2**	**SiO_2/PDLA**
μ ($cm^2 V^{-1} s^{-1}$)	0.0033	0.11
V_{th} (V)	-110	-44
I_{on}/I_{off}	~10^2	~10^5

OFET devices incorporating the PDLA have improved operating characteristics with respect to all identified device properties. The mobility, threshold voltage and on/off ratio were all significantly affected by the change in dielectric surface. This is explained by the change in surface chemistry and surface energy. Changes induced in the structure and morphology of the pentacene layer were likely responsible for the change in device mobility, while reduction in interfacial trapping at the OSC/dielectric interface likely resulted in the reduction of $|V_{th}|$. The increased thickness of the dielectric layer combined with the high resistivity of the PDLA layer resulted in a decrease of the off current, which when combined with the increase in on current due to the higher mobility, explain the improved on/off ratio. This behaviour is similar to studies in which OFET devices were deposited onto SiO_2 surfaces subject to modification of the surface chemistry and surface energy through hexamethyldisilazane (HMDS) and the improvement in device behaviour attributed to the difference in pentacene morphology induced by the different dielectric surface [155]. These results are additionally in good agreement with results in Section 6.4 investigating the influence of the PDLA surface properties over the growth and morphology of the n-type semiconductor PDI-8CN_2. While the semiconductors differ, it is reasonable to assume a similar degree of influence over the OSC layer in this case as well.

6.6 Conclusions

The compatibility of PDLA thin films with fabrication techniques utilised in the creation of organic electronic devices has been investigated in this chapter. Two processes were identified as being used frequently in organic electronics processing; thermal evaporation and annealing, and deposition of OSC solutions. In these processes, the previously deposited layers, including PDLA thin films, may be exposed to high temperatures and organic solvents. The thermal degradation of PDLA thin films was investigated through VASE measurements, and its surface properties investigated through CA measurements.

It was found that onset of thermal degradation began at approximately 200 °C for all samples, inferred by a reduction in thickness and significant changes in the optical profiles. Up to this temperature, the thickness, refractive index and extinction coefficient remained stable. This indicated that temperatures up to 200 °C could safely be applied to the material or any substrate it is adhered to during either thermal evaporation or annealing processes without adversely affecting the optical properties (such as transparency) of the material or changing its thickness. As there was no indication of structural changes (e.g. densification) in the refractive index and thickness, which remained constant, it is not expected that the dielectric properties of the material would change significantly through the heating process. From these studies it was concluded that PDLA layers are suitable for use in organic electronic devices requiring thermal evaporation and annealing stages, up to 200 °C.

Table 6.10: Summary of chapter results

Property Investigated	Parameter	Remarks	Power Dependence	Relationship
Thermal Degradation	Thickness	Begins to reduce at 200 °C	Very small - none	-
	Refractive Index	Unaffected up to 200 °C		
	Extinction Coefficient	Unaffected up to 200 °C		
Surface Parameters	Contact Angle	Hydrophilic	Moderate	CA increased as power increased
	Surface Energy	~42 mJ m^{-2}	None	-
	Surface Energy Components	Monopolar, LW dominated	Moderate	AB component decreased as power increased
	Wetting Envelope	Wettable for low AB liquids	Moderate	Samples less hydrophilic as power increased
	Interfacial Tension	Positive in all cases	Small	Generally larger with increased power
	Solubility	Insoluble in most solvents	Small	Generally less soluble with increased power
Growth of OSC	Optical profile of PDI-8CN_2	Minimal changes in anisotropy	-	-
	Surface Morphology of PDI-8CN_2	Increased roughness and change in morphology	-	-

CA measurements were then performed, with the principle goal of determining the solubility of the material in key liquids used as solvents in solution processing of OSCs, such as chloroform and dichlorobenze. Three analysis techniques were used to determine the total surface energies, and where made available by the technique, the Lifshitz-van der Waals and acid-base components were also determined. The VCG, Neumann and Fowkes method all resulted in a total surface energy of ~42 mJ m^{-2}, the VCG and Neumann methods providing the highest estimate of ~43 mJ m^{-2} while the Fowkes method resulted in a value of ~39 mJ m^{-2}. The VCG method showed that the surfaces were largely monopolar in nature, evidenced by the large value of γ^- relative to γ^+, which was negligible for all samples investigated. The acid-base component of the surface energy derived from both the VCG and Fowkes methods showed a tendency to decrease as the power density increased, and a larger value of ~7 mJ m^{-2} was obtained through the Fowkes analysis compared to ~2 mJ m^{-2} from the VCG method. The Neumann method provided no additional information regarding the component surface energies.

To obtain a better understanding of the material and its expected interactions with a variety of liquids, the component surface energy values for the material derived from the VCG and Fowkes analyses were used to generate wetting curves for each surface investigated, and boundaries of 0°, 20°, 40°, 60° and 80° used. All curves showed that the samples became more hydrophobic as the power density was increased, seen by the tendency for the constant angle boundaries to move closer toward the origin as power density was increased, indicating that the same probe liquid would have a higher contact angle. Curves derived from parameters determined using Fowkes analysis tended to have better agreement with the experimentally measured contact angles for the three probe liquids. Chloroform and dichlorobenzene were both shown to fall within the 0° boundary, indicating they would completely wet the surface and not provide a measurable contact angle.

The interfacial tension between the surface and a variety of common solvents was then investigated to determine the solubility of the material. In all cases it was found that PDLA is insoluble, including in chloroform and dichlorobenzene, solvents commonly used to produce

OSC solutions. In the case of EG and DIM, the value of interfacial tension was small and near to zero, indicating that the material may swell when in contact with these liquids, explaining the initially higher rate of change of CA in the transient measurements performed. No such behaviour in chloroform or dichlorobenzene was predicted. It was therefore concluded that PDLA dielectric layers could be compatible with solution processing of organic electronics, though the solubility in solvents not investigated here should be checked prior to device fabrication. Additionally, while the material is not soluble in these solvents, other practical issues may arise, such as changes in adhesion, or the dielectric properties of the material.

Layers of the n-type OSC PDI-8CN$_2$ were thermally deposited on PDLA layers, and their optical and morphological properties compared to PDI-8CN$_2$ films deposited on standard SiO$_2$ surfaces. This resulted in the optical characterisation of the OSC, previously unreported until this study. It was found that the morphology of the PDI-8CN$_2$ layers was different when grown on PDLA surfaces, having higher surface roughness and an increased crystallite island dimension, comparable to PDI-8CN$_2$ layers grown on OTS surfaces. These differences were attributed to the change in surface energy and surface chemistry of the PDLA layers when compared to SiO$_2$ layers. Investigation of the degree of optical anisotropy of the PDI-8CN$_2$ layers grown on the different substrates revealed that the molecular chain axis tilt remained approximately the same, indicating no significant structural changes in the film.

OFET devices utilising pentacene as the active channel were fabricated. Two devices, one utilising 500 nm SiO$_2$ dielectric layer and one utilising a 500 nm/100 nm SiO$_2$/PDLA dielectric structure were compared. It was found that inclusion of the 100 nm PDLA layer improved the device performance with respect to the mobility by two orders of magnitude and significantly improved both the threshold voltage and on/off ratio. These improvements were attributed to the influence of the PDLA surface over the OSC layer. This work represents an important step towards integration of PDLA layers into organic electronic devices, highlighting the compatibility of the PDLA surface with OSC layers and demonstrating the potential for improved device operating characteristics.

This chapter has then established that PDLA dielectric layers are compatible with high temperature processing, up to 200 °C and solution processing using solvents such as dichlorobenzene and chloroform, both of these processes being common in the fabrication of organic electronic devices. This was further established by the thermal deposition of an OSC on the dielectric surface, and the demonstration that the structure of the organic layer remains largely unchanged. OFET devices were then fabricated, and shown to provide significant improvements in the performance over devices fabricated in similar conditions without PDLA layers. The material's desirable dielectric and optical properties, its compatibility with common fabrication techniques and demonstrated improvement over device operating characteristics make it a viable candidate for use in organic electronic devices.

Chapter 7: Conclusions and Future Work

7.1 Outcomes

In recent years, organic electronics has undergone rapid growth and development as materials and devices approach commercial viability and adoption. However, much research still focuses on devices utilising Si substrates that do not exploit the advantages offered by organic technology such as optical transparency and mechanical flexibility. Materials which share these qualities in addition to being low in cost and compatible with organic electronic devices and fabrication methods are required. In this thesis, an environmentally friendly, low cost and transparent thin film material suitable for applications in organic electronics was developed. This material was derived from the monomer linalyl acetate, the dominant component of *Lavandula angustifolia* essential oil, and fabricated using PECVD. The fundamental and electrical properties of the material were investigated, in addition to the compatibility of the material with current processing techniques used in fabrication of organic electronic devices. The outcomes of these studies are outlined below.

7.1.1 Fabrication of Linalyl Acetate Thin Films and their Fundamental Properties

Using PECVD, linalyl acetate thin films were successfully fabricated and their fundamental properties determined. Fundamental properties were defined based upon the attributes most commonly reported in literature for new materials, and included the material’s optical, morphological and chemical properties. To investigate PDLA thin film optical properties, VASE and UV-Vis spectroscopy measurements were undertaken. VASE measurements confirmed that the films were optically transparent, with a refractive index of approximately 1.55 at 589 nm. UV-Vis spectroscopy measurements also showed the films to be optically transparent, with only one absorbance peak at approximately 300 nm. From these absorbance measurements, the optical band gap of the films was determined to be 3 eV, categorising the films as insulating materials though with the possibility of becoming semiconducting with appropriate doping. The optical properties of the films were shown to be independent of their thickness, and the films were also found to be optically isotropic.

The topographical properties of the material were investigated using AFM to measure the surface topography and nano-indentation was used to measure its hardness. The PDLA layers were found to be amorphous, free of pinholes and other defects, and smooth. From analysis of the topography, the roughness was precisely quantified across a scan area of 1 μm x 1 μm and determined to have an average value of 0.2 nm. The hardness of the material, determined from nano-indentation studies, was found to be 0.4 GPa.

Chemical studies were undertaken to investigate both the bulk and surface chemical properties of PDLA thin films. Bulk chemical functionality was measured utilising ATR-FTIR and the samples were found to possess predominately hydrocarbon functionalities, with oxygen present in the form of hydroxyl and ketone functional groups, likely from oxygen containing functionalities in the original monomer and post-deposition ageing reactions between radicals embedded in the plasma deposited thin film and atmospheric O_2 and H_2O. XPS measurements of the surface chemistry provided additional confirmation of the chemical properties of the material, through analysis of high resolution C 1s spectra showing predominately hydrocarbon bonding environments in addition to some oxygen-containing moieties.

7.1.2 Electrical Properties of PDLA

The electrical properties of PDLA thin films were investigated in the frequency range of 0 Hz - 20 GHz. As the measurement technique was dependent upon the frequency range at which the properties were investigated, the spectrum was divided into three frequency regimes; the dc region, the ac region and the MW region. In the dc region, IV characterisation from 0 V - 200 V was used to determine the charge transport mechanism in the material, the dc conductivity and the dielectric breakdown strength. Analysis of the shape of the JV curves and comparison to standard charge transport models for insulating thin films showed that RS conduction was the predominate mechanism of charge transport in the films. The dc conductivity was found to be on the order of 10^{-11} Ω^{-1} m^{-1}, and at the high limits of applied electric fields dielectric breakdown occurred at of 1.8 MV cm^{-1}. Dielectric breakdown was tested for films of low, moderate and high thicknesses and found to be dependent only on applied field and not film thickness.

In the ac frequency region, between 10 Hz and 100 kHz, IS measurements were used to determine the dielectric function of the PDLA thin films. These measurements were performed under heating in order to excite relaxation phenomena to frequencies within the experimental measurement range to allow better modelling of the material’s dielectric function. This modelling was performed using a generalised relaxation function, dependent on a distribution of relaxation times and the dielectric constant of the material. Through modelling, it was found that the low frequency permittivity of the material was approximately 11, while the high frequency permittivity was found to be approximately 3. The distribution of relaxation times was found to possess multiple peaks, one of which clearly dominated and was responsible for the main peak in the measured loss spectrum. The high frequency dielectric constant was then directly verified by MW measurements at 10 GHz and 20 GHz using the SPDR method, where the dielectric constant was found to be 2.4. Electrical characterisation of the material resulted in a description of its complex dielectric function, experimentally verified at 0 Hz, 10 Hz - 100 kHz, 10 GHz and 20 GHz, though theoretically available for all frequencies. Knowledge of this function allows calculation of a device capacitance given a particular operating frequency, temperature and dimensions, which is of considerable design importance. Very low conductivity was observed which was maintained up until the occurrence of dielectric breakdown at 1.8 MV cm^{-1}. Due to the low conductivity and low permittivity characteristics, the material was then considered as a potential insulating layer in OFET devices.

7.1.3 Identification and Investigation of PDLA in Organic Electronics Applications

Electrical measurements showed the material to demonstrate highly insulating, low permittivity behaviour. Optically the material is transparent and possesses a smooth topography. The combination of these properties makes PDLA thin films an ideal candidate for dielectric layers in OFET devices, where SiO_2 dielectric layers remain common. To be implemented in an OFET device, it was identified that PDLA should be capable of withstanding the processing procedures required for deposition of OSC layers, namely, exposure to high temperatures and exposure to organic solvents such as chloroform and dichlorobenzene. The thermal and chemical stability were therefore investigated using temperature dependent VASE and CA measurements respectively. Onset of thermal degradation was found to occur at 200 °C, well above annealing temperatures commonly utilised in fabrication of OSC layers, therefore demonstrating the films meet the thermal requirement. CA measurements were analysed using multiple methods found the surface free energy of the PDLA layers to be ~44 $mJ\ m^{-2}$ and showed the surface to be monopolar. Interaction of the material with different solvents was then modelled through the calculation of interfacial tensions and production of wetting curves, which showed that the films were insoluble in common solvents such as chloroform and dichlorobenzene, and would completely wet when in contact with them. As they are insoluble in the investigated organic solvents, the thin films also meet the insolubility processing requirement. Additionally, as the dispersive and polar components of the surface free energy of the material are known, and with the aid of wetting curves, the expected interaction with any other solvent desired can be determined in future work.

The literature review identified that the structural ordering of OSC thin films was a critical determining factor for their overall performance, particularly with respect to their carrier mobility. This property was shown to be sensitive to a variety of factors, including the surface on which the OSC is deposited. PDI-8CN_2 layers were therefore deposited on standard SiO_2 substrates and on PDLA layers and their optical and morphological features compared using VASE and AFM measurements. This required the optical modelling of the PDI-8CN_2 OSC, which was shown to be optically anisotropic. The degree of anisotropy is correlated to the structural ordering of the material, and hence this property was used to verify that no bulk structural changes were induced in the material when grown on PDLA layers as there was no change in the degree of anisotropy. Morphological changes were induced, and the morphology of the OSC layer when deposited on PDLA was similar to that when deposited on OTS treated SiO_2, most likely due to their similar surface free energies. PDLA layers were successfully used in a pentacene OFET device as a buffer layer above the existing SiO_2 dielectric. They were found to improve the device operating characteristics over those deposited under the same conditions without the PDLA layer, as evidenced through an increase in mobility and on/off ratio and decrease of the threshold voltage.

7.1.4 Investigation into the Link between Deposition Conditions and Film Properties

In nearly all studies the parameter W/FM was varied by changing in the RF power delivered to the deposition chamber during film fabrication while keeping the flow rate and monomer fixed. This parameter was shown in literature to be the principle determining factor in the overall film properties. It was found that PDLA tended to have properties which were relatively constant, independent of the power density used, with a few notable exceptions. With respect to fundamental properties, the absorbance (i.e. transparency of the film) and optical bandgap were found to be unaffected by the power density, while the refractive index showed a very small dependence, increasing slightly as power density decreased. The surface topography was shown to be unaffected by changing deposition conditions, and the surface roughness remained constant across all powers investigated. The hardness of the material did however undergo significant variation, increasing from 0.35 GPa to 0.45 GPa as RF power increased from 10 W to 75 W. This was attributed to an increase in crosslinking in the film, expected from literature reports and an increase in carbon content, corroborated by XPS measurements which showed an increase in surface carbon content from 75% to 85% as RF power was varied. Despite the change in surface chemistry, no significant change in bulk chemical functionality was observed in FTIR measurements.

The JV curves showed a decrease in dc conductivity as power density increased, and IS measurements showed a similar trend with permittivity. The reduction in permittivity at higher

RF energies is attributed to the reduction in more polar oxygen functionalities, while the decrease in conductivity is attributed to the increase in crosslinking in samples fabricated in higher energy conditions. Films could be fabricated with an increased permittivity at the cost of a decrease in resistivity, or an increased resistivity with lower permittivity; generally the latter is considered more desirable.

Finally, as part of CA studies, the influence of the power density on surface energy parameters was investigated. It was found that as the power density increased, the polar contribution to the total surface energy decreased while the dispersive component increased, though the total surface free energy remained relatively constant. The decrease in the polar component of surface energy was again attributed to the reduction in the more polar oxygen functionalities at the surface observed in XPS measurements. No significant trend was observed in the solubility of the material in various solvents as a function of RF power; films deposited at all power densities were shown to be insoluble in all liquids investigated. Onset of thermal degradation was also found to be slightly delayed in films deposited at higher power densities.

As a result of these studies, it was determined that samples fabricated at higher power densities are generally preferred; they are harder, less conductive, lower permittivity, contain less surface oxygen and still possess desirable properties such as transparency, low surface roughness and high breakdown strength. For OFET devices, films were deposited at higher power densities to decrease the dielectric conductivity and hence reduce leakage currents. In addition, the reduction of surface oxygen functionality is expected to reduce the availability of trapping sites and hence improve device mobility and threshold voltage, confirmed by measurements of a pentacene OFET including a PDLA buffer layer. Outside of OFET devices, the relation to deposition parameters of all key material properties is now available, and can be utilised to guide design choices during the fabrication of PDLA thin films for other applications. A summary of all investigated material properties is given in Table 7.1.

7.2 Contributions to Knowledge

As a result of this thesis and addressing the stated research objectives, the following contributions to knowledge in the field of materials science and engineering have been made:

1. A new material has been developed from a non-synthetically derived monomer.

Development of a new product is a fundamental area of research and an important aspect of materials research. In this thesis, a transparent, environmentally stable, smooth and defect free thin film material has been developed from the previously unreported monomer linalyl acetate, derived non-synthetically from essential oils. The extraction of the monomer from agriculture produce through distillation, and the PECVD process resulted in films which are cheap, environmentally friendly and useful for a variety of applications. The fundamental properties of this material and their relationship to the deposition conditions are well understood.

2. The electrical properties of the material have been determined in detail.

To assess the viability of PDLA thin films in organic electronic applications and to assist the design process, the charge carrier mechanism, conductivity, breakdown field and complex dielectric function from dc to optical frequencies have been determined. In addition, many of these properties were studied as a function of power density and operating temperature. Knowledge of these parameters allows for the design of devices with precise electrical characteristics to elicit an optimised response.

3. A specific application has been identified, the compatibility of the material with modern OSC fabrication techniques assessed and a proof-of-concept device successfully fabricated.

In this work, studies towards assessing the viability of PDLA thin films in organic electronics have been completed, and the critically important factor of processing compatibility addressed. These studies allow further research into device design and testing. Additionally, they allow for immediate elimination of some potential issues should devices not function as expected.

7.3 Recommendations and Future Work

This research has provided a large basis for further work utilising the newly developed PDLA thin films. The focus of the work was electrical applications, however the properties described in this thesis allow for study of the material in optical and protective applications as well. The primary recommendation for future work is therefore to investigate the potential of the material in these, using the information provided in this thesis. Further recommendations for future work are based solely on the prospect of specific organic electronic applications.

Firstly, while the thermal degradation and solubility of PDLA thin films have been shown to be sufficient for organic electronic applications, further study on the influence of these processes on specific properties should be undertaken. For example the dielectric function and conductivity should be determined after exposure to various solvents to ensure the electrical properties remain unaffected. Additionally, solvent exposure and heating were in this work considered separate and independent processes; studies should be performed using sequential steps to simulate more accurately the device fabrication process.

Secondly, only specific types of OFET device and two OSCs have been investigated. While these are incredibly important proof-of-concept studies, possible avenues of future research could involve investigations into different device architectures and modification of deposition parameters and procedures to accommodate these, and investigations into the interaction between PDLA layers and different OSC layers. Further investigations into optimisation of device performance through modification of the dielectric (for example through surface treatments, UV treatments etc.) may also be investigated.

Finally, in device applications, predominately thermally deposited layers were investigated. As organic electronics research progresses, more effort is being devoted towards solution processed materials, fabricated quickly on flexible substrates. There is rich potential in this area to investigate integration of PDLA layers into these processes.

Table 7.1: Summary of key material properties

Property	**Deposition Energy**			
	10 W	**25 W**	**50 W**	**75 W**
Refractive index (λ = 589 nm)	1.55	1.56	1.57	1.58
Extinction coefficient (λ = 589 nm)	0.003	0.003	0.003	0.003
Optical band gap (eV)	3.02	2.96	2.96	2.95
Average surface roughness (nm)	0.2	0.2	0.2	0.2
Hardness (GPa)	0.3	0.35	0.37	0.45
Conductivity (Ω^{-1} m^{-1})	4×10^{-11}	2.25×10^{-11}	1.75×10^{-11}	5×10^{-13}
High frequency dielectric constant	3.5	3.2	3.15	3
Breakdown strength (MV cm^{-1})	-	-	-	1.8
Thermal degradation onset (°C)	195	205	215	225
Surface free energy (mJ m^{-2})	46	47	46	45
Solubility in chloroform	Insoluble	Insoluble	Insoluble	Insoluble

References

[1] M. P. v. Wilde, "Vermischte Mittheilungen," *Ber. Dtsch. Chem. Ges.,* vol. 7, pp. 352-357, 1874.

[2] J. Goodman, "The formation of thin polymer films in the gas discharge," *J. Polym. Sci.,* vol. 44, pp. 551-552, 1960.

[3] X. Hu, X. Zhao, A. Uddin, and C. B. Lee, "Preparation, characterization and electronic and optical properties of plasma-polymerized nitriles," *Thin Solid Films,* vol. 477, pp. 81-87, 2005.

[4] A. Doucouré, C. Guizard, J. Durand, R. Berjoan, and L. Cot, "Plasma polymerization of fluorinated monomers on mesoporous silica membranes and application to gas permeation," *J. Membr. Sci.,* vol. 117, pp. 143-150, 1996.

[5] N. D. Tran, N. K. Dutta, and N. R. Choudhury, "Plasma-polymerized perfluoro(methylcyclohexane) coating on ethylene propylene diene elastomer surface: Effect of plasma processing condition on the deposition kinetics, morphology and surface energy of the film," *Thin Solid Films,* vol. 491, pp. 123-132, 2005.

[6] T. Shirafuji, Y. Nishimura, and K. Tachibana, "Plasma polymerization of fluorocarbon thin films on high temperature substrate and its application to low-k films," *Thin Solid Films,* vol. 515, pp. 4111-4115, 2007.

[7] A. J. Choudhury, J. Chutia, S. A. Barve, H. Kakati, A. R. Pal, Jagannath, N. Mithal, R. Kishore, M. Pandey, and D. S. Patil, "Studies of physical and chemical properties of styrene-based plasma polymer films deposited by radiofrequency Ar/styrene glow discharge," *Prog. Org. Coat.,* vol. 70, pp. 75-82, 2011.

[8] D. Hegemann, H. Brunner, and C. Oehr, "Evaluation of deposition conditions to design plasma coatings like SiOx and a-C:H on polymers," *Surf. Coat. Technol.,* vol. 174–175, pp. 253-260, 2003.

[9] A. Hiratsuka and I. Karube, "Plasma Polymerized Films for Sensor Devices," *Electroanalysis,* vol. 12, pp. 695-702, 2000.

[10] H. Yasuda and T. Yasuda, "The competitive ablation and polymerization (CAP) principle and the plasma sensitivity of elements in plasma polymerization and treatment," *J. Polym. Sci., Part A: Polym. Chem.,* vol. 38, pp. 943-953, 2000.

[11] H. Yasuda, L. Ledernez, F. Olcaytug, and G. Urban, "Electron dynamics of low-pressure deposition plasma," *Pure and Applied Chemistry,* vol. 80, pp. 1883-1892, 2008.

[12] K. K. Gleason, "A Chemical Engineering Perspective on “Views on Macroscopic Kinetics of Plasma Polymerisation”," *Plasma Process. Polym.,* vol. 7, pp. 380-381, 2010.

[13] M. C. M. van de Sanden, "Views on Macroscopic Kinetics of Plasma Polymerization: Acrylic Acid Revisited," *Plasma Process. Polym.,* vol. 7, pp. 887-888, 2010.

[14] P. Favia and R. d’Agostino, "Plasma treatments and plasma deposition of polymers for biomedical applications," *Surface and Coatings Technology,* vol. 98, pp. 1102-1106, 1998.

[15] H. Yasuda and Q. Yu, "Creation of Polymerizable Species in Plasma Polymerization," *Plasma Chem. Plasma Process.,* vol. 24, pp. 325-351, 2004.

[16] D. Hegemann, M. M. Hossain, E. Körner, and D. J. Balazs, "Macroscopic Description of Plasma Polymerization," *Plasma Process. Polym.,* vol. 4, pp. 229-238, 2007.

[17] J. Friedrich, "Mechanisms of Plasma Polymerization – Reviewed from a Chemical Point of View," *Plasma Process. Polym.,* vol. 8, pp. 783-802, 2011.

[18] M. R. Alexander and T. M. Duc, "A study of the interaction of acrylic acid/1,7-octadiene plasma deposits with water and other solvents," *Polymer,* vol. 40, pp. 5479-5488, 1999.

[19] L. Denis, D. Cossement, T. Godfroid, F. Renaux, C. Bittencourt, R. Snyders, and M. Hecq, "Synthesis of Allylamine Plasma Polymer Films: Correlation between Plasma

Diagnostic and Film Characteristics," *Plasma Process. Polym.,* vol. 6, pp. 199-208, 2009.

[20] D. Mangindaan, W.-H. Kuo, C.-C. Chang, S.-L. Wang, H.-C. Liu, and M.-J. Wang, "Plasma polymerization of amine-containing thin films and the studies on the deposition kinetics," *Surf. Coat. Technol.,* vol. 206, pp. 1299-1306, 2011.

[21] L. Denis, P. Marsal, Y. Olivier, T. Godfroid, R. Lazzaroni, M. Hecq, J. Cornil, and R. Snyders, "Deposition of Functional Organic Thin Films by Pulsed Plasma Polymerization: A Joint Theoretical and Experimental Study," *Plasma Process. Polym.,* vol. 7, pp. 172-181, 2010.

[22] D. Hegemann, E. Körner, and S. Guimond, "Plasma Polymerization of Acrylic Acid Revisited," *Plasma Process. Polym.,* vol. 6, pp. 246-254, 2009.

[23] C. Corbella, I. Bialuch, M. Kleinschmidt, and K. Bewilogua, "Up-scaling the production of modified a-C:H coatings in the framework of plasma polymerization processes," *Solid State Sci.,* vol. 11, pp. 1768-1772, 2009.

[24] L.-g. Wu, C.-l. Zhu, and M. Liu, "Study on plasma polymerization of 1.1.1-trifluoroethane: deposition and structure of plasma polymer films," *Desalination,* vol. 192, pp. 234-240, 2006.

[25] K. Hosono, I. Matsubara, N. Murayama, W. Shin, and N. Izu, "Effects of discharge power on the structure and electrical properties of plasma polymerized polypyrrole films," *Mater. Lett.,* vol. 58, pp. 1371-1374, 2004.

[26] Y. Martin, D. Boutin, and P. Vermette, "Study of the effect of process parameters for n-heptylamine plasma polymerization on final layer properties," *Thin Solid Films,* vol. 515, pp. 6844-6852, 2007.

[27] L. Ledernez, H. Yasuda, F. Olcaytug, F. Gemetz, and G. Urban, "Pressure Dependence of Plasma Polymerization of Methane at Constant W/FM," *Plasma Process. Polym.,* vol. 4, pp. S794-S796, 2007.

[28] A. von Keudell and J. Benedikt, "A Physicist's Perspective on “Views on Macroscopic Kinetics of Plasma Polymerisation”," *Plasma Process. Polym.,* vol. 7, pp. 376-379, 2010.

[29] A. Kiesow and A. Heilmann, "Deposition and properties of plasma polymer films made from thiophenes," *Thin Solid Films,* vol. 343–344, pp. 338-341, 1999.

[30] C. L. Chapman, D. Bhattacharyya, R. C. Eberhart, R. B. Timmons, and C.-J. Chuong, "Plasma polymer thin film depositions to regulate gas permeability through nanoporous track etched membranes," *J. Membr. Sci.,* vol. 318, pp. 137-144, 2008.

[31] D. Hegemann, E. Körner, and S. Guimond, "Reply to: “Testing the Hypothesis: Comments on Plasma Polymerization of Acrylic Acid Revisited”," *Plasma Process. Polym.,* vol. 7, pp. 371-375, 2010.

[32] J. D. Whittle, R. D. Short, and D. A. Steele, "Reply to “Testing the Hypothesis: Comments on Plasma Polymerization of Acrylic Acid Revisited”," *Plasma Process. Polym.,* vol. 8, pp. 687-688, 2011.

[33] D. Hegemann, U. Schütz, and E. Körner, "Macroscopic Approach to Plasma Polymerization Using the Concept of Energy Density," *Plasma Process. Polym.,* vol. 8, pp. 689-694, 2011.

[34] H. Biederman and O. Kylián, "Some Remarks to Macroscopic Kinetics of Plasma Polymerization," *Plasma Process. Polym.,* vol. 8, pp. 475-477, 2011.

[35] I. S. Bae, C. K. Jung, S. J. Cho, Y. H. Song, and J. H. Boo, "A comparative study of plasma polymerized organic thin films on their electrical and optical properties," *Journal of Alloys and Compounds,* vol. 449, pp. 393-396, 2008.

[36] S. Krüger, R. D. Schulze, K. Brademann-Jock, S. Swaraj, and J. Friedrich, "Characterisation of plasma polymers by thermoluminescence," *Surf. Coat. Technol.,* vol. 201, pp. 543-552, 2006.

[37] J. Zhang, X. Feng, H. Xie, Y. Shi, T. Pu, and Y. Guo, "The characterization of structure-tailored plasma films deposited from the pulsed RF discharge," *Thin Solid Films,* vol. 435, pp. 108-115, 2003.

[38] H. Biederman, Y. Chevolot, P. Chabrecek, R. Houriet, H. Hofmann, and H. J. Mathieu, "X-ray photoelectron spectroscopy investigation and characterisation of plasma polymerised isocyanatoethyl methacrylate," *Vacuum*, vol. 68, pp. 161-169, 2002.

[39] H. Biederman and D. Slavínská, "Plasma polymer films and their future prospects," *Surf. Coat. Technol.*, vol. 125, pp. 371-376, 2000.

[40] H. K. Yasuda, "Some Important Aspects of Plasma Polymerization," *Plasma Process. Polym.*, vol. 2, pp. 293-304, 2005.

[41] R. Prikryl, V. Cech, L. Zajickova, J. Vanek, S. Behzadi, and F. R. Jones, "Mechanical and optical properties of plasma-polymerized vinyltriethoxysilane," *Surface and Coatings Technology*, vol. 200, pp. 468-471, 2005.

[42] B. D. Beake, G. J. Leggett, and M. R. Alexander, "Scanning force microscopy of plasma polymerised hexane: information on the mechanical properties of thin films from tip-induced wear," *Polymer*, vol. 42, pp. 2647-2653, 2001.

[43] M. C. Kim, S. H. Cho, J. G. Han, B. Y. Hong, Y. J. Kim, S. H. Yang, and J. H. Boo, "High-rate deposition of plasma polymerized thin films using PECVD method and characterization of their optical properties," *Surf. Coat. Technol.*, vol. 169–170, pp. 595-599, 2003.

[44] C. D. Easton and M. V. Jacob, "Optical characterisation of radio frequency plasma polymerised Lavandula angustifolia essential oil thin films," *Thin Solid Films*, vol. 517, pp. 4402-4407, 2009.

[45] S. H. Cho, Z. T. Park, J. G. Kim, and J. H. Boo, "Physical and optical properties of plasma polymerized thin films deposited by PECVD method," *Surf. Coat. Technol.*, vol. 174–175, pp. 1111-1115, 2003.

[46] I. S. Bae, C. K. Jung, S. H. Jeong, S. J. Cho, Y. J. Yu, J. G. Kim, and J. H. Boo, "Comparison of their electrical, optical, and electrochemical properties of as-grown plasma polymerized organic thin films by PECVD," *Thin Solid Films*, vol. 515, pp. 407-410, 2006.

[47] K. Bazaka and M. V. Jacob, "Solubility and Surface Interactions of RF Plasma Polymerized Polyterpenol Thin Films," *Materials Express*, vol. 2, pp. 285-293, 2012.

[48] F. Truica-Marasescu, P.-L. Girard-Lauriault, A. Lippitz, W. E. S. Unger, and M. R. Wertheimer, "Nitrogen-rich plasma polymers: Comparison of films deposited in atmospheric- and low-pressure plasmas," *Thin Solid Films*, vol. 516, pp. 7406-7417, 2008.

[49] C. J. Mathai, S. Saravanan, M. R. Anantharaman, S. Venkitachalam, and S. Jayalekshmi, "Characterization of low dielectric constant polyaniline thin film synthesized by ac plasma polymerization technique," *J. Phys. D: Appl. Phys.*, vol. 35, pp. 240-245, 2002.

[50] H. Jiang, L. Hong, N. Venkatasubramanian, J. T. Grant, K. Eyink, K. Wiacek, S. Fries-Carr, J. Enlow, and T. J. Bunning, "The relationship between chemical structure and dielectric properties of plasma-enhanced chemical vapor deposited polymer thin films," *Thin Solid Films*, vol. 515, pp. 3513-3520, 2007.

[51] F. U. Z. Chowdhury and A. H. Bhuiyan, "Dielectric properties of plasma-polymerized diphenyl thin films," *Thin Solid Films*, vol. 370, pp. 78-84, 2000.

[52] D. Sakthi Kumar and Y. Yoshida, "Dielectric properties of plasma polymerized pyrrole thin film capacitors," *Surface and Coatings Technology*, vol. 169-170, pp. 600-603, 2003.

[53] R. d'Agostino, P. Favia, C. Oehr, and M. R. Wertheimer, "Low-Temperature Plasma Processing of Materials: Past, Present, and Future," *Plasma Process. Polym.*, vol. 2, pp. 7-15, 2005.

[54] A. Bradley and J. P. Hammes, "Electrical Properties of Thin Organic Films," *J. Electrochem. Soc.*, vol. 110, pp. 15-22, January 1, 1963 1963.

[55] M. Uhlig, A. Bertz, J. W. Erben, S. E. Schulz, T. Gessner, D. Zeidler, C. Wenzel, and J. Bartha, "Experimental results on the integration of copper and CVD ultra low k material," *Microelectron. Eng.*, vol. 70, pp. 314-319, 2003.

[56] M. Uhlig, A. Bertz, M. Rennau, S. E. Schulz, T. Werner, and T. Gessner, "Electrical and adhesion properties of plasma-polymerised ultra-low k dielectric films with high thermal stability," *Microelectron. Eng.*, vol. 50, pp. 7-14, 2000.

[57] B. E. Volland and I. W. Rangelow, "Aspect ratio dependent plasma polymer deposition of fluorocarbons," *Microelectron. Eng.*, vol. 83, pp. 1174-1177, 2006.

[58] G. Maier, "Low dielectric constant polymers for microelectronics," *Progress in Polymer Science*, vol. 26, pp. 3-65, 2001.

[59] I. S. Bae, S. H. Cho, Y. S. Park, B. Hong, Z. T. Park, J. G. Kim, and J. H. Boo, "Synthesis and application perspective of advanced plasma polymerized organic thin films," *Thin Solid Films*, vol. 506–507, pp. 2-7, 2006.

[60] M. Zaman and A. H. Bhuiyan, "Direct current electrical conduction mechanism in plasma polymerized thin films of tetraethylorthosilicate," *Thin Solid Films*, vol. 517, pp. 5431-5434, 2009.

[61] X. P. Zou, E. T. Kang, K. G. Neoh, C. Q. Cui, and T. B. Lim, "Surface modification of poly(tetrafluoroethylene) films by plasma polymerization of glycidyl methacrylate for adhesion enhancement with evaporated copper," *Polymer*, vol. 42, pp. 6409-6418, 2001.

[62] S.-J. Cho and J.-H. Boo, "Characteristics of multilayered plasma-polymer thin films using toluene and TEOS by PECVD," *Microelectron. Eng.*, vol. 89, pp. 19-22, 2012.

[63] G. Borvon, A. Goullet, X. Mellhaoui, N. Charrouf, and A. Granier, "Electrical properties of low-dielectric-constant films prepared by PECVD in O2/CH4/HMDSO," *Mater. Sci. Semicond. Process.*, vol. 5, pp. 279-284, 2002.

[64] Y. Zhang, J. Arfsten, S. A. Pihan, T. Kaule, R. Förch, and R. Berger, "Interface roughness of plasma deposited polymer layers," *J. Colloid Interface Sci.*, vol. 351, pp. 532-536, 2010.

[65] H. Yatsuda, M. Nara, T. Kogai, H. Aizawa, and S. Kurosawa, "STW gas sensors using plasma-polymerized allylamine," *Thin Solid Films*, vol. 515, pp. 4105-4110, 2007.

[66] M. Nakamura, I. Sugimoto, and H. Kuwano, "Application of plasma-polymer-film-coated sensors to gas identification using linear filters," *Sensors Actuators B: Chem.*, vol. 33, pp. 122-127, 1996.

[67] J. Janča and L. Sodomka, "Plasma-polymerised organosiloxane thin films as selective gas sensors," *Surf. Coat. Technol.*, vol. 98, pp. 851-854, 1998.

[68] M. L. P. da Silva, I. H. Tan, A. P. Nascimento Filho, E. Galeazzo, and D. P. Jesus, "Use of plasma polymerized highly hydrophobic hexamethyldissilazane (HMDS) films for sensor development," *Sensors Actuators B: Chem.*, vol. 91, pp. 362-369, 2003.

[69] C. Zhang, J. Wyatt, S. P. Russell, and D. H. Weinkauf, "Methanol vapor sorption in plasma polymerized thin films," *Polymer*, vol. 45, pp. 7655-7663, 2004.

[70] R. A. M. Carvalho, R. R. Lima, A. P. Nascimento Filho, M. L. P. Silva, and N. R. Demarquette, "Plasma polymerized TEOS films for nanochannels formation and sensor development," *Sensors Actuators B: Chem.*, vol. 108, pp. 955-963, 2005.

[71] N. D. Boscher, D. Duday, P. Heier, K. Heinze, F. Hilt, and P. Choquet, "Atmospheric pressure plasma polymerisation of metalloporphyrins containing mesoporous membranes for gas sensing applications," *Surf. Coat. Technol.*

[72] A. P. Nascimento Filho, M. L. P. da Silva, E. Galeazzo, and N. R. Demarquette, "Use of plasma polymerized highly polar organic compound films for sensor development," *Sensors Actuators B: Chem.*, vol. 91, pp. 370-377, 2003.

[73] A. Hiratsuka, H. Muguruma, K.-H. Lee, and I. Karube, "Organic plasma process for simple and substrate-independent surface modification of polymeric BioMEMS devices," *Biosens. Bioelectron.*, vol. 19, pp. 1667-1672, 2004.

[74] M. Dhayal, H. G. Jeong, and J. S. Choi, "Use of plasma polymerisation process for fabrication of bio-MEMS for micro-fluidic devices," *Appl. Surf. Sci.*, vol. 252, pp. 1710-1715, 2005.

[75] Z. Jiang, Z.-j. Jiang, and Y. Meng, "Optimization and synthesis of plasma polymerized proton exchange membranes for direct methanol fuel cells," *J. Membr. Sci.*, vol. 372, pp. 303-313, 2011.

[76] F. Finsterwalder and G. Hambitzer, "Proton conductive thin films prepared by plasma polymerization," *J. Membr. Sci.,* vol. 185, pp. 105-124, 2001.

[77] Z. Jiang and Z.-j. Jiang, "Synthesis and optimization of proton exchange membranes by a pulsed plasma enhanced chemical vapor deposition technique," *Int. J. Hydrogen Energy,* vol. 37, pp. 11276-11289, 2012.

[78] K. Matsuoka, S. Chiba, Y. Iriyama, T. Abe, M. Matsuoka, K. Kikuchi, and Z. Ogumi, "Preparation of anion-exchange membrane by plasma polymerization and its use in alkaline fuel cells," *Thin Solid Films,* vol. 516, pp. 3309-3313, 2008.

[79] H. I. Kim and S. S. Kim, "Fabrication of reverse osmosis membrane via low temperature plasma polymerization," *J. Membr. Sci.,* vol. 190, pp. 21-33, 2001.

[80] D. T. Tran, S. Mori, and M. Suzuki, "Characteristics of polyimide-based composite membranes fabricated by low-temperature plasma polymerization," *Thin Solid Films,* vol. 516, pp. 4384-4390, 2008.

[81] H. A. Gulec, A. Topacli, C. Topacli, N. Albayrak, and M. Mutlu, "Modification of cellulose acetate membrane via low-pressure plasma polymerization for sugar separation applications: Part I. Membrane development and characterization," *J. Membr. Sci.,* vol. 350, pp. 310-321, 2010.

[82] L. Favre-Quattropani, P. Groening, D. Ramseyer, and L. Schlapbach, "The protection of metallic archaeological objects using plasma polymer coatings," *Surface and Coatings Technology,* vol. 125, pp. 377-382, 2000.

[83] C. Vautrin-Ul, C. Boisse-Laporte, N. Benissad, A. Chausse, P. Leprince, and R. Messina, "Plasma-polymerized coatings using HMDSO precursor for iron protection," *Prog. Org. Coat.,* vol. 38, pp. 9-15, 2000.

[84] J. Schindhelm, M. Giza, K. Nikolov, N. Weiher, B. Schuhmacher, and C. P. Klages, "Combination of zinc alloy coating with thin plasma polymer films for novel corrosion protective systems on coated steel," *Surf. Coat. Technol.,* vol. 205, Supplement 2, pp. S137-S140, 2011.

[85] M. I. Totolin and I. Neamțu, "Positive findings for plasma polymer (meth)acrylate thin films in heritage protective applications," *J. Cult. Herit.,* vol. 12, pp. 392-398, 2011.

[86] M. Dhayal and S.-I. Cho, "Leukemia cells interaction with plasma-polymerized acrylic acid coatings," *Vacuum,* vol. 80, pp. 636-642, 2006.

[87] F. Brétagnol, M. Lejeune, A. Papadopoulou-Bouraoui, M. Hasiwa, H. Rauscher, G. Ceccone, P. Colpo, and F. Rossi, "Fouling and non-fouling surfaces produced by plasma polymerization of ethylene oxide monomer," *Acta Biomater.,* vol. 2, pp. 165-172, 2006.

[88] S. Mutlu, D. Çökeliler, and M. Mutlu, "Modification of food contacting surfaces by plasma polymerization technique. Part II: Static and dynamic adsorption behavior of a model protein “bovine serum albumin” on stainless steel surface," *J. Food Eng.,* vol. 78, pp. 494-499, 2007.

[89] Q. Chen, R. Förch, and W. Knoll, "Characterization of Pulsed Plasma Polymerization Allylamine as an Adhesion Layer for DNA Adsorption/Hybridization," *Chem. Mater.,* vol. 16, pp. 614-620, 2004/02/01 2004.

[90] M. Muratsugu, S. Kurosawa, and N. Kamo, "Adsorption and desorption of F(ab′)2Anti-hIgG on plasma-polymerized allylamine thin film: The application of the film to immunoassay," *J. Colloid Interface Sci.,* vol. 147, pp. 378-386, 1991.

[91] A. Artemenko, O. Kylián, A. Choukourov, I. Gordeev, M. Petr, M. Vandrovcová, O. Polonskyi, L. Bačáková, D. Slavinska, and H. Biederman, "Effect of sterilization procedures on properties of plasma polymers relevant to biomedical applications," *Thin Solid Films,* vol. 520, pp. 7115-7124, 2012.

[92] M. Losurdo, M. M. Giangregorio, P. Capezzuto, G. Bruno, F. Babudri, D. Colangiuli, G. M. Farinola, and F. Naso, "Spectroscopic ellipsometry for characterization of organic semiconductor polymeric thin films," *Synth. Met.,* vol. 138, pp. 49-53, 2003.

[93] C. Videlot-Ackermann, J. Ackermann, K. Kawamura, N. Yoshimoto, H. Brisset, P. Raynal, A. El Kassmi, and F. Fages, "Environmentally stable organic thin-films

transistors: Terminal styryl vs central divinyl benzene building blocks for p-type oligothiophene semiconductors," *Org. Electron.*, vol. 7, pp. 465-473, 2006.

[94] Y. Ai, Y. Liu, T. Cui, and K. Varahramyan, "Thin film deposition of an n-type organic semiconductor by ink-jet printing technique," *Thin Solid Films,* vol. 450, pp. 312-315, 2004.

[95] A. Facchetti, "Semiconductors for organic transistors," *Materials Today,* vol. 10, pp. 28-37, 2007.

[96] K. N. Narayanan Unni, S. Dabos-Seignon, A. K. Pandey, and J.-M. Nunzi, "Influence of the polymer dielectric characteristics on the performance of pentacene organic field-effect transistors," *Solid-State Electronics,* vol. 52, pp. 179-181, 2008.

[97] D. Gupta and Y. Hong, "Understanding the effect of semiconductor thickness on device characteristics in organic thin film transistors by way of two-dimensional simulations," *Org. Electron.,* vol. 11, pp. 127-136, 2010.

[98] L. Jiang, J. Zhang, D. Gamota, and C. G. Takoudis, "Enhancement of the field-effect mobility of solution processed organic thin film transistors by surface modification of the dielectric," *Org. Electron.*, vol. 11, pp. 344-350, 2010.

[99] F. Garnier, "Thin-film transistors based on organic conjugated semiconductors," *Chemical Physics,* vol. 227, pp. 253-262, 1998.

[100] T. Kushida, T. Nagase, and H. Naito, "Mobility enhancement in solution-processable organic transistors through polymer chain alignment by roll-transfer printing," *Org. Electron.,* vol. 12, pp. 2140-2143, 2011.

[101] Y. Chen and I. Shih, "Fabrication of vertical channel top contact organic thin film transistors," *Org. Electron.,* vol. 8, pp. 655-661, 2007.

[102] J. B. Kim, C. Fuentes-Hernandez, D. K. Hwang, S. P. Tiwari, W. J. Potscavage Jr, and B. Kippelen, "Vertically stacked complementary inverters with solution-processed organic semiconductors," *Org. Electron.,* vol. 12, pp. 1132-1136, 2011.

[103] T. D. Anthopoulos, B. Singh, N. Marjanovic, N. S. Sariciftci, A. M. Ramil, H. Sitter, M. Colle, and D. M. de Leeuw, "High performance n-channel organic field-effect transistors and ring oscillators based on C[sub 60] fullerene films," *Appl. Phys. Lett.,* vol. 89, pp. 213504-3, 2006.

[104] M. Kitamura, S. Aomori, J. H. Na, and Y. Arakawa, "Bottom-contact fullerene C[sub 60] thin-film transistors with high field-effect mobilities," *Appl. Phys. Lett.,* vol. 93, pp. 033313-3, 2008.

[105] C. R. Newman, C. D. Frisbie, D. A. da Silva Filho, J.-L. Brédas, P. C. Ewbank, and K. R. Mann, "Introduction to Organic Thin Film Transistors and Design of n-Channel Organic Semiconductors," *Chem. Mater.*, vol. 16, pp. 4436-4451, 2004.

[106] H. Nagashima, M. Saito, H. Nakamura, T. Yasuda, and T. Tsutsui, "Organic field-effect transistors based on naphthyl end-capped divinylbenzene: Performance, stability and molecular packing," *Org. Electron.*, vol. 11, pp. 658-663, 2010.

[107] E. M. García-Frutos, E. Gutierrez-Puebla, M. A. Monge, R. Ramírez, P. d. Andrés, A. d. Andrés, and B. Gómez-Lor, "Crystal structure and charge-transport properties of N-trimethyltriindole: Novel p-type organic semiconductor single crystals," *Org. Electron.,* vol. 10, pp. 643-652, 2009.

[108] N. Karl, "Charge carrier transport in organic semiconductors," *Synthetic Metals,* vol. 133-134, pp. 649-657, 2003.

[109] J. Takeya, M. Yamagishi, Y. Tominari, and Y. Nakazawa, "Gate dielectric materials for high-mobility organic transistors of molecular semiconductor crystals," *Solid-State Electron.,* vol. 51, pp. 1338-1343, 2007.

[110] G. Horowitz and M. E. Hajlaoui, "Grain size dependent mobility in polycrystalline organic field-effect transistors," *Synth. Met.,* vol. 122, pp. 185-189, 2001.

[111] H. B. Akkerman, A. C. Chang, E. Verploegen, C. J. Bettinger, M. F. Toney, and Z. Bao, "Fabrication of organic semiconductor crystalline thin films and crystals from solution by confined crystallization," *Org. Electron.*, vol. 13, pp. 235-243, 2012.

[112] L. Lin, H. Geng, Z. Shuai, and Y. Luo, "Theoretical insights into the charge transport in perylene diimides based n-type organic semiconductors," *Org. Electron.*, vol. 13, pp. 2763-2772, 2012.

[113] C. Piliego, D. Jarzab, G. Gigli, Z. Chen, A. Facchetti, and M. A. Loi, "High Electron Mobility and Ambient Stability in Solution-Processed Perylene-Based Organic Field-Effect Transistors," *Adv. Mater.*, vol. 21, pp. 1573-1576, 2009.

[114] J. Jang, J. W. Kim, N. Park, and J.-J. Kim, "Air stable C60 based n-type organic field effect transistor using a perfluoropolymer insulator," *Org. Electron.*, vol. 9, pp. 481-486, 2008.

[115] C. Videlot-Ackermann, J. Zhang, J. Ackermann, H. Brisset, Y. Didane, P. Raynal, A. El Kassmi, and F. Fages, "p-Type and n-type quaterthiophene based semiconductors for thin film transistors operating in air?," *Curr. Appl. Phys.*, vol. 9, pp. 26-33, 2009.

[116] M. M. Ling, P. Erk, M. Gomez, M. Koenemann, J. Locklin, and Z. Bao, "Air-Stable n-Channel Organic Semiconductors Based on Perylene Diimide Derivatives without Strong Electron Withdrawing Groups," *Adv. Mater.*, vol. 19, pp. 1123-1127, 2007.

[117] S. Allard, M. Forster, B. Souharce, H. Thiem, and U. Scherf, "Organic Semiconductors for Solution-Processable Field-Effect Transistors (OFETs)," *Angew. Chem. Int. Ed.*, vol. 47, pp. 4070-4098, 2008.

[118] M. Barra, D. Viggiano, P. Ambrosino, F. Bloisi, F. V. Di Girolamo, M. V. Soldovieri, M. Taglialatela, and A. Cassinese, "Addressing the use of PDIF-CN2 molecules in the development of n-type organic field-effect transistors for biosensing applications," *Biochim. Biophys. Acta*.

[119] F. V. Di Girolamo, F. Ciccullo, M. Barra, A. Carella, and A. Cassinese, "Investigation on bias stress effects in n-type PDI8-CN2 thin-film transistors," *Org. Electron.*, vol. 13, pp. 2281-2289, 2012.

[120] S. Zhang, Y. Guo, H. Xi, C.-a. Di, J. Yu, K. Zheng, R. Liu, X. Zhan, and Y. Liu, "Effect of substituents on electronic properties, thin film structure and device performance of dithienothiophene–phenylene cooligomers," *Thin Solid Films*, vol. 517, pp. 2968-2973, 2009.

[121] T. Yasuda, M. Saito, H. Nakamura, and T. Tsutsui, "Conjugation-length dependency of unsubstituted oligo-p-phenylenevinylenes on the performance of organic field-effect transistors," *Chem. Phys. Lett.*, vol. 452, pp. 110-114, 2008.

[122] N. A. Azarova, J. W. Owen, C. A. McLellan, M. A. Grimminger, E. K. Chapman, J. E. Anthony, and O. D. Jurchescu, "Fabrication of organic thin-film transistors by spray-deposition for low-cost, large-area electronics," *Org. Electron.*, vol. 11, pp. 1960-1965, 2010.

[123] R. Centore, L. Ricciotti, A. Carella, A. Roviello, M. Causà, M. Barra, F. Ciccullo, and A. Cassinese, "Perylene diimides functionalized with N-thiadiazole substituents: Synthesis and electronic properties in OFET devices," *Organic Electronics*, vol. 13, pp. 2083-2093, 2012.

[124] Y. Li, C. Liu, Y. Xu, T. Minari, P. Darmawan, and K. Tsukagoshi, "Solution-processed organic crystals for field-effect transistor arrays with smooth semiconductor/dielectric interface on paper substrates," *Organic Electronics*, vol. 13, pp. 815-819, 2012.

[125] A. R. Brown, C. P. Jarrett, D. M. de Leeuw, and M. Matters, "Field-effect transistors made from solution-processed organic semiconductors," *Synth. Met.*, vol. 88, pp. 37-55, 1997.

[126] M. Campoy-Quiles, M. Schmidt, D. Nassyrov, O. Peña, A. R. Goñi, M. I. Alonso, and M. Garriga, "Real-time studies during coating and post-deposition annealing in organic semiconductors," *Thin Solid Films*, vol. 519, pp. 2678-2681, 2011.

[127] M. J. Joung, C. A. Kim, S. Y. Kang, K.-H. Baek, G. H. Kim, S. D. Ahn, I. K. You, J. H. Ahn, and K. S. Suh, "The application of soluble and regioregular poly(3-hexylthiophene) for organic thin-film transistors," *Synth. Met.*, vol. 149, pp. 73-77, 2005.

[128] D. Kim, H. Kim, H. So, Y. U. Lee, and M. Hong, "Effect of the high vacuum seasoning process on poly (4-vinyl phenol) as Organic Gate Dielectric in all solution-processed organic thin-film transistors," *Thin Solid Films,* vol. 521, pp. 235-238, 2012.

[129] C.-M. Keum, J.-H. Bae, M.-H. Kim, W. Choi, and S.-D. Lee, "Solution-processed low leakage organic field-effect transistors with self-pattern registration based on patterned dielectric barrier," *Org. Electron.,* vol. 13, pp. 778-783, 2012.

[130] S. H. Kim, Y. S. Yang, J. H. Lee, J.-I. Lee, H. Y. Chu, H. Lee, J. Oh, L.-M. Do, and T. Zyung, "Organic field-effect transistors using perylene," *Optical Materials,* vol. 21, pp. 439-443, 2003.

[131] T. Matsushima, K. Shiomura, S. Naka, and H. Murata, "Optical, morphological, structural, electrical, molecular orientation, and electroluminescence characteristics of organic semiconductor films prepared at various deposition rates," *Thin Solid Films,* vol. 520, pp. 2283-2288, 2012.

[132] H. H. Sung, I. H. Kim, K. N. Byun, and H. S. Yoo, "Characterization of new red dopants for red color OLED," *Curr. Appl. Phys.,* vol. 5, pp. 345-347, 2005.

[133] M. Eritt, C. May, K. Leo, M. Toerker, and C. Radehaus, "OLED manufacturing for large area lighting applications," *Thin Solid Films,* vol. 518, pp. 3042-3045, 2010.

[134] L. M. Leung, C. F. Kwong, C. C. Kwok, and S. K. So, "Organic polymer thick film light emitting diodes (PTF-OLED)," *Displays,* vol. 21, pp. 199-201, 2000.

[135] B. A. Bailey, M. O. Reese, D. C. Olson, S. E. Shaheen, and N. Kopidakis, "Air-processed organic photovoltaic devices fabricated with hot press lamination," *Org. Electron.,* vol. 12, pp. 108-112, 2011.

[136] E. Bundgaard and F. C. Krebs, "Low band gap polymers for organic photovoltaics," *Sol. Energy Mater. Sol. Cells,* vol. 91, pp. 954-985, 2007.

[137] R. Steim, T. Ameri, P. Schilinsky, C. Waldauf, G. Dennler, M. Scharber, and C. J. Brabec, "Organic photovoltaics for low light applications," *Sol. Energy Mater. Sol. Cells,* vol. 95, pp. 3256-3261, 2011.

[138] H. J. Egelhaaf, J. Gierschner, and D. Oelkrug, "Polarizability effects and energy transfer in quinquethiophene doped bithiophene and OPV films," *Synth. Met.,* vol. 127, pp. 221-227, 2002.

[139] A. Roigé, M. Campoy-Quiles, J. O. Ossó, M. I. Alonso, L. F. Vega, and M. Garriga, "Surface vs bulk phase transitions in semiconducting polymer films for OPV and OLED applications," *Synth. Met.,* vol. 161, pp. 2570-2574, 2012.

[140] C. Fan, P. Yang, X. Wang, G. Liu, X. Jiang, H. Chen, X. Tao, M. Wang, and M. Jiang, "Synthesis and organic photovoltaic (OPV) properties of triphenylamine derivatives based on a hexafluorocyclopentene “core”," *Sol. Energy Mater. Sol. Cells,* vol. 95, pp. 992-1000, 2011.

[141] H. Yan, Y. Zheng, R. Blache, C. Newman, S. Lu, J. Woerle, and A. Facchetti, "Solution Processed Top-Gate n-Channel Transistors and Complementary Circuits on Plastics Operating in Ambient Conditions," *Adv. Mater.,* vol. 20, pp. 3393-3398, 2008.

[142] G. Horowitz, R. Hajlaoui, R. Bourguiga, and M. Hajlaoui, "Theory of the organic field-effect transistor," *Synthetic Metals,* vol. 101, pp. 401-404, 1999.

[143] S. Richter, M. Ploetner, W. J. Fischer, M. Schneider, P. T. Nguyen, W. Plieth, N. Kiriy, and H. J. P. Adler, "Development of organic thin film transistors based on flexible substrates," *Thin Solid Films,* vol. 477, pp. 140-147, 2005.

[144] S. H. Ko, J. Chung, H. Pan, C. P. Grigoropoulos, and D. Poulikakos, "Fabrication of multilayer passive and active electric components on polymer using inkjet printing and low temperature laser processing," *Sens. Actuators, A,* vol. 134, pp. 161-168, 2007.

[145] T. Bilkay, K. Schulze, T. Egorov-Brening, K. Fink, and S. Janietz, "Solution processable TIPS-benzodithiophene small molecules with improved semiconducting properties in organic field effect transistors," *Org. Electron.,* vol. 14, pp. 344-353, 2013.

[146] T. Q. Trung, N. T. Tien, Y. G. Seol, and N.-E. Lee, "Transparent and flexible organic field-effect transistor for multi-modal sensing," *Org. Electron.,* vol. 13, pp. 533-540, 2012.

[147] S. K. Park, T. N. Jackson, J. E. Anthony, and D. A. Mourey, "High mobility solution processed 6,13-bis(triisopropyl-silylethynyl) pentacene organic thin film transistors," *Appl. Phys. Lett.*, vol. 91, pp. 063514-3, 2007.

[148] G.-P. Chang and K.-H. Hsieh, "High-mobility and solution-processable organic field-effect transistors based on carbazole-dihexylquaterthiophenes with controllable morphology," *Synth. Met.,* vol. 165, pp. 1-6, 2013.

[149] F. Zhang, C. Melzer, A. Gassmann, H. v. Seggern, T. Schwalm, C. Gawrisch, and M. Rehahn, "High-performance n-channel thin-film transistors with acene-based semiconductors," *Org. Electron.*

[150] F. Zhang, Y. Hu, T. Schuettfort, C.-a. Di, X. Gao, C. R. McNeill, L. Thomsen, S. C. B. Mannsfeld, W. Yuan, H. Sirringhaus*, et al.*, "Critical Role of Alkyl Chain Branching of Organic Semiconductors in Enabling Solution-Processed N-Channel Organic Thin-Film Transistors with Mobility of up to 3.50 cm2 V–1 s–1," *J. Am. Chem. Soc.,* 2013.

[151] D. M. de Leeuw and E. Cantatore, "Organic electronics: Materials, technology and circuit design developments enabling new applications," *Mater. Sci. Semicond. Process.,* vol. 11, pp. 199-204, 2008.

[152] H. Sakai, K. Konno, and H. Murata, "Control of threshold voltage of organic field-effect transistors by space charge polarization," *Thin Solid Films,* vol. 518, pp. 510-513, 2009.

[153] C. Feng, T. Mei, X. Hu, and N. Pavel, "A pentacene field-effect transistor with light-programmable threshold voltage," *Org. Electron.,* vol. 11, pp. 1713-1718, 2010.

[154] G. Nie, J. Peng, L. Lan, R. Xu, J. Zou, and Y. Cao, "Tuning on threshold voltage of organic field-effect transistor with a copper oxide layer," *Org. Electron.,* vol. 12, pp. 429-434, 2011.

[155] J. B. Koo, S. H. Kim, J. H. Lee, C. H. Ku, S. C. Lim, and T. Zyung, "The effects of surface treatment on device performance in pentacene-based thin film transistor," *Synthetic Metals,* vol. 156, pp. 99-103, 2006.

[156] J.-S. Lim, P.-K. Shin, B.-J. Lee, and S. Lee, "Plasma polymerized methyl methacrylate gate dielectric for organic thin film transistors," *Organic Electronics,* vol. In Press, Accepted Manuscript, 2010.

[157] M. V. Jacob, K. Bazaka, M. Weis, D. Taguchi, T. Manaka, and M. Iwamoto, "Fabrication and characterization of polyterpenol as an insulating layer and incorporated organic field effect transistor," *Thin Solid Films,* vol. 518, pp. 6123-6129, 2010.

[158] C. Celle, C. Suspène, J.-P. Simonato, S. Lenfant, M. Ternisien, and D. Vuillaume, "Self-assembled monolayers for electrode fabrication and efficient threshold voltage control of organic transistors with amorphous semiconductor layer," *Org. Electron.,* vol. 10, pp. 119-126, 2009.

[159] N. Cernetic, O. Acton, T. Weidner, D. O. Hutchins, J. E. Baio, H. Ma, and A. K. Y. Jen, "Bottom-contact small-molecule n-type organic field effect transistors achieved via simultaneous modification of electrode and dielectric surfaces," *Org. Electron.,* vol. 13, pp. 3226-3233, 2012.

[160] K. Hong, S. Y. Yang, C. Yang, S. H. Kim, D. Choi, and C. E. Park, "Reducing the contact resistance in organic thin-film transistors by introducing a PEDOT:PSS hole-injection layer," *Org. Electron.,* vol. 9, pp. 864-868, 2008.

[161] J. Frisch, H. Glowatzki, S. Janietz, and N. Koch, "Solution-based metal electrode modification for improved charge injection in polymer field-effect transistors," *Org. Electron.,* vol. 10, pp. 1459-1465, 2009.

[162] H. Fujiwara, *Spectroscopic Ellipsometry: Principles and Applications*: John Wiley and Sons, Ltd, 2007.

[163] K. Vedam, "Spectroscopic Ellipsometry: a historical overview," *Thin Solid Films,* vol. 313-314, pp. 1-9, 1998.

[164] I. J.A. Woollam Co., *Guide to Using WVASE32*, 2001.

[165] H. W. Lin, C. L. Lin, H. H. Chang, Y. T. Lin, C. C. Wu, Y. M. Chen, R. T. Chen, Y. Y. Chien, and K. T. Wong, "Anisotropic optical properties and molecular orientation in

vacuum-deposited ter(9,9-diarylfluorene)s thin films using spectroscopic ellipsometry," *Journal of Applied Physics,* vol. 95, pp. 881-886, 2004.

[166] M. I. Alonso, M. Garriga, N. Karl, J. O. Osso, and F. Schreiber, "Anisotropic optical properties of single crystalline PTCDA studied by spectroscopic ellipsometry," *Organic Electronics,* vol. 3, pp. 23-31, 2002.

[167] D. Gonçalves and E. A. Irene, "Fundamentals and applications of spectroscopic ellipsometry," *Química Nova,* vol. 25, pp. 794-800, 2002.

[168] T. Tiwald. (2008, 14 July 2009). *The Gaussian Oscillator (9 ed.)*. Available: http://www.jawoollam.com/toolbox/Newletters/TechNotes/gaussian_oscillator.pdf

[169] J. Albaugh, C. O'Sullivan, and L. O'Neill, "Controlling deposition rates in an atmospheric pressure plasma system," *Surface and Coatings Technology,* vol. 203, pp. 844-847, 2008.

[170] F. F. Shi, "Recent advances in polymer thin films prepared by plasma polymerization Synthesis, structural characterization, properties and applications," *Surface and Coatings Technology,* vol. 82, 1996.

[171] H. Goktas, F. G. Ince, A. Iscan, I. Yildiz, M. Kurt, and I. Kaya, "The molecular structure of plasma polymerized thiophene and pyrrole thin films produced by double discharge technique," *Synthetic Metals,* vol. 159, pp. 2001-2008, 2009.

[172] W. Sellmeier, "Zur Erklärung der abnormen Farbenfolge im Spectrum einiger Substanzen," *Annalen der Physik*, vol. 219, pp. 272-282, 1871.

[173] F. Yakuphanoglu, A. Cukurovali, and İ. Yilmaz, "Determination and analysis of the dispersive optical constants of some organic thin films," *Physica B: Condensed Matter,* vol. 351, pp. 53-58, 2004.

[174] J. Yu, X. Tao, H. Tam, and M. S. Demokan, "Modulation of refractive index and thickness of poly(methyl methacrylate) thin films with UV irradiation and heat treatment," *Applied Surface Science,* vol. 252, pp. 1283-1292, 2005.

[175] K. Bazaka, M. V. Jacob, and B. F. Bowden, "Optical and chemical properties of polyterpenol thin films deposited via plasma-enhanced chemical vapor deposition," *J. Mater. Res.,* vol. 26, pp. 1018-1025, 2011.

[176] C. D. Easton and M. V. Jacob, "Optical characterisation of radio frequency plasma polymerised Lavandula angustifolia essential oil thin films," *Thin Solid Films,* vol. 517, pp. 4402-4407, 2009.

[177] R. P. Mota, D. Galvão, S. F. Durrant, M. A. B. De Moraes, S. de Oliveira Dantas, and M. Cantão, "HMDSO plasma polymerization and thin film optical properties," *Thin Solid Films,* vol. 270, pp. 109-113, 1995.

[178] S. K. Al-Ani, C. A. Hogarth, and M. Ilyas, "The optical absorption edge in thin amorphous oxide films based on germania," *Journal of Materials Science Letters,* vol. 3, pp. 391-394, May 1984.

[179] M. Salagram, V. Krishna Prasad, and K. Subrahmanyam, "Optical band gap studies on xPb_3O_4-$(1-x)P_2O_5$ lead[(II, IV)] phosphate glasses," *Optical Materials,* vol. 18, pp. 367-372, 2002.

[180] J. Tauc, R. Grigorovici, and A. Vancu, "Optical Properties and Electronic Structure of Amorphous Germanium," *physica status solidi (b),* vol. 15, pp. 627-637, 1966.

[181] A. A. Al-Ghamdi, "Optical band gap and optical constants in amorphous $Se_{96-x}Te_4Ag_x$ thin films," *Vacuum,* vol. 80, pp. 400-405, 2006.

[182] A. Jain, P. Sagar, and R. M. Mehra, "Band gap widening and narrowing in moderately and heavily doped n-ZnO films," *Solid-State Electronics,* vol. 50, pp. 1420-1424, 2006/8// 2006.

[183] Z. Z. You and G. J. Hua, "Refractive index, optical bandgap and oscillator parameters of organic films deposited by vacuum evaporation technique," *Vacuum,* vol. 83, pp. 984-988, 2009.

[184] J. Wang, K. G. Neoh, and E. T. Kang, "Comparative study of chemically synthesized and plasma polymerized pyrrole and thiophene thin films," *Thin Solid Films,* vol. 446, pp. 205-217, 2004.

[185] P. Gailly, C. Petermann, P. Tihon, and K. Fleury-Frenette, "Ripple topography and roughness evolution on surface of polycrystalline gold and silver thin films under low energy Ar-ion beam sputtering," *Applied Surface Science,* vol. 258, pp. 7717-7725, 2012.

[186] H. M. Lee, H. Moon, H.-S. Kim, Y. N. Kim, S.-M. Choi, S. Yoo, and S. O. Cho, "Abrupt heating-induced high-quality crystalline rubrene thin films for organic thin-film transistors," *Organic Electronics,* vol. 12, pp. 1446-1453, 2011.

[187] J. Lv, C. Liu, W. Gong, Z. Zi, X. Chen, K. Huang, T. Wang, G. He, X. Song, and Z. Sun, "Effect of solution concentrations on crystal structure, surface topographies and photoluminescence properties of ZnO thin films," *Superlattices Microstruct.,* vol. 51, pp. 886-892, 2012.

[188] K. E. Mayerhofer, J. Heier, Y. Maniglio, and B. A. Keller, "Three dimensional analysis of self-structuring organic thin films using time-of-flight secondary ion mass spectrometry," *Thin Solid Films,* vol. 519, pp. 6183-6189, 2011.

[189] E. Meyer, "Atomic force microscopy," *Progress in Surface Science,* vol. 41, pp. 3-49, 1992.

[190] P. Systems. (2012, 11/12/12). *Non-Contact Mode AFM in Ambient Atmosphere*. Available: http://www.parkafm.com/AFM_guide/true_non_contact_mode_1.php

[191] A. Workshop. (2012). *Introduction to Atomic Force Microscopy*.

[192] C. f. B. Biology. (2012, 11/12/12). *Biomechanical Testing of Bone*. Available: http://www.mc.vanderbilt.edu/root/vumc.php?site=CenterForBoneBiology&doc=20412

[193] Hysitron, *TriboScope Users Manual*, 2005.

[194] J. M. Soro, L. Lelait, J. C. van Duysen, G. Zacharie, and J. von Stebut, "Influence of substrate roughness and lateral spacing on morphology and brittleness of different Cr-C PVD coatings," *Surface and Coatings Technology,* vol. 98, pp. 1490-1496, 1998.

[195] S. Steudel, S. D. Vusser, S. D. Jonge, D. Janssen, S. Verlaak, J. Genoe, and P. Heremans, "Influence of the dielectric roughness on the performance of pentacene transistors," *Applied Physics Letters,* vol. 85, pp. 4400-4402, 2004.

[196] S. E. Fritz, T. W. Kelley, and C. D. Frisbie, "Effect of Dielectric Roughness on Performance of Pentacene TFTs and Restoration of Performance with a Polymeric Smoothing Layer," *The Journal of Physical Chemistry B,* vol. 109, pp. 10574-10577, 2005.

[197] Z. Bao and J. Locklin, *Organic Field Effect Transistors*: CRC Press, 2007.

[198] C. D. Easton, M. V. Jacob, R. A. Shanks, and B. F. Bowden, "Surface and Chemical Characterization of PolyLA Thin Films Fabricated Using Plasma Polymerization," *Chem. Vap. Deposition,* vol. 15, pp. 179-185, 2009.

[199] K. Bazaka and M. V. Jacob, "Nanotribological and nanomechanical properties of plasma-polymerized polyterpenol thin films," *J. Mater. Res.,* vol. 26, pp. 2952-2961, 2011.

[200] E. C. Rangel, N. C. Cruz, D. C. R. Santos, M. A. Algatti, R. P. Mota, R. Y. Honda, P. A. F. Silva, M. S. Costa, and M. H. Tabacniks, "Argon ion implantation inducing modifications in the properties of benzene plasma polymers," *Nuclear Instruments and Methods in Physics Research Section B: Beam Interactions with Materials and Atoms,* vol. 191, pp. 700-703, 2002.

[201] E. C. Rangel, N. C. Cruz, and C. M. Lepienski, "Effect of helium implantation on the properties of plasma polymer films," *Nuclear Instruments and Methods in Physics Research Section B: Beam Interactions with Materials and Atoms,* vol. 191, pp. 704-707, 2002.

[202] E. C. Rangel, N. C. da Cruz, M. A. B. de Moraes, and C. M. Lepienski, "Influence of Ar+ ion irradiation on the properties of plasma polymerized acetylene films," *Surface and Coatings Technology,* vol. 127, pp. 93-98, 2000.

[203] W. S. Choi, I. Chung, Y.-Z. Lee, and B. Hong, "Characterization of diamond-like carbon thin films prepared by a microwave plasma enhanced chemical vapor deposition method," *Surface and Coatings Technology,* vol. 180-181, pp. 254-258, 2004.

[204] P. B. Fellgett, "On the Ultimate Sensitivity and Practical Performance of Radiation Detectors," *J. Opt. Soc. Am.,* vol. 39, pp. 970-976, 1949.

[205] T. E. Corporation. (2004, FT-IR vs. Dispersive Infrared.

[206] P. Elmer. (2005), FT-IR Spectroscopy: Attenuated Total Reflectance (ATR).

[207] C. L. Rinsch, X. Chen, V. Panchalingam, R. C. Eberhart, J.-H. Wang, and R. B. Timmons, "Pulsed Radio Frequency Plasma Polymerization of Allyl Alcohol: Controlled Deposition of Surface Hydroxyl Groups," *Langmuir,* vol. 12, pp. 2995-3002, 1996.

[208] L. Groenewoud, G. Engbers, J. Terlingen, H. Wormeester, and J. Feijen, "Pulsed plasma polymerization of thiophene," *Langmuir,* vol. 16, pp. 6278-6286, 2000.

[209] M. Barra, F. V. D. Girolamo, F. Chiarella, M. Salluzzo, Z. Chen, A. Facchetti, L. Anderson, and A. Cassinese, "Transport Property and Charge Trap Comparison for N-Channel Perylene Diimide Transistors with Different Air-Stability " *The Journal of Physical Chemistry C,* vol. 114, pp. 20387-20393, 2010.

[210] S. C. Lim, S. H. Kim, J. H. Lee, M. K. Kim, D. J. Kim, and T. Zyung, "Surface-treatment effects on organic thin-film transistors," *Synthetic Metals,* vol. 148, pp. 75-79, 2005.

[211] E. Spassova, I. Jivkov, G. Danev, T. Dimitrova, J. Koprinarova, and A. Paskaleva, "Low-permittivity evaporated polymer-polyimide," *Vacuum,* vol. 47, pp. 1345-1346, 1996.

[212] E. Perret, N. Zerounian, S. David, and F. Aniel, "Complex permittivity characterization of benzocyclobutene for terahertz applications," *Microelectronic Engineering,* vol. 85, pp. 2276-2281, 2008.

[213] J. Mollá, A. Ibarra, and C. Maffiotte, "Dielectric losses of self-supporting chemically vapour deposited diamond materials," *Diamond and Related Materials,* vol. 9, pp. 1071-1075, 2000.

[214] A. Moliton, W. Rammal, and B. Lucas, "A new method for the determination of electronic mobility in organic materials associated with optoelectronic devices," *EPL (Europhysics Letters),* vol. 72, p. 754, 2005.

[215] T. Machappa and M. V. N. Ambika Prasad, "AC conductivity and dielectric behavior of polyaniline/sodium metavenadate (PANI/NaVO3) composites," *Physica B: Condensed Matter,* vol. 404, pp. 4168-4172, 2009.

[216] J. Mazierska, M. V. Jacob, A. Harring, J. Krupka, P. Barnwell, and T. Sims, "Measurements of loss tangent and relative permittivity of LTCC ceramics at varying temperatures and frequencies," *J. Eur. Ceram. Soc.,* vol. 23, pp. 2611-2615, 2003.

[217] Agilent. (2006, Basics of Measuring the Dielectric Properties of Materials: Application Note.

[218] J. Krupka, A. P. Gregory, O. C. Rochard, R. N. Clarke, B. Riddle, and J. Baker-Jarvis, "Uncertainty of complex permittivity measurements by split-post dielectric resonator technique," *J. Eur. Ceram. Soc.,* vol. 21, pp. 2673-2676, 2001.

[219] A. A. Dakhel, "Mechanisms of dc-current transfer in tris(acetylacetonato)iron(III) films," *Journal of Non-Crystalline Solids,* vol. 353, pp. 1529-1533, 2007.

[220] R. Matin and A. H. Bhuniyan, "Electrical transport mechanism in plasma polymerized 2, 6, diethylaniline thin films," *Thin Solid Films,* vol. 519, pp. 3462-3467, 2011.

[221] J. G. Simmons, "Poole-Frenkel effect and Schottky effect in Metal-Insulator-Metal systems," *Physical Review,* vol. 155, pp. 657 - 660, 1967.

[222] N. Nagaraj, C. V. Subba Reddy, A. K. Sharma, and V. V. R. Narasimha Rao, "DC conduction mechanism in polyvinyl alcohol films doped with potassium thiocyanate," *J. Power Sources,* vol. 112, pp. 326-330, 2002.

[223] R. Çapan and F. Davis, "Electrical properties of a calix[4]acid/amine Langmuir-Blodgett thin film," *Materials Chemistry and Physics,* vol. 125, pp. 883-886, 2011.

[224] Y. Shirota and H. Kageyama, "Charge carrier transporting molecular materials and their applications in devices," *Chem. Rev.,* vol. 107, pp. 953-1010, 2007.

[225] O. Rana, R. Srivastava, R. Grover, M. Zulfequar, M. Husain, and M. N. Kamalasanan, "Charge transport studies in thermally evaporated 2,2′,7,7′-tetrakis-(N,N-di-4-

methoxyphenylamino)-9,9′-spirobifluorene (spiro-MeOTAD) thin film," *Synthetic Metals,* vol. 161, pp. 828-832, 2011.

[226] G. J. Cruz, J. Morales, M. M. Castillo-Ortega, and R. Olayo, "Synthesis of polyaniline films by plasma polymerization," *Synthetic Metals,* vol. 88, pp. 213-218, 1997.

[227] H. Jiang, L. Hong, N. Venkatasubramanian, J. T. Grant, K. Eyink, K. Wiacek, S. Fries-Carr, J. Enlow, and T. J. Bunning, "The relationship between chemical structure and dielectric properties of plasma-enhanced chemical vapor deposited polymer thin films," *Thin Solid Films,* vol. 515, pp. 3513-3520, 2007.

[228] M. A. Lampert, "Simplified Theory of Space-Charge-Limited Currents in an Insulator with Traps," *Physical Review,* vol. 103, pp. 1648-1656, 1956.

[229] S. I. Shihub and R. D. Gould, "Frequency dependence of electronic conduction parameters in evaporated thin films of cobalt phthalocyanine," *Thin Solid Films,* vol. 254, pp. 187-193, 1995.

[230] J. G. Simmons, G. S. Nadkarni, and M. C. Lancaster, "Alternating current electrical properties of highly doped insulating films," *Journal of applied Physics,* vol. 41, pp. 538 - 544, 1970.

[231] A. Bello, E. Laredo, and M. Grimau, "Distribution of relaxation times from dielectric spectroscopy using Monte Carlo simulated annealing: Application to α-PVDF," *Physical Review B,* vol. 60, pp. 12764-12774, 1999.

[232] J. Macutkevic, J. Banys, and A. Matulis, "Determination of the distribution of the relaxation times from dielectric spectra," *Nonlinear Analysis: Modelling and Control,* vol. 9, pp. 75-88, 2004.

[233] H. Schäfer and E. Sternin, "Inverse ill-posed problems in experimental data analysis in physics," *Physics in Canada,* vol. 53, pp. 77-85, 1997.

[234] H. Schäfer, E. Sternin, R. Stannarius, M. Arndt, and F. Kremer, "Novel Approach to the Analysis of Broadband Dielectric Spectra," *Physical Review Letters,* vol. 76, pp. 2177-2180, 1996.

[235] H. G. Choi, A. N. Thite, and D. J. Thompson, "Comparison of methods for parameter selection in Tikhonov regularization with application to inverse force determination," *Journal of Sound and Vibration,* vol. 304, pp. 894-917, 2007.

[236] P. C. Hanson, "Anaylsis of discrete ill-posed problems by means of the L-curve," *SIAM Review,* vol. 34, pp. 561-580, 1992.

[237] P. R. Johnston and R. M. Gulrajani, "Selecting the corner in the L-curve approach to Tikhonov regularization," *Biomedical Engineering, IEEE Transactions on,* vol. 47, pp. 1293-1296, 2000.

[238] D. Calvetti, S. Morigi, L. Reichel, and F. Sgallari, "Tikhonov regularization and the L-curve for large discrete ill-posed problems," *Journal of Computational and Applied Mathematics,* vol. 123, pp. 423-446, 2000.

[239] L. Hardy, I. Stevenson, G. Boiteux, G. Seytre, and A. Schönhals, "Dielectric and dynamic mechanical relaxation behaviour of poly(ethylene 2,6 naphthalene dicarboxylate). I. Amorphous films," *Polymer,* vol. 42, pp. 5679-5687, 2001.

[240] R. R. Santos, E. Prokhorov, J. González-Hernández, G. Luna-Bárcenas, and Y. Kovalenko, "Dielectric relaxation processes in stoichiometric Ge:Sb:Te amorphous films," *Journal of Non-Crystalline Solids,* vol. 356, pp. 2541-2545, 2010.

[241] O. Becker, G. P. Simon, T. Rieckmann, J. Forsythe, R. Rosu, S. Völker, and M. O'Shea, "Dielectric relaxation spectroscopy of reactively blended amorphous poly(ethylene terephthalate)–poly(ethylene naphthalate) films," *Polymer,* vol. 42, pp. 1921-1929, 2001.

[242] C. D. Easton, M. V. Jacob, and J. Krupka, "Non-destructive complex permittivity measurement of low permittivity thin film materials," *Measurement Science and Technology,* vol. 18, pp. 2869-2877, 2007.

[243] Y. Lu, Y. Wang, Z. Feng, Y. Ning, X. Liu, Y. Lü, and Y. Hou, "Temperature-dependent morphology evolution of P3HT:PCBM blend solar cells during annealing processes," *Synthetic Metals,* vol. 162, pp. 2039-2046, 2012.

[244] K. Song, D. Kim, X.-S. Li, T. Jun, Y. Jeong, and J. Moon, "Solution processed invisible all-oxide thin film transistors," *Journal of Materials Chemistry*, vol. 19, pp. 8881-8886, 2009.

[245] B. Yoo, B. A. Jones, D. Basu, D. Fine, T. Jung, S. Mohapatra, A. Facchetti, K. Dimmler, M. R. Wasielewski, T. J. Marks, *et al.*, "High-Performance Solution-Deposited n-Channel Organic Transistors and their Complementary Circuits," *Adv. Mater.*, vol. 19, pp. 4028-4032, 2007.

[246] C. D. Easton and M. V. Jacob, "Ageing and thermal degradation of plasma polymerised thin films derived from Lavandula angustifolia essential oil," *Polymer Degradation and Stability*, vol. 94, pp. 597-603, 2008.

[247] K. Bazaka and M. V. Jacob, "Post-deposition ageing reactions of plasma derived polyterpenol thin films," *Polymer Degradation and Stability*, vol. 95, pp. 1123-1128, 2010.

[248] T. Ahn, H. Jung, H. J. Suk, and M. H. Yi, "Effect of postfabrication thermal annealing on the electrical performance of pentacene organic thin-film transistors," *Synthetic Metals*, vol. 159, pp. 1277-1280, 2009.

[249] A. K. Pandey and J.-M. Nunzi, "Impact of selective thermal annealing on rubrene–C60 heterojunction solar cells," *Synthetic Metals*, vol. 162, pp. 2171-2175, 2012.

[250] K. A. Osipov, V. N. Pavlovskii, E. V. Lutsenko, A. L. Gurskii, G. P. Yablonskii, S. Hartmann, A. Janssen, H. H. Johannes, R. Caspary, W. Kowalsky, *et al.*, "Influence of thermal annealing on photoluminescence and structural properties of N,N′-diphenyl-N,N′-bis(1-naphthylphenyl)-1,1′-biphenyl-4,4′-diamine (α-NPD) organic thin films," *Thin Solid Films*, vol. 515, pp. 4834-4837, 2007.

[251] F. Dinelli, M. Murgia, F. Biscarini, and D. M. De Leeuw, "Thermal annealing effects on morphology and electrical response in ultrathin film organic transistors," *Synthetic Metals*, vol. 146, pp. 373-376, 2004.

[252] C. D. Easton and M. V. Jacob, "Solubility and adhesion characteristics of plasma polymerized thin films derived from Lavandula angustifolia essential oil," *J. Appl. Polym. Sci.*, vol. 115, pp. 404-415, 2010.

[253] K. Bazaka, "Fabrication and Characterization of Plasma Polymer Thin Films from Monoterpene Alcohols for Applications in Organic Electronics and Biotechnology," Doctor of Philosophy, School of Engineering and Physical Sciences, James Cook University, Townsville, 2011.

[254] C. J. Van Oss, M. K. Chaudhury, and R. J. Good, "Interfacial Lifshitz-van der Waals and polar interactions in macroscopic systems," *Chem. Rev.*, vol. 88, pp. 927-941, 1988/09/01 1988.

[255] C. J. Van Oss, R. J. Good, and M. K. Chaudhury, "Additive and nonadditive surface tension components and the interpretation of contact angles," *Langmuir*, vol. 4, pp. 884-891, 1988/07/01 1988.

[256] R. R. Deshmukh and A. R. Shetty, "Comparison of surface energies using various approaches and their suitability," *J. Appl. Polym. Sci.*, vol. 107, pp. 3707-3717, 2008.

[257] W. Wu, R. F. Giese, Jr., and C. J. van Oss, "Evaluation of the Lifshitz-van der Waals/Acid-Base Approach To Determine Surface Tension Components," *Langmuir*, vol. 11, pp. 379-382, 1995/01/01 1995.

[258] L.-H. Lee, "Correlation between Lewis Acid−Base Surface Interaction Components and Linear Solvation Energy Relationship Solvatochromic α and β Parameters," *Langmuir*, vol. 12, pp. 1681-1687, 1996/01/01 1996.

[259] D. Y. Kwok and A. W. Neumann, "Contact angle measurement and contact angle interpretation," *Adv. Colloid Interface Sci.*, vol. 81, pp. 167-249, 1999.

[260] M. Żenkiewicz, "Methods for the calculation of surface free energy of solids," *Journal of Achievements in Materials and Manufacturing Engineering*, vol. 24, pp. 137-145, 2007.

[261] D. Janssen, R. De Palma, S. Verlaak, P. Heremans, and W. Dehaen, "Static solvent contact angle measurements, surface free energy and wettability determination of

various self-assembled monolayers on silicon dioxide," *Thin Solid Films,* vol. 515, pp. 1433-1438, 2006.

[262] X. Cheng, M. Caironi, Y.-Y. Noh, C. Newman, J. Wang, M. J. Lee, K. Banger, R. Di Pietro, A. Facchetti, and H. Sirringhaus, "Downscaling of n-channel organic field-effect transistors with inkjet-printed electrodes," *Organic Electronics,* vol. 13, pp. 320-328, 2012.

[263] K.-J. Baeg, D. Khim, J.-H. Kim, M. Kang, I.-K. You, D.-Y. Kim, and Y.-Y. Noh, "Improved performance uniformity of inkjet printed n-channel organic field-effect transistors and complementary inverters," *Organic Electronics,* vol. 12, pp. 634-640, 2011.

[264] M. Greiveldinger and M. E. R. Shanahan, "Acid base contributions to interfacial free energy: self-consistency considerations," *Comptes Rendus de l'Académie des Sciences - Series IIB - Mechanics-Physics-Astronomy,* vol. 327, pp. 275-283, 1999.

[265] J. Sturm, S. Tasch, A. Niko, G. Leising, E. Toussaere, J. Zyss, T. C. Kowalczyk, K. D. Singer, U. Scherf, and J. Huber, "Optical anisotropy in thin films of a blue electroluminescent conjugated polymer," *Thin Solid Films,* vol. 298, pp. 138-142, 1997.

[266] C. Flueraru, S. Schrader, H. Motschmann, and V. Zauls, "Sensitivity analysis of ellipsometry applied to uniaxial optical films," *Thin Solid Films,* vol. 379, pp. 15-22, 2000.

[267] D. E. Aspnes, "Approximate solution of ellipsometric equations for optically biaxial crystals," *Journal of the Optical Society of America,* vol. 70, pp. 1275-1277, 1980.

[268] O. D. Gordan, T. Sakurai, M. Friedrich, K. Akimoto, and D. R. T. Zahn, "Ellipsometric study of an organic template effect: H_2P_c/PTCDA," *Organic Electronics,* vol. 7, pp. 521-527, 2006.

[269] A. Hinderhofer, U. Heinemeyer, A. Gerlach, S. Kowarik, R. M. J. Jacobs, Y. Sakamoto, T. Suzuki, and F. Schreiber, "Optical properties of pentacene and perfluoropentacene thin films," *J. Chem. Phys.,* vol. 127, 2007.

[270] B. A. Jones, A. Facchetti, M. R. Wasielewski, and T. J. Marks, "Effects of Arylene Diimide Thin Film Growth Conditions on n-Channel OFET Performance," *Advanced Functional Materials,* vol. 18, pp. 1329-1339, 2008.

[271] A. J. Ferguson and T. S. Jones, "Spectroscopic evidence for aggregate formation in N,N'-bis(phenylethyl)-perylene-3,4,9,10-bis(dicarboximide) (PPEI) films grown at room termperature," *Chemical Physics Letters,* vol. 474, pp. 137-140, 2009.

[272] G. Palasantzas, "Roughness spectrum and surface width of self-affine fractal surfaces via the K-correlation model," *Physical Review B,* vol. 48, p. 14472, 1993.

[273] J. Lin, M. Weis, D. Taguchi, T. Manaka, and M. Iwamoto, "Carrier injection and transport in organic field-effect transistor investigated by impedance spectroscopy," *Thin Solid Films,* vol. 518, pp. 448-451, 2009.